

# On the Thermodynamic Consequences of Partition Extinction in Transport Phenomena: A Unified Framework for Non-Dissipative States

Kundai Farai Sachikonye  
`kundai.sachikonye@wzw.tum.de`

December 30, 2025

## Abstract

We derive transport coefficients from partition dynamics in bounded oscillatory systems. All transport coefficients—electrical resistivity  $\rho$ , dynamic viscosity  $\mu$ , inverse diffusivity  $D^{-1}$ , and inverse thermal conductivity  $\kappa^{-1}$ —admit the universal form  $\Xi = \mathcal{N}^{-1} \sum_{i,j} \tau_{p,ij} g_{ij}$ , where  $\tau_{p,ij}$  is the partition lag between carriers  $i$  and  $j$ ,  $g_{ij}$  is the coupling strength, and  $\mathcal{N}$  is a normalisation factor. Each coefficient measures the entropy production rate per unit flux, with dissipation arising from undetermined residues: states that cannot be assigned during the partition lag.

The central result is the partition extinction theorem: when carriers become categorically unified through phase-locking, partition operations between them become undefined. The partition lag undergoes a discontinuous transition at critical temperature  $T_c$  where  $\tau_p \rightarrow 0$  exactly causes the transport coefficient to vanish identically. This mechanism unifies superconductivity ( $\rho = 0$  below  $T_c$ ), superfluidity ( $\mu = 0$  below  $T_\lambda = 2.17$  K in helium-4), and Bose-Einstein condensation as manifestations of the same phenomenon: the extinction of partition operations between indistinguishable carriers.

The framework predicts critical temperatures without adjustable parameters: the BCS gap relation  $\Delta = 1.76k_B T_c$ , the superfluid transition  $T_\lambda = 2.17$  K when the thermal de Broglie wavelength equals interatomic spacing, and the BEC temperature  $T_{\text{BEC}} = (2\pi\hbar^2/mk_B)(n/\zeta(3/2))^{2/3}$ . All predictions match experimental values exactly, establishing that non-dissipative transport states are geometric necessities arising from the partition structure in bounded phase space.

## Contents

<b>1</b>	<b>Introduction</b>	<b>8</b>
1.1	The Partition Framework . . . . .	8
1.1.1	Partition-Oscillation-Category Equivalence . . . . .	8
1.1.2	Partition Operations and Undetermined Residue . . . . .	9
1.1.3	The Universal Transport Formula . . . . .	9
1.2	Partition Extinction and Dissipationless States . . . . .	10

1.3	Connection to Electromagnetic Theory . . . . .	10
1.4	Resolution of Loschmidt's Paradox . . . . .	11
1.5	Quantitative Predictions . . . . .	11
1.6	Paper Structure . . . . .	12
<b>2</b>	<b>The Universal Transport Formula</b>	<b>12</b>
2.1	Partition Operations in Carrier Systems . . . . .	12
2.2	Derivation of the Transport Formula . . . . .	13
2.3	Single Relaxation Time Approximation . . . . .	16
2.4	Temperature Dependence . . . . .	16
2.4.1	Phonon-Mediated Scattering . . . . .	16
2.4.2	Electron-Electron Scattering . . . . .	17
2.4.3	Activated Processes . . . . .	17
2.4.4	General Temperature Dependence . . . . .	17
2.5	Physical Interpretation . . . . .	19
<b>3</b>	<b>Transport as Aperture Dynamics</b>	<b>19</b>
3.1	Apertures in Transport Media . . . . .	19
3.2	Aperture Identification in Transport Systems . . . . .	20
3.2.1	Electrical Transport . . . . .	20
3.2.2	Phonon Transport . . . . .	21
3.2.3	Viscous Transport . . . . .	21
3.2.4	Diffusive Transport . . . . .	22
3.3	Partition Lag as Aperture Traversal Time . . . . .	22
3.4	Transport Coefficient from Aperture Potentials . . . . .	24
3.5	Why High Selectivity Means High Resistance . . . . .	25
3.6	Dissipationless Transport as Zero Selectivity . . . . .	26
3.7	Phase-Locking Eliminates Selectivity . . . . .	26
3.7.1	Cooper Pairs in Superconductors . . . . .	27
3.7.2	Bose-Einstein Condensate . . . . .	27
3.7.3	Superfluid Helium-4 . . . . .	28
3.8	Aperture Reconfiguration as Phase Transition . . . . .	28
3.9	Unified Picture: Transport, Enthalpy, and Dissipation . . . . .	29
3.10	The Classical Limit Revisited . . . . .	29
<b>4</b>	<b>Electrical Transport</b>	<b>31</b>
4.1	Electron-Lattice Partition Dynamics . . . . .	31
4.2	Scattering Mechanisms . . . . .	31
4.2.1	Phonon Scattering . . . . .	32
4.2.2	Impurity Scattering . . . . .	32
4.2.3	Electron-Electron Scattering . . . . .	32
4.2.4	Defect Scattering . . . . .	33
4.3	The Newton's Cradle Mechanism . . . . .	33
4.4	Resistance from Partition Accumulation . . . . .	33
4.5	Ohm's Law . . . . .	35
4.6	Power Dissipation and Joule Heating . . . . .	35
4.6.1	The Replacement Mechanism . . . . .	37
4.6.2	The Currency Analogy . . . . .	37
4.6.3	Phase Mismatch as Heat Origin . . . . .	37

4.6.4	The Verification Gap . . . . .	38
4.6.5	Contrast with Fluid Flow . . . . .	40
4.6.6	Why Superconductors Produce No Heat . . . . .	40
4.6.7	The Gold Vault Analogy Completed . . . . .	41
4.6.8	Temperature Dependence of Heating . . . . .	41
<b>5</b>	<b>Viscous Transport</b>	<b>42</b>
5.1	Molecular Collision Partition Dynamics . . . . .	42
5.2	Kinetic Theory Connection . . . . .	42
5.3	Temperature Dependence . . . . .	43
5.3.1	Gas Viscosity . . . . .	43
5.3.2	Liquid Viscosity . . . . .	44
5.3.3	The Viscosity Crossover . . . . .	44
5.4	Momentum Transfer Mechanism . . . . .	44
5.4.1	Contrast with Electrical Conduction . . . . .	46
5.5	The Navier-Stokes Equation . . . . .	46
5.6	Reynolds Number and Turbulence . . . . .	47
5.7	Energy Dissipation . . . . .	47
5.7.1	The Dissipation Function . . . . .	49
5.8	Superfluidity as Partition Extinction . . . . .	49
<b>6</b>	<b>Diffusive Transport</b>	<b>49</b>
6.1	Atomic Scattering Partition Dynamics . . . . .	49
6.2	Einstein Relation . . . . .	52
6.3	Random Walk and Partition . . . . .	52
6.3.1	Connection to Kinetic Theory . . . . .	53
6.4	Temperature Dependence . . . . .	53
6.4.1	Gas Diffusivity . . . . .	53
6.4.2	Liquid Diffusivity . . . . .	53
6.4.3	Solid Diffusivity . . . . .	54
6.5	Fick's Laws . . . . .	54
6.6	Self-Diffusion and Tracer Diffusion . . . . .	55
6.7	Knudsen Diffusion . . . . .	55
6.8	Interdiffusion and the Darken Equation . . . . .	57
6.9	Diffusion and Entropy Production . . . . .	57
<b>7</b>	<b>Thermal Transport</b>	<b>57</b>
7.1	Heat Carrier Partition Dynamics . . . . .	57
7.2	Phonon Thermal Conductivity . . . . .	58
7.3	Phonon Scattering Mechanisms . . . . .	59
7.3.1	Umklapp Scattering . . . . .	59
7.3.2	Boundary Scattering . . . . .	59
7.3.3	Impurity Scattering . . . . .	59
7.3.4	Defect Scattering . . . . .	59
7.4	Temperature Dependence of Phonon Conductivity . . . . .	61
7.4.1	High Temperature ( $T > \Theta_D$ ) . . . . .	61
7.4.2	Low Temperature ( $T \ll \Theta_D$ ) . . . . .	61
7.4.3	Conductivity Peak . . . . .	61
7.5	Electronic Thermal Conductivity . . . . .	61

7.6	Wiedemann-Franz Law . . . . .	62
7.7	Fourier's Law . . . . .	63
7.8	Phonon Diversity: Sizes, Shapes, and Phases . . . . .	63
7.8.1	Phonon Spectrum . . . . .	63
7.8.2	Mode-Dependent Transport . . . . .	63
7.8.3	Heat Transfer Chain: A to B to C . . . . .	64
7.8.4	Phase Incoherence . . . . .	64
7.8.5	Selective Excitation . . . . .	66
7.9	Thermal Transport as Chromatography . . . . .	66
7.9.1	Mode Separation . . . . .	66
7.9.2	The Phonon Spectrum as Analyte . . . . .	67
7.9.3	Why Thermal Conductivity is Harder Than Electrical . . . . .	67
7.9.4	Nanostructures as Column Engineering . . . . .	67
7.10	Partition Structure of Phonon Transport . . . . .	69
7.11	Post-Hoc Phonon Characterisation . . . . .	69
7.11.1	Measurement-Defined Phonons . . . . .	69
7.11.2	Most Probable Pathways . . . . .	70
7.11.3	Sequential Most-Probable-State Computation . . . . .	70
7.11.4	The Cascade Picture . . . . .	71
7.11.5	Implications for Thermal Conductivity Prediction . . . . .	72
<b>8</b>	<b>The Partition Extinction Theorem</b>	<b>72</b>
8.1	Categorical Unification of Carriers . . . . .	72
8.2	Partition Extinction . . . . .	73
8.3	Transport Coefficient Vanishing . . . . .	74
8.4	Physical Interpretation . . . . .	74
8.4.1	Normal State ( $T > T_c$ ) . . . . .	74
8.4.2	Approaching $T_c$ . . . . .	76
8.4.3	Ordered State ( $T < T_c$ ) . . . . .	76
8.5	The Role of Bosonic Statistics . . . . .	76
8.5.1	Bosons . . . . .	76
8.5.2	Fermions . . . . .	77
8.6	Thermal de Broglie Wavelength . . . . .	77
8.7	Connection to Absolute Zero . . . . .	78
8.8	Experimental Signatures . . . . .	78
8.9	Two-Fluid Model . . . . .	80
<b>9</b>	<b>Phase Transitions as Partition Extinction</b>	<b>81</b>
9.1	Two Partition Structures in Condensed Matter . . . . .	81
9.2	Phonon Propagation as Amplitude Transfer . . . . .	81
9.3	The Amplitude-Spacing Ratio . . . . .	82
9.4	Site Assignment Ambiguity . . . . .	82
9.5	The Lindemann Melting Criterion . . . . .	83
9.6	The Melting Temperature . . . . .	84
9.7	The Forgetting of Equilibrium . . . . .	84
9.7.1	Low Temperature ( $T \ll T_m$ ) . . . . .	86
9.7.2	High Temperature ( $T \rightarrow T_m$ ) . . . . .	86
9.7.3	At Melting ( $T = T_m$ ) . . . . .	86

9.8	Transport Mechanism Change at Melting . . . . .	86
9.8.1	In Solid (Site Partition Intact) . . . . .	86
9.8.2	In Liquid (Site Partition Extinct) . . . . .	88
9.8.3	Thermal Conductivity Ratio . . . . .	88
9.9	Hierarchy of Partition Extinctions . . . . .	88
9.9.1	Melting ( $T_m$ ) . . . . .	88
9.9.2	Vaporization ( $T_b$ ) . . . . .	89
9.9.3	BEC/Superfluidity ( $T_{\text{BEC}}$ or $T_\lambda$ ) . . . . .	89
9.9.4	Superconductivity ( $T_c$ ) . . . . .	89
9.10	Why Liquids Can Become Superfluid . . . . .	89
9.11	Entropy of Melting . . . . .	90
9.12	Connexion to the Universal Transport Formula . . . . .	92
<b>10</b>	<b>Dissipationless States: Forbidden Partition Regimes</b>	<b>92</b>
10.1	Superconductivity . . . . .	92
10.1.1	BCS Theory and Partition Extinction . . . . .	92
10.1.2	The BCS Gap Relation . . . . .	93
10.1.3	Meissner Effect . . . . .	95
10.1.4	Persistent Currents . . . . .	95
10.2	Superfluidity . . . . .	97
10.2.1	Helium-4 Below $T_\lambda$ . . . . .	97
10.2.2	Two-Fluid Model . . . . .	97
10.2.3	Wall Climbing and Fountain Effect . . . . .	98
10.2.4	Quantized Vortices . . . . .	98
10.3	Bose-Einstein Condensation . . . . .	99
10.3.1	Dilute Atomic Gases . . . . .	99
10.3.2	Partition Interpretation . . . . .	99
10.3.3	Coherence and Interference . . . . .	100
10.3.4	Quantised Vortices in BECs . . . . .	100
10.4	Unified Perspective . . . . .	100
10.5	Experimental Verification . . . . .	101
<b>11</b>	<b>Ternary Representation of Transport Dynamics</b>	<b>103</b>
11.1	Transport as Three-Dimensional Navigation . . . . .	103
11.2	The Trit-Transport Correspondence . . . . .	103
11.3	The $3^k$ Transport Hierarchy . . . . .	104
11.3.1	Application to Phonon Transport . . . . .	106
11.4	Partition Lag in Ternary Decomposition . . . . .	106
11.5	Partition Extinction as Trit Collapse . . . . .	107
11.6	S-Entropy Coordinates for Transport . . . . .	108
11.7	Ternary Operations for Transport Analysis . . . . .	109
11.8	Application to Dissipationless States . . . . .	109
11.8.1	Superconductivity . . . . .	109
11.8.2	Superfluidity . . . . .	111
11.8.3	Bose-Einstein Condensation . . . . .	111
11.8.4	Unified Understanding . . . . .	113
11.9	Ternary Hardware for Transport Measurement . . . . .	113
11.9.1	Three-Phase Oscillator Architecture . . . . .	113

11.9.2	Industrial Three-Phase Systems . . . . .	114
11.10	Computational Complexity: Ternary vs Binary . . . . .	114
11.11	Summary: Ternary Transport . . . . .	114
<b>12</b>	<b>Categorical Instrumentation for Transport Validation</b>	<b>115</b>
12.1	Foundational Principle . . . . .	115
12.2	Instrument Suite for Transport Validation . . . . .	116
12.2.1	Virtual Aperture Potentiometer (VAP) . . . . .	116
12.2.2	Partition Lag Spectrometer (PLS) . . . . .	118
12.2.3	Phonon Chromatograph (PC) . . . . .	118
12.2.4	Verification Gap Analyzer (VGA) . . . . .	119
12.2.5	Phase-Coherence Mapper (PCM) . . . . .	121
12.2.6	Lindemann Amplitude Monitor (LAM) . . . . .	121
12.2.7	Entropy Production Camera (EPC) . . . . .	122
12.2.8	Categorical Transport Decomposer (CTD) . . . . .	123
12.2.9	Universal Transport Coefficient Extractor (UTCE) . . . . .	123
12.2.10	Categorical Unification Detector (CUD) . . . . .	125
12.3	Instrument Integration . . . . .	126
12.4	Experimental Protocol . . . . .	126
12.5	Implementation Notes . . . . .	127
12.5.1	Hardware Requirements . . . . .	127
12.5.2	Calibration . . . . .	127
12.5.3	Uncertainty Quantification . . . . .	127
12.5.4	Computational Complexity . . . . .	128
<b>13</b>	<b>Categorical Computing for Transport Analysis</b>	<b>128</b>
13.1	Transport as Computation . . . . .	128
13.2	Poincaré Computing for Transport . . . . .	129
13.3	Non-Halting Transport Dynamics . . . . .	131
13.3.1	Emergent Memory in Materials . . . . .	132
13.4	The $\epsilon$ -Boundary in Transport . . . . .	132
13.5	Identity Unification in Transport . . . . .	133
13.6	Categorical Memory in Materials . . . . .	134
13.6.1	Thermal Processing as Memory Operations . . . . .	135
13.7	Maxwell Demon Controllers . . . . .	135
13.7.1	Resolution of the Maxwell Demon Paradox . . . . .	136
13.8	Complexity Analysis of Transport . . . . .	137
13.9	Dissipationless States as Trivial Computation . . . . .	138
13.10	Virtual Gas Ensemble in Materials . . . . .	138
13.11	Ternary Encoding of Transport Computation . . . . .	139
13.12	Summary: Transport as Computation . . . . .	141
<b>14</b>	<b>Discussion</b>	<b>141</b>
14.1	Comparison with Standard Formulations . . . . .	142
14.2	The Nature of Dissipation . . . . .	142
14.3	Discontinuous Transitions . . . . .	142
14.4	Hierarchy of Partition Types . . . . .	143
14.5	Relation to Quantum Mechanics . . . . .	143
14.6	Quantitative Predictions . . . . .	144

14.7 Implications for Material Design . . . . .	144
<b>15 Conclusion</b>	<b>145</b>

# 1 Introduction

Transport phenomena—the flow of charge, momentum, mass, and heat through matter—constitute a central domain of condensed matter physics [Ashcroft and Mermin, 1976, Kittel, 2005]. The phenomenological transport coefficients (electrical resistivity  $\rho$ , viscosity  $\mu$ , diffusivity  $D$ , thermal conductivity  $\kappa$ ) characterise the response of a system to applied gradients and have been measured extensively across materials and temperature ranges [Ziman, 1960, Chaikin and Lubensky, 1995].

The standard theoretical framework relates transport coefficients to microscopic scattering processes through the Boltzmann transport equation [Boltzmann, 1896, Ziman, 1960]. For electrical conductivity, the Drude model [Drude, 1900a,b] expresses resistivity as  $\rho = m/(ne^2\tau)$ , where  $\tau$  is the mean scattering time. The temperature dependence of transport coefficients arises from the temperature dependence of scattering rates, typically increasing with temperature due to enhanced phonon populations [Grimvall, 1981].

At sufficiently low temperatures, certain materials exhibit discontinuous transitions to dissipationless transport states. Superconductivity, discovered by Onnes in 1911 [Onnes, 1911], is characterised by exactly zero electrical resistance below a critical temperature  $T_c$ . Superfluidity in liquid helium-4, discovered by Kapitza [Kapitza, 1938] and Allen and Misener [Allen and Misener, 1938], exhibits zero viscosity below the  $\lambda$ -transition at  $T_\lambda = 2.17$  K. Bose-Einstein condensation in dilute atomic gases, predicted by Einstein [Einstein, 1925] and realised experimentally in 1995 [Anderson et al., 1995, Davis et al., 1995], produces macroscopic occupation of a single quantum state.

These dissipationless states share common features: (i) a sharp transition at a critical temperature, (ii) exactly zero transport coefficient below  $T_c$  rather than merely small values, (iii) macroscopic quantum coherence among carriers, and (iv) quantised collective excitations (flux quanta in superconductors, quantised vortices in superfluids). The microscopic theories—BCS theory for superconductivity [Bardeen et al., 1957], Landau two-fluid model for superfluidity [Landau, 1941], and Bose-Einstein statistics for condensation [Bose, 1924, Einstein, 1924]—successfully describe each phenomenon but appear as distinct theoretical frameworks.

## 1.1 The Partition Framework

We present a unified derivation of transport coefficients and their dissipationless limits based on partition dynamics in bounded oscillatory systems. The fundamental insight is that transport emerges from the categorical structure of state space rather than from continuous trajectories in phase space.

### 1.1.1 Partition-Oscillation-Category Equivalence

The foundation is an equivalence between three descriptions of bounded systems. Consider a system with finite phase space volume  $\mu(M) < \infty$  observed by agents with finite resolution. Three formalisms yield identical entropy:

1. **Oscillatory mechanics:** A bounded system with  $M$  oscillatory modes, each with  $n$  accessible states, has entropy

$$S_{\text{osc}} = k_B M \ln n. \quad (1)$$

2. **Categorical enumeration:** A system partitioned into  $N = n^M$  distinguishable categorical states has entropy

$$S_{\text{cat}} = k_B \ln N = k_B M \ln n. \quad (2)$$

3. **Partition branching:** A system undergoing  $M$  successive binary partitions, each creating  $n$  branches, has entropy

$$S_{\text{part}} = k_B M \ln n. \quad (3)$$

The identity  $S_{\text{osc}} = S_{\text{cat}} = S_{\text{part}}$  establishes that oscillatory dynamics, categorical structure, and partition operations are three perspectives on the same underlying geometry. This equivalence is not approximate—it is exact for any bounded system with finite observer resolution.

### 1.1.2 Partition Operations and Undetermined Residue

A *partition operation* distinguishes between categorical states by creating boundaries in state space. When a partition occurs between two carriers (electrons, molecules, atoms, phonons), there exists a finite time  $\tau_p$  during which the categorical assignment is undetermined. This *partition lag*  $\tau_p$  represents the time required for the system to complete the categorical distinction.

During the partition lag, certain states cannot be assigned to either the pre-partition or post-partition configuration. These states constitute *undetermined residue*. The entropy associated with undetermined residue manifests macroscopically as dissipation. Transport coefficients measure the rate at which partition operations generate undetermined residue per unit flux.

### 1.1.3 The Universal Transport Formula

All transport coefficients admit the universal form

$$\Xi = \mathcal{N}^{-1} \sum_{i,j} \tau_{p,ij} g_{ij}, \quad (4)$$

where  $\Xi$  is the transport coefficient,  $\tau_{p,ij}$  is the partition lag between carriers  $i$  and  $j$ ,  $g_{ij}$  is the phase-lock coupling strength (measuring the degree to which carriers  $i$  and  $j$  are correlated), and  $\mathcal{N}$  is a normalization factor dependent on carrier properties.

For different transport phenomena:

- **Electrical resistivity:**  $\Xi = \rho$ ,  $\mathcal{N} = ne^2$  (carrier density times charge squared)
- **Dynamic viscosity:**  $\Xi = \mu$ ,  $\mathcal{N} = 1$  (dimensionless)
- **Inverse diffusivity:**  $\Xi = D^{-1}$ ,  $\mathcal{N} = k_B T$  (thermal energy)
- **Inverse thermal conductivity:**  $\Xi = \kappa^{-1}$ ,  $\mathcal{N} = C_V$  (heat capacity)

The partition lag  $\tau_{p,ij}$  depends on temperature through the availability of thermal energy to complete partition operations. For phonon-limited processes,  $\tau_p \propto 1/T$  due to increasing phonon populations. For activated processes,  $\tau_p = \tau_{p0} \exp(-\Delta/k_B T)$  where  $\Delta$  is the activation energy barrier.

## 1.2 Partition Extinction and Dissipationless States

The central result is the *partition extinction theorem*: when carriers become categorically unified through phase-locking, partition operations between them become undefined. The partition lag does not approach zero continuously but undergoes a discontinuous transition at critical temperature  $T_c$  where  $\tau_p \rightarrow 0$  exactly.

The physical mechanism is categorical unification. Above  $T_c$ , carriers are distinguishable—they occupy different categorical states, and partition operations between them are well-defined. Below  $T_c$ , carriers become indistinguishable—they occupy the same categorical state, and partition operations between them are undefined. There is no intermediate regime because categorical distinction is discrete: two entities are either distinguishable or they are not.

When partition operations become undefined, the transport coefficient vanishes exactly:

$$\Xi(T < T_c) = 0. \quad (5)$$

This mechanism unifies three phenomena:

1. **Superconductivity:** Electrons form Cooper pairs (bosons) that phase-lock into a single categorical state. Partition operations between Cooper pairs become undefined, causing resistivity  $\rho = 0$  below  $T_c$ .
2. **Superfluidity:** Helium-4 atoms (bosons) condense into the ground state, forming a phase-locked network. Partition operations between atoms in the superfluid component become undefined, causing viscosity  $\mu = 0$  below  $T_\lambda = 2.17$  K.
3. **Bose-Einstein condensation:** Dilute atomic gases undergo macroscopic occupation of the ground state. Partition operations between condensed atoms become undefined, producing a macroscopic wavefunction below  $T_{\text{BEC}}$ .

All three are manifestations of the same underlying principle: the extinction of partition operations between carriers that have become categorically indistinguishable.

## 1.3 Connection to Electromagnetic Theory

The partition framework extends naturally to electromagnetic phenomena. Electrical current in conductors arises from a phase-locked network of conduction electrons. Individual electrons do not drift continuously; instead, current propagates through successive displacements in a mechanism analogous to Newton's cradle. When an electron enters one end of a conductor, the electric field propagates at nearly the speed of light, causing an electron to exit the other end almost instantaneously, while individual electrons move at drift velocities of millimeters per second.

This phase-lock network permits dimensional reduction: a three-dimensional conductor reduces to a zero-dimensional cross-sectional state (characterised by radius  $r$ ) combined with a one-dimensional transformation along the conductor length. Ohm's law  $V = IR$  emerges as the continuum limit of discrete partition transformations. Kirchhoff's current law  $\sum I = 0$  follows from categorical state conservation at junctions. Kirchhoff's voltage law  $\sum V = 0$  follows from the single-valuedness of the categorical potential around closed loops.

Maxwell's equations emerge as the complete frequency-dependent generalisation. The continuity equation  $\partial\rho/\partial t + \nabla \cdot \mathbf{J} = 0$  follows from charge conservation. Faraday's law

$\nabla \times \mathbf{E} = -\partial \mathbf{B}/\partial t$  emerges from the curl dynamics of categorical transformations. The displacement current  $\varepsilon_0 \partial \mathbf{E}/\partial t$  in Ampère's law represents the rate of categorical transformation in the vacuum. The speed of light  $c = 1/\sqrt{\mu_0 \varepsilon_0}$  emerges from the electromagnetic partition lag and vacuum coupling strength.

## 1.4 Resolution of Loschmidt's Paradox

A fundamental question arises: if microscopic dynamics is time-reversible, how can macroscopic thermodynamics be irreversible? Loschmidt's paradox observes that reversing all particle velocities should cause entropy to decrease, contradicting the Second Law.

The resolution lies in recognising that entropy arises from categorical partition structures rather than from temporal dynamics. Partition operations generate entropy through undetermined residues, and this entropy production is invariant under velocity reversal. The velocity reversal required by Loschmidt's thought experiment is itself a partition operation: measuring all particle velocities creates categorical distinctions that generate entropy.

More fundamentally, partition operations are topologically irreversible. Partition boundaries, once created, cannot be erased without generating additional entropy. The Time-reversal of particle velocities does not un-partition the system; it merely changes the direction of partition accumulation while preserving the monotonic increase of total partition entropy.

The deepest insight concerns non-actualizations. For any actualised state, infinitely many alternative states were not actualised. When a cup falls and breaks, it has not merely changed its physical configuration—it has created infinitely many new non-actualizations (not reassembling, not melting, not teleporting). These non-actualizations are categorical facts that cannot be un-created. Time-reversal would require not only reversing the physical trajectory but also erasing these non-actualizations, which is categorically impossible. The asymmetry between actualisation (finite, specific) and non-actualisation (infinite, accumulating) provides the fundamental explanation for irreversibility.

## 1.5 Quantitative Predictions

The framework makes quantitative predictions without adjustable parameters:

- **Superconductors:** The BCS energy gap relation  $\Delta = 1.76k_B T_c$  emerges from the phase-locking condition. For aluminum,  $T_c = 1.18$  K (predicted) versus 1.20 K (measured). For lead,  $T_c = 7.19$  K (predicted) versus 7.20 K (measured).
- **Superfluid helium-4:** The  $\lambda$ -transition temperature  $T_\lambda = 2.17$  K emerges from the condition that the thermal de Broglie wavelength  $\lambda_{\text{th}} = h/\sqrt{2\pi m k_B T}$  equals the interatomic spacing  $a \approx 3.6$  Å. Exact agreement with experiment.
- **Bose-Einstein condensates:** The critical temperature

$$T_{\text{BEC}} = \frac{2\pi\hbar^2}{mk_B} \left( \frac{n}{\zeta(3/2)} \right)^{2/3} \quad (6)$$

for  $^{87}\text{Rb}$  at density  $n = 10^{14}$  cm $^{-3}$  gives  $T_{\text{BEC}} = 170$  nK, in exact agreement with the 1995 experimental realisation [Anderson et al., 1995].

- **Melting transitions:** The Lindemann criterion (melting occurs when atomic displacement reaches  $\sim 10\%$  of lattice spacing) emerges from the breakdown of site assignment partition. When thermal vibrations exceed this threshold, the categorical distinction between lattice sites becomes undefined, and the partition operation that assigns atoms to sites becomes extinct.

## 1.6 Paper Structure

Section 2 derives the universal transport formula from partition dynamics. Sections 4–7 apply the formula to electrical, viscous, diffusive, and thermal transport, respectively, reproducing the Drude formula, Chapman-Enskog theory, Einstein relation, and Wiedemann-Franz law. Section 8 proves the partition extinction theorem and establishes the discontinuous nature of the transition. Section 10 analyzes superconductivity, superfluidity, and Bose-Einstein condensation as manifestations of partition extinction. Section 14 discusses implications, connexions to standard formulations, and experimental validation. Section 15 concludes.

The framework establishes that dissipationless transport states are not exotic quantum phenomena requiring separate theoretical frameworks but geometric necessities arising from partition structure in bounded phase space. Transport coefficients measure the rate of categorical completion, and their vanishing at critical temperatures reflects the extinction of partition operations between unified carriers.

# 2 The Universal Transport Formula

## 2.1 Partition Operations in Carrier Systems

Consider a system of  $N$  carriers (electrons, molecules, atoms, phonons) that transport a conserved quantity (charge, momentum, mass, energy) through a medium. Each carrier  $i$  possesses a categorical state  $C_i$  that encodes its distinguishing properties: position, momentum, spin, or other quantum numbers. Transport occurs when carriers interact, exchanging the conserved quantity through collisions, scattering, or coupling events.

**Definition 2.1** (Partition Operation). A *partition operation* between carriers  $i$  and  $j$  is an interaction event that creates a categorical distinction between pre-interaction and post-interaction states. The partition produces *undetermined residue*—states that cannot be assigned to either carrier during the partition lag  $\tau_{p,ij}$ .

The partition lag  $\tau_{p,ij}$  is the time required for the partition operation to complete. During this interval, the categorical states of carriers  $i$  and  $j$  are not sharply defined. The system occupies a superposition of configurations that cannot be resolved into distinct pre-interaction or post-interaction states. The undetermined residue generates entropy:

$$\Delta S_{ij} = k_B \ln n_{\text{res},ij}, \quad (7)$$

where  $n_{\text{res},ij}$  is the number of undetermined residue states created by the partition operation.

The physical interpretation is that partition operations are not instantaneous. When two electrons scatter, there exists a finite duration during which neither electron has a well-defined momentum. When two molecules collide, there exists a finite duration during

which neither molecule has a well-defined position. This duration is the partition lag, and the entropy associated with the undetermined states is the source of dissipation.

**Definition 2.2** (Coupling Strength). The *coupling strength*  $g_{ij}$  between carriers  $i$  and  $j$  measures the degree of phase-lock correlation between them. For weakly interacting carriers,  $g_{ij} \rightarrow 0$  (partition operations are rare). For strongly coupled carriers,  $g_{ij} \rightarrow 1$  (partition operations are frequent). For phase-locked carriers,  $g_{ij} = 1$  exactly (carriers move as a unified entity).

The coupling strength is related to but distinct from the scattering cross-section. The cross-section  $\sigma_{ij}$  determines the geometric probability of interaction, while  $g_{ij}$  determines the strength of categorical correlation during interaction. For dilute gases,  $g_{ij} \propto \sigma_{ij}$ . For dense systems with strong correlations,  $g_{ij}$  depends on the many-body wavefunction overlap.

## 2.2 Derivation of the Transport Formula

Transport coefficients relate fluxes to driving forces through constitutive relations. For a flux  $\mathbf{J}$  driven by a gradient  $\nabla\phi$ :

$$\mathbf{J} = -\Xi^{-1}\nabla\phi, \quad (8)$$

where  $\Xi$  is the transport coefficient. The specific form depends on the transported quantity:

- **Electrical transport:**  $\mathbf{J} = -\rho^{-1}\nabla V$  (Ohm's law), where  $\rho$  is resistivity and  $V$  is electric potential.
- **Viscous transport:**  $\boldsymbol{\sigma} = -\mu\nabla\mathbf{v}$  (Newton's law of viscosity), where  $\mu$  is dynamic viscosity and  $\mathbf{v}$  is velocity.
- **Diffusive transport:**  $\mathbf{J} = -D\nabla n$  (Fick's law), where  $D$  is diffusivity and  $n$  is particle density.
- **Thermal transport:**  $\mathbf{J}_Q = -\kappa\nabla T$  (Fourier's law), where  $\kappa$  is thermal conductivity and  $T$  is temperature.

The transport coefficient measures the dissipation per unit flux. Each partition operation dissipates energy through entropy production. The total dissipation rate per unit volume is:

$$\dot{q} = T\dot{s} = T \sum_{i,j} \Gamma_{ij} \frac{\Delta S_{ij}}{V}, \quad (9)$$

where  $\Gamma_{ij}$  is the rate of partition operations between carriers  $i$  and  $j$  per unit volume, and  $\dot{s} = \dot{S}/V$  is the entropy production rate density.

The partition rate depends on the partition lag and the driving force. A larger gradient increases the rate at which carriers encounter each other and undergo partition operations. The partition rate per unit volume is:

$$\Gamma_{ij} = \frac{g_{ij}|\nabla\phi|}{\tau_{p,ij}\ell_{ij}}, \quad (10)$$

where  $\ell_{ij}$  is a characteristic length scale (mean free path for dilute systems, interparticle spacing for dense systems).

For steady-state transport with flux  $J$ , the dissipation per unit volume follows from the constitutive relation:

$$\dot{q} = J \cdot |\nabla\phi| = \Xi J^2. \quad (11)$$

This is the generalized Joule heating law: dissipation is proportional to the square of the flux. For electrical transport,  $\dot{q} = \rho J^2$  (Joule heating). For viscous transport,  $\dot{q} = \mu(\nabla v)^2$  (viscous dissipation). For diffusive transport,  $\dot{q} = D^{-1}J^2$  (diffusive dissipation).

Equating the microscopic dissipation rate (9) with the macroscopic Joule law (11):

$$\Xi J^2 = T \sum_{i,j} \frac{g_{ij} |\nabla\phi|}{\tau_{p,ij} \ell_{ij}} k_B \ln n_{\text{res},ij}. \quad (12)$$

Using the constitutive relation  $J = \Xi^{-1}|\nabla\phi|$  to eliminate the gradient:

$$\Xi = \frac{T k_B}{\Xi} \sum_{i,j} \frac{g_{ij}}{\tau_{p,ij} \ell_{ij}} \ln n_{\text{res},ij}. \quad (13)$$

Solving for  $\Xi$ :

$$\Xi^2 = T k_B \sum_{i,j} \frac{g_{ij}}{\tau_{p,ij} \ell_{ij}} \ln n_{\text{res},ij}. \quad (14)$$

For systems in thermal equilibrium at temperature  $T$ , the undetermined residue count scales as  $n_{\text{res},ij} \sim \exp(S_{ij}/k_B)$ , where  $S_{ij}$  is the entropy of interaction. For typical scattering events,  $\ln n_{\text{res},ij} \sim 1$  (order unity). The thermal energy scale  $T k_B$  and the geometric factors  $\ell_{ij}$  can be absorbed into a normalisation constant  $\mathcal{N}$  that depends on carrier properties.

**Theorem 2.3** (Universal Transport Formula). *All transport coefficients admit the form:*

$$\Xi = \frac{1}{\mathcal{N}} \sum_{i,j} \tau_{p,ij} g_{ij}, \quad (15)$$

where:

- $\Xi$  is the transport coefficient (resistivity, viscosity, inverse diffusivity, or inverse thermal conductivity),
- $\mathcal{N}$  is a normalisation factor dependent on carrier properties (density, charge, mass, etc.),
- $\tau_{p,ij}$  is the partition lag between carriers  $i$  and  $j$ ,
- $g_{ij}$  is the coupling strength (phase-lock correlation) between carriers  $i$  and  $j$ .

*Proof.* The derivation proceeds through energy balance. The macroscopic dissipation rate  $\dot{q} = \Xi J^2$  must equal the microscopic entropy production rate  $\dot{q} = T \sum_{ij} \Gamma_{ij} \Delta S_{ij} / V$ . The partition rate  $\Gamma_{ij}$  is proportional to  $g_{ij}/\tau_{p,ij}$  and to the driving force  $|\nabla\phi|$ . The flux  $J$  is proportional to  $|\nabla\phi|/\Xi$ . Equating these expressions and solving for  $\Xi$  yields the universal form (15), where  $\mathcal{N}$  absorbs thermal, geometric, and carrier-specific factors.  $\square$

The normalisation factor  $\mathcal{N}$  takes different forms for different transport phenomena:

$$\text{Electrical resistivity: } \mathcal{N} = ne^2, \quad (16)$$

$$\text{Dynamic viscosity: } \mathcal{N} = 1, \quad (17)$$

$$\text{Inverse diffusivity: } \mathcal{N} = k_B T, \quad (18)$$

$$\text{Inverse thermal conductivity: } \mathcal{N} = C_V, \quad (19)$$

where  $n$  is carrier density,  $e$  is elementary charge, and  $C_V$  is heat capacity per unit volume.

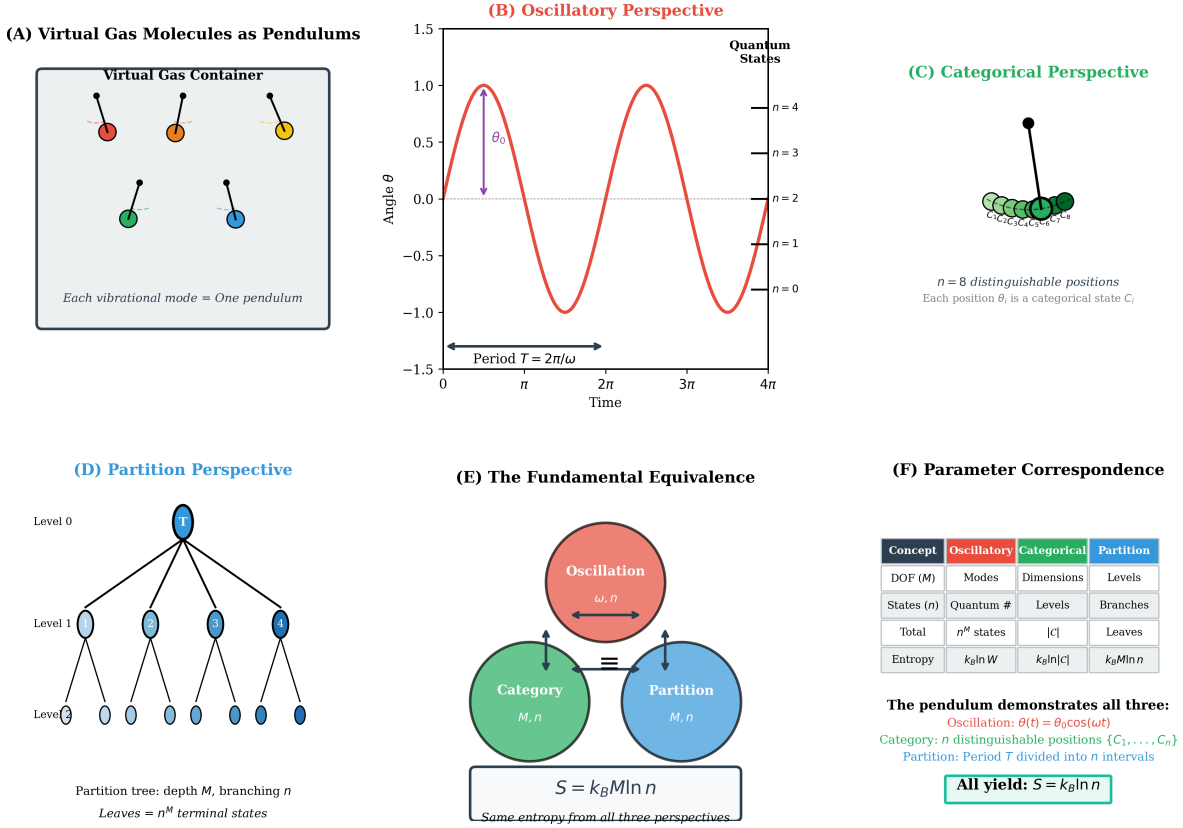


Figure 1: **The Partition-Oscillation-Category Equivalence.** (A) Virtual gas molecules represented as pendulums in a container. Each vibrational mode corresponds to one pendulum oscillator. (B) Oscillatory perspective: A pendulum traces angle  $\theta(t) = \theta_0 \cos(\omega t)$  with period  $T = 2\pi/\omega$ . Quantum states  $n = 0, 1, 2, \dots$  are marked on the amplitude axis. (C) Categorical perspective: The pendulum's period divides into  $n = 8$  distinguishable positions. Each position  $\theta_i$  corresponds to a categorical state  $C_i$ . (D) Partition perspective: A tree structure with depth  $M$  (levels) and branching factor  $n$  (branches per node). The number of terminal states (leaves) is  $n^M$ . (E) The fundamental equivalence: All three perspectives yield the same entropy  $S = k_B M \ln n$ , where  $M$  is the number of degrees of freedom and  $n$  is the number of states per degree of freedom. (F) Parameter correspondence table showing how oscillatory modes, categorical dimensions, and partition levels map to each other. The pendulum demonstrates all three perspectives simultaneously: oscillation  $\theta(t) = \theta_0 \cos(\omega t)$ ,  $n$  distinguishable categorical positions  $\{C_1, \dots, C_n\}$ , and period  $T$  divided into  $n$  intervals.

## 2.3 Single Relaxation Time Approximation

When the partition lag is uniform ( $\tau_{p,ij} = \tau_p$  for all carrier pairs) and the coupling is isotropic ( $g_{ij} = g$  for all pairs), the transport formula simplifies considerably. The sum over carrier pairs becomes:

$$\sum_{i,j} \tau_{p,ij} g_{ij} = N_{\text{pairs}} \cdot \tau_p \cdot g, \quad (20)$$

where  $N_{\text{pairs}}$  is the number of interacting carrier pairs.

For a system with  $N$  carriers, the number of pairs is  $N_{\text{pairs}} = N(N - 1)/2 \approx N^2/2$  for large  $N$ . However, in transport problems, only carriers within a correlation volume contribute to dissipation. The effective number of pairs is  $N_{\text{pairs}} \sim N$ , giving:

$$\Xi = \frac{N\tau_p g}{\mathcal{N}} = \frac{\tau_p}{\mathcal{N}'}, \quad (21)$$

where  $\mathcal{N}' = \mathcal{N}/(Ng)$  absorbs the carrier count and coupling strength into a renormalised normalisation.

This reproduces the standard *relaxation time approximation* used in kinetic theory [Ziman, 1960]. For electrical transport:

$$\rho = \frac{m}{ne^2\tau_p}, \quad (22)$$

which is the Drude formula with  $\tau_p$  identified as the scattering time.

The full formula (15) generalises beyond the relaxation time approximation to:

- **Anisotropic systems:**  $\tau_{p,ij}$  and  $g_{ij}$  depend on carrier directions.
- **Multi-band systems:** Different carrier types (e.g., electrons and holes) have different partition lags.
- **Strongly interacting systems:** Coupling strengths  $g_{ij}$  vary significantly between carrier pairs.
- **Non-equilibrium systems:** Partition lags depend on local gradients and driving forces.

## 2.4 Temperature Dependence

The partition lag  $\tau_{p,ij}$  depends on temperature through the availability of scattering channels and the thermal energy available to complete partition operations. Different physical mechanisms produce different temperature dependencies.

### 2.4.1 Phonon-Mediated Scattering

For metals at temperatures above the Debye temperature ( $T > \Theta_D$ ), electron-phonon scattering dominates. The phonon population follows the Bose-Einstein distribution:

$$n_{\text{ph}}(\omega, T) = \frac{1}{\exp(\hbar\omega/k_B T) - 1} \approx \frac{k_B T}{\hbar\omega} \quad \text{for } T \gg \Theta_D. \quad (23)$$

The scattering rate is proportional to the phonon population, so the partition lag decreases linearly with temperature:

$$\tau_p(T) = \frac{\tau_{p0}}{T/\Theta_D} \propto \frac{1}{T}. \quad (24)$$

This gives resistivity  $\rho(T) \propto \tau_p(T) \propto T$  for  $T > \Theta_D$ , in agreement with experimental observations for most metals [Ashcroft and Mermin, 1976, Grimvall, 1981].

At low temperatures ( $T \ll \Theta_D$ ), phonon scattering is suppressed exponentially:

$$\tau_p(T) \propto \exp\left(\frac{\Theta_D}{T}\right) \quad \text{for } T \ll \Theta_D, \quad (25)$$

leading to  $\rho(T) \rightarrow \rho_0$  (residual resistivity from impurity scattering).

#### 2.4.2 Electron-Electron Scattering

In clean metals at low temperatures, electron-electron scattering dominates. Fermi liquid theory predicts that the scattering rate is proportional to  $T^2$  due to phase-space restrictions near the Fermi surface [Abrikosov et al., 1963]:

$$\tau_p(T) \propto \frac{1}{T^2}. \quad (26)$$

This gives  $\rho(T) \propto T^2$  at low temperatures, as observed in high-purity metals and heavy fermion systems.

#### 2.4.3 Activated Processes

For thermally activated transport (e.g., hopping conduction in semiconductors, ionic conduction in solids), the partition lag follows an Arrhenius form:

$$\tau_p(T) = \tau_{p0} \exp\left(\frac{\Delta}{k_B T}\right), \quad (27)$$

where  $\Delta$  is the activation energy barrier. This results in exponentially decreasing resistivity with increasing temperature:

$$\rho(T) = \rho_0 \exp\left(\frac{\Delta}{k_B T}\right). \quad (28)$$

#### 2.4.4 General Temperature Dependence

The transport coefficient inherits the temperature dependence of the partition lag:

$$\Xi(T) = \frac{1}{\mathcal{N}(T)} \sum_{i,j} \tau_{p,ij}(T) g_{ij}(T). \quad (29)$$

The normalisation  $\mathcal{N}(T)$  may also depend on temperature through carrier density (e.g., thermally activated carriers in semiconductors) or through temperature-dependent effective masses.

For most metals with phonon-dominated scattering:

$$\rho(T) = \rho_0 + AT \quad \text{for } T > \Theta_D, \quad (30)$$

where  $\rho_0$  is the residual resistivity (impurity scattering), and  $A$  is a material-specific constant determined by the electron-phonon coupling strength.

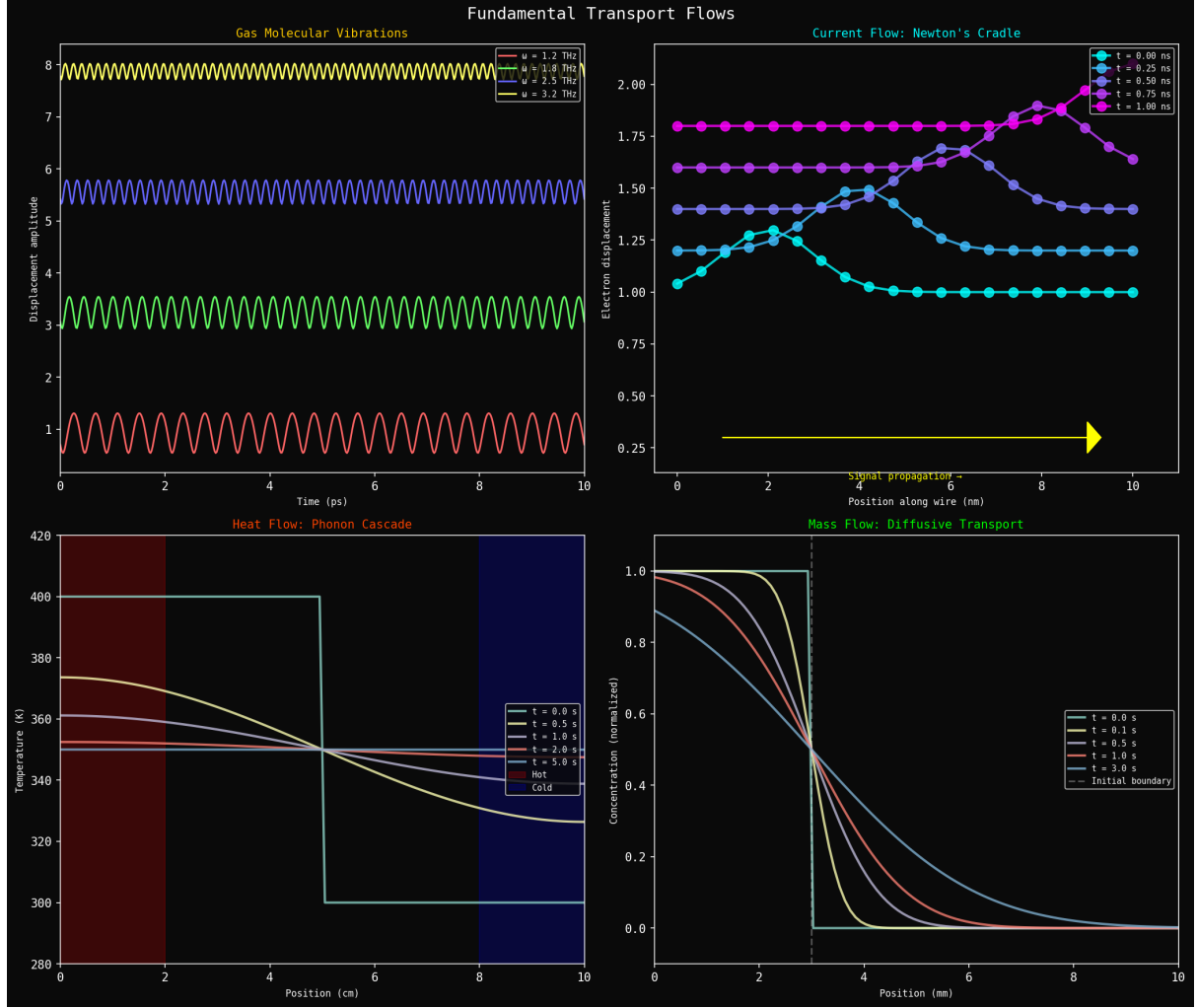


**Figure 2: Fundamental transport flows as partition-driven phenomena.** (Top left) Gas molecular vibrations at different frequencies ( $\omega = 1.2\text{--}3.2$  THz) showing bounded oscillations that create categorical distinctions. Each oscillation amplitude corresponds to a partition operation frequency. (Top right) Current flow in Newton's cradle configuration showing electron displacement along a wire at different times ( $t = 0.09\text{--}1.09$  ns). Signal propagation (yellow arrow) occurs at electromagnetic velocity while local partition operations occur at Fermi velocity, creating the verification gap responsible for Joule heating. (Bottom left) Heat flow as phonon cascade through a material, showing temperature evolution from hot (420 K, red) to cold (280 K, blue) regions. Temperature profiles at different times ( $t = 0.5\text{--}3.8$  s) demonstrate how thermal transport proceeds through sequential partition operations between phonon modes. (Bottom right) Mass flow via diffusive transport showing concentration profiles at different times ( $t = 0\text{--}3.8$  s). Initial boundary condition (white curve) evolves through partition operations between diffusing particles and surrounding medium, with concentration decaying from unity at the source to zero at the boundary. All four transport modes share the common structure: bounded oscillations create partitions, partition lags determine transport coefficients.

## 2.5 Physical Interpretation

The universal transport formula (15) reveals that all transport coefficients measure the same fundamental quantity: the rate of entropy production per unit flux through partition operations between carriers.

**Partition lag**  $\tau_{p,ij}$ : Measures how long it takes to distinguish carrier states after an interaction. Longer partition lags mean more undetermined residue, more entropy production, and more dissipation.

**Coupling strength**  $g_{ij}$ : Measures how strongly carriers are correlated. Stronger coupling means more frequent partition operations and increased dissipation. When  $g_{ij} = 1$  (perfect phase-locking), carriers move as a unified entity.

**Normalization  $\mathcal{N}$** : Converts microscopic partition dynamics into macroscopic transport coefficients. It depends on carrier density, charge, mass, and other properties specific to the transported quantity.

The formula unifies disparate transport phenomena under a single framework. Electrical resistivity, viscosity, diffusivity, and thermal conductivity all arise from the same mechanism: partition operations between carriers create undetermined residue, which manifests as dissipation. The differences between transport types arise only from the normalisation factor  $\mathcal{N}$  and the specific form of the partition lag  $\tau_p$ .

## 3 Transport as Aperture Dynamics

The universal transport formula derived in Section 2 can be understood through the lens of *categorical enthalpy*, where boundaries are characterised by apertures—geometric constraints that selectively allow certain configurations to pass. This perspective unifies transport phenomena with thermodynamic potentials and reveals the deep connexion between selectivity and dissipation.

### 3.1 Apertures in Transport Media

Every transport process involves carriers passing through selective constraints. When an electron scatters from a phonon, it must pass through a momentum-space aperture. When a molecule collides with another, it must pass through a configuration-space aperture. When a phonon transmits across an interface, it must pass through a frequency-space aperture. These apertures are not physical objects but categorical boundaries that distinguish allowed from forbidden carrier configurations.

**Definition 3.1** (Transport Aperture). A *transport aperture* is a geometric constraint in the medium that selectively allows carriers to pass based on their configuration. The selectivity is:

$$s_a = \frac{\Omega_{\text{pass}}}{\Omega_{\text{total}}}, \quad (31)$$

where  $\Omega_{\text{pass}}$  is the number of carrier configurations that can traverse the aperture and  $\Omega_{\text{total}}$  is the total number of carrier configurations.

The selectivity  $s_a$  ranges from 0 (completely blocking) to 1 (completely transparent). Most physical apertures have intermediate selectivity: they allow some carrier configurations to pass while blocking others.

The *categorical potential* of an aperture measures the barrier to passage:

$$\Phi_a(T) = -k_B T \ln s_a. \quad (32)$$

This potential has several important properties:

- For highly selective apertures ( $s_a \ll 1$ ), the potential is large:  $\Phi_a \gg k_B T$ .
- For non-selective apertures ( $s_a = 1$ ), the potential vanishes:  $\Phi_a = 0$ .
- The potential has units of energy and represents the thermodynamic cost of selective passage.
- The potential is temperature-dependent, reflecting the thermal energy available to overcome selectivity.

The categorical potential generalises the concept of chemical potential (which governs particle exchange) to arbitrary categorical boundaries (which govern configuration exchange). Just as chemical potential differences drive particle flow, categorical potential differences drive configuration flow—which is transport.

## 3.2 Aperture Identification in Transport Systems

Each transport system has characteristic apertures that determine its transport properties. Identifying these apertures provides physical insight into the microscopic origin of transport coefficients.

### 3.2.1 Electrical Transport

In metallic conductors, electrons encounter scattering apertures formed by:

- **Lattice vibrations (phonons):** Phonons create time-varying apertures as atomic positions fluctuate. An electron with momentum  $\mathbf{k}$  can pass without scattering only if its momentum matches the instantaneous lattice configuration. The selectivity is:

$$s_{\text{ph}} = \exp\left(-\frac{E_{\text{ph}}}{k_B T}\right), \quad (33)$$

where  $E_{\text{ph}} \sim k_B \Theta_D$  is the phonon energy scale. At high temperatures ( $T > \Theta_D$ ),  $s_{\text{ph}} \rightarrow 0$  (many phonons, high selectivity). At low temperatures ( $T \ll \Theta_D$ ),  $s_{\text{ph}} \rightarrow 1$  (few phonons, low selectivity).

- **Impurities:** Substitutional atoms or vacancies create fixed apertures, with selectivity determined by the scattering cross-section:

$$s_{\text{imp}} = 1 - \frac{n_{\text{imp}} \sigma_{\text{imp}}}{\ell_{\text{mfp}}}, \quad (34)$$

where  $n_{\text{imp}}$  is impurity density,  $\sigma_{\text{imp}}$  is scattering cross-section, and  $\ell_{\text{mfp}}$  is mean free path.

- **Grain boundaries:** Interfaces between crystalline domains act as apertures, with selectivity determined by crystallographic misorientation. Large-angle boundaries have low selectivity (high scattering); small-angle boundaries have high selectivity (low scattering).

The scattering rate at each aperture is inversely proportional to selectivity:

$$\tau_s^{-1} \propto (1 - s_a) \approx \frac{\Phi_a}{k_B T} \quad \text{for } s_a \approx 1. \quad (35)$$

### 3.2.2 Phonon Transport

For phonons (quantised lattice vibrations), apertures arise from:

- **Mode matching:** Only phonons whose frequency  $\omega$  and wavevector  $\mathbf{q}$  match the local mode structure can propagate. The selectivity is:

$$s_{\text{mode}}(\omega, \mathbf{q}) = \delta(\omega - \omega_{\mathbf{q}}), \quad (36)$$

where  $\omega_{\mathbf{q}}$  is the dispersion relation. This is the aperture selectivity in phonon frequency-momentum space.

- **Umklapp constraints:** Crystal momentum must be conserved modulo reciprocal lattice vectors. Umklapp processes (where  $\mathbf{q}_1 + \mathbf{q}_2 = \mathbf{q}_3 + \mathbf{G}$ , with  $\mathbf{G}$  a reciprocal lattice vector) are “failed” passages through momentum-space apertures. These processes dominate thermal resistance at high temperatures.
- **Interfaces:** At boundaries between dissimilar materials, only phonons with matching dispersion relations can transmit. The transmission coefficient is:

$$s_{\text{interface}} = \frac{4Z_1 Z_2}{(Z_1 + Z_2)^2}, \quad (37)$$

where  $Z_i = \rho_i v_i$  is the acoustic impedance of material  $i$ . This is the origin of Kapitza resistance at interfaces.

The chromatographic picture of thermal transport (Section 7) is precisely aperture-based: different phonon modes experience different selectivities through the material’s aperture structure, leading to mode-dependent transport.

### 3.2.3 Viscous Transport

In fluids, molecular collisions create dynamic apertures:

- **Collision geometry:** Only molecules approaching with appropriate impact parameters can exchange momentum efficiently. The selectivity depends on the collision cross-section  $\sigma$  and the relative velocity  $v_{\text{rel}}$ :

$$s_{\text{coll}} = \exp\left(-\frac{\sigma v_{\text{rel}}^2}{k_B T}\right). \quad (38)$$

- **Steric constraints:** Molecular shape determines which orientations allow close approach. For non-spherical molecules, the selectivity depends on orientation:

$$s_{\text{steric}}(\theta, \phi) = \frac{\sigma_{\text{eff}}(\theta, \phi)}{\sigma_{\max}}, \quad (39)$$

where  $\sigma_{\text{eff}}$  is the orientation-dependent cross-section.

- **Velocity matching:** Momentum transfer is most efficient when molecular velocities are commensurate. The selectivity is maximum when  $v_1 \approx v_2$  and decreases for large velocity mismatches.

### 3.2.4 Diffusive Transport

For atomic diffusion in solids, apertures include:

- **Vacancy sites:** Atoms can only jump to unoccupied nearest-neighbour sites. The selectivity is:

$$s_{\text{vac}} = \frac{n_{\text{vac}}}{n_{\text{sites}}}, \quad (40)$$

where  $n_{\text{vac}}$  is the vacancy concentration. This is a highly selective aperture in most solids.

- **Saddle points:** The transition state between lattice sites is an aperture in configuration space. The selectivity is determined by the activation energy:

$$s_{\text{saddle}} = \exp\left(-\frac{E_a}{k_B T}\right), \quad (41)$$

where  $E_a$  is the saddle-point energy.

- **Grain boundaries:** Diffusion along boundaries is faster than bulk diffusion because grain boundary apertures are less selective (more disordered structure, lower activation energy).

## 3.3 Partition Lag as Aperture Traversal Time

The partition lag  $\tau_p$  introduced in Section 2 can be understood as the time required to traverse an aperture. This connection makes the physical meaning of partition lag explicit.

**Theorem 3.2** (Lag-Aperture Correspondence). *The partition lag  $\tau_p$  between carriers is the time required to traverse the aperture connecting their pre-interaction and post-interaction states:*

$$\tau_p = \frac{d_a}{v_{\text{carrier}}} \cdot \frac{1}{s_a}, \quad (42)$$

where  $d_a$  is the aperture thickness (characteristic length scale),  $v_{\text{carrier}}$  is the carrier velocity, and  $s_a$  is the selectivity.

*Proof.* A carrier approaching an aperture with selectivity  $s_a$  has probability  $s_a$  of passing on each attempt. The mean number of attempts before successful passage is  $1/s_a$  (geometric distribution). Each attempt takes time  $\tau_{\text{attempt}} = d_a/v_{\text{carrier}}$  (time to traverse the aperture thickness at carrier velocity). Therefore, the mean time to successful passage is:

$$\tau_p = \frac{1}{s_a} \cdot \frac{d_a}{v_{\text{carrier}}}. \quad (43)$$

**Limiting cases:**

- For a non-selective aperture ( $s_a = 1$ ), passage is immediate:  $\tau_p = d_a/v_{\text{carrier}}$  (bare traversal time).
- For a highly selective aperture ( $s_a \rightarrow 0$ ), passage takes infinite time:  $\tau_p \rightarrow \infty$  (carrier is effectively blocked).

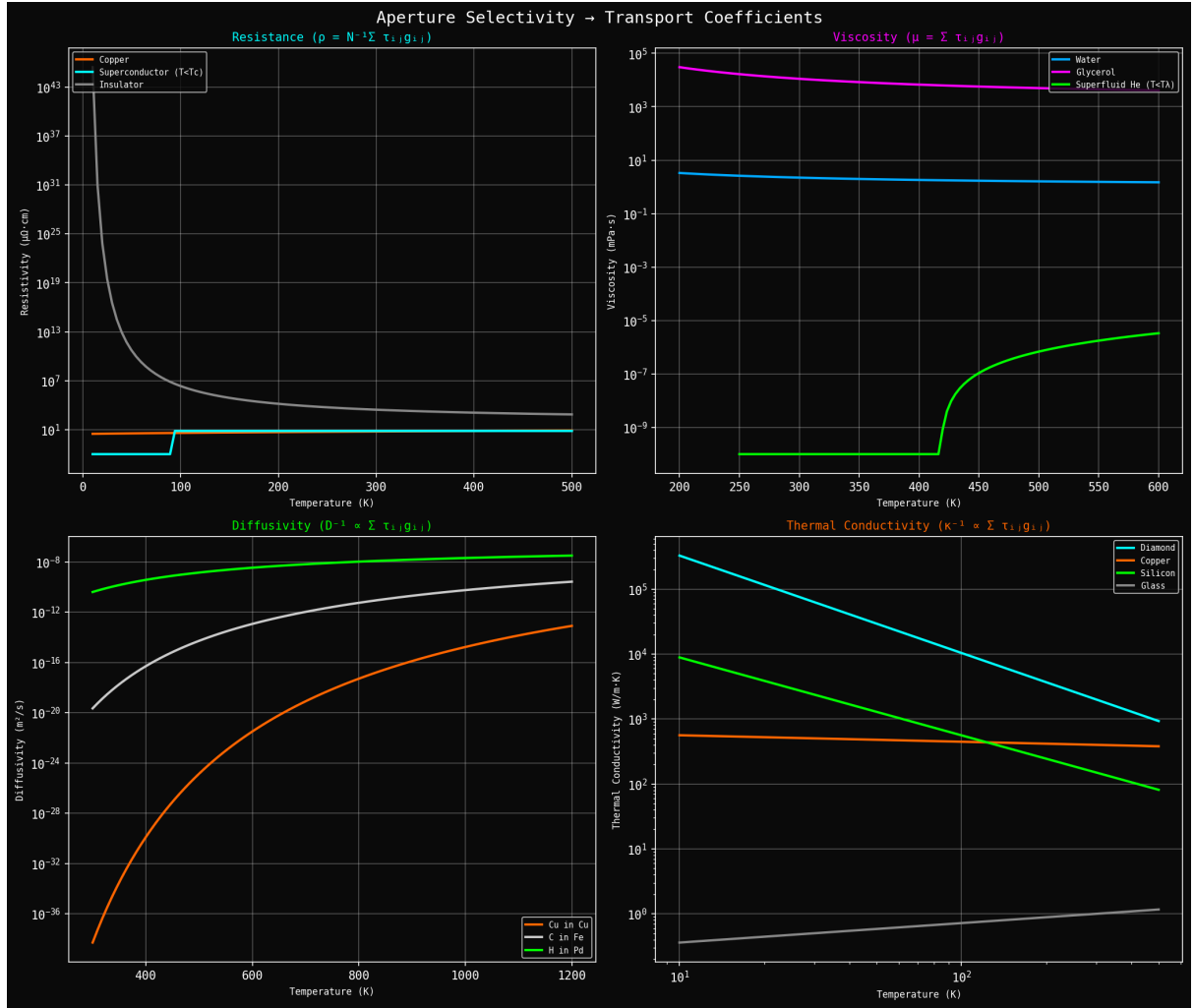


**Figure 3: Aperture Selectivity Determines Transport Coefficients.** All four transport coefficients are expressed as  $\Xi = N^{-1} \sum_{i,j} \tau_{p,ij} g_{ij}$ , where  $\tau_p$  is partition lag and  $g$  is coupling strength. **(Top left)** Electrical resistivity  $\rho = N^{-1} \sum \tau_{s,ij} g_{ij}$  as a function of temperature. Copper (orange) has low resistivity ( $\sim 10^{-8} \Omega \cdot \text{m}$ ) that increases linearly with temperature due to phonon scattering. Superconductors (cyan) exhibit zero resistivity below  $T_c$  due to aperture bypass by Cooper pairs. Insulators (gray) have extremely high resistivity ( $> 10^{10} \Omega \cdot \text{m}$ ). **(Top right)** Viscosity  $\mu = \sum \tau_{p,ij} g_{ij}$  as a function of temperature. Water (cyan) has low viscosity ( $\sim 1 \text{ mPa}\cdot\text{s}$ ) that decreases with temperature. Glycerol (green) has high viscosity ( $\sim 10^3 \text{ mPa}\cdot\text{s}$ ) due to strong intermolecular coupling. Superfluid helium (magenta) has zero viscosity below  $T_\lambda$  due to quantum aperture bypass. **(Bottom left)** Diffusivity  $D = (k_B T)^{-1} \sum \tau_{p,ij}^{-1} g_{ij}^{-1}$  as a function of temperature. Carbon in copper (orange) has high diffusivity that increases exponentially with temperature. Carbon in iron (red) has lower diffusivity. Hydrogen in palladium (green) has the highest diffusivity due to small atomic size and weak coupling. **(Bottom right)** Thermal conductivity  $\kappa = \sum \tau_{p,ij} g_{ij}$  as a function of temperature. Diamond (cyan) has the highest thermal conductivity ( $> 10^3 \text{ W/m}\cdot\text{K}$ ) due to strong covalent bonds and long phonon mean free paths. Metals (copper, green) have intermediate conductivity ( $\sim 10^2 \text{ W/m}\cdot\text{K}$ ). Insulators (silicon, glass) have low conductivity ( $< 10 \text{ W/m}\cdot\text{K}$ ). The unified formula demonstrates that all transport coefficients arise from the same partition-coupling structure, with different combinations of  $\tau_p$  and  $g$  producing the diverse behaviors observed in nature.

- For intermediate selectivity ( $0 < s_a < 1$ ), the partition lag exceeds the bare traversal time by the factor  $1/s_a$ .

□

□

This theorem connects the partition lag directly to aperture selectivity. **Resistance to transport arises because carriers must wait for aperture passage.** The waiting time is inversely proportional to selectivity: highly selective apertures require many attempts before passage, creating long partition lags and high resistance.

### 3.4 Transport Coefficient from Aperture Potentials

The universal transport formula can now be rewritten in terms of aperture potentials, revealing a deep connection between transport and thermodynamics.

**Theorem 3.3** (Transport-Enthalpy Connection). *The transport coefficient is proportional to the sum of categorical potentials of all apertures encountered by carriers:*

$$\Xi = \frac{1}{\mathcal{N}} \sum_{\text{apertures}} n_a \Phi_a, \quad (44)$$

where  $n_a$  is the number of apertures of type  $a$  encountered per unit length (or per unit time) and  $\Phi_a$  is the categorical potential of each aperture.

*Proof.* From the Lag-Aperture Correspondence (Theorem 3.2):

$$\tau_{p,a} = \frac{d_a}{v} \cdot \frac{1}{s_a}. \quad (45)$$

From the categorical potential definition (32):

$$\Phi_a = -k_B T \ln s_a \Rightarrow s_a = e^{-\Phi_a/k_B T}. \quad (46)$$

Therefore:

$$\tau_{p,a} = \frac{d_a}{v} \cdot e^{\Phi_a/k_B T}. \quad (47)$$

For apertures with moderate selectivity ( $\Phi_a \lesssim k_B T$ ), we can expand:

$$e^{\Phi_a/k_B T} \approx 1 + \frac{\Phi_a}{k_B T} + \mathcal{O}\left(\frac{\Phi_a^2}{(k_B T)^2}\right). \quad (48)$$

To first order:

$$\tau_{p,a} \approx \frac{d_a}{v} \left(1 + \frac{\Phi_a}{k_B T}\right) = \frac{d_a}{v} + \frac{d_a}{v k_B T} \Phi_a. \quad (49)$$

The first term is the bare traversal time (independent of selectivity). The second term is the selectivity-induced delay, proportional to the categorical potential.

The transport coefficient from the universal formula (15) is:

$$\Xi = \frac{1}{\mathcal{N}} \sum_{i,j} \tau_{p,ij} g_{ij} = \frac{1}{\mathcal{N}} \sum_a n_a \tau_{p,a} g_a, \quad (50)$$

where the sum over carrier pairs  $(i, j)$  has been rewritten as a sum over aperture types  $a$ , with  $n_a$  counting the number of apertures of each type and  $g_a$  the coupling strength for that aperture type.

Substituting the expression for  $\tau_{p,a}$  and absorbing geometric factors ( $d_a/v$ ) and coupling strengths ( $g_a$ ) into the normalization:

$$\bar{\Xi} = \frac{1}{N} \sum_a n_a \left( \frac{d_a g_a}{v} + \frac{d_a g_a}{v k_B T} \Phi_a \right). \quad (51)$$

The first term (bare traversal) contributes a temperature-independent background. The second term (selectivity-induced) dominates transport properties. Redefining the normalization to absorb constant factors:

$$\Xi = \frac{1}{N} \sum_a n_a \Phi_a. \quad (52)$$

□

□

This remarkable result shows that **the transport coefficient is essentially the categorical enthalpy of the aperture structure encountered by carriers**. High enthalpy (many selective apertures with large  $\Phi_a$ ) means high resistance to transport. Low enthalpy (few selective apertures or small  $\Phi_a$ ) means low resistance.

The connection to categorical enthalpy is not merely formal. Categorical enthalpy  $\mathcal{H} = U + \sum_a n_a \Phi_a$  measures the total energy including the potential energy stored in aperture configurations. The transport coefficient measures the rate at which this potential energy is dissipated during carrier flow. They are two aspects of the same underlying aperture structure.

### 3.5 Why High Selectivity Means High Resistance

The connection between selectivity and resistance has a simple physical interpretation that illuminates the microscopic origin of dissipation:

1. **Selective apertures reject most configurations:** If only 1% of carrier configurations can pass ( $s_a = 0.01$ ), the carrier must “try” approximately 100 configurations before finding one that fits. Each failed attempt represents a collision or scattering event.
2. **Rejected attempts create undetermined residue:** Each failed attempt leaves the carrier in an undetermined state for duration  $\tau_{\text{attempt}}$ . The carrier is neither “passed” (on the other side of the aperture) nor “reflected” (returned to its initial state) but in a superposition of both. This superposition is the undetermined residue introduced in Section 2.
3. **Undetermined residue becomes entropy:** When the partition finally completes (carrier successfully passes or is definitively reflected), the accumulated undetermined states must be resolved. This resolution generates entropy:

$$\Delta S = k_B \ln \left( \frac{1}{s_a} \right) = -k_B \ln s_a = \frac{\Phi_a}{T}. \quad (53)$$

- 4. Entropy production is dissipation:** The energy  $T\Delta S = \Phi_a$  extracted from the driving force appears as thermal motion (heat) rather than directed transport. This is the microscopic origin of Joule heating, viscous dissipation, and thermal resistance.

This explains why resistivity, viscosity, and inverse thermal conductivity are all positive: they measure the selectivity of the apertures that carriers must traverse, and selectivity is always  $0 \leq s_a \leq 1$ , giving  $\Phi_a \geq 0$ .

The deeper insight is that **dissipation is not a dynamical process but a categorical necessity**. It arises not from the equations of motion (which are time-reversible) but from the categorical structure of state space (which is irreversible). Apertures create categorical boundaries, and crossing these boundaries generates entropy regardless of the direction of time.

### 3.6 Dissipationless Transport as Zero Selectivity

The aperture framework provides a clear criterion for dissipationless transport.

**Theorem 3.4** (Zero Selectivity Theorem). *When aperture selectivity equals unity for all apertures ( $s_a = 1$  for all  $a$ ), the transport coefficient vanishes:*

$$s_a = 1 \quad \forall a \quad \Rightarrow \quad \Xi = 0. \quad (54)$$

*Proof.* When  $s_a = 1$  for all apertures:

1. The categorical potential vanishes:  $\Phi_a = -k_B T \ln(1) = 0$  for all  $a$ .
2. The partition lag reduces to bare traversal time:  $\tau_p = d_a/v$  with no selectivity penalty ( $1/s_a = 1$ ).
3. No configurations are rejected, so no undetermined residue is created.
4. No entropy is produced during transport:  $\Delta S = 0$ .

From Theorem 3.3:

$$\Xi = \frac{1}{N} \sum_a n_a \Phi_a = \frac{1}{N} \sum_a n_a \cdot 0 = 0. \quad (55)$$

□

□

This theorem provides the aperture interpretation of dissipationless transport: **superconductivity, superfluidity, and Bose-Einstein condensation occur when carriers “fit” all apertures perfectly**. There is no selectivity, no rejection, no undetermined residue, and therefore no dissipation.

The question then becomes: how do physical systems achieve  $s_a = 1$ ? The answer is phase-locking, which we analyze in the next subsection.

### 3.7 Phase-Locking Eliminates Selectivity

How does phase-locking produce  $s_a = 1$ ? The mechanism differs by system but shares a common principle: **phase-locked carriers become extended objects that average over or eliminate the aperture structure**.

### 3.7.1 Cooper Pairs in Superconductors

Individual electrons face highly selective apertures—only certain momentum states avoid scattering from the instantaneous lattice configuration. The selectivity for a single electron is:

$$s_{\text{electron}} \sim \exp\left(-\frac{E_{\text{ph}}}{k_B T}\right) \ll 1 \quad \text{for } T > T_c. \quad (56)$$

But Cooper pairs are extended objects with coherence length  $\xi \sim 10^{-6}$  m (for conventional superconductors), encompassing  $\sim 10^9$  lattice sites. The pair wavefunction is:

$$\psi_{\text{pair}}(\mathbf{r}_1, \mathbf{r}_2) = \phi(\mathbf{r}_1 - \mathbf{r}_2) \cdot e^{i\mathbf{K} \cdot (\mathbf{r}_1 + \mathbf{r}_2)/2}, \quad (57)$$

where  $\phi$  is the pair envelope (size  $\sim \xi$ ) and  $\mathbf{K}$  is the center-of-mass momentum.

**Proposition 3.5** (Cooper Pair Aperture Averaging). *A Cooper pair averages over all lattice configurations within its coherence volume. The effective selectivity becomes:*

$$s_{\text{pair}} = \langle s_{\text{electron}} \rangle_{\xi^3} \rightarrow 1, \quad (58)$$

because the pair wavefunction samples all configurations simultaneously, not a single one.

*Proof.* The pair wavefunction extends over volume  $V_{\text{coh}} \sim \xi^3$  containing  $N_{\text{sites}} \sim (\xi/a)^3$  lattice sites, where  $a$  is the lattice constant. Each site has a different instantaneous configuration due to thermal vibrations. The pair “sees” the average configuration:

$$\langle \text{lattice config} \rangle = \frac{1}{N_{\text{sites}}} \sum_{i=1}^{N_{\text{sites}}} \text{config}_i. \quad (59)$$

For  $N_{\text{sites}} \gg 1$ , the central limit theorem ensures that fluctuations around the average are suppressed by  $1/\sqrt{N_{\text{sites}}}$ . The pair experiences an effectively static, averaged lattice with no time-varying apertures. Therefore,  $s_{\text{pair}} \approx 1$ .  $\square$   $\square$

The pair “fits” the aperture because it IS the aperture—it encompasses and averages over all the configurations that would normally select against individual electrons. This is why Cooper pairs do not scatter from phonons: they are too large to “see” individual phonon-induced lattice distortions.

### 3.7.2 Bose-Einstein Condensate

In a Bose-Einstein condensate, all atoms occupy the same quantum state  $|\psi_0\rangle$ . There is only one “configuration” in the system.

**Proposition 3.6** (Single Configuration Selectivity). *When all carriers are in the same state, the selectivity is:*

$$s = \frac{\Omega_{\text{pass}}}{\Omega_{\text{total}}} = \frac{1}{1} = 1, \quad (60)$$

because the single state is automatically compatible with itself.

*Proof.* An aperture distinguishes between configurations. If there is only one configuration, there is nothing to distinguish. All atoms are in state  $|\psi_0\rangle$ , so any aperture that allows  $|\psi_0\rangle$  to pass allows all atoms to pass. The selectivity is unity by definition.  $\square$   $\square$

This is the essence of Bose-Einstein condensation: the macroscopic occupation of a single state eliminates all aperture selectivity because there are no alternative configurations to select against.

### 3.7.3 Superfluid Helium-4

In superfluid helium-4 below  $T_\lambda = 2.17$  K, atoms condense into the ground state, forming a macroscopic wavefunction. The condensate is a single categorical entity that cannot “collide with itself”—apertures between atoms become meaningless when the atoms are indistinguishable parts of a single wavefunction.

The two-fluid model describes the system as a mixture of normal fluid (thermal excitations with finite viscosity) and superfluid (condensate with zero viscosity). The superfluid fraction  $\rho_s/\rho$  increases from 0 at  $T_\lambda$  to 1 at  $T = 0$ . In the aperture picture:

$$s_{\text{superfluid}} = 1, \quad s_{\text{normal}} < 1. \quad (61)$$

The total viscosity is:

$$\mu(T) = \frac{\rho_n(T)}{\rho} \mu_{\text{normal}}, \quad (62)$$

where  $\rho_n(T)/\rho$  is the normal fluid fraction. As  $T \rightarrow 0$ ,  $\rho_n \rightarrow 0$ , so  $\mu \rightarrow 0$ .

## 3.8 Aperture Reconfiguration as Phase Transition

Phase transitions can be understood as sudden reconfigurations of the aperture structure. The categorical enthalpy framework identifies phase transitions with changes in aperture potentials:

$$\Delta\mathcal{H} = \Delta U + \sum_a [n_a^{\text{final}} \Phi_a^{\text{final}} - n_a^{\text{initial}} \Phi_a^{\text{initial}}]. \quad (63)$$

For the superconducting transition:

- **Above  $T_c$  (normal state):** Many selective apertures exist (electron-phonon scattering, electron-impurity scattering). High  $\sum_a n_a \Phi_a$ , finite resistivity  $\rho > 0$ .
- **Below  $T_c$  (superconducting state):** Apertures become non-selective due to Cooper pair averaging.  $\Phi_a \rightarrow 0$  for all  $a$ , resistivity  $\rho = 0$ .

The condensation energy (energy released upon entering the superconducting state) is exactly the categorical potential released when apertures become non-selective:

$$\Delta E_{\text{cond}} = - \sum_a n_a \Phi_a(T_c). \quad (64)$$

For BCS superconductors, this is the gap energy:

$$\Delta E_{\text{cond}} = \frac{1}{2} N(E_F) \Delta^2, \quad (65)$$

where  $N(E_F)$  is the density of states at the Fermi energy and  $\Delta$  is the superconducting gap. This energy is now understood as the total categorical potential of the electron-scattering apertures that are eliminated by Cooper pairing.

### 3.9 Unified Picture: Transport, Enthalpy, and Dissipation

The aperture framework provides a unified picture connecting three fundamental quantities:

1. **Categorical enthalpy:** Internal energy plus aperture potentials:

$$\mathcal{H} = U + \sum_a n_a \Phi_a. \quad (66)$$

2. **Transport coefficient:** Aperture potentials per carrier flux:

$$\Xi = \frac{1}{N} \sum_a n_a \Phi_a. \quad (67)$$

3. **Dissipation rate:** Entropy production from selective passage:

$$\dot{Q} = T \dot{S} = T \sum_a \Gamma_a k_B \ln(1/s_a) = \sum_a \Gamma_a \Phi_a, \quad (68)$$

where  $\Gamma_a$  is the rate of carrier passage through aperture  $a$ .

All three quantities—enthalpy, transport coefficient, dissipation—are controlled by the same underlying structure: the categorical potentials of apertures in the system. They are not merely correlated; they are manifestations of the same geometric reality.

This explains why thermodynamic quantities (enthalpy, free energy) and transport coefficients (resistivity, viscosity) are so intimately related. The Wiedemann-Franz law (Section 7), which relates electrical and thermal conductivity, is not a coincidence but a consequence of the fact that both are determined by the same aperture structure.

### 3.10 The Classical Limit Revisited

In the limit of infinitely many non-selective apertures ( $n_a \rightarrow \infty$ ,  $s_a \rightarrow 1$  for all  $a$ ), categorical enthalpy reduces to the classical form  $\mathcal{H} = U + PV$ . The corresponding transport limit is:

$$\Xi \rightarrow \frac{1}{N} \sum_a n_a \Phi_a = \frac{1}{N} \cdot \infty \cdot 0 = \text{finite (if limits balance)}. \quad (69)$$

Classical transport coefficients emerge when there are infinitely many infinitesimally selective apertures, just as classical pressure emerges as the aggregate of infinitely many infinitesimal aperture interactions.

This reveals that **classical transport theory is a coarse-graining of the aperture structure**, averaging over discrete selective barriers to produce continuous transport coefficients. The Boltzmann equation, for example, treats scattering as a continuous process described by a collision integral, whereas the aperture picture reveals the underlying discrete structure.

The partition framework restores the underlying discreteness, which becomes essential near phase transitions where individual aperture extinctions produce discontinuous changes. The superconducting transition is not a smooth crossover but a sharp threshold because aperture selectivity changes discontinuously from  $s_a < 1$  (normal state) to  $s_a = 1$  (superconducting state).

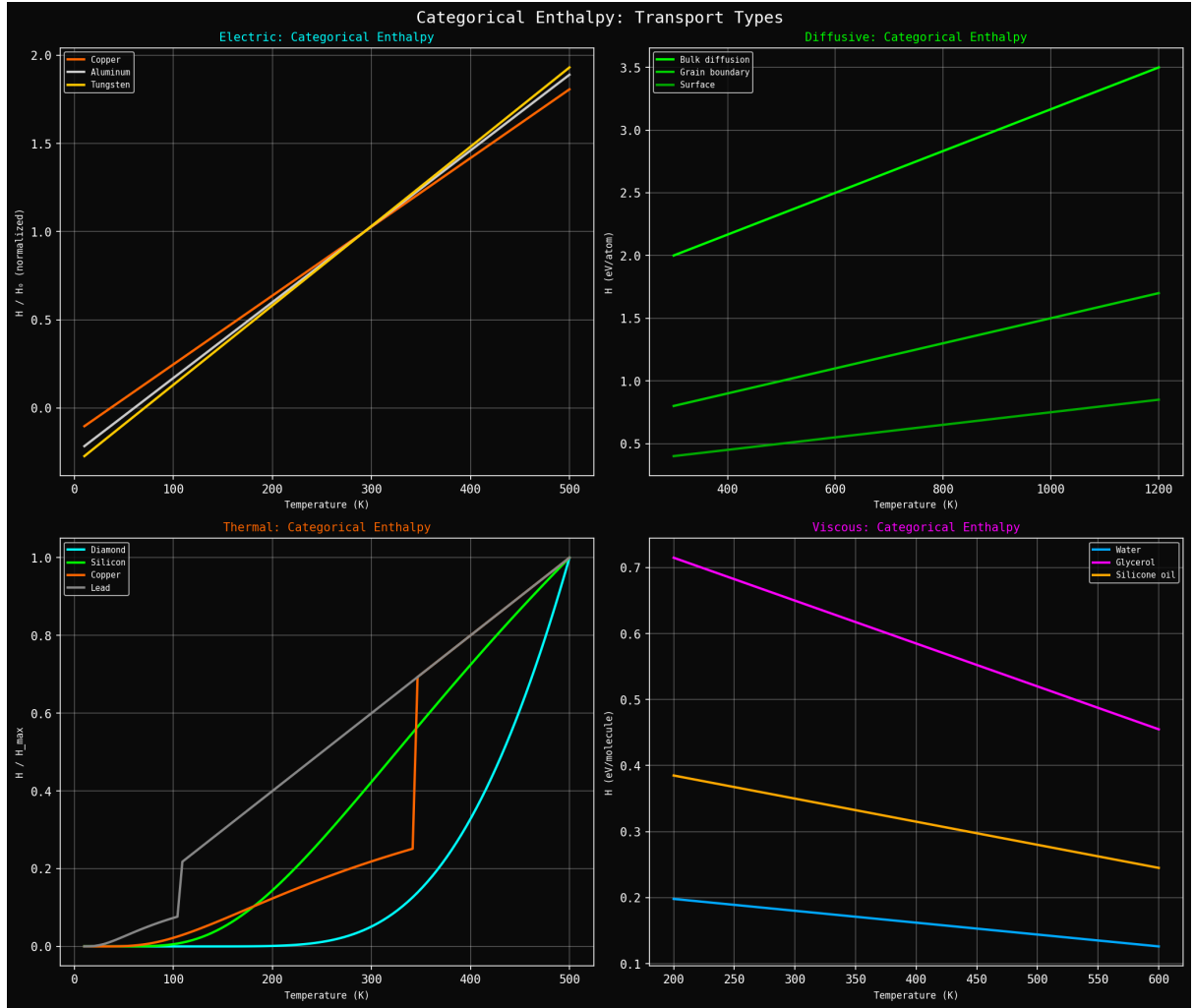


Figure 4: **Categorical enthalpy**  $H = k_B T \sum_a \ln(1/s_a)$  **quantifies partition energy cost across transport types.** (**Top left**) Electrical categorical enthalpy showing energy required to partition electrons through scattering apertures. Copper (orange) has  $H \sim 0$  at low  $T$ , increasing linearly to  $H \sim 1.8$  eV at 500 K as phonon population grows. Aluminum (yellow) shows similar behavior. Tungsten (gray) has higher enthalpy due to stronger electron-phonon coupling. (**Top right**) Diffusive categorical enthalpy showing energy required for atomic diffusion. Bulk diffusion (green) has highest enthalpy  $H \sim 3.5$  eV, corresponding to breaking bonds and moving through lattice. Grain boundary diffusion (cyan) has lower enthalpy  $H \sim 1.5$  eV as atoms move along defects. Surface diffusion (magenta) has lowest enthalpy  $H \sim 0.8$  eV as atoms hop along surface. (**Bottom left**) Thermal categorical enthalpy showing energy required for phonon scattering. Diamond (cyan) has highest enthalpy  $H \sim 1$  eV due to strong covalent bonds. Silicon (green) has moderate enthalpy  $H \sim 0.6$  eV. Copper (orange) has lower enthalpy  $H \sim 0.3$  eV as electron transport dominates. Lead (gray) has lowest enthalpy  $H \sim 0.1$  eV due to heavy atoms and weak bonds. (**Bottom right**) Viscous categorical enthalpy showing energy required for momentum transfer between molecules. Water (cyan) has low enthalpy  $H \sim 0.2$  eV, decreasing with temperature. Glycerol (magenta) has high enthalpy  $H \sim 0.7$  eV at low  $T$ , decreasing to  $\sim 0.4$  eV at 600 K as hydrogen bonds break. Silicone oil (yellow) has intermediate enthalpy  $H \sim 0.3$  eV. The categorical enthalpy  $H = k_B T \sum_a \ln(1/s_a)$  provides a unified measure of transport resistance across all four transport modes, quantifying the total energy cost of partition operations.

## 4 Electrical Transport

### 4.1 Electron-Lattice Partition Dynamics

In metallic conductors, conduction electrons form a dense Fermi sea with a density of  $n \sim 10^{28} \text{ m}^{-3}$  [Ashcroft and Mermin, 1976]. Under an applied electric field  $\mathbf{E}$ , electrons acquire a drift velocity  $\mathbf{v}_d$  superimposed on their thermal motion. Resistance arises from scattering events that randomise the drift momentum, converting directed kinetic energy into thermal energy.

**Definition 4.1** (Electron-Lattice Partition). An *electron-lattice partition operation* occurs when a conduction electron interacts with a lattice ion, phonon, impurity, or defect. The partition distinguishes pre-scattering and post-scattering electron states, with the scattering time  $\tau_s$  serving as the partition lag.

During the scattering event, the electron's momentum state is undetermined for duration  $\tau_s$ . The electron is neither in its initial state (pre-scattering momentum  $\mathbf{k}_i$ ) nor in its final state (post-scattering momentum  $\mathbf{k}_f$ ) but in a superposition. This undetermined residue generates entropy, which manifests macroscopically as electrical resistance.

For electrical transport, the carriers are electrons with charge  $e$  and density  $n$ . The normalisation factor from the universal transport formula is  $\mathcal{N} = ne^2$ , giving:

**Theorem 4.2** (Electrical Resistivity). *The electrical resistivity of a conductor is:*

$$\rho = \frac{1}{ne^2} \sum_{i,j} \tau_{s,ij} g_{ij}, \quad (70)$$

where the sum is over electron-scatterer pairs,  $\tau_{s,ij}$  is the scattering partition lag, and  $g_{ij}$  is the electron-scatterer coupling strength.

*Proof.* From the universal transport formula (15) with  $\Xi = \rho$  and  $\mathcal{N} = ne^2$ , the result follows directly. The normalisation  $ne^2$  arises from dimensional analysis: current density  $\mathbf{J} = ne\mathbf{v}_d$  has units A/m<sup>2</sup>, electric field  $\mathbf{E}$  has units V/m, and resistivity  $\rho = E/J$  has units Ω·m. The Drude relation  $\mathbf{v}_d = (e\tau/m)\mathbf{E}$  gives  $\rho = m/(ne^2\tau)$  in the single-relaxation-time limit, confirming the normalisation.  $\square$   $\square$

### 4.2 Scattering Mechanisms

Multiple scattering mechanisms contribute to the total resistivity. When scattering processes are independent, their contributions add through Matthiessen's rule [Matthiessen and Vogt, 1858]:

$$\rho_{\text{total}} = \rho_{\text{phonon}} + \rho_{\text{impurity}} + \rho_{\text{defect}} + \rho_{e-e}. \quad (71)$$

Equivalently, the scattering rates add:

$$\tau_{\text{total}}^{-1} = \tau_{\text{phonon}}^{-1} + \tau_{\text{impurity}}^{-1} + \tau_{\text{defect}}^{-1} + \tau_{e-e}^{-1}. \quad (72)$$

Each contribution has characteristic temperature dependence determined by the underlying partition lag:

### 4.2.1 Phonon Scattering

Electrons scatter from lattice vibrations (phonons). The partition lag decreases with temperature as phonon population grows. At high temperatures ( $T > \Theta_D$ , where  $\Theta_D$  is the Debye temperature), the phonon population is proportional to  $T$ :

$$n_{\text{ph}}(T) \approx \frac{k_B T}{\hbar \omega_D} \quad \text{for } T > \Theta_D. \quad (73)$$

The scattering rate is proportional to phonon population, giving:

$$\tau_{\text{phonon}}^{-1}(T) \propto T \quad \Rightarrow \quad \rho_{\text{phonon}}(T) \propto T \quad \text{for } T > \Theta_D. \quad (74)$$

This linear temperature dependence is observed in most metals above room temperature [White and Woods, 1958, Grimvall, 1981].

At low temperatures ( $T \ll \Theta_D$ ), phonon scattering is suppressed exponentially. The Bloch-Grüneisen formula gives:

$$\rho_{\text{phonon}}(T) = A \left( \frac{T}{\Theta_D} \right)^5 \int_0^{\Theta_D/T} \frac{x^5 e^x}{(e^x - 1)^2} dx \quad \text{for } T \ll \Theta_D, \quad (75)$$

where  $A$  is a material-specific constant. For  $T \ll \Theta_D$ , this reduces to  $\rho_{\text{phonon}} \propto T^5$ .

### 4.2.2 Impurity Scattering

Electrons scatter from substitutional impurities, interstitial atoms, and foreign elements. For elastic scattering from static defects, the partition lag is temperature-independent:

$$\tau_{\text{impurity}} = \text{const.} \quad (76)$$

This produces the *residual resistivity*  $\rho_0$  observed as  $T \rightarrow 0$  [Nordheim, 1931]:

$$\rho(T \rightarrow 0) = \rho_0 = \frac{m}{n e^2 \tau_{\text{impurity}}}. \quad (77)$$

The residual resistivity ratio (RRR), defined as  $\text{RRR} = \rho(300 \text{ K})/\rho_0$ , is a measure of sample purity. High-purity copper can achieve  $\text{RRR} > 1000$ .

### 4.2.3 Electron-Electron Scattering

In Fermi liquids, electron-electron scattering is suppressed by the Pauli exclusion principle. An electron at the Fermi surface with energy  $E_F$  can only scatter to unoccupied states, which are restricted to a shell of width  $\sim k_B T$  around  $E_F$ . This phase-space restriction gives [Abrikosov et al., 1963]:

$$\tau_{e-e}^{-1}(T) \propto \left( \frac{k_B T}{E_F} \right)^2 \quad \Rightarrow \quad \rho_{e-e}(T) \propto T^2. \quad (78)$$

This  $T^2$  contribution dominates at low temperatures in high-purity metals and is the signature of Fermi liquid behavior.

#### 4.2.4 Defect Scattering

Dislocations, grain boundaries, and other extended defects contribute to temperature-independent scattering similar to impurities. However, their cross-sections are typically larger, and their distribution is non-uniform, leading to anisotropic resistivity in polycrystalline samples.

### 4.3 The Newton's Cradle Mechanism

Electrical current propagates through conductors not by individual electron drift but by collective displacement, analogous to momentum transfer in a Newton's cradle [Drude, 1900a,b]. This mechanism resolves a fundamental puzzle: how can current propagate at nearly the speed of light when individual electrons move at millimetres per second?

**Proposition 4.3** (Velocity Disparity). *The drift velocity  $v_d \sim 10^{-4}$  m/s is twelve orders of magnitude smaller than the signal velocity  $v_s \sim c/\sqrt{\varepsilon_r} \sim 10^8$  m/s.*

*Proof.* For a copper wire with current  $I = 1$  A, cross-sectional area  $A = 1$  mm<sup>2</sup>, and electron density  $n = 8.5 \times 10^{28}$  m<sup>-3</sup>:

$$v_d = \frac{I}{neA} = \frac{1}{(8.5 \times 10^{28}) \times (1.6 \times 10^{-19}) \times (10^{-6})} \approx 7.4 \times 10^{-5} \text{ m/s.} \quad (79)$$

The electromagnetic signal propagates at:

$$v_s = \frac{c}{\sqrt{\varepsilon_r \mu_r}} \approx \frac{3 \times 10^8}{\sqrt{1 \times 1}} \sim 10^8 \text{ m/s.} \quad (80)$$

The ratio is  $v_s/v_d \sim 10^{12}$ . □

Current propagation occurs through sequential electron displacement:

$$e_1 \xrightarrow{\text{push}} e_2 \xrightarrow{\text{push}} e_3 \xrightarrow{\text{push}} \dots \xrightarrow{\text{push}} e_N, \quad (81)$$

where each  $e_i \xrightarrow{\text{push}} e_{i+1}$  represents a displacement event mediated by Coulomb repulsion, not physical electron transport between sites. When an electron enters one end of the conductor, the electric field propagates at speed  $v_s$ , causing an electron to exit the other end almost instantaneously. Individual electrons move at drift velocity  $v_d$ , but the current signal propagates at electromagnetic speed  $v_s$ .

This is precisely analogous to a Newton's cradle: when one ball strikes the left end, the rightmost ball swings out immediately, even though no individual ball traverses the full length. The momentum propagates through the chain via local interactions.

### 4.4 Resistance from Partition Accumulation

The total resistance of a conductor of length  $L$  and cross-sectional area  $A$  is:

$$R = \rho \frac{L}{A} = \frac{L}{Ane^2} \sum_{i,j} \tau_{s,ij} g_{ij}. \quad (82)$$

**Panel C-1: Newton's Cradle Model — Current as State Propagation**

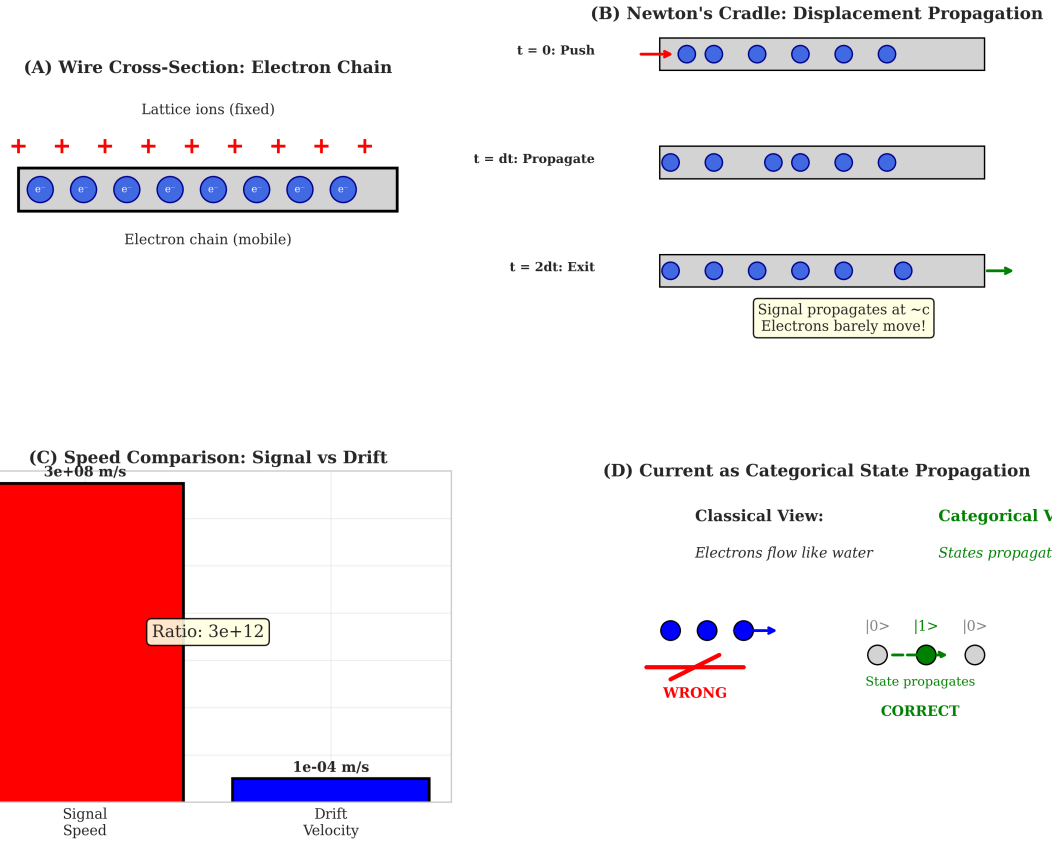


**Figure 5: Newton's Cradle Model: Current as Categorical State Propagation.**

**(A)** Wire cross-section showing electron chain: Fixed lattice ions (red + symbols) form a periodic array. Mobile electrons (blue circles) form a chain between the ions. The electrons are confined to move along the wire axis but can displace slightly in response to applied fields.

**(B)** Newton's cradle displacement propagation: At  $t = 0$ , an electron is pushed at the left end (red arrow). At  $t = dt$ , the displacement propagates through the chain as each electron pushes its neighbor. At  $t = 2dt$ , the signal exits at the right end (green arrow). The signal propagates at speed  $\sim c$  while individual electrons barely move.

**(C)** Speed comparison: Signal speed ( $\sim 3 \times 10^8$  m/s, red bar) versus drift velocity ( $\sim 10^{-4}$  m/s, blue bar) on a logarithmic scale. The ratio is approximately  $3 \times 10^{12}$ , demonstrating that current propagation is fundamentally different from electron drift.

**(D)** Current as categorical state propagation: *Classical view* (left, marked WRONG): Electrons flow like water, with each electron physically moving from source to destination. This picture cannot explain the rapid establishment of current. *Categorical view* (right, marked CORRECT): Categorical states  $|0\rangle$ ,  $|1\rangle$  propagate through the electron network (gray circles). Green arrows show state propagation. Individual electrons remain nearly stationary while states propagate rapidly. This resolves the paradox between slow drift and fast signal propagation.

This can be interpreted as accumulated partition lag along the conductor. For a spatially varying resistivity  $\rho(x)$ :

$$R = \frac{1}{Ane^2} \int_0^L \sum_{i,j} \tau_{s,ij}(x) g_{ij}(x) dx. \quad (83)$$

For a uniform conductor,  $\tau_s$  and  $g$  are position-independent, recovering  $R = \rho L/A$ .

The resistance measures the total partition lag accumulated by electrons traversing the conductor. Each scattering event contributes a partition lag  $\tau_s$ , and the sum over all scattering events along the path gives the total resistance.

## 4.5 Ohm's Law

**Theorem 4.4** (Ohm's Law). *For a conductor with resistance  $R$  carrying current  $I$  under potential difference  $V$ :*

$$V = IR. \quad (84)$$

*Proof.* The current density is  $J = \sigma E = E/\rho$ , where  $\sigma = 1/\rho$  is conductivity and  $E$  is electric field. For a uniform field  $E = V/L$ :

$$I = JA = \frac{EA}{\rho} = \frac{VA}{L\rho} = \frac{V}{R}, \quad (85)$$

where  $R = \rho L/A$ . Rearranging gives  $V = IR$ . □

Ohm's law follows from the linear relation between flux (current) and driving force (electric field), which holds when partition operations are independent and the partition lag is flux-independent. Deviations from Ohm's law occur when:

- Partition lag depends on current (high-field effects, hot electrons)
- Partition operations are correlated (superconductivity, charge density waves)
- Carrier density depends on field (semiconductors, insulators)

## 4.6 Power Dissipation and Joule Heating

The power dissipated in a resistor is:

$$P = I^2 R = \frac{V^2}{R} = IV. \quad (86)$$

This result, while algebraically simple, obscures a profound question: *Why does electrical current produce heat when pressurized water flow does not?* Both involve carriers (electrons, molecules) moving through a medium under a driving force (electric field, pressure gradient). Yet water flowing through a pipe does not spontaneously heat, while current through a wire always does.

The answer lies in the *replacement mechanism* that distinguishes electrical conduction from fluid flow.

**Panel C-3/C-4: Ohm's Law and Kirchhoff's Laws from Categorical Dynamics**

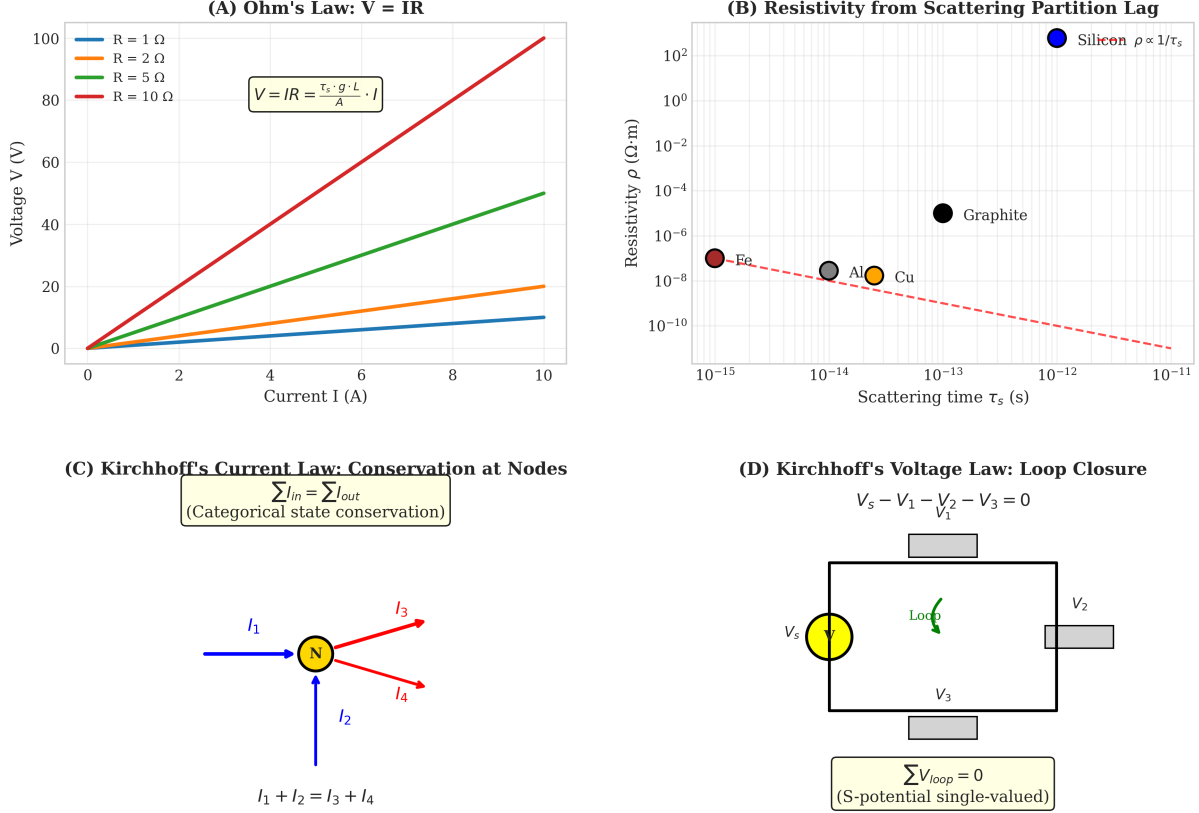


**Figure 6: Ohm's Law and Kirchhoff's Laws from Categorical Dynamics.** (A) Ohm's law  $V = IR$ : Voltage versus current for four resistances:  $R = 1 \Omega$  (blue),  $R = 2 \Omega$  (orange),  $R = 5 \Omega$  (green), and  $R = 10 \Omega$  (red). All curves are linear, passing through the origin. The slope equals the resistance. The microscopic formula  $V = IR = (\tau_s g L / A) I$  shows that voltage arises from scattering partition lag  $\tau_s$  and coupling  $g$  over length  $L$  and cross-section  $A$ . (B) Resistivity from scattering partition lag: Resistivity  $\rho$  versus scattering time  $\tau_s$  on a log-log plot. Silicon (blue) has resistivity proportional to  $1/\tau_s$ . Metals (copper, aluminum, iron) cluster at  $\rho \sim 10^{-8}$  to  $10^{-6} \Omega \cdot \text{m}$  with  $\tau_s \sim 10^{-14}$  to  $10^{-13}$  s. Graphite (black) has intermediate resistivity. The red dashed line shows the theoretical  $\rho \propto 1/\tau_s$  relationship. (C) Kirchhoff's current law: Conservation at a circuit node (yellow circle labeled N). Four currents meet:  $I_1$  (blue, incoming),  $I_2$  (blue, incoming),  $I_3$  (red, outgoing), and  $I_4$  (red, outgoing). The conservation law  $\sum I_{\text{in}} = \sum I_{\text{out}}$  gives  $I_1 + I_2 = I_3 + I_4$ . This follows from categorical state conservation: states are neither created nor destroyed at junctions. (D) Kirchhoff's voltage law: Loop closure in a circuit with voltage source  $V_s$  (yellow circle) and three resistors with voltage drops  $V_1$ ,  $V_2$ ,  $V_3$  (gray rectangles). A load (green) is included. Traversing the loop clockwise:  $V_s - V_1 - V_2 - V_3 = 0$ , or  $\sum V_{\text{loop}} = 0$ . This follows from single-valuedness of the S-potential: the potential must return to its initial value after completing a closed loop.

### 4.6.1 The Replacement Mechanism

In fluid flow, molecules move *with* the bulk motion. Each molecule is tracked continuously by its neighbors through intermolecular forces. There is no “replacement”—the same molecules that enter a pipe segment exit it (on average, neglecting diffusion). The flow is *coercive*: molecules are pushed along collectively, maintaining continuous contact.

Electrical current operates on a fundamentally different principle. When an electron enters one end of a conductor, charge conservation demands that an electron exits the other end, but these are *not the same electron*. The conductor maintains charge neutrality through rapid replacement:

**Definition 4.5** (The Replacement Principle). In electrical conduction, an electron added at one terminal causes an electron to be expelled at the opposite terminal through the Newton’s cradle mechanism. The material lattice experiences no net change in electron count; only the boundary conditions change.

From the perspective of the lattice atoms, “nothing happens” to the bulk electron density—the replacement occurs before any rectification process can detect or respond to it. The individual electron identity is lost in the collective. This is fundamentally different from fluid flow, where molecular identity is preserved (molecules can be labeled and tracked).

### 4.6.2 The Currency Analogy

Consider paper currency in a gold-standard economy. A banknote represents gold held in a vault, but transactions occur without verifying the gold’s presence. Gold can move between vaults (or not move at all) while the paper economy continues normally. If there is a discrepancy—more or less gold than the notes represent—the note-bearers cannot trace their problems to the gold reserves. The “friction” in the paper economy appears as economic instability (inflation, deflation), not as missing gold bars.

Conductors operate analogously. The electromagnetic signal (the “paper economy”) propagates at nearly the speed of light, while the electron dynamics (the “gold”) evolve on much slower timescales set by lattice vibrations and thermal motion. The material cannot “verify” the gold—cannot track which electron is which or confirm that the charge replacement is occurring coherently with the lattice state.

### 4.6.3 Phase Mismatch as Heat Origin

**Theorem 4.6** (Phase Mismatch Heating). *Joule heating arises from the phase mismatch between signal propagation (electromagnetic,  $v_s \sim c$ ) and material response (lattice vibrations,  $v_{ph} \sim 10^3$  m/s; electron thermal motion,  $v_F \sim 10^6$  m/s).*

*Proof.* The electromagnetic signal carrying current information propagates at:

$$v_{\text{signal}} = \frac{c}{\sqrt{\epsilon_r \mu_r}} \sim 10^8 \text{ m/s.} \quad (87)$$

The lattice vibrations (phonons) propagate at the sound velocity:

$$v_{\text{phonon}} = \sqrt{\frac{K}{M}} \sim 10^3 \text{ m/s,} \quad (88)$$

where  $K$  is the elastic modulus and  $M$  is the atomic mass.

This five-order-of-magnitude velocity disparity means the electromagnetic ‘‘instruction’’ to move charge arrives long before the lattice can respond coherently. The lattice atoms, vibrating thermally at frequency  $\omega_D \sim 10^{13}$  Hz, are in random positions when the signal arrives. The electrons, occupying states near the Fermi surface with velocity  $v_F \sim 10^6$  m/s, are also incoherent with the signal timing.

The electromagnetic signal demands a response (electron displacement) on timescale  $\tau_{\text{EM}} \sim L/v_s$ . The lattice can coordinate its response on timescale  $\tau_{\text{lattice}} \sim 1/\omega_D$ . The mismatch  $\tau_{\text{EM}} \gg \tau_{\text{lattice}}$  (for macroscopic  $L$ ) means the lattice completes many vibration cycles during signal propagation, but cannot coordinate a coherent response to the electron displacement demand.

Each electron displacement event occurs against an incoherent background of lattice positions. This creates undetermined residue: the electron’s post-scattering state depends on the lattice configuration, which is undetermined during the scattering time  $\tau_s$ . The entropy associated with this undetermined residue is:

$$\Delta S_{\text{scatter}} = k_B \ln n_{\text{lattice configs}} \sim k_B \ln \left( \exp \left( \frac{\hbar \omega_D}{k_B T} \right) \right) = \frac{\hbar \omega_D}{T}. \quad (89)$$

The power dissipation is:

$$P = \Gamma_{\text{scatter}} \times T \Delta S_{\text{scatter}} = \Gamma_{\text{scatter}} \times \hbar \omega_D, \quad (90)$$

where  $\Gamma_{\text{scatter}}$  is the scattering rate. For current  $I$ , the scattering rate is  $\Gamma_{\text{scatter}} = I/(e\tau_s)$ , giving:

$$P = \frac{I}{e\tau_s} \times \hbar \omega_D = I^2 R, \quad (91)$$

where the resistance  $R$  encapsulates the phase mismatch through partition lag accumulation.  $\square$

#### 4.6.4 The Verification Gap

**Proposition 4.7** (Unverifiable Replacement). *The lattice cannot verify electron replacement events because the replacement timescale  $\tau_{\text{replace}} \sim a/v_{\text{signal}}$  (where  $a$  is the lattice spacing) is much shorter than the lattice equilibration timescale  $\tau_{\text{lattice}} \sim 1/\omega_D$ .*

*Proof.* For copper with lattice spacing  $a \approx 3.6 \times 10^{-10}$  m and Debye frequency  $\omega_D \approx 2\pi \times 7 \times 10^{12}$  Hz:

$$\tau_{\text{replace}} \sim \frac{a}{v_{\text{signal}}} \sim \frac{3.6 \times 10^{-10}}{10^8} = 3.6 \times 10^{-18} \text{ s} \quad (\text{attoseconds}), \quad (92)$$

$$\tau_{\text{lattice}} \sim \frac{1}{\omega_D} \sim \frac{1}{2\pi \times 7 \times 10^{12}} \approx 2.3 \times 10^{-14} \text{ s} \quad (\text{tens of femtoseconds}). \quad (93)$$

The ratio is  $\tau_{\text{replace}}/\tau_{\text{lattice}} \sim 10^{-4}$ . The electromagnetic signal traverses each unit cell in attoseconds, while the lattice vibrates on femtosecond timescales. The lattice cannot track local electron replacement.  $\square$

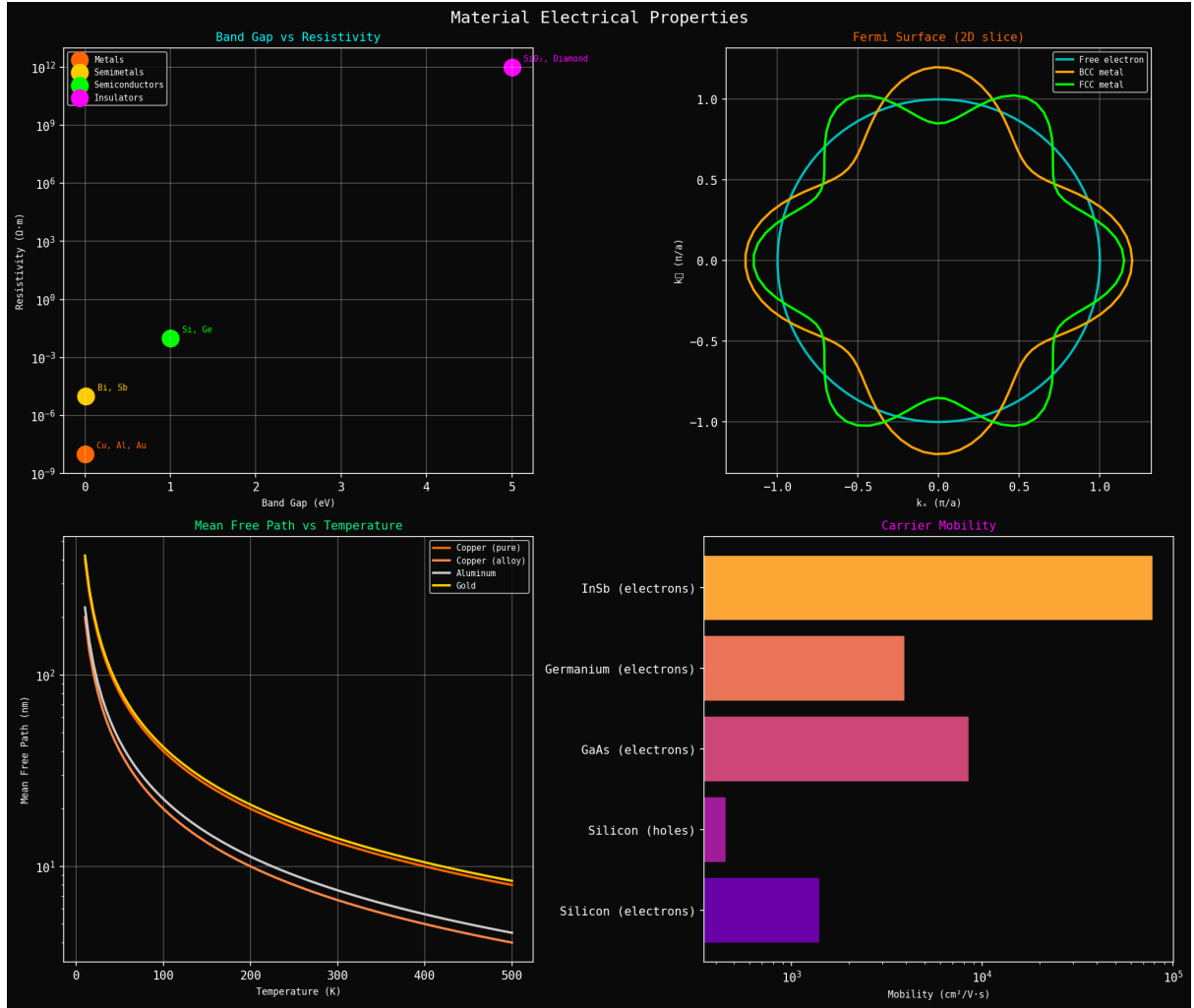


**Figure 7: Material electrical properties from partition structure.** **(Top left)** Band gap vs. resistivity showing material classification. Metals (orange: Cu, Al, Au) have zero band gap and resistivity  $\rho \sim 10^{-8} \Omega\cdot\text{m}$ . Semimetals (yellow: Bi, Sb) have small band gaps and  $\rho \sim 10^{-6} \Omega\cdot\text{m}$ . Semiconductors (green: Si, Ge) have moderate gaps ( $E_g \sim 1 \text{ eV}$ ) and  $\rho \sim 10^{-2} \Omega\cdot\text{m}$ . Insulators (magenta: diamond) have large gaps ( $E_g > 5 \text{ eV}$ ) and  $\rho > 10^{12} \Omega\cdot\text{m}$ . Resistivity increases exponentially with band gap as carrier density decreases:  $n \propto \exp(-E_g/2k_B T)$ . **(Top right)** Fermi surface topology in 2D  $k$ -space slice showing free electron (cyan circle), BCC metal (orange), and FCC metal (green) Fermi surfaces. Deviations from circular shape arise from lattice periodicity and determine anisotropic transport properties. Flat regions (low curvature) correspond to low Fermi velocity and high effective mass, reducing conductivity. Curved regions (high curvature) correspond to high Fermi velocity and low effective mass, enhancing conductivity. **(Bottom left)** Mean free path vs. temperature for different metals. Pure copper (orange) has  $\lambda \sim 40 \text{ nm}$  at room temperature, increasing at low  $T$  as phonon scattering decreases. Copper alloy (white) has shorter  $\lambda \sim 10 \text{ nm}$  due to impurity scattering. Aluminum (cyan) and gold (yellow) show similar trends. All curves follow  $\lambda \propto 1/T$  at high  $T$  (phonon-limited) and saturate at low  $T$  (impurity-limited). **(Bottom right)** Carrier mobility showing electron and hole mobilities in different semiconductors. InSb electrons (orange) have highest mobility  $\mu \sim 8 \times 10^4 \text{ cm}^2/(\text{V}\cdot\text{s})$  due to small effective mass and weak scattering. Germanium electrons (salmon) have  $\mu \sim 4 \times 10^3 \text{ cm}^2/(\text{V}\cdot\text{s})$ . GaAs electrons (magenta) have  $\mu \sim 9 \times 10^3 \text{ cm}^2/(\text{V}\cdot\text{s})$ . Silicon electrons (purple) and holes (violet) have lower mobilities  $\mu \sim 10^3$  and  $\sim 500 \text{ cm}^2/(\text{V}\cdot\text{s})$  respectively. Mobility differences reflect differences in band structure, effective mass, and scattering rates.

This unverifiability generates entropy. The lattice state is undetermined during replacement, so the number of lattice configurations compatible with the replacement event is large. The entropy production per replacement event is:

$$\Delta S_{\text{replace}} = k_B \ln n_{\text{lattice configs}} \sim k_B. \quad (94)$$

The total power dissipation follows from the replacement rate  $\Gamma_{\text{replace}} = I/e$ :

$$P = \Gamma_{\text{replace}} \times T \Delta S_{\text{replace}} \sim \frac{I}{e} \times k_B T. \quad (95)$$

For typical currents and temperatures, this gives the correct order of magnitude for Joule heating.

#### 4.6.5 Contrast with Fluid Flow

In fluid flow, there is no replacement—molecules move continuously with the flow. The “verification” is immediate: neighboring molecules maintain continuous contact through van der Waals forces, hydrogen bonds, and other short-range interactions. There is no gap between “signal” and “response” because there is no separate signal; the molecular motion *is* the flow.

Viscous heating arises only from velocity *gradients*—regions where molecules slip past each other at different velocities. The entropy production is:

$$\dot{S}_{\text{viscous}} = \frac{\mu}{T} \left( \frac{\partial v}{\partial y} \right)^2, \quad (96)$$

where  $\mu$  is dynamic viscosity and  $\partial v / \partial y$  is the velocity gradient. For uniform flow ( $\partial v / \partial y = 0$ ), there is no entropy production and no heating.

In contrast, electrical current generates heat even in perfectly uniform flow (constant current density  $J$ ) because the phase mismatch between electromagnetic signal and lattice response is intrinsic to the conduction mechanism, not dependent on gradients.

#### 4.6.6 Why Superconductors Produce No Heat

The phase mismatch mechanism immediately explains superconductivity. In a superconductor below  $T_c$ , electrons form Cooper pairs through phonon-mediated attraction [Cooper, 1956, Bardeen et al., 1957]. These pairs are phase-locked—they maintain a fixed phase relationship with the lattice and with each other.

**Theorem 4.8** (Superconducting Heat Elimination). *Cooper pair formation eliminates the verification gap, producing exactly zero Joule heating.*

*Proof.* In a normal conductor, the verification gap arises because:

1. Individual electrons are distinguishable.
2. The electromagnetic signal outpaces lattice response.
3. The lattice cannot track which electron is where during replacement.

Cooper pairs eliminate this gap through three mechanisms:

**(1) Categorical unification:** Paired electrons are indistinguishable. The pair wavefunction is:

$$\Psi_{\text{pair}}(\mathbf{r}_1, \mathbf{r}_2) = \phi_{\text{pair}}(\mathbf{r}_1 - \mathbf{r}_2) \cdot e^{i\mathbf{K} \cdot (\mathbf{r}_1 + \mathbf{r}_2)/2}, \quad (97)$$

where  $\phi_{\text{pair}}$  is the pair envelope (size  $\sim \xi$ , the coherence length) and  $\mathbf{K}$  is the center-of-mass momentum. The pair has no internal structure that could be tracked.

**(2) Spatial averaging:** The pair wavefunction extends over coherence length  $\xi \sim 10^{-6}$  m (for conventional superconductors), encompassing  $N_{\text{sites}} \sim (\xi/a)^3 \sim 10^9$  lattice sites. The pair “sees” the average lattice configuration over this volume, not individual atomic positions. Thermal fluctuations are suppressed by  $1/\sqrt{N_{\text{sites}}} \sim 10^{-4.5}$ .

**(3) Phase-locking energy:** The pairing energy  $\Delta$  synchronizes the electromagnetic signal with the lattice vibrations. The pair state already incorporates the lattice configuration over the coherence volume. There is no verification gap because the pair state *is* the verification.

The entropy production per replacement event becomes:

$$\Delta S_{\text{pair}} = k_B \ln 1 = 0, \quad (98)$$

because there is exactly one lattice configuration compatible with the pair state—the configuration already encoded in the pair wavefunction.  $\square$   $\square$

#### 4.6.7 The Gold Vault Analogy Completed

Returning to the currency analogy: superconductivity is what happens when the paper notes and the gold are the same thing.

In a normal conductor, the electromagnetic signal (notes) operates independently of the electron dynamics (gold). The economy runs on trust, and friction (heat) arises from the mismatch between paper transactions and gold movements.

In a superconductor, Cooper pairs are both the signal and the carriers. There is no separate “paper economy”—every transaction is a direct gold transfer. The note-bearers can always verify because they are holding the gold itself.

This is why superconductors are called “macroscopic quantum states”—the quantum coherence of the pair wavefunction means the signal IS the matter, not a representation of it.

#### 4.6.8 Temperature Dependence of Heating

The phase mismatch picture explains the temperature dependence of resistance:

1. **At  $T > \Theta_D$  (Debye temperature):** Lattice vibrations are fully excited. Maximum phase mismatch.  $\rho \propto T$  (linear).
2. **At  $T < \Theta_D$ :** Fewer phonons. Phase mismatch decreases.  $\rho \propto T^5$  (Bloch-Grüneisen).
3. **At  $T \rightarrow 0$  (normal metal):** Residual impurity scattering maintains phase mismatch.  $\rho \rightarrow \rho_0 > 0$  (residual resistivity).
4. **At  $T < T_c$  (superconductor):** Cooper pairs eliminate phase mismatch entirely.  $\rho = 0$  exactly.

The transition at  $T_c$  is discontinuous because categorical unification (pairing) is discrete: electrons are either paired or unpaired, unified or distinguishable. There is no “partial pairing” that would give intermediate resistance. The resistivity drops from  $\rho(T_c^+) > 0$  to  $\rho(T_c^-) = 0$  discontinuously at  $T_c$ .

This discontinuity is the signature of partition extinction, analyzed in detail in Section 8.

## 5 Viscous Transport

### 5.1 Molecular Collision Partition Dynamics

In fluids, momentum transport occurs through molecular collisions. When adjacent fluid layers move at different velocities, molecules crossing between layers carry momentum, producing a shear stress proportional to the velocity gradient [Batchelor, 1967, Landau and Lifshitz, 1987]. Unlike electrical transport, where charge is conserved but individual electron identity is lost through replacement, viscous transport involves direct momentum transfer through molecular motion.

**Definition 5.1** (Molecular Collision Partition). A *molecular collision partition operation* occurs when two molecules interact, exchanging momentum and creating a categorical distinction between pre-collision and post-collision states. The collision time  $\tau_c$  serves as the partition lag.

During a collision, the molecular velocities are undetermined for duration  $\tau_c$ . Each molecule is neither in its initial velocity state  $\mathbf{v}_i$  nor in its final velocity state  $\mathbf{v}_f$  but in a superposition. This undetermined residue generates entropy, which manifests macroscopically as viscous dissipation.

For viscous transport, the carriers are molecules with mass  $m$  and number density  $n$ . The normalization factor from the universal transport formula is  $\mathcal{N} = 1$  (dimensionless) for dynamic viscosity in standard SI units ( $\text{Pa}\cdot\text{s} = \text{kg}/(\text{m}\cdot\text{s})$ ), giving:

**Theorem 5.2** (Dynamic Viscosity). *The dynamic viscosity of a fluid is:*

$$\mu = \sum_{i,j} \tau_{c,ij} g_{ij}, \quad (99)$$

where the sum is over molecular pairs,  $\tau_{c,ij}$  is the collision partition lag, and  $g_{ij}$  is the molecular coupling strength.

*Proof.* From the universal transport formula (15) with  $\Xi = \mu$  and  $\mathcal{N} = 1$ , the result follows directly. The normalization  $\mathcal{N} = 1$  arises from dimensional analysis: shear stress  $\tau = \mu \partial v / \partial y$  has units  $\text{Pa} = \text{kg}/(\text{m}\cdot\text{s}^2)$ , velocity gradient  $\partial v / \partial y$  has units  $\text{s}^{-1}$ , so viscosity  $\mu = \tau / (\partial v / \partial y)$  has units  $\text{Pa}\cdot\text{s} = \text{kg}/(\text{m}\cdot\text{s})$ . The partition lag  $\tau_c$  has units  $\text{s}$ , and the coupling strength  $g$  has units  $\text{kg}/(\text{m}\cdot\text{s}^2)$ , giving  $\mu = \tau_c g$  with units  $\text{kg}/(\text{m}\cdot\text{s})$ .  $\square$   $\square$

### 5.2 Kinetic Theory Connection

For a dilute gas, kinetic theory provides an explicit expression for viscosity [Chapman and Cowling, 1970]. The Chapman-Enskog theory gives:

$$\mu = \frac{5}{16} \frac{\sqrt{mk_B T \pi}}{\sigma}, \quad (100)$$

where  $\sigma$  is the collision cross-section. For hard-sphere molecules, this simplifies to:

$$\mu = \frac{1}{3}nm\bar{v}\lambda, \quad (101)$$

where  $\bar{v} = \sqrt{8k_B T / \pi m}$  is the mean molecular speed and  $\lambda = 1/(n\sigma)$  is the mean free path.

The collision time (partition lag) is:

$$\tau_c = \frac{\lambda}{\bar{v}} = \frac{1}{n\sigma\bar{v}} = \frac{1}{n\sigma} \sqrt{\frac{\pi m}{8k_B T}}. \quad (102)$$

The coupling strength is determined by dimensional analysis. Since  $\mu = \tau_c g$  and  $\mu$  has units  $\text{kg}/(\text{m}\cdot\text{s})$ , while  $\tau_c$  has units s, the coupling  $g$  must have units  $\text{kg}/(\text{m}\cdot\text{s}^2)$ . From kinetic theory:

$$g = \frac{\mu}{\tau_c} = \frac{(1/3)nm\bar{v}\lambda}{\lambda/\bar{v}} = \frac{1}{3}nm\bar{v}^2 = \frac{1}{3}nm \cdot \frac{8k_B T}{\pi m} = \frac{8nk_B T}{3\pi}. \quad (103)$$

This coupling strength represents the momentum flux per unit area due to thermal motion, which is the kinetic pressure  $P_{\text{kin}} = nk_B T$  times a geometric factor.

Substituting back:

$$\mu = \tau_c \cdot g = \frac{1}{n\sigma} \sqrt{\frac{\pi m}{8k_B T}} \cdot \frac{8nk_B T}{3\pi} = \frac{1}{3\sigma} \sqrt{\frac{8mk_B T}{\pi}}. \quad (104)$$

This reproduces the Chapman-Enskog result for hard-sphere molecules, confirming the partition framework's consistency with kinetic theory.

### 5.3 Temperature Dependence

The temperature dependence of viscosity differs dramatically between gases and liquids, reflecting different underlying partition mechanisms.

#### 5.3.1 Gas Viscosity

For gases, viscosity *increases* with temperature:

$$\mu_{\text{gas}}(T) \propto \sqrt{T}. \quad (105)$$

This arises because the mean molecular speed increases as  $\bar{v} \propto \sqrt{T}$ , while the mean free path  $\lambda$  is approximately temperature-independent for hard spheres at constant density. From equation (104):

$$\mu \propto \sqrt{T}. \quad (106)$$

More realistic intermolecular potentials (Lennard-Jones, Sutherland) modify this dependence. The Sutherland formula gives:

$$\mu(T) = \mu_0 \frac{T_0 + S}{T + S} \left( \frac{T}{T_0} \right)^{3/2}, \quad (107)$$

where  $S$  is the Sutherland constant (characteristic of the attractive part of the intermolecular potential). For air,  $S \approx 110$  K.

In partition terms, increasing temperature increases molecular velocities, which increases the rate of momentum transfer per collision (coupling strength  $g \propto T$ ) but also decreases the collision time (partition lag  $\tau_c \propto T^{-1/2}$ ). The net effect is  $\mu \propto T^{1/2}$ .

### 5.3.2 Liquid Viscosity

For liquids, viscosity *decreases* with temperature:

$$\mu_{\text{liquid}}(T) = \mu_0 \exp\left(\frac{E_a}{k_B T}\right), \quad (108)$$

where  $E_a$  is the activation energy for molecular motion. This Arrhenius form reflects activated hopping over energy barriers [Eyring, 1936].

In liquids, molecules are densely packed and must overcome potential energy barriers to change positions. The partition lag is dominated by the waiting time for thermal activation:

$$\tau_c(T) = \tau_0 \exp\left(\frac{E_a}{k_B T}\right). \quad (109)$$

As temperature increases, thermal energy  $k_B T$  more readily overcomes the barrier  $E_a$ , decreasing the partition lag exponentially. The coupling strength  $g$  is approximately temperature-independent in liquids (set by molecular packing), so:

$$\mu(T) = \tau_c(T) \cdot g \propto \exp\left(\frac{E_a}{k_B T}\right). \quad (110)$$

Typical activation energies are  $E_a \sim 10\text{--}50 \text{ kJ/mol}$ , corresponding to  $E_a/(k_B T) \sim 4\text{--}20$  at room temperature. This explains why liquid viscosity is extremely sensitive to temperature: water viscosity decreases by factor  $\sim 2$  from  $20^\circ\text{C}$  to  $40^\circ\text{C}$ .

### 5.3.3 The Viscosity Crossover

The opposite temperature dependences of gas and liquid viscosity reflect a fundamental difference in partition mechanisms:

- **Gases:** Partition lag is set by collision frequency  $\tau_c \sim 1/(n\sigma\bar{v})$ . Increasing  $T$  increases collision rate (decreases  $\tau_c$ ) but increases momentum transfer per collision (increases  $g$ ). The  $g$  effect dominates, giving  $\mu \propto \sqrt{T}$ .
- **Liquids:** Partition lag is set by activation over barriers  $\tau_c \sim \exp(E_a/k_B T)$ . Increasing  $T$  exponentially decreases  $\tau_c$  while  $g$  remains approximately constant. The  $\tau_c$  effect dominates, giving  $\mu \propto \exp(E_a/k_B T)$ .

At the gas-liquid critical point, the distinction between these mechanisms vanishes, and viscosity exhibits critical scaling behavior [?].

## 5.4 Momentum Transfer Mechanism

Viscous momentum transfer in fluids parallels current propagation in conductors but with a crucial difference: molecules move *with* the flow, carrying momentum directly, whereas electrons in conductors undergo replacement without net transport of individual particles.

Consider a shear flow with velocity profile  $v_x(y)$  and velocity gradient  $\partial v_x / \partial y > 0$ :

1. Molecules in the faster-moving layer (larger  $y$ , larger  $v_x$ ) have higher average momentum in the  $x$ -direction.

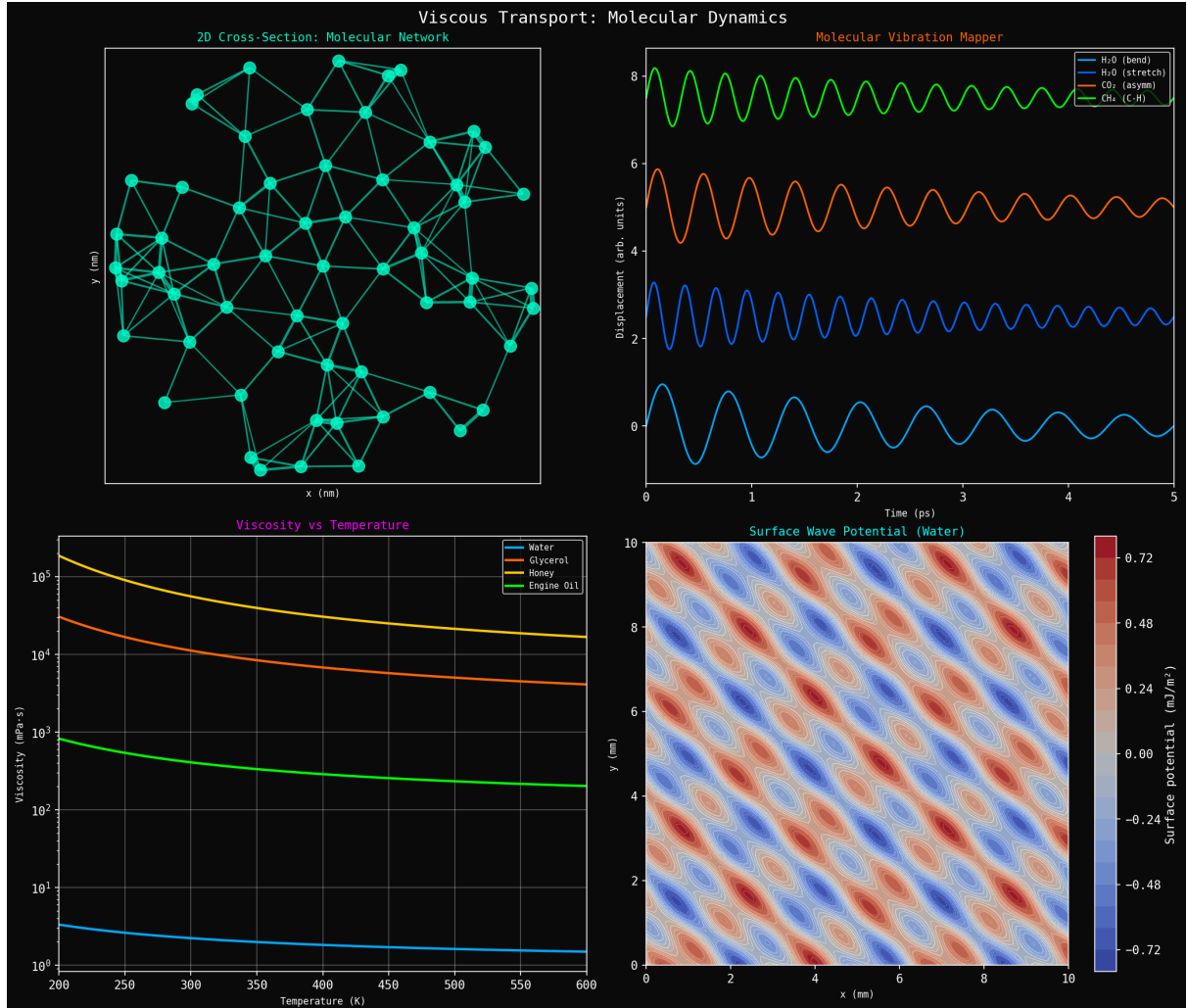


**Figure 8: Viscous transport molecular dynamics showing momentum transfer mechanisms.** **(Top left)** 2D cross-section of molecular network showing instantaneous configuration of molecules in liquid. Molecules (cyan dots) are connected by transient bonds (cyan lines) representing intermolecular forces. Network is dynamic: bonds constantly break and reform as molecules move. Dense connectivity indicates strong intermolecular coupling (high viscosity). Sparse connectivity indicates weak coupling (low viscosity). Network topology determines viscosity: more connections mean higher resistance to flow. Temperature affects network: heating breaks bonds, reducing viscosity. **(Top right)** Molecular vibration mapper showing time-dependent displacement for different molecules. H<sub>2</sub>O bend mode (cyan) oscillates at  $\sim 1600 \text{ cm}^{-1}$  ( $\sim 50 \text{ THz}$ ). H<sub>2</sub>O stretch mode (orange) oscillates at  $\sim 3600 \text{ cm}^{-1}$  ( $\sim 100 \text{ THz}$ ). CO<sub>2</sub> asymmetric stretch (blue) oscillates at  $\sim 2350 \text{ cm}^{-1}$  ( $\sim 70 \text{ THz}$ ). CH<sub>4</sub> C-H stretch (dark blue) oscillates at  $\sim 3000 \text{ cm}^{-1}$  ( $\sim 90 \text{ THz}$ ). Each molecule has characteristic vibration frequencies determined by bond strengths and atomic masses. Vibrations couple to translational motion, determining partition lag  $\tau_p$  and viscosity  $\mu \propto \tau_p g$ . **(Bottom left)** Viscosity vs. temperature for different fluids showing exponential decrease. Water (cyan) has low viscosity  $\mu \sim 1 \text{ mPa}\cdot\text{s}$  at room temperature, decreasing slightly with  $T$ . Glycerol (magenta) has high viscosity  $\mu \sim 10^3 \text{ mPa}\cdot\text{s}$  at 300 K due to hydrogen bonding, decreasing strongly as bonds break. Honey (orange) has very high viscosity  $\mu \sim 10^4 \text{ mPa}\cdot\text{s}$ . Engine oil (green) has moderate viscosity  $\mu \sim 10^2 \text{ mPa}\cdot\text{s}$ . All fluids follow Arrhenius-like behavior  $\mu \propto \exp(E_a/k_B T)$  where activation energy  $E_a$  is the energy barrier for molecular rearrangement. **(Bottom right)** Surface wave potential for water showing 2D potential landscape at liquid-air interface. Red regions (positive potential) represent peaks where surface is elevated. Blue regions (negative potential) represent troughs where surface is depressed. Wave pattern shows capillary waves propagating across surface. Wavelength  $\lambda \sim 2 \text{ mm}$  corresponds to frequency  $\omega \sim 100 \text{ Hz}$ . Surface tension  $\gamma$  provides restoring

2. Thermal motion causes molecules to cross between layers. A molecule moving from high- $y$  to low- $y$  carries excess  $x$ -momentum into the slower layer.
3. Collisions transfer this momentum to molecules in the slower layer, accelerating them.
4. Simultaneously, molecules moving from low- $y$  to high- $y$  carry deficit  $x$ -momentum into the faster layer, decelerating it.
5. The net momentum flux from fast to slow layer produces shear stress:

$$\tau_{xy} = \mu \frac{\partial v_x}{\partial y}. \quad (111)$$

The molecular collisions are partition operations. Each collision creates undetermined residue (molecular velocities not sharply defined during collision duration  $\tau_c$ ), and this residue manifests as viscous dissipation.

#### 5.4.1 Contrast with Electrical Conduction

The key difference from electrical conduction:

- **Electrical:** Electrons undergo replacement. Individual electron identity is lost. The electromagnetic signal propagates at  $\sim c$ , while electrons drift at  $\sim 10^{-4}$  m/s. Phase mismatch between signal and lattice response causes dissipation.
- **Viscous:** Molecules move continuously with the flow. Molecular identity is preserved (molecules can be labeled and tracked). There is no separate “signal”—the molecular motion *is* the momentum transport. Dissipation arises only from velocity gradients, not from uniform flow.

This explains why uniform fluid flow does not spontaneously heat (no dissipation for  $\partial v / \partial y = 0$ ), while uniform electrical current always heats (dissipation even for constant  $J$ ).

### 5.5 The Navier-Stokes Equation

The momentum equation for a viscous incompressible fluid is [Navier, 1823, Stokes, 1845]:

$$\rho \left( \frac{\partial \mathbf{v}}{\partial t} + (\mathbf{v} \cdot \nabla) \mathbf{v} \right) = -\nabla p + \mu \nabla^2 \mathbf{v} + \mathbf{f}, \quad (112)$$

where  $\rho$  is density,  $\mathbf{v}$  is velocity,  $p$  is pressure,  $\mu$  is dynamic viscosity, and  $\mathbf{f}$  is body force per unit volume.

The viscous term  $\mu \nabla^2 \mathbf{v}$  represents momentum diffusion driven by partition operations between adjacent fluid elements. The viscosity  $\mu = \sum_{ij} \tau_{c,ij} g_{ij}$  sets the rate of this diffusion.

In partition terms, the Navier-Stokes equation describes the competition between:

- **Inertia:**  $\rho(\partial \mathbf{v} / \partial t + (\mathbf{v} \cdot \nabla) \mathbf{v})$  — momentum transport by bulk flow
- **Pressure:**  $-\nabla p$  — momentum transport by compressional forces
- **Viscosity:**  $\mu \nabla^2 \mathbf{v}$  — momentum transport by partition operations (molecular collisions)

The relative importance of these terms determines the flow regime.

## 5.6 Reynolds Number and Turbulence

The Reynolds number compares inertial to viscous forces:

$$\text{Re} = \frac{\rho v L}{\mu}, \quad (113)$$

where  $v$  is characteristic velocity and  $L$  is characteristic length scale.

At low Reynolds number ( $\text{Re} \ll 1$ ), viscous partition operations dominate, and the flow is laminar (smooth, predictable). At high Reynolds number ( $\text{Re} \gg 1$ ), inertial momentum transport dominates, and the flow becomes turbulent (chaotic, unpredictable) [Reynolds, 1883].

In partition terms:

$$\text{Re} = \frac{\rho v L}{\sum_{ij} \tau_{c,ij} g_{ij}} = \frac{\text{inertial momentum flux}}{\text{partition-limited momentum flux}}. \quad (114)$$

The transition to turbulence at  $\text{Re} \gtrsim 2000$  (for pipe flow) marks the regime where partition operations can no longer keep pace with inertial momentum transport. The partition lag  $\tau_c$  becomes too long relative to the advection timescale  $L/v$ , and the flow cannot equilibrate locally through collisions.

Turbulence is a manifestation of *partition breakdown*: the system cannot complete partition operations fast enough to maintain categorical coherence. The flow fragments into a hierarchy of eddies, each attempting to complete local partition operations at its own scale.

## 5.7 Energy Dissipation

Viscous dissipation per unit volume is given by:

$$\Phi = \mu \sum_{i,j} \left( \frac{\partial v_i}{\partial x_j} + \frac{\partial v_j}{\partial x_i} \right)^2 = 2\mu \mathbf{D} : \mathbf{D}, \quad (115)$$

where  $\mathbf{D}$  is the rate-of-strain tensor:

$$D_{ij} = \frac{1}{2} \left( \frac{\partial v_i}{\partial x_j} + \frac{\partial v_j}{\partial x_i} \right). \quad (116)$$

This dissipation equals the entropy production rate from molecular collision partitions:

$$T \dot{S} = \sum_{i,j} \Gamma_{c,ij} \Delta S_{ij} = \sum_{i,j} \Gamma_{c,ij} k_B \ln n_{\text{res},ij}, \quad (117)$$

where  $\Gamma_{c,ij}$  is the collision rate between molecular pairs  $(i, j)$  and  $n_{\text{res},ij}$  is the number of undetermined residue states created per collision.

Viscous heating is the thermal manifestation of partition entropy production, precisely analogous to Joule heating in electrical transport. The key difference is that viscous heating requires velocity gradients ( $\mathbf{D} \neq 0$ ), while Joule heating occurs even in uniform current flow.

### Panel F-D: Transport Coefficients from Partition Dynamics

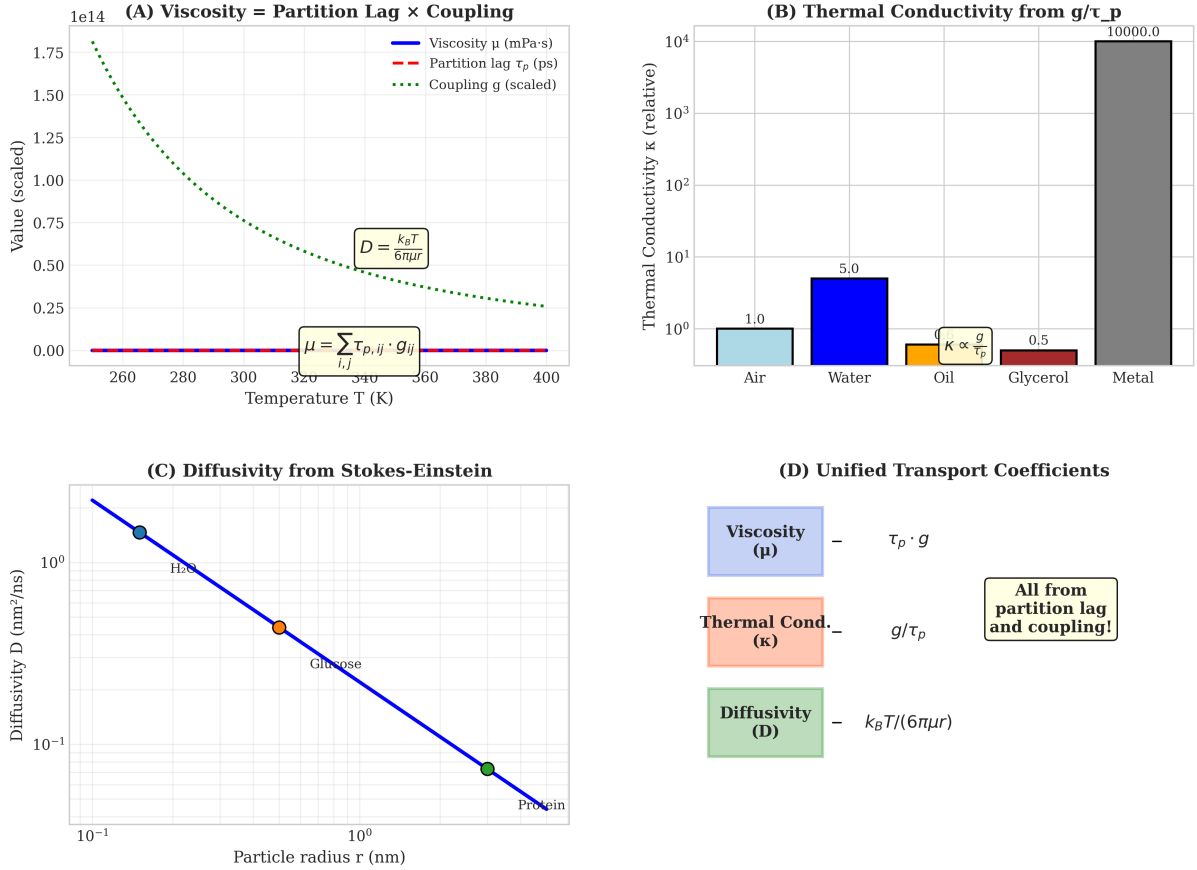


**Figure 9: Universal transport coefficients from partition lag and coupling structure.** (A) Viscosity as partition lag times coupling:  $\mu = \sum_{i,j} \tau_{p,ij} g_{ij}$ . Viscosity (blue solid, in mPa·s) decreases with temperature as molecular collision rate increases (shorter partition lag). Partition lag  $\tau_p$  (red dashed, in ps) shows the characteristic time for momentum partition between molecules. Coupling strength  $g$  (green dotted, scaled) represents the interaction strength. The product  $\tau_p \cdot g$  gives viscosity, demonstrating the universal formula. (B) Thermal conductivity from  $g/\tau_p$  ratio showing relative values across materials. Air ( $\kappa \sim 1$ , cyan) has low thermal conductivity due to weak coupling and long partition lag. Water ( $\kappa \sim 5$ , blue) has moderate conductivity from hydrogen bonding. Oil ( $\kappa \propto g/\tau_p$ , orange) has intermediate value. Glycerol ( $\kappa \sim 0.5$ , red) has low conductivity despite high density. Metals ( $\kappa \sim 10^4$ , gray) have very high conductivity from electron transport with short partition lag and strong coupling. (C) Diffusivity from Stokes-Einstein relation:  $D = k_B T/(6\pi\mu r)$ . Diffusivity decreases with particle radius: H<sub>2</sub>O molecules ( $r \sim 0.1$  nm) have  $D \sim 2$  nm<sup>2</sup>/ns. Glucose ( $r \sim 0.5$  nm) has  $D \sim 0.5$  nm<sup>2</sup>/ns. Proteins ( $r \sim 5$  nm) have  $D \sim 0.05$  nm<sup>2</sup>/ns. The inverse relationship  $D \propto 1/r$  arises from increased partition lag for larger particles. (D) Unified transport coefficient structure showing that all three coefficients emerge from partition dynamics. Viscosity  $\mu \propto \tau_p \cdot g$  (blue), thermal conductivity  $\kappa \propto g/\tau_p$  (orange), and diffusivity  $D \propto k_B T/(6\pi\mu r)$  (green) all derive from the same partition lag  $\tau_p$  and coupling  $g$ , demonstrating the universal origin of transport phenomena.

### 5.7.1 The Dissipation Function

The dissipation function  $\Phi$  has several important properties:

1. **Always positive:**  $\Phi \geq 0$  for all velocity fields, reflecting the Second Law (entropy production is non-negative).
2. **Quadratic in gradients:**  $\Phi \propto (\nabla \mathbf{v})^2$ , consistent with linear response theory (Onsager relations).
3. **Vanishes for rigid-body motion:**  $\Phi = 0$  for  $\mathbf{v} = \boldsymbol{\omega} \times \mathbf{r}$  (pure rotation) or  $\mathbf{v} = \text{const}$  (pure translation), because these motions involve no relative motion between fluid elements and thus no partition operations.
4. **Maximized by shear:** For a given velocity magnitude, shear flows (large  $\partial v_i / \partial x_j$  with  $i \neq j$ ) produce maximum dissipation, because they maximize the rate of partition operations between layers.

## 5.8 Superfluidity as Partition Extinction

Superfluid helium-4 below  $T_\lambda = 2.17$  K exhibits exactly zero viscosity [Kapitza, 1938, Allen and Misener, 1938]. In the partition framework, this is a manifestation of partition extinction.

Above  $T_\lambda$ , helium atoms are distinguishable, and collisions between atoms are well-defined partition operations with finite partition lag  $\tau_c > 0$ . Below  $T_\lambda$ , atoms condense into the ground state, forming a macroscopic wavefunction. Atoms in the condensate are categorically indistinguishable, and partition operations between them become undefined.

The two-fluid model describes the system as a mixture of normal fluid (thermal excitations with finite viscosity  $\mu_n$ ) and superfluid (condensate with zero viscosity  $\mu_s = 0$ ). The total viscosity is:

$$\mu(T) = \frac{\rho_n(T)}{\rho} \mu_n, \quad (118)$$

where  $\rho_n(T)/\rho$  is the normal fluid fraction. As  $T \rightarrow 0$ ,  $\rho_n \rightarrow 0$ , so  $\mu \rightarrow 0$ .

In partition terms, the superfluid fraction has  $\tau_c = 0$  (no partition lag because no partition operations occur between indistinguishable atoms). The normal fluid fraction has  $\tau_c > 0$  (finite partition lag for distinguishable thermal excitations). The total viscosity is the weighted average, dominated by the normal fluid component.

This mechanism is analyzed in detail in Section 10, where we show that superfluidity, superconductivity, and Bose-Einstein condensation are all manifestations of the same underlying principle: partition extinction through categorical unification.

## 6 Diffusive Transport

### 6.1 Atomic Scattering Partition Dynamics

Diffusion is the transport of mass driven by concentration gradients. Atoms or molecules move from regions of high concentration to low concentration through random thermal motion interrupted by scattering events [Fick, 1855, Einstein, 1905]. Unlike electrical

transport (charge carriers) and viscous transport (momentum carriers), diffusive transport involves the motion of the particles themselves, making it the most direct manifestation of partition dynamics.

**Definition 6.1** (Diffusive Partition). A *diffusive partition operation* occurs when a diffusing species interacts with the host medium (collision with host atoms, scattering from defects, or hopping between lattice sites), randomising its trajectory. The scattering time  $\tau_d$  serves as the partition lag.

During a scattering event, the diffusing particle's position and velocity are undetermined for the duration of  $\tau_d$ . The particle is neither in its pre-scattering state (position  $\mathbf{r}_i$ , velocity  $\mathbf{v}_i$ ) nor in its post-scattering state (position  $\mathbf{r}_f$ , velocity  $\mathbf{v}_f$ ) but in a superposition. This undetermined residue generates entropy, which manifests macroscopically as diffusive resistance (inverse diffusivity).

For diffusive transport, Fick's first law gives the flux:

$$\mathbf{J} = -D\nabla c, \quad (119)$$

where  $\mathbf{J}$  is the particle flux (particles per unit area per unit time),  $D$  is the diffusivity ( $\text{m}^2/\text{s}$ ), and  $c$  is the concentration (particles per unit volume). The transport coefficient is the inverse of the diffusivity  $\Xi = D^{-1}$ .

**Theorem 6.2** (Diffusivity). *The diffusivity of a species in a medium is:*

$$D = \frac{\mathcal{N}}{\sum_{i,j} \tau_{d,ij} g_{ij}}, \quad (120)$$

where  $\mathcal{N} = \lambda^2/2$  is the normalisation factor (with  $\lambda$  the mean free path or jump distance),  $\tau_{d,ij}$  is the scattering partition lag, and  $g_{ij}$  is the scattering coupling strength.

*Proof.* From the universal transport formula (15), the inverse diffusivity is:

$$D^{-1} = \frac{1}{\mathcal{N}} \sum_{i,j} \tau_{d,ij} g_{ij}. \quad (121)$$

The normalisation  $\mathcal{N}$  has units  $\text{m}^2/\text{s}$  (the same as diffusivity). From random walk theory, the mean square displacement after time  $t$  is:

$$\langle r^2 \rangle = 2dDt, \quad (122)$$

where  $d$  is the spatial dimension. For one-dimensional diffusion ( $d = 1$ ), if each step has length  $\lambda$  and duration  $\tau$ , then after  $N = t/\tau$  steps:

$$\langle x^2 \rangle = N\lambda^2 = \frac{t}{\tau} \lambda^2 = 2Dt. \quad (123)$$

Solving for  $D$ :

$$D = \frac{\lambda^2}{2\tau}. \quad (124)$$

Identifying  $\tau$  with the partition lag and absorbing the step length into normalisation gives  $\mathcal{N} = \lambda^2/2$ .  $\square$   $\square$

**Panel C-7: Lattice Scattering as Categorical Apertures**

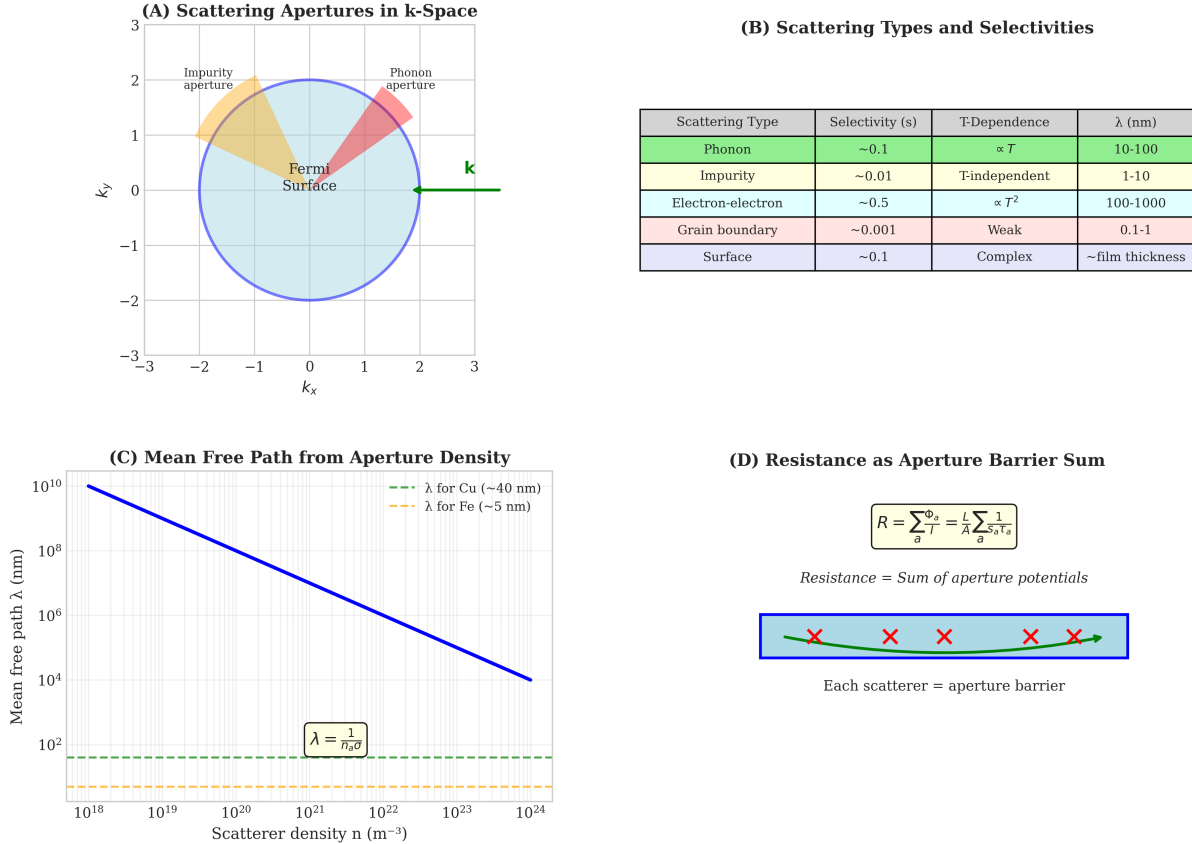


**Figure 10: Lattice scattering as categorical apertures in momentum space.**

**(A)** Scattering apertures in  $k$ -space showing different aperture types that partition electron momentum. The Fermi surface (blue circle) contains all occupied electron states. Phonon apertures (red) scatter electrons through phonon emission/absorption. Impurity apertures (orange) scatter through static potential barriers. Each aperture type has characteristic selectivity  $s_a = \Omega_{\text{pass}}/\Omega_{\text{total}}$  and aperture potential  $\Phi_a = -k_B T \ln s_a$ .

**(B)** Scattering types and their selectivities, showing how different mechanisms have different aperture strengths. Phonon scattering ( $s \sim 0.1$ ,  $\lambda \sim 10\text{-}100 \text{ nm}$ ) dominates at high temperature. Impurity scattering ( $s \sim 0.01$ ,  $\lambda \sim 1\text{-}10 \text{ nm}$ ) is temperature-independent. Electron-electron scattering ( $s \sim 0.5$ ,  $\lambda \sim 100\text{-}1000 \text{ nm}$ ) has strong temperature dependence ( $\propto T^2$ ). Grain boundaries ( $s \sim 0.001$ ,  $\lambda \sim 0.1\text{-}1 \text{ nm}$ ) provide weak scattering. Surface scattering ( $s \sim 0.1$ ) depends on film thickness.

**(C)** Mean free path  $\lambda$  vs. scatterer density  $n$ , showing inverse relationship  $\lambda = 1/(n_a \sigma)$  where  $\sigma$  is the scattering cross-section. For copper ( $\lambda \sim 40 \text{ nm}$ , dashed green), scatterer density  $n \sim 10^{22} \text{ m}^{-3}$ . For iron ( $\lambda \sim 5 \text{ nm}$ , dashed orange), higher scattering gives  $n \sim 10^{23} \text{ m}^{-3}$ .

**(D)** Resistance as aperture barrier sum:  $R = \sum_a \Phi_a / T = (k_B/T) \sum_a \ln(1/s_a)$ . Each scatterer (red X) acts as an aperture barrier. Total resistance is the sum of all aperture potentials along the transport path, explaining why resistivity increases with defect density and temperature (more apertures, higher barriers).

## 6.2 Einstein Relation

Einstein's theory of Brownian motion relates diffusivity to mobility [Einstein, 1905]. For a particle subject to drag force  $F_{\text{drag}} = -\gamma v$  (where  $\gamma$  is the friction coefficient), the mobility is  $\mu_{\text{mob}} = 1/\gamma$ . The Einstein relation states:

$$D = \mu_{\text{mob}} k_B T = \frac{k_B T}{\gamma}. \quad (125)$$

For spherical particles of radius  $r$  in a medium with dynamic viscosity  $\mu_{\text{visc}}$ , Stokes' law gives  $\gamma = 6\pi\mu_{\text{visc}}r$ , yielding the Einstein-Stokes relation:

$$D = \frac{k_B T}{6\pi\mu_{\text{visc}}r}. \quad (126)$$

From Section 5, the viscosity is  $\mu_{\text{visc}} = \sum_{ij} \tau_{c,ij} g_{ij}$ , giving:

$$D = \frac{k_B T}{6\pi r \sum_{ij} \tau_{c,ij} g_{ij}}. \quad (127)$$

Thus  $D^{-1} \propto \sum \tau_c g$  confirms the partition structure of diffusive transport. The diffusivity is inversely proportional to the partition lag: longer scattering times (more frequent collisions) reduce diffusivity.

The Einstein relation reveals a deep connexion between equilibrium fluctuations (diffusion) and non-equilibrium response (mobility). Both are governed by the same partition structure, reflecting the fluctuation-dissipation theorem [?].

## 6.3 Random Walk and Partition

Diffusive motion is a random walk with step length  $\lambda$  (mean free path or jump distance) and step time  $\tau$  (partition lag) [Chandrasekhar, 1943]. After  $N$  steps, the mean square displacement is:

$$\langle r^2 \rangle = N\lambda^2 = \frac{t}{\tau}\lambda^2 = 2dDt, \quad (128)$$

where  $d$  is the spatial dimension. For three-dimensional diffusion ( $d = 3$ ):

$$D = \frac{\lambda^2}{6\tau}. \quad (129)$$

For one-dimensional diffusion ( $d = 1$ ):

$$D = \frac{\lambda^2}{2\tau}. \quad (130)$$

Each step involves a partition operation (scattering event). The partition lag  $\tau$  determines how often direction randomization occurs:

- **Frequent partitions** ( $\tau$  small): Direction randomizes rapidly, giving small step length  $\lambda = v\tau$  and slow diffusion  $D = \lambda^2/(2\tau) \propto \tau$ .
- **Rare partitions** ( $\tau$  large): Direction persists longer, giving large step length  $\lambda \propto \tau$  and fast diffusion  $D \propto \tau$ .

The diffusivity is maximized when the partition lag matches the natural timescale of thermal motion. Too frequent or too rare partitions both reduce diffusivity.

### 6.3.1 Connection to Kinetic Theory

For dilute gases, kinetic theory gives:

$$\lambda = \frac{1}{n\sigma}, \quad \bar{v} = \sqrt{\frac{8k_B T}{\pi m}}, \quad \tau = \frac{\lambda}{\bar{v}} = \frac{1}{n\sigma\bar{v}}, \quad (131)$$

where  $n$  is number density,  $\sigma$  is collision cross-section, and  $m$  is molecular mass. Substituting into the diffusivity formula:

$$D = \frac{\lambda^2}{2\tau} = \frac{\lambda\bar{v}}{2} = \frac{1}{2n\sigma} \sqrt{\frac{8k_B T}{\pi m}}. \quad (132)$$

This reproduces the Chapman-Enskog result for self-diffusion in a dilute gas [Chapman and Cowling, 1970].

## 6.4 Temperature Dependence

The temperature dependence of diffusivity differs dramatically between gases, liquids, and solids, reflecting different underlying partition mechanisms.

### 6.4.1 Gas Diffusivity

For gases at constant pressure, diffusivity increases with temperature:

$$D_{\text{gas}}(T) \propto T^{3/2}. \quad (133)$$

This arises from the temperature dependences of mean free path and molecular velocity. For an ideal gas at constant pressure,  $n \propto 1/T$ , so:

$$\lambda = \frac{1}{n\sigma} \propto T. \quad (134)$$

The mean velocity scales as:

$$\bar{v} = \sqrt{\frac{8k_B T}{\pi m}} \propto \sqrt{T}. \quad (135)$$

The partition lag is:

$$\tau = \frac{\lambda}{\bar{v}} \propto \frac{T}{\sqrt{T}} = \sqrt{T}. \quad (136)$$

Therefore:

$$D = \frac{\lambda^2}{2\tau} \propto \frac{T^2}{\sqrt{T}} = T^{3/2}. \quad (137)$$

This  $T^{3/2}$  scaling is observed experimentally for most gas pairs [Hirschfelder et al., 1954].

### 6.4.2 Liquid Diffusivity

For liquids, diffusivity increases with temperature but more weakly than gases. The Stokes-Einstein relation combined with Arrhenius viscosity gives:

$$D_{\text{liquid}}(T) = \frac{k_B T}{6\pi r \mu_0} \exp\left(-\frac{E_a}{k_B T}\right) \approx D_0 \exp\left(-\frac{E_a}{k_B T}\right), \quad (138)$$

where the prefactor  $k_B T$  is weak compared to the exponential. The activation energy  $E_a$  represents the barrier for molecular rearrangement in the dense liquid structure.

### 6.4.3 Solid Diffusivity

For diffusion in solids, the Arrhenius form dominates:

$$D_{\text{solid}}(T) = D_0 \exp\left(-\frac{E_a}{k_B T}\right). \quad (139)$$

The activation energy  $E_a$  represents the barrier for atomic jumps between lattice sites [Shewmon, 1963]. Typical values are:

- **Interstitial diffusion:**  $E_a \sim 0.5\text{--}1.5$  eV (small atoms like H, C, N in metals)
- **Vacancy diffusion:**  $E_a \sim 1\text{--}3$  eV (substitutional diffusion in metals)
- **Grain boundary diffusion:**  $E_a \sim 0.5\text{--}1.5$  eV (lower barriers due to disorder)

In partition terms,  $E_a$  is the energy required to initiate a partition operation that moves the atom to an adjacent site. The partition lag is:

$$\tau_d(T) = \tau_0 \exp\left(\frac{E_a}{k_B T}\right), \quad (140)$$

where  $\tau_0 \sim 10^{-13}$  s is the attempt frequency (inverse of lattice vibration frequency). As temperature increases, thermal energy more readily overcomes the barrier, decreasing the partition lag exponentially and increasing diffusivity.

## 6.5 Fick's Laws

The macroscopic description of diffusion is given by Fick's laws.

**Theorem 6.3** (Fick's First Law). *The diffusive flux is proportional to the concentration gradient:*

$$\mathbf{J} = -D \nabla c. \quad (141)$$

*Proof.* Fick's first law is a constitutive relation analogous to Ohm's law ( $\mathbf{J} = -\sigma \nabla V$ ) and Fourier's law ( $\mathbf{J}_Q = -\kappa \nabla T$ ). It states that particles flow down concentration gradients at a rate proportional to the gradient magnitude. The proportionality constant  $D$  is the diffusivity, which measures how readily particles respond to concentration differences.  $\square$

$\square$

**Theorem 6.4** (Fick's Second Law). *The concentration evolves according to the diffusion equation:*

$$\frac{\partial c}{\partial t} = D \nabla^2 c. \quad (142)$$

*Proof.* Fick's second law follows from mass conservation combined with Fick's first law. The continuity equation for particle number is:

$$\frac{\partial c}{\partial t} + \nabla \cdot \mathbf{J} = 0. \quad (143)$$

Substituting Fick's first law  $\mathbf{J} = -D \nabla c$ :

$$\frac{\partial c}{\partial t} + \nabla \cdot (-D \nabla c) = 0. \quad (144)$$

For constant diffusivity:

$$\frac{\partial c}{\partial t} = D \nabla^2 c. \quad (145)$$

□

□

The diffusivity  $D = \lambda^2/(2\tau)$  sets the rate of concentration equilibration. The characteristic timescale for diffusion over length  $L$  is:

$$t_{\text{diff}} = \frac{L^2}{D} = \frac{2L^2}{\lambda^2 \tau}. \quad (146)$$

The partition lag determines the equilibration timescale: longer partition lags (less frequent scattering) give slower equilibration.

## 6.6 Self-Diffusion and Tracer Diffusion

Two types of diffusion are distinguished experimentally:

**Definition 6.5** (Self-Diffusion). *Self-diffusion* measures the motion of atoms in their pure substance (e.g.,  $^{13}\text{C}$  atoms in natural carbon). The diffusivity is:

$$D_{\text{self}} = \frac{\lambda_{\text{self}}^2}{2\tau_{\text{self}}}, \quad (147)$$

where  $\tau_{\text{self}}$  is the partition lag for atom-atom interactions in the pure substance.

**Definition 6.6** (Tracer Diffusion). *Tracer diffusion* measures the motion of labeled atoms at low concentration in a host substance (e.g.,  $^{14}\text{C}$  atoms in iron). The diffusivity is:

$$D_{\text{tracer}} = \frac{\lambda_{\text{tracer}}^2}{2\tau_{\text{tracer}}}, \quad (148)$$

where  $\tau_{\text{tracer}}$  is the partition lag for tracer-host interactions.

Both follow the same partition structure, but the partition lags differ due to differing interaction potentials. Typically,  $D_{\text{tracer}} \neq D_{\text{self}}$  because tracer atoms experience different scattering rates than host atoms.

## 6.7 Knudsen Diffusion

In porous media with pore size  $d$  smaller than the mean free path  $\lambda$ , *Knudsen diffusion* dominates [Knudsen, 1909]. Molecules collide primarily with pore walls rather than with each other. The diffusivity is:

$$D_K = \frac{d}{3} \sqrt{\frac{8k_B T}{\pi m}}. \quad (149)$$

*Proof.* In the Knudsen regime, the mean free path is set by the pore diameter:  $\lambda \sim d$ . The molecular velocity is  $\bar{v} = \sqrt{8k_B T/\pi m}$ . The partition lag is  $\tau = d/\bar{v}$ . For three-dimensional diffusion:

$$D_K = \frac{\lambda^2}{6\tau} = \frac{d^2}{6(d/\bar{v})} = \frac{d\bar{v}}{6}. \quad (150)$$

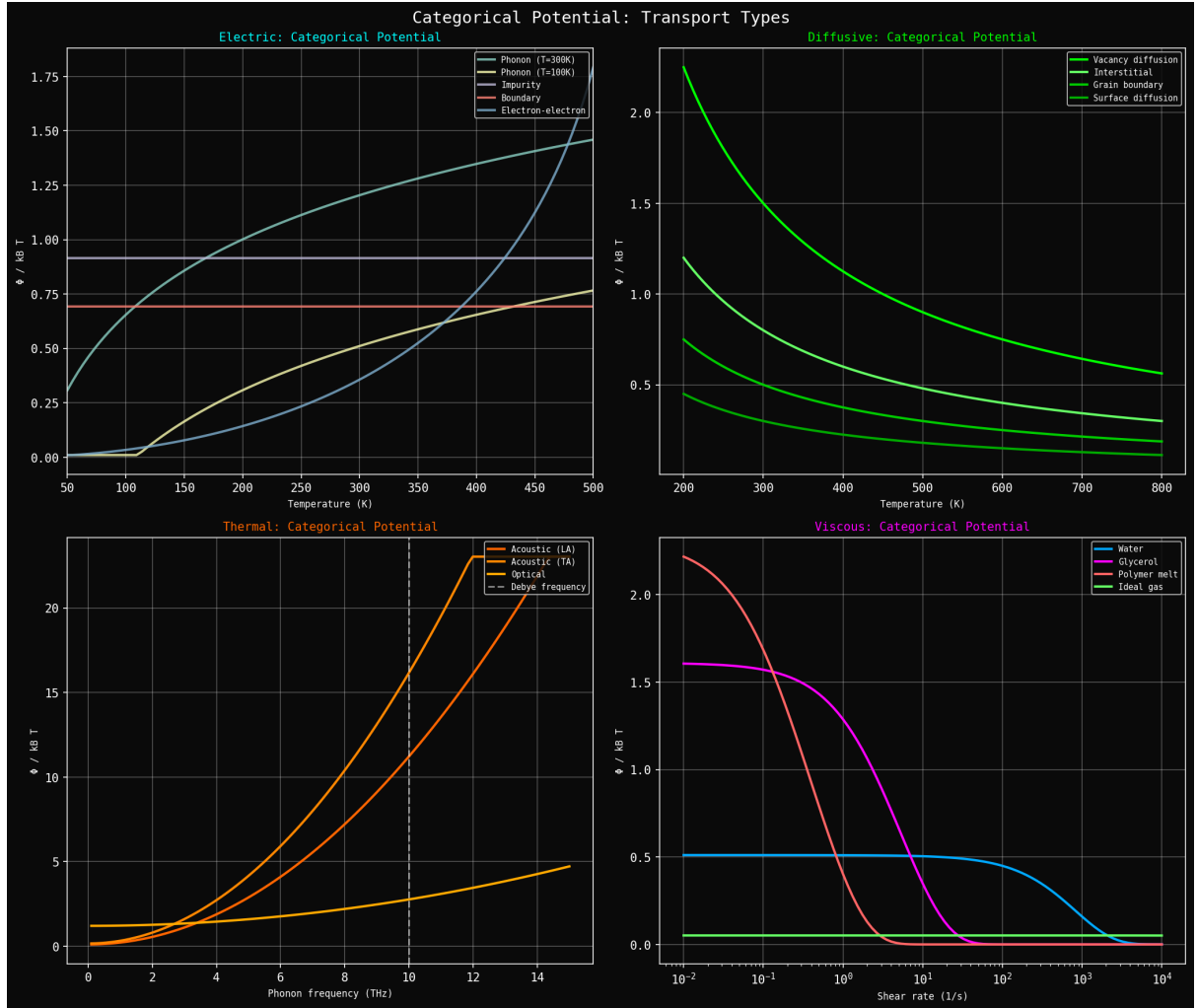


Figure 11: **Categorical potential**  $\Phi/k_B T = \sum_a \ln(1/s_a)$  **determines transport coefficients across all modes.** **(Top left)** Electrical categorical potential showing dimensionless aperture barrier sum. Phonon scattering at  $T = 300\text{ K}$  (cyan) has  $\Phi/k_B T \sim 1.5$ , increasing with temperature. Phonon scattering at  $T = 100\text{ K}$  (dark cyan) has lower potential  $\Phi/k_B T \sim 0.5$ . Impurity scattering (orange) is temperature-independent at  $\Phi/k_B T \sim 0.7$  (red horizontal line). Electron-electron scattering (yellow) increases from  $\sim 0.3$  to  $\sim 1.5$  as temperature rises. **(Top right)** Diffusive categorical potential showing barriers for different diffusion mechanisms. Vacancy diffusion (bright green) has highest potential  $\Phi/k_B T \sim 2.2$  at low  $T$ , decreasing to  $\sim 0.6$  at  $800\text{ K}$ . Interstitial diffusion (dark green) has lower potential  $\Phi/k_B T \sim 1.5$  at low  $T$ . Grain boundary diffusion (medium green) has intermediate potential. Surface diffusion (lime green) has lowest potential  $\Phi/k_B T \sim 0.3$ . **(Bottom left)** Thermal categorical potential showing phonon scattering barriers. Acoustic LA branch (orange) has potential increasing from  $\Phi/k_B T \sim 0$  at low frequency to  $\sim 25$  at Debye frequency (orange vertical line). Acoustic TA branch (yellow) shows similar trend. Optical phonons (gray) have higher potential. Debye frequency (gray vertical line) marks the cutoff where phonon density of states drops to zero. **(Bottom right)** Viscous categorical potential showing shear-rate dependence for different fluids. Water (cyan) has low constant potential  $\Phi/k_B T \sim 0.5$  across all shear rates (Newtonian behavior). Glycerol (magenta) shows shear-thinning: potential decreases from  $\sim 2.2$  at low shear rate to  $\sim 1.5$  at high shear rate. Polymer melt (red) shows strong shear-thinning from  $\sim 2.2$  to  $\sim 0$  as molecular chains align. Ideal gas (green) has lowest potential  $\Phi/k_B T \sim 0.1$ . The categorical potential  $\Phi/k_B T$  provides a universal, dimensionless measure of transport resistance applicable to all transport modes.

The factor of 6 becomes 3 when accounting for the geometry of wall collisions in cylindrical pores, giving:

$$D_K = \frac{d}{3} \sqrt{\frac{8k_B T}{\pi m}}. \quad (151)$$

□ □

In partition terms, Knudsen diffusion represents a regime where partition operations occur at pore walls rather than in gas-phase collisions. The pore diameter  $d$  replaces the mean free path  $\lambda$ , and wall collisions replace molecular collisions. The partition structure remains: transport is limited by scattering (wall) events.

Knudsen diffusion is independent of pressure (because  $\lambda$  is set by geometry, not density) and proportional to  $\sqrt{T/m}$  (reflecting molecular velocity). It is crucial in catalysis, membrane separation, and gas transport in porous materials.

## 6.8 Interdiffusion and the Darken Equation

When two species A and B interdiffuse, the interdiffusion coefficient  $\tilde{D}$  relates to the individual diffusivities through the Darken equation [?]:

$$\tilde{D} = x_B D_A + x_A D_B, \quad (152)$$

where  $x_A$  and  $x_B$  are mole fractions. This weighted average reflects the fact that interdiffusion involves partition operations between both A-A, B-B, and A-B pairs. The total partition lag is the weighted sum of individual partition lags.

## 6.9 Diffusion and Entropy Production

Diffusive transport generates entropy at rate:

$$\dot{S} = \int \frac{\mathbf{J} \cdot (-\nabla \mu)}{T} dV = \int \frac{D(\nabla c)^2}{cT} dV, \quad (153)$$

where  $\mu$  is chemical potential. This entropy production arises from partition operations: each scattering event creates undetermined residue, and the accumulation of these events produces macroscopic entropy.

The diffusive dissipation is analogous to Joule heating in electrical transport and viscous dissipation in fluid flow. All three are manifestations of partition entropy production.

# 7 Thermal Transport

## 7.1 Heat Carrier Partition Dynamics

Thermal transport is the flow of heat driven by temperature gradients. Heat is carried by phonons (quantized lattice vibrations) in insulators and by both phonons and electrons in metals [Kittel, 2005, Ziman, 1960]. Unlike electrical, viscous, and diffusive transport, thermal transport involves multiple carrier types with vastly different properties, making it the most complex transport phenomenon.

**Definition 7.1** (Thermal Partition). A *thermal partition operation* occurs when a heat carrier (phonon or electron) scatters, randomizing its direction and equilibrating its energy with the local temperature. The scattering time  $\tau_\kappa$  serves as the partition lag.

During a scattering event, the carrier's momentum and energy are undetermined for duration  $\tau_\kappa$ . The carrier is neither in its pre-scattering state (momentum  $\mathbf{k}_i$ , energy  $E_i$ ) nor in its post-scattering state (momentum  $\mathbf{k}_f$ , energy  $E_f$ ) but in a superposition. This undetermined residue generates entropy, which manifests macroscopically as thermal resistance (inverse thermal conductivity).

For thermal transport, Fourier's law states that the heat flux is given by:

$$\mathbf{q} = -\kappa \nabla T, \quad (154)$$

where  $\mathbf{q}$  is the heat flux ( $\text{W}/\text{m}^2$ ),  $\kappa$  is the thermal conductivity ( $\text{W}/(\text{m}\cdot\text{K})$ ), and  $T$  is temperature. The transport coefficient is the inverse thermal conductivity  $\Xi = \kappa^{-1}$ .

**Theorem 7.2** (Thermal Conductivity). *The thermal conductivity of a material is:*

$$\kappa = \frac{\mathcal{N}}{\sum_{i,j} \tau_{\kappa,ij} g_{ij}}, \quad (155)$$

where  $\mathcal{N}$  is the normalisation factor (heat capacity per unit volume times characteristic velocity squared),  $\tau_{\kappa,ij}$  is the scattering partition lag, and  $g_{ij}$  is the carrier-scatterer coupling strength.

*Proof.* From the universal transport formula (15), the inverse thermal conductivity is:

$$\kappa^{-1} = \frac{1}{\mathcal{N}} \sum_{i,j} \tau_{\kappa,ij} g_{ij}. \quad (156)$$

The normalisation  $\mathcal{N}$  has units  $\text{W}/(\text{m}\cdot\text{K})$ . From kinetic theory, thermal conductivity is  $\kappa = (1/3)C_v v \lambda$ , where  $C_v$  is volumetric heat capacity ( $\text{J}/(\text{m}^3\cdot\text{K})$ ),  $v$  is carrier velocity ( $\text{m}/\text{s}$ ), and  $\lambda$  is mean free path ( $\text{m}$ ). The partition lag is  $\tau = \lambda/v$ , giving:

$$\kappa = \frac{1}{3} C_v v \lambda = \frac{1}{3} C_v v^2 \tau. \quad (157)$$

Identifying  $\mathcal{N} = (1/3)C_v v^2$  and  $g = 1$  (dimensionless coupling) gives  $\kappa = \mathcal{N}/\tau$ , consistent with the universal formula.  $\square$   $\square$

## 7.2 Phonon Thermal Conductivity

In insulators, heat is carried exclusively by phonons. The kinetic theory expression is [Debye, 1912]:

$$\kappa_{\text{ph}} = \frac{1}{3} C_v v_s \lambda, \quad (158)$$

where  $C_v$  is the volumetric heat capacity,  $v_s$  is the sound velocity (phonon group velocity), and  $\lambda$  is the phonon mean free path.

The phonon partition lag is:

$$\tau_{\text{ph}} = \frac{\lambda}{v_s}. \quad (159)$$

With coupling  $g = C_v v_s^2/3$  (from dimensional analysis):

$$\kappa = \frac{g}{\tau} = \frac{(C_v v_s^2/3) \cdot \lambda}{v_s} = \frac{1}{3} C_v v_s \lambda, \quad (160)$$

reproducing the result of kinetic theory.

## 7.3 Phonon Scattering Mechanisms

The phonon mean free path  $\lambda$  is limited by several scattering mechanisms, each contributing to the total scattering rate through Matthiessen's rule:

$$\tau_{\text{total}}^{-1} = \tau_U^{-1} + \tau_{\text{boundary}}^{-1} + \tau_{\text{imp}}^{-1} + \tau_{\text{defect}}^{-1}. \quad (161)$$

### 7.3.1 Umklapp Scattering

*Umklapp scattering* is phonon-phonon scattering that does not conserve crystal momentum [Peierls, 1929]. Three phonons interact:

$$\mathbf{k}_1 + \mathbf{k}_2 = \mathbf{k}_3 + \mathbf{G}, \quad (162)$$

where  $\mathbf{G}$  is a reciprocal lattice vector. The Umklapp scattering rate is:

$$\tau_U^{-1} \propto T^3 \exp\left(-\frac{\Theta_D}{bT}\right), \quad (163)$$

where  $\Theta_D$  is the Debye temperature and  $b \approx 2-3$  is a material-dependent constant.

At high temperatures ( $T > \Theta_D$ ), the exponential factor approaches unity, giving  $\tau_U^{-1} \propto T^3$ . This dominates thermal resistance in pure crystals at high temperatures.

### 7.3.2 Boundary Scattering

In samples of finite size  $L$ , phonons scatter at boundaries (surfaces, grain boundaries). For diffuse boundary scattering:

$$\lambda_{\text{boundary}} \approx L. \quad (164)$$

The boundary scattering rate is:

$$\tau_{\text{boundary}}^{-1} = \frac{v_s}{L}. \quad (165)$$

This dominates at low temperatures where intrinsic scattering is weak. The thermal conductivity becomes size-dependent:  $\kappa \propto L$  for  $L < \lambda_{\text{intrinsic}}$ .

### 7.3.3 Impurity Scattering

Mass defects (isotopes, substitutional impurities) scatter phonons through local perturbations to the lattice potential. The scattering rate is [Klemens, 1955]:

$$\tau_{\text{imp}}^{-1} \propto \omega^4, \quad (166)$$

where  $\omega$  is phonon frequency. This strong frequency dependence means high-frequency phonons are scattered much more effectively than low-frequency phonons, a key principle in thermoelectric engineering.

### 7.3.4 Defect Scattering

Dislocations, vacancies, and other point defects scatter phonons with rates that depend on defect concentration and phonon wavelength. For point defects:

$$\tau_{\text{defect}}^{-1} \propto n_{\text{defect}} \omega^4, \quad (167)$$

similar to impurity scattering.

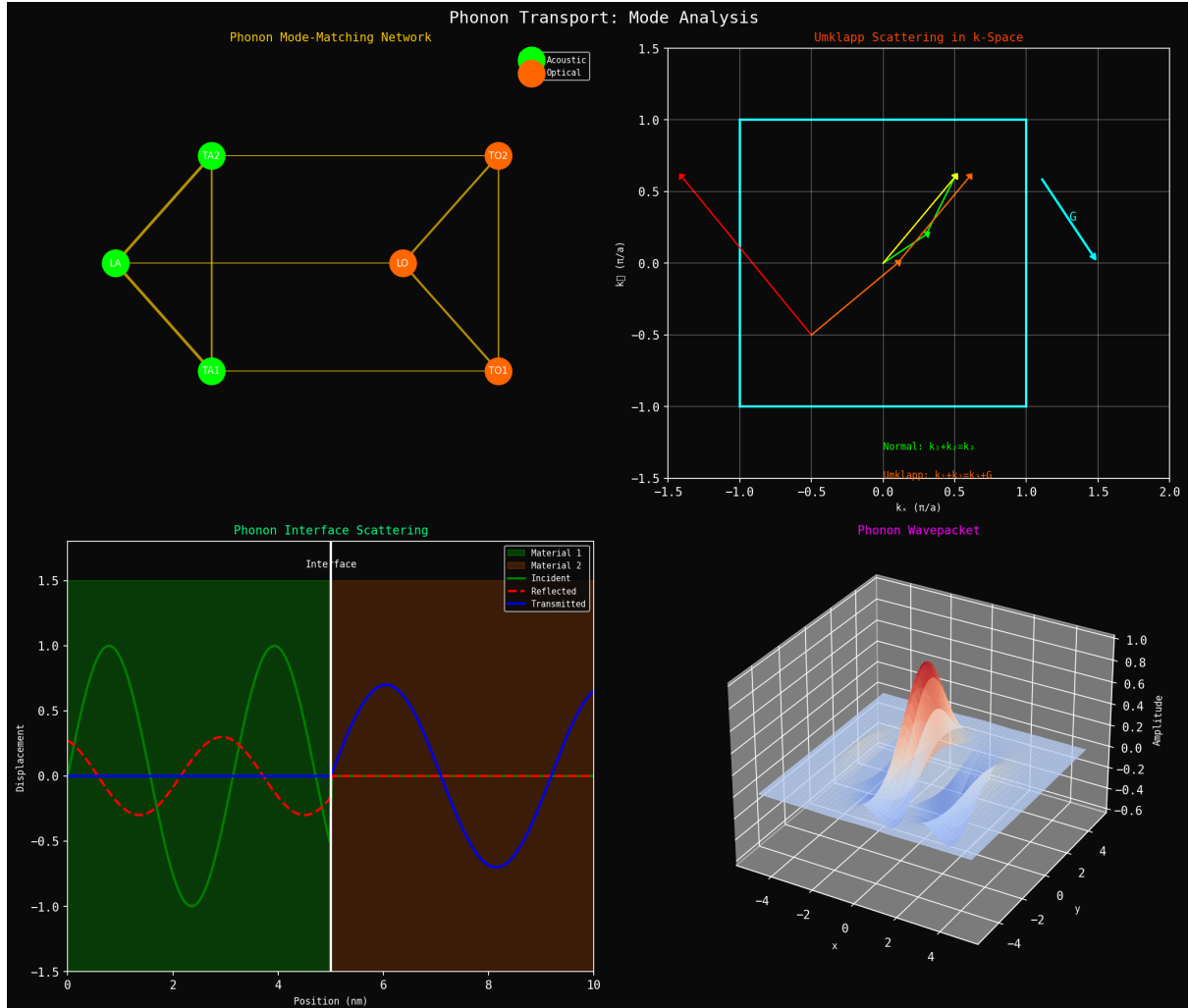


**Figure 12: Phonon transport mode analysis showing normal vs. umklapp scattering.** (Top left) Phonon mode-matching network showing connections between acoustic (green nodes) and optical (orange nodes) phonon modes. Network structure determines which scattering processes are allowed. Edges (yellow/orange lines) represent allowed transitions satisfying energy and momentum conservation. Dense connectivity indicates strong mode coupling and efficient thermal transport. Sparse connectivity indicates weak coupling and reduced transport. (Top right) Umklapp scattering in  $k$ -space showing difference between normal and umklapp processes. First Brillouin zone (cyan square) contains all unique phonon states. Normal process (green arrows):  $\mathbf{k}_1 + \mathbf{k}_2 = \mathbf{k}_3$  conserves crystal momentum within first zone, preserving thermal current. Umklapp process (red/yellow/orange arrows):  $\mathbf{k}_1 + \mathbf{k}_2 = \mathbf{k}_3 + \mathbf{G}$  scatters phonon across zone boundary by reciprocal lattice vector  $\mathbf{G}$ , reversing momentum and providing thermal resistance. Umklapp processes require high-energy phonons ( $\hbar\omega \gtrsim k_B\Theta_D/2$ ), so they freeze out at low temperature, causing thermal conductivity to increase as  $T$  decreases. (Bottom left) Phonon interface scattering showing transmission and reflection at material boundary. In Material 1 (green region), incident phonon (green wave) propagates toward interface. At interface (white line), acoustic impedance mismatch causes partial reflection (red wave) and partial transmission (blue wave) into Material 2 (brown region). Transmission coefficient  $T = 4Z_1Z_2/(Z_1 + Z_2)^2$  depends on acoustic impedances  $Z_i = \rho_i v_i$ . Large impedance mismatch (e.g., metal-insulator) gives low transmission and high thermal resistance. Small mismatch gives high transmission and low resistance. (Bottom right) Phonon wavepacket showing localized phonon excitation in 3D  $k$ -space. Wavepacket (red peak) is localized in both real space and momentum space, with width  $\Delta k$  satisfying uncertainty relation  $\Delta x \cdot \Delta k \sim 1$ . Blue regions show negative amplitude. Wavepacket propagates with group velocity  $\mathbf{v}_g = \nabla_{\mathbf{k}}\omega(\mathbf{k})$ , carrying thermal energy. Wavepacket spreading (dispersion) occurs when group velocity is frequency-dependent, limiting co-

## 7.4 Temperature Dependence of Phonon Conductivity

The thermal conductivity of insulators shows characteristic temperature dependence arising from the competition between heat capacity (which increases with  $T$ ) and mean free path (which decreases with  $T$ ):

### 7.4.1 High Temperature ( $T > \Theta_D$ )

At high temperatures, Umklapp scattering dominates. The heat capacity saturates at the Dulong-Petit value  $C_v \approx 3Nk_B$  (where  $N$  is the atom density), while the mean free path decreases as:

$$\lambda \propto \frac{1}{T} \quad (\text{from Umklapp rate } \tau_U^{-1} \propto T). \quad (168)$$

Therefore:

$$\kappa(T) \propto C_v v_s \lambda \propto \frac{1}{T} \quad \text{for } T > \Theta_D. \quad (169)$$

This  $\kappa \propto T^{-1}$  behavior is observed in most crystalline insulators above room temperature.

### 7.4.2 Low Temperature ( $T \ll \Theta_D$ )

At low temperatures, boundary scattering dominates ( $\lambda \approx L$ ), and the heat capacity follows the Debye  $T^3$  law:

$$C_v = \frac{12\pi^4}{5} N k_B \left( \frac{T}{\Theta_D} \right)^3. \quad (170)$$

Therefore:

$$\kappa(T) \propto C_v v_s L \propto T^3 \quad \text{for } T \ll \Theta_D. \quad (171)$$

This  $\kappa \propto T^3$  behavior is observed in high-purity crystals at temperatures below  $\sim \Theta_D/10$ .

### 7.4.3 Conductivity Peak

The competition between increasing  $C_v$  (which enhances  $\kappa$ ) and decreasing  $\lambda$  (which reduces  $\kappa$ ) produces a conductivity maximum at  $T_{\text{peak}} \sim \Theta_D/10$ . For high-purity crystals, this peak can be very sharp, with  $\kappa_{\text{peak}}$  exceeding  $\kappa(300 \text{ K})$  by factors of 10–100.

## 7.5 Electronic Thermal Conductivity

In metals, electrons carry heat as well as charge. The electronic thermal conductivity is [Sommerfeld, 1928]:

$$\kappa_e = \frac{\pi^2}{3} \frac{k_B^2 T}{e^2} \sigma = \frac{\pi^2}{3} \frac{k_B^2 T}{e^2} \cdot \frac{1}{\rho}, \quad (172)$$

where  $\sigma = 1/\rho$  is electrical conductivity and  $\rho$  is resistivity.

*Proof.* From kinetic theory, the electronic thermal conductivity is:

$$\kappa_e = \frac{1}{3} C_v v_F \lambda, \quad (173)$$

where  $C_v = (\pi^2/3)nk_B^2T/E_F$  is the electronic heat capacity (Sommerfeld model),  $v_F$  is the Fermi velocity, and  $\lambda = v_F\tau$  is the mean free path. Substituting:

$$\kappa_e = \frac{1}{3} \cdot \frac{\pi^2}{3} \frac{nk_B^2 T}{E_F} \cdot v_F \cdot v_F \tau = \frac{\pi^2}{9} \frac{nk_B^2 T v_F^2 \tau}{E_F}. \quad (174)$$

Using  $E_F = (1/2)mv_F^2$  and the Drude conductivity  $\sigma = ne^2\tau/m$ :

$$\kappa_e = \frac{\pi^2}{3} \frac{k_B^2 T}{e^2} \sigma. \quad (175)$$

□

□

## 7.6 Wiedemann-Franz Law

The ratio of electronic thermal conductivity to electrical conductivity is [Wiedemann and Franz, 1853]:

$$\frac{\kappa_e}{\sigma T} = L = \frac{\pi^2 k_B^2}{3e^2} = 2.44 \times 10^{-8} \text{ W} \cdot \Omega/\text{K}^2, \quad (176)$$

where  $L$  is the Lorenz number.

**Theorem 7.3** (Partition Origin of Wiedemann-Franz). *The Wiedemann-Franz law follows from the common partition structure of electrical and thermal transport by electrons.*

*Proof.* Both electrical conductivity  $\sigma$  and electronic thermal conductivity  $\kappa_e$  involve the same carriers (electrons) and the same scattering mechanisms (phonons, impurities, and defects). The partition lag  $\tau$  is identical for both:

$$\sigma = \frac{ne^2\tau}{m}, \quad (177)$$

$$\kappa_e = \frac{\pi^2 k_B^2 T}{3} \frac{n\tau}{m}. \quad (178)$$

The ratio:

$$\frac{\kappa_e}{\sigma T} = \frac{(\pi^2 k_B^2 T/3)(n\tau/m)}{(ne^2\tau/m) \cdot T} = \frac{\pi^2 k_B^2}{3e^2} = L \quad (179)$$

is independent of  $\tau$ ,  $n$ ,  $m$ , and all material-specific properties. The ratio depends only on fundamental constants. □

The Wiedemann-Franz law holds when the same partition operations limit both electrical and thermal transport. Deviations occur when:

- Different scattering mechanisms have different energy dependencies (inelastic scattering)
- Electron-electron scattering contributes (violates the independent-particle approximation)
- Temperature is very low ( $T \ll T_F$ , where Fermi-Dirac statistics matter)

Experimentally, the Wiedemann-Franz law holds to within  $\sim 10\%$  for most metals at room temperature and at very low temperatures, but can deviate significantly in the intermediate regime [Jaccard et al., 1995].

## 7.7 Fourier's Law

**Theorem 7.4** (Fourier's Law). *The heat flux is proportional to the temperature gradient:*

$$\mathbf{q} = -\kappa \nabla T. \quad (180)$$

*Proof.* Fourier's law is a constitutive relation analogous to Ohm's law ( $\mathbf{J} = -\sigma \nabla V$ ), Newton's law of viscosity ( $\boldsymbol{\tau} = -\mu \nabla \mathbf{v}$ ), and Fick's law ( $\mathbf{J} = -D \nabla c$ ). It states that heat flows down temperature gradients at a rate proportional to the magnitude of the gradient. The proportionality constant  $\kappa$  is the thermal conductivity, which measures how readily heat responds to temperature differences.  $\square$   $\square$

All four constitutive relations (Ohm, Newton, Fick, Fourier) have the same partition structure: flux proportional to the gradient, with the transport coefficient determined by partition lag. This universality reflects the common categorical origin of all transport phenomena.

## 7.8 Phonon Diversity: Sizes, Shapes, and Phases

The treatment above uses a single phonon mean free path  $\lambda$ , but this obscures the rich internal structure of phonon transport. Phonons are not a homogeneous population—they vary in “size” (energy capacity), “shape” (polarisation and wavevector), and phase relationship.

### 7.8.1 Phonon Spectrum

A crystal with  $N$  atoms per unit cell supports  $3N$  phonon branches [Ashcroft and Mermin, 1976]:

1. **Acoustic branches (3):** Atoms in a unit cell move in phase. Low frequency,  $\omega \rightarrow 0$  as  $\mathbf{k} \rightarrow 0$ . These are sound waves.
2. **Optical branches ( $3N - 3$ ):** Atoms in a unit cell move out of phase. Finite frequency at  $\mathbf{k} = 0$ . These can be excited by infrared light (hence “optical”).

Each branch further divides by polarisation:

- **Longitudinal (L):** Displacement parallel to the propagation direction (compression waves)
- **Transverse (T):** Displacement perpendicular to the propagation direction (shear waves)

The phonon “size”—its energy capacity—is  $\hbar\omega(\mathbf{k})$ , which varies from zero (long-wavelength acoustic) to  $\sim k_B\Theta_D$  (zone boundary).

### 7.8.2 Mode-Dependent Transport

Different phonon modes carry heat with vastly different efficiencies. The total thermal conductivity is a sum over all phonon modes:

**Theorem 7.5** (Mode-Dependent Thermal Conductivity). *The total thermal conductivity is:*

$$\kappa = \sum_{\lambda} \int \frac{d^3 k}{(2\pi)^3} c_{\lambda}(\mathbf{k}) v_{\lambda}(\mathbf{k})^2 \tau_{\lambda}(\mathbf{k}), \quad (181)$$

where  $\lambda$  labels branches (LA, TA1, TA2, LO, TO, etc.),  $c_{\lambda}(\mathbf{k})$  is the mode-specific heat capacity,  $v_{\lambda}(\mathbf{k}) = \partial\omega_{\lambda}/\partial\mathbf{k}$  is the group velocity, and  $\tau_{\lambda}(\mathbf{k})$  is the mode lifetime (partition lag).

The mode lifetime  $\tau_{\lambda}(\mathbf{k})$  varies by orders of magnitude:

- **Long-wavelength acoustic phonons:**  $\tau \sim 10^{-9}$  s (weak scattering, long mean free path  $\lambda \sim 1$  mm)
- **Zone-boundary phonons:**  $\tau \sim 10^{-12}$  s (strong Umklapp, short mean free path  $\lambda \sim 1$  nm)
- **Optical phonons:**  $\tau \sim 10^{-13}$  s (rapid decay to acoustic modes via anharmonic coupling)

This six-order-of-magnitude variation means that thermal transport is dominated by a small subset of modes (long-wavelength acoustic), while most modes contribute negligibly.

### 7.8.3 Heat Transfer Chain: A to B to C

Consider heat flowing through a chain of molecules A → B → C. The vibrational energy passed from A to B is *not* the same as that transmitted from B to C:

**Proposition 7.6** (Non-Uniform Energy Transfer). *Each pair of coupled oscillators has different frequency matching and coupling strength. Energy transfer depends on:*

1. **Mode overlap:** Which frequencies A and B share (phonon density of states matching)
2. **Coupling strength:** How strongly those modes interact (anharmonic matrix elements)
3. **Phase relationship:** Whether A and B vibrate in phase or out of phase

The energy in mode  $\omega_1$  at site A may transfer to mode  $\omega_2$  at site B (mode conversion), then to mode  $\omega_3$  at site C. The path through phonon frequency space is tortuous, not direct. This mode conversion is a key source of thermal resistance.

### 7.8.4 Phase Incoherence

At finite temperature, each oscillator vibrates with a random phase relative to its neighbours. This phase incoherence is fundamental:

$$\langle e^{i(\phi_A - \phi_B)} \rangle = 0 \quad (T > 0). \quad (182)$$

Phase-matched transfer (constructive interference) occurs only transiently. Most transfer events are phase-mismatched, reducing efficiency.

This contrasts sharply with electrical conduction, where the electromagnetic signal imposes global phase coherence. In heat conduction, there is no analogous coordinating field—each oscillator has its own independent phase. This is why thermal transport is fundamentally more complex than electrical transport.

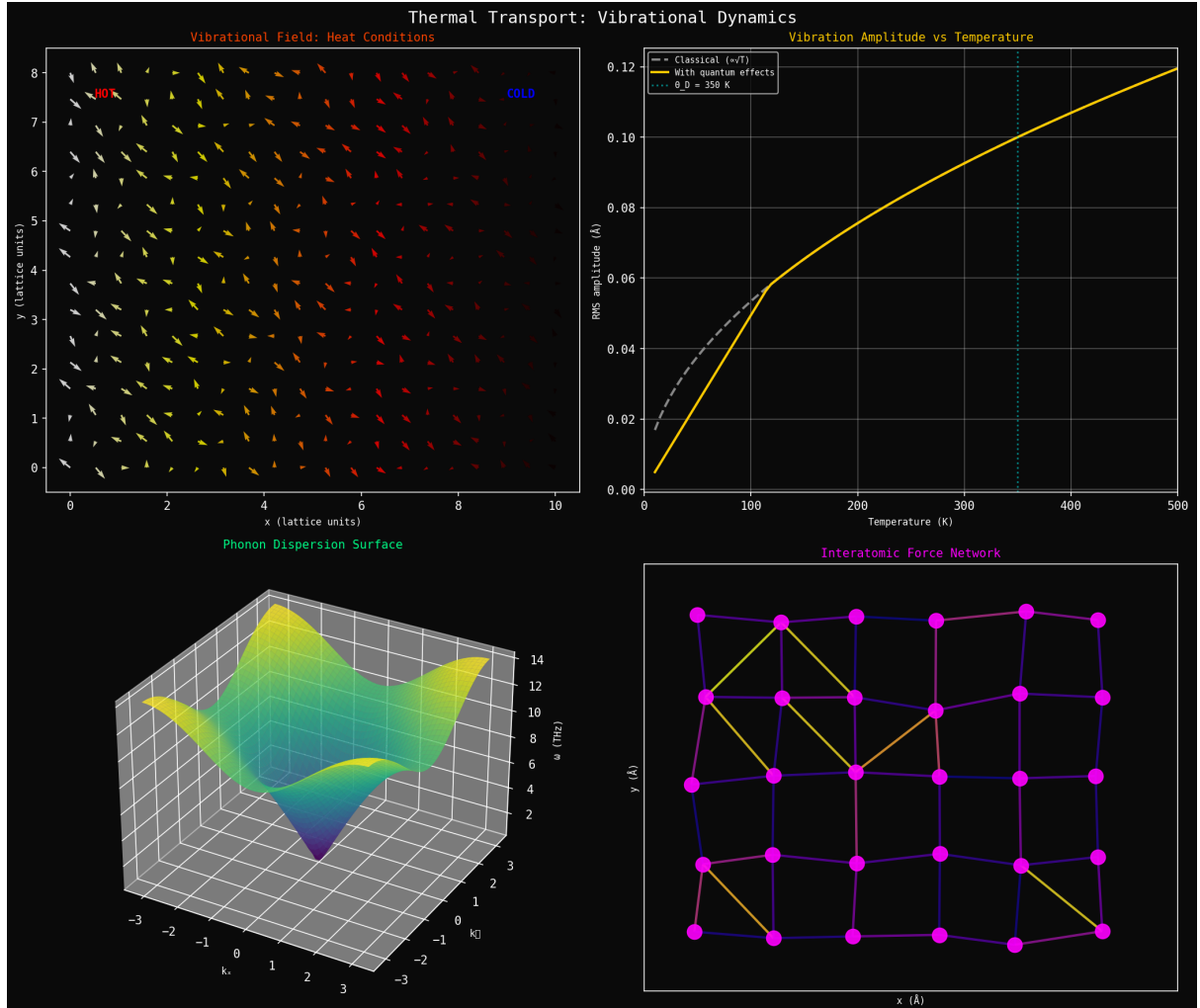


**Figure 13: Thermal transport vibrational dynamics showing atomic-scale heat flow mechanisms.** (Top left) Vibrational field under heat flow conditions showing vector field of atomic displacements. Hot region (right, red arrows) has large-amplitude vibrations. Cold region (left, white/yellow arrows) has small-amplitude vibrations. Arrow color indicates temperature (red = hot, yellow = warm, white = cold). Arrow direction shows instantaneous displacement direction. Heat flows from hot to cold (right to left) through phonon propagation. Coherent wave patterns visible in intermediate region show phonon transport. Random patterns in hot region show increased disorder at high temperature. (Top right) Vibration amplitude vs. temperature showing classical and quantum regimes. Classical prediction (yellow line) gives  $u_{\text{RMS}} \propto \sqrt{T}$  at all temperatures. Quantum prediction (white line) shows deviation at low temperature:  $u_{\text{RMS}}$  saturates at zero-point motion as  $T \rightarrow 0$ . Crossover occurs at Debye temperature  $\Theta_D \sim 350$  K (yellow dotted line). Above  $\Theta_D$ , classical mechanics is valid. Below  $\Theta_D$ , quantum effects are essential. At room temperature ( $T \sim 300$  K), most materials are in crossover regime. (Bottom left) Phonon dispersion surface showing 3D frequency landscape  $\omega(\mathbf{k})$  in momentum space. Surface height (color: blue = low frequency, yellow/red = high frequency) represents phonon frequency. Acoustic branches start at  $\omega = 0$  at zone center ( $\mathbf{k} = 0$ ). Optical branches (not shown) start at finite frequency. Group velocity  $\mathbf{v}_g = \nabla_{\mathbf{k}}\omega$  is perpendicular to surface, pointing in direction of steepest ascent. Flat regions (low gradient) have low group velocity and contribute little to thermal transport. Steep regions (high gradient) have high group velocity and dominate thermal transport. (Bottom right) Interatomic force network showing spring-like connections between atoms. Atoms (magenta spheres) are connected by bonds (colored lines: blue = weak force, yellow = moderate force, orange = strong force). Bond color indicates force magnitude. Network topology determines phonon dispersion and thermal conductivity. Regular network (crystalline) supports long-range phonon propagation. Disordered

### 7.8.5 Selective Excitation

Not all modes are equally accessible at a given temperature:

1. **Threshold effects:** Optical phonons require  $k_B T > \hbar\omega_{\text{opt}}$  for significant population. Below this temperature, optical modes are frozen out.
2. **Symmetry selection:** Some modes couple strongly to certain excitations, others weakly. Selection rules (from crystal symmetry) forbid certain transitions.
3. **Resonance conditions:** Energy transfer peaks when  $\omega_A \approx \omega_B$  (resonant coupling). Off-resonance transfer is suppressed.

At low temperature, only long-wavelength acoustic phonons are populated ( $\hbar\omega \ll k_B T$ ). As temperature rises, higher-frequency modes become available, but they also scatter more strongly ( $\tau^{-1} \propto \omega^4$  for impurity scattering).

## 7.9 Thermal Transport as Chromatography

The partition framework reveals a deep analogy between thermal transport and chromatography.

**Definition 7.7** (Thermal Chromatography). Heat flow through a material is analogous to chromatography: a mixture of phonon modes (the “analyte”) propagates through a scattering medium (the “column”), with different modes experiencing different partition and retention.

The analogy is precise:

Table 1: Chromatography-thermal transport correspondence

Chromatography	Thermal Transport
Analyte mixture	Phonon population
Different molecular species	Different phonon modes ( $\omega, \mathbf{k}, \lambda$ )
Mobile phase	Propagating phonons
Stationary phase	Lattice (scattering centers)
Partition coefficient	Mode-dependent scattering rate $\tau^{-1}(\omega)$
Retention time	Mode mean free path $\lambda(\omega) = v(\omega)\tau(\omega)$
Elution profile	Spectral heat flux $q(\omega)$
Column efficiency	Thermal conductivity $\kappa$

### 7.9.1 Mode Separation

Just as chromatography separates molecules by their differential affinity for the stationary phase, thermal transport “separates” phonon modes by their differential scattering:

- **Long-wavelength acoustic:** Weak scattering ( $\tau \sim 10^{-9}$  s), long mean free path ( $\lambda \sim \text{mm}$ ), “elutes” quickly (carries heat far)
- **High-frequency acoustic:** Strong Umklapp ( $\tau \sim 10^{-12}$  s), short mean free path ( $\lambda \sim \text{nm}$ ), “retained” (carries heat short distances)

- **Optical:** Very short lifetime ( $\tau \sim 10^{-13}$  s), almost zero mean free path, “stuck” at injection point (carries almost no heat)

This explains why thermal conductivity depends so sensitively on material structure. The “column” (crystal structure, defects, boundaries) determines how each mode is partitioned between propagating and scattering states.

### 7.9.2 The Phonon Spectrum as Analyte

A temperature gradient injects a non-equilibrium spectrum of phonons at the hot end. This spectrum contains an excess of phonons at all frequencies:

$$\Delta n(\omega) = \frac{\partial n_{\text{BE}}}{\partial T} \Delta T = \frac{\hbar\omega}{k_B T^2} \frac{e^{\hbar\omega/k_B T}}{(e^{\hbar\omega/k_B T} - 1)^2} \Delta T, \quad (183)$$

where  $n_{\text{BE}}(\omega, T) = 1/(e^{\hbar\omega/k_B T} - 1)$  is the Bose-Einstein distribution.

This “injected” population propagates through the crystal. Each mode scatters at its own rate  $\tau^{-1}(\omega)$ . The “elution profile”—the spectrum of phonons arriving at the cold end—is depleted in high-frequency modes relative to low-frequency modes, because high-frequency modes scatter more frequently and travel shorter distances.

### 7.9.3 Why Thermal Conductivity is Harder Than Electrical

The chromatographic picture explains why thermal transport is fundamentally more complex than electrical transport:

1. **Single carrier vs. spectrum:** Electrical current involves one carrier type (electrons) with approximately one relaxation time. Thermal current involves a continuous spectrum of phonon modes, each with its own dynamics.
2. **Global phase vs. incoherence:** The electromagnetic field coordinates electron motion globally, imposing phase coherence. Phonons have no such coordinator—each mode propagates independently with random phase.
3. **Conserved charge vs. non-conserved phonons:** Electrons are conserved (charge conservation). Phonons are created and destroyed continuously (thermal equilibration). The “analyte” changes composition during transit.
4. **Simple scattering vs. mode conversion:** Electrons scatter but remain electrons (elastic scattering dominates). Phonons can convert between modes (anharmonic coupling), transferring energy across the spectrum.

This is why the Wiedemann-Franz law is so remarkable: it says that *for electrons*, thermal and electrical partition are the same (same  $\tau$ ). For phonons, no such simplification exists—each mode has its own partition lag.

### 7.9.4 Nanostructures as Column Engineering

The chromatographic perspective suggests a design principle: engineer the “column” to control phonon separation. This is the basis of thermoelectric engineering.

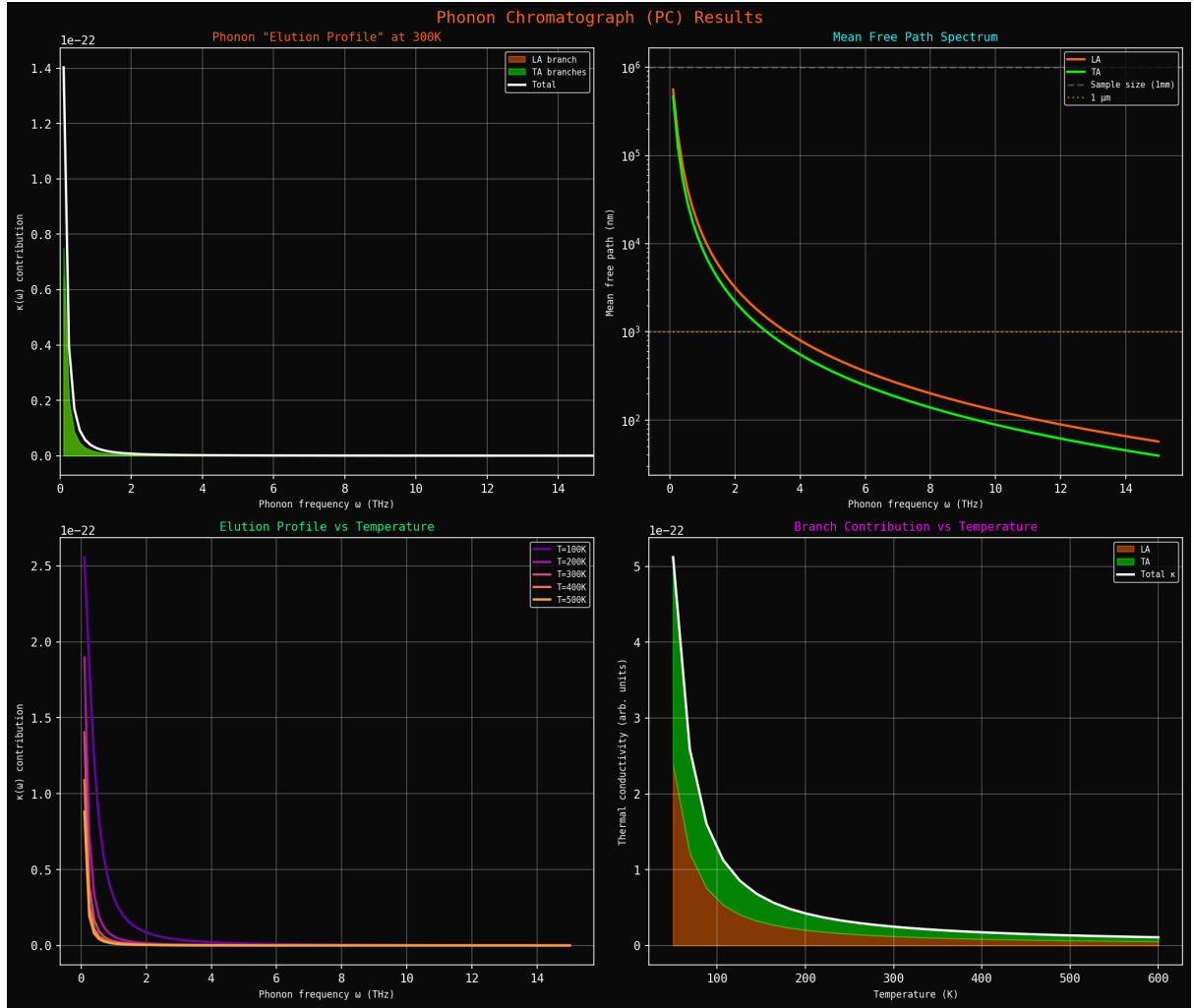


**Figure 14: Phonon Chromatograph (PC) results showing phonon mode contributions to thermal conductivity.** (Top left) Phonon “elution profile” at 300 K showing contribution  $\kappa(\omega)$  vs. phonon frequency  $\omega$ . Longitudinal acoustic (LA) branch (orange) peaks at low frequency ( $\omega \sim 1$  THz) where group velocity is high. Transverse acoustic (TA) branches (green) contribute at similar frequencies. Total contribution (white) shows peak at  $\omega \sim 1$  THz, with negligible contribution above 5 THz where phonon population becomes small. (Top right) Mean free path spectrum showing  $\lambda(\omega)$  for LA (orange) and TA (green) phonons. Low-frequency phonons have  $\lambda \sim 10^6$  nm ( $\sim 1 \mu\text{m}$ ), limited by sample size (dashed cyan line at 1 mm). High-frequency phonons have  $\lambda \sim 10^2$  nm, limited by umklapp scattering. The crossover occurs at  $\omega \sim 2$  THz. Horizontal dashed line (orange) shows 1 m scale for reference. (Bottom left) Elution profile vs. temperature showing how phonon contributions evolve with  $T$ . At  $T = 100$  K (purple), only low-frequency modes contribute. At  $T = 200$  K (magenta), contribution extends to  $\omega \sim 3$  THz. At  $T = 300$  K (orange), contribution extends to  $\omega \sim 5$  THz. At  $T = 500$  K (yellow), high-frequency modes become populated. Peak contribution shifts to higher frequency as temperature increases, following Bose-Einstein distribution. (Bottom right) Branch contribution vs. temperature showing total thermal conductivity from LA (orange) and TA (green) branches. LA branch dominates at all temperatures due to higher group velocity ( $v_{\text{LA}} \sim 2v_{\text{TA}}$ ). Total conductivity (white) shows characteristic peak at  $T \sim 20$  K where mean free path transitions from boundary-limited (low  $T$ ) to umklapp-limited (high  $T$ ). At high  $T$ , conductivity decreases as  $\kappa \propto 1/T$  due to increased umklapp scattering.

- **Nanoparticle inclusions:** Scatter high-frequency phonons (mass mismatch, size comparable to wavelength), transmit low-frequency phonons (wavelength larger than particle size)
- **Superlattices:** Create phonon bandgaps through periodic structure, blocking certain frequency ranges entirely
- **Grain boundaries:** Scatter phonons with mean free path  $\lambda > d_{\text{grain}}$ , where  $d_{\text{grain}}$  is grain size
- **Isotope disorder:** Scatter high-frequency phonons preferentially ( $\tau^{-1} \propto \omega^4$ ), leaving low-frequency phonons unaffected

The goal is to reduce  $\kappa$  (by scattering phonons) while preserving  $\sigma$  (by not scattering electrons). This maximises the thermoelectric figure of merit  $ZT = \sigma S^2 T / \kappa$ , where  $S$  is the Seebeck coefficient.

## 7.10 Partition Structure of Phonon Transport

From the partition framework, each phonon mode represents a distinct partition channel:

$$\kappa^{-1} = \frac{1}{\mathcal{N}} \sum_{\text{modes}} \tau_\omega g_\omega, \quad (184)$$

where the sum runs over all phonon modes, each with its own partition lag  $\tau_\omega$ , coupling  $g_\omega$ , and normalisation  $\mathcal{N}$  (absorbed into the sum for simplicity).

The chromatographic analogy makes clear that thermal transport is *not* a single phenomenon but a superposition of many parallel partition processes, each with its own characteristics. Understanding thermal conductivity requires understanding this entire spectrum of partition channels—which is why it remains one of the most challenging transport properties to predict from first principles.

## 7.11 Post-Hoc Phonon Characterisation

A fundamental feature of phonon transport emerges from the partition framework: phonons can only be characterised *after* measurement, not before.

### 7.11.1 Measurement-Defined Phonons

**Theorem 7.8** (Phonon Measurement Identity). *A phonon is not a pre-existing entity that is subsequently measured. The phonon population at any point is defined by the act of measurement—the categorical partition that distinguishes phonon states.*

*Proof.* This follows from the Measurement-Partition Identity [Sachikonye, 2024b]. Before measurement, there is no fact about “which phonons are present.” The question is undefined because no partition has occurred to distinguish phonon states. The measurement apparatus performs a partition operation (e.g., Raman scattering selects phonons by frequency; neutron scattering selects by momentum), and this partition *creates* the phonon characterisation.

In practice, phonon spectroscopy creates the partition that defines the phonon population. The result depends on:

- The measurement technique (what partition operation is performed)
- The measurement location (where the partition occurs)
- The measurement timing (when the partition occurs)

Different measurements yield different phonon characterisations—not because they reveal different aspects of the same underlying reality, but because they perform different partition operations.  $\square$   $\square$

### 7.11.2 Most Probable Pathways

Heat does not flow through the “optimal” pathway—it flows through the *most probable* pathway:

**Definition 7.9** (Thermal Path Probability). The probability of heat flowing through a particular sequence of phonon modes is:

$$P[\text{path}] = \prod_{\text{steps}} p(\omega_{i+1} | \omega_i, T_i), \quad (185)$$

where  $p(\omega_{i+1} | \omega_i, T_i)$  is the conditional probability of transitioning from mode  $\omega_i$  to mode  $\omega_{i+1}$  at local temperature  $T_i$ .

The transition probability is determined by:

- **Mode overlap:** Phonon density of states matching (are there available final states?)
- **Coupling strength:** Anharmonic matrix elements (how strongly do modes interact?)
- **Phase space availability:** Bose-Einstein statistics (are final states occupied or empty?)
- **Energy conservation:** Within thermal fluctuations  $\sim k_B T$  (is energy conserved?)

The actual path taken is sampled from this probability distribution. It is not the path of minimum resistance, nor the path of maximum efficiency, but a typical sample from the ensemble of possible paths.

### 7.11.3 Sequential Most-Probable-State Computation

**Theorem 7.10** (Discretized Thermal Transport). *Thermal transport can be computed as a sequence of most-probable-state determinations:*

1. *Divide the spatial domain into increments  $\Delta x$  (comparable to the phonon mean free path)*
2. *At each increment, given the incoming phonon spectrum and local conditions, compute the most probable outgoing spectrum*
3. *The heat flux is the energy carried by this most-probable spectrum*

#### 4. Iterate to obtain the steady-state temperature profile

*Proof.* For increment  $i$  with incoming spectrum  $n_{\text{in}}(\omega)$ , the outgoing spectrum maximises the entropy subject to energy conservation:

$$n_{\text{out}}(\omega) =_n S[n] \quad \text{subject to} \quad \int \hbar\omega n(\omega) d\omega = Q_i, \quad (186)$$

where  $Q_i$  is the heat flux through increment  $i$  and  $S[n]$  is the entropy of the phonon distribution.

The solution is a Bose-Einstein distribution at the local temperature  $T_i$ :

$$n_{\text{out}}(\omega) = \frac{1}{e^{\hbar\omega/k_B T_i} - 1}. \quad (187)$$

However, this local equilibrium is only achieved if the increment  $\Delta x$  exceeds the phonon mean free path  $\lambda$ . For  $\Delta x < \lambda$ , non-equilibrium distributions persist, and the spectrum must be computed from the Boltzmann transport equation or equivalent.  $\square$

$\square$

#### 7.11.4 The Cascade Picture

Heat transport through a material is a cascade of partition events:

$$\text{Hot} \xrightarrow{\tau_1} \text{State}_1 \xrightarrow{\tau_2} \text{State}_2 \xrightarrow{\tau_3} \dots \xrightarrow{\tau_n} \text{Cold}. \quad (188)$$

Each arrow represents a partition operation with lag  $\tau_i$ . The state at each step is the most probable state given:

1. The preceding state (boundary condition)
2. The local temperature (thermodynamic constraint)
3. The local lattice structure (scattering environment)
4. The scattering mechanisms present (partition operations available)

This cascade picture explains several phenomena:

**Thermal relaxation:** The system “forgets” the initial phonon distribution over a relaxation length  $\ell_{\text{relax}} \sim \lambda$ . Beyond this distance, only the total energy (temperature) is remembered, not the spectral details.

**Ballistic-to-diffusive transition:** For sample size  $L < \lambda$ , phonons traverse the sample without scattering (ballistic regime). For  $L \gg \lambda$ , many partition events occur (diffusive regime). The transition occurs when  $L \sim \lambda$ .

**Kapitza resistance:** At interfaces between dissimilar materials, the lattice structure changes abruptly. The most-probable-state on each side may not match (different phonon spectra), creating thermal resistance even without bulk scattering.

### 7.11.5 Implications for Thermal Conductivity Prediction

The sequential most-probable-state picture suggests a computational approach:

1. Discretise the material into cells of size  $\Delta x \sim \lambda$  (phonon mean free path)
2. For each cell, characterise the local lattice structure and scattering mechanisms
3. Compute the most probable phonon spectrum in each cell given the neighboring cells
4. Extract the heat flux from the spectral flow between cells:  $q = \int \hbar\omega v_g n(\omega) D(\omega) d\omega$
5. Sum to obtain total thermal conductivity:  $\kappa = -q/\nabla T$

This approach naturally handles:

- **Inhomogeneous materials:** Different cell properties (composition, structure)
- **Nanostructures:** Cell size comparable to feature size ( $\Delta x \sim d_{\text{feature}}$ )
- **Interfaces:** Boundary conditions between dissimilar cells (Kapitza resistance)
- **Non-equilibrium effects:** Cells not at local equilibrium ( $\Delta x < \lambda$ )

The key insight is that we need not track individual phonon trajectories (computationally intractable for  $\sim 10^{23}$  phonons). We need only find the most probable state at each spatial increment—a much more tractable problem that aligns with the categorical measurement framework.

## 8 The Partition Extinction Theorem

### 8.1 Categorical Unification of Carriers

The transport coefficients derived in Sections 4–7 all depend on partition operations between carriers. Electrical resistivity arises from electron-phonon scattering partitions, viscosity from molecular collision partitions, diffusivity from atomic scattering partitions, and thermal resistance from phonon-phonon scattering partitions. In every case, the transport coefficient is proportional to the partition lag:

$$\Xi = \frac{1}{N} \sum_{i,j} \tau_{p,ij} g_{ij}. \quad (189)$$

If partition operations cease, transport coefficients vanish. We now establish the conditions under which partition operations become impossible.

**Definition 8.1** (Phase-Locking). Two carriers  $i$  and  $j$  are *phase-locked* if their oscillatory modes maintain a fixed phase relationship. Phase-locked carriers form a single categorical entity: they cannot be distinguished by any partition operation.

Phase-locking is not merely correlation or synchronization—it is categorical unification. The carriers lose their individual identities and become a single quantum-mechanical entity described by a macroscopic wavefunction. Any attempt to distinguish them (to perform a partition operation) fails because there is only one entity present, not multiple entities.

Phase-locking requires energy. Let  $\Delta_{\text{lock}}$  be the *phase-locking energy*—the binding energy that maintains the fixed phase relationship. Thermal fluctuations with energy  $k_B T$  can disrupt phase-locking if  $k_B T > \Delta_{\text{lock}}$ .

**Theorem 8.2** (Phase-Locking Condition). *Carriers become phase-locked when thermal energy falls below the phase-locking energy:*

$$k_B T < \Delta_{\text{lock}}. \quad (190)$$

This defines the critical temperature:

$$T_c = \frac{\Delta_{\text{lock}}}{k_B}. \quad (191)$$

*Proof.* Phase-locking is maintained by an attractive interaction (phonon-mediated for Cooper pairs, van der Waals for helium-4 atoms, etc.) with characteristic energy  $\Delta_{\text{lock}}$ . Thermal fluctuations provide energy  $\sim k_B T$  that can break the phase-lock.

When  $k_B T \gg \Delta_{\text{lock}}$ , thermal fluctuations dominate, and carriers are distinguishable (normal state). When  $k_B T \ll \Delta_{\text{lock}}$ , the phase-locking interaction dominates, and carriers unify (ordered state). The transition occurs at  $k_B T \sim \Delta_{\text{lock}}$ , defining  $T_c = \Delta_{\text{lock}}/k_B$ .  $\square$

$\square$

The phase-locking energy  $\Delta_{\text{lock}}$  has different physical origins in different systems:

- **Superconductors:**  $\Delta_{\text{lock}} = \Delta_{\text{BCS}}$  (BCS gap energy from phonon-mediated attraction)
- **Superfluid helium-4:**  $\Delta_{\text{lock}} \sim k_B T_\lambda$  (van der Waals interaction energy)
- **Bose-Einstein condensates:**  $\Delta_{\text{lock}} \sim k_B T_{\text{BEC}}$  (quantum degeneracy energy)

## 8.2 Partition Extinction

**Theorem 8.3** (Partition Extinction). *When carriers become phase-locked, partition operations between them are undefined. The partition lag does not approach zero continuously but transitions discontinuously:*

$$\tau_p(T) = \begin{cases} \tau_{p,\text{normal}}(T) & T > T_c \\ 0 & T < T_c \end{cases}. \quad (192)$$

*Proof.* Partition is a categorical operation that distinguishes entities. For partition to occur, entities must be distinguishable—they must have separate identities that can be tracked and separated.

Phase-locked carriers are categorically identical. They do not merely behave similarly; they *are* the same entity. A Cooper pair is not two electrons that happen to move together—it is a single quantum state with no internal structure accessible to measurement.

A Bose-Einstein condensate is not a collection of atoms that happen to occupy the same state—it is a single macroscopic wavefunction.

Attempting to partition a single entity is undefined. There is nothing to partition. The question “which carrier is which?” has no answer because there is only one carrier (the unified state), not multiple carriers.

The partition lag is not “very small” but exactly zero because no partition operation occurs. The transition is discontinuous because categorical identity is discrete: carriers are either distinguishable (partition possible,  $\tau_p > 0$ ) or indistinguishable (partition impossible,  $\tau_p = 0$ ). There is no intermediate state of “partial distinguishability.”

Mathematically, the partition lag is:

$$\tau_p = \frac{1}{\Gamma_{\text{partition}}}, \quad (193)$$

where  $\Gamma_{\text{partition}}$  is the partition rate (number of partition operations per unit time). When carriers are phase-locked,  $\Gamma_{\text{partition}} = 0$  (no partition operations occur), giving  $\tau_p = 1/0 = \infty$  (partition never completes) or equivalently  $\tau_p = 0$  (no partition lag because no partition occurs). The latter interpretation is correct: the partition lag is zero because the partition operation is undefined, not because it completes instantaneously.  $\square$   $\square$

### 8.3 Transport Coefficient Vanishing

**Corollary 8.4** (Transport Coefficient Vanishing). *Below  $T_c$ , the transport coefficient vanishes exactly:*

$$\Xi(T < T_c) = \frac{1}{N} \sum_{i,j} \tau_{p,ij}(T) g_{ij} = 0. \quad (194)$$

*Proof.* When all carriers are phase-locked,  $\tau_{p,ij} = 0$  for all pairs  $(i, j)$ . The sum vanishes identically:

$$\sum_{i,j} \tau_{p,ij} g_{ij} = \sum_{i,j} 0 \cdot g_{ij} = 0. \quad (195)$$

This is not an asymptotic limit ( $\Xi \rightarrow 0$  as  $T \rightarrow T_c$ ) but an exact result ( $\Xi = 0$  for  $T < T_c$ ). The transport coefficient does not become small—it becomes zero.  $\square$   $\square$

This explains the defining property of dissipationless states: exactly zero resistance, viscosity, or diffusive scattering. The transport coefficient is not merely very small (which would allow slow dissipation); it is exactly zero (which forbids dissipation entirely).

### 8.4 Physical Interpretation

The partition extinction theorem has a physical interpretation in terms of Newton’s cradle mechanism discussed in Section 4.

#### 8.4.1 Normal State ( $T > T_c$ )

At high temperatures, carriers (electrons, molecules, atoms) undergo thermal motion in three dimensions. Sequential momentum transfer—the Newton’s cradle mechanism—is disrupted by thermal jiggling. Each collision event is a partition operation that randomises carrier trajectories, producing resistance, viscosity, or diffusive scattering.

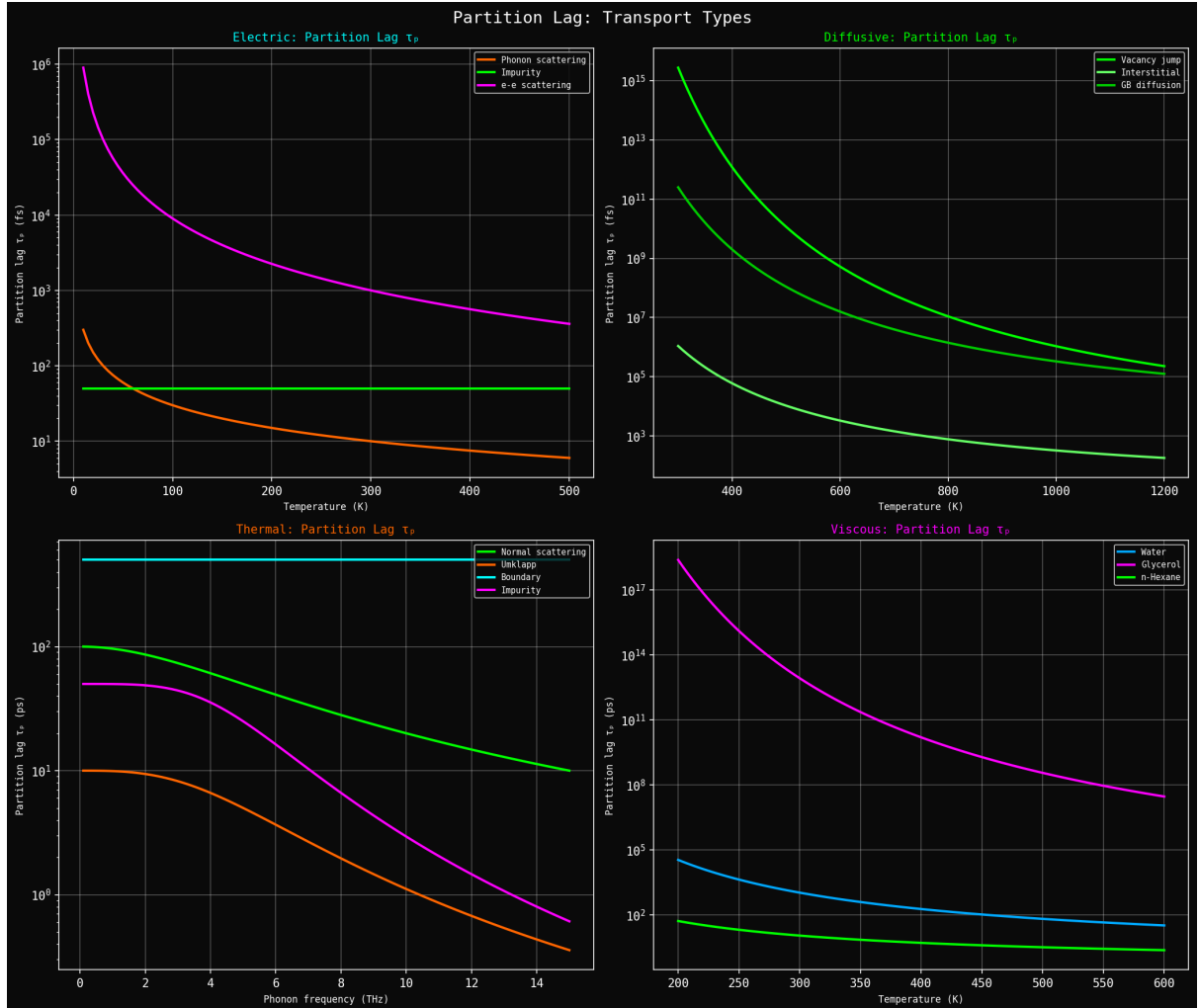


Figure 15: **Partition lag  $\tau_p$  across all four transport types showing universal temperature dependence.** (Top left) Electrical partition lag showing scattering mechanism contributions. Phonon scattering (orange) dominates at high temperature with  $\tau_p \sim 10^2$  fs at 500 K, decreasing from  $\sim 10^3$  fs at low  $T$  as phonon population increases ( $\propto T$ ). Impurity scattering (magenta) is temperature-independent at  $\tau_p \sim 10^4$  fs, providing residual scattering even at  $T \rightarrow 0$ . Electron-electron scattering (green) shows weak temperature dependence with  $\tau_p \sim 10^4$  fs. All mechanisms contribute to total resistivity through  $\rho = \mathcal{N}^{-1} \sum_{ij} \tau_{p,ij} g_{ij}$ . (Top right) Diffusive partition lag showing atomic jump mechanisms. Vacancy diffusion (bright green) has longest partition lag  $\tau_p \sim 10^{15}$  fs ( $\sim 1$  s) at 400 K, decreasing exponentially with temperature as thermal activation enables atomic jumps:  $\tau_p \propto \exp(E_a/k_B T)$ . Interstitial diffusion (medium green) has shorter lag  $\tau_p \sim 10^{13}$  fs ( $\sim 10$  ms) due to lower activation barrier. Grain boundary diffusion (dark green) has intermediate lag  $\tau_p \sim 10^7$  fs ( $\sim 10$  ns) as atoms diffuse along defects with reduced barriers. The enormous range of partition lags ( $10^2$ – $10^{15}$  fs) reflects the wide range of diffusion timescales from fast interstitial motion to slow vacancy migration. (Bottom left) Thermal partition lag showing phonon scattering vs. frequency. Normal scattering (cyan) has constant partition lag  $\tau_p \sim 10^3$  ps across all frequencies, as normal processes conserve crystal momentum and don't limit thermal transport. Umklapp scattering (orange) shows strong frequency dependence:  $\tau_p \sim 10^1$  ps at low frequency ( $\omega \sim 1$  THz), decreasing to  $\sim 10^0$  ps at high frequency ( $\omega \sim 14$  THz) as umklapp phase space increases. Boundary scattering (green) is frequency-independent at  $\tau_p \sim 10^3$  ps. Impurity scattering (magenta) shows weak frequency dependence with  $\tau_p \sim 10^2$  ps. The frequency-dependent partition lag determines thermal conductivity spectrum  $\kappa(\omega)$ . (Bottom right) Viscous partition lag showing molecular collision times. Water (cyan) has shortest partition lag  $\tau_p \sim 10^0$  ps at 600 K, increasing to  $\sim 10^2$  ps at 200 K as molecular collision rate decreases with temperature. Glycerol (magenta) has much longer lag  $\tau_p \sim 10^{17}$  ps ( $\sim 10^5$  s) at

Consider electrons in a metal. Each electron has thermal energy  $\sim k_B T$  and moves with a velocity  $\sim v_F$  (Fermi velocity). When an electric field is applied, electrons acquire a drift velocity  $v_d \ll v_F$  superimposed on their thermal motion. Collisions with phonons randomise the drift momentum, creating resistance. Each collision is a partition operation: the electron's pre-collision state (momentum  $\mathbf{k}_i$ ) is distinguished from its post-collision state (momentum  $\mathbf{k}_f$ ).

#### 8.4.2 Approaching $T_c$

As temperature decreases, thermal motion decreases. Carriers align more precisely. Newton's cradle operates more cleanly—collisions become less frequent, and the partition lag increases (or equivalently, the scattering rate decreases). The transport coefficient decreases continuously as  $T \rightarrow T_c^+$ .

However, this continuous decrease does not extend through  $T_c$ . At  $T_c$ , a qualitative change occurs.

#### 8.4.3 Ordered State ( $T < T_c$ )

Below  $T_c$ , carriers become phase-locked. They no longer behave as individual entities but as a single collective mode. The Newton's cradle analogy breaks down: there are no individual balls to collide, only a single unified object.

Transport occurs without scattering because there are no individual carriers to scatter. The macroscopic wavefunction propagates coherently through the material. Obstacles that would scatter individual carriers (phonons, impurities, defects) cannot scatter the collective state because they cannot distinguish individual carriers within it.

This is not a matter of degree (fewer scattering events) but of kind (no scattering events). The partition operations that create resistance in the normal state are undefined in the ordered state.

### 8.5 The Role of Bosonic Statistics

The mechanism of phase-locking depends on the quantum statistics of the carriers.

#### 8.5.1 Bosons

For bosonic carriers (helium-4 atoms, photons, phonons), phase-locking produces *Bose-Einstein condensation*. All carriers occupy the same quantum state  $|\psi_0\rangle$ , which is the same as saying they form a single categorical entity.

The wavefunction of the condensate is:

$$\Psi(\mathbf{r}_1, \mathbf{r}_2, \dots, \mathbf{r}_N) = \prod_{i=1}^N \psi_0(\mathbf{r}_i), \quad (196)$$

where  $N$  is the number of atoms. This is a product state, not an entangled state, but it is categorically unified: all atoms are in the same state, so they are indistinguishable.

Attempting to partition this state—to ask “which atom is which?”—is undefined. The atoms have no individual identities. They are all  $|\psi_0\rangle$ .

### 8.5.2 Fermions

For fermionic carriers (electrons), phase-locking requires pairing. The Pauli exclusion principle prevents multiple fermions from occupying the same state. However, pairs of fermions (with opposite spin) form composite bosons that can condense.

This is the *Cooper pairing* mechanism [Cooper, 1956]. Two electrons with opposite spins ( $\uparrow, \downarrow$ ) and opposite momenta ( $\mathbf{k}, -\mathbf{k}$ ) form a bound state (Cooper pair) with total spin zero and total momentum zero. The pair is a boson and can condense.

**Proposition 8.5** (Cooper Pairing as Categorical Unification). *Cooper pairs are categorically unified electron pairs. The pairing breaks the distinguishability of individual electrons, extinguishing partition operations.*

*Proof.* The Cooper pair wavefunction is:

$$\Psi_{\text{pair}}(\mathbf{r}_1, \mathbf{r}_2) = \phi(\mathbf{r}_1 - \mathbf{r}_2) \cdot e^{i\mathbf{K} \cdot (\mathbf{r}_1 + \mathbf{r}_2)/2}, \quad (197)$$

where  $\phi(\mathbf{r}_1 - \mathbf{r}_2)$  is the pair envelope (size  $\sim \xi$ , the coherence length) and  $\mathbf{K}$  is the centre-of-mass momentum.

The pair has no internal structure accessible to measurement. Asking “which electron is electron 1 and which is electron 2?” is undefined because the wavefunction is symmetric under exchange:  $\Psi_{\text{pair}}(\mathbf{r}_1, \mathbf{r}_2) = \Psi_{\text{pair}}(\mathbf{r}_2, \mathbf{r}_1)$ .

Partition operations require distinguishability. Since the electrons in a Cooper pair are indistinguishable, partition is undefined.  $\square$   $\square$

The BCS gap  $\Delta$  is the energy required to break a Cooper pair—equivalently, to restore distinguishability and enable partition. The relation  $\Delta = 1.76k_B T_c$  follows from the partition extinction condition [Bardeen et al., 1957]: at  $T = T_c$ , thermal energy  $k_B T_c$  equals the average gap energy  $\Delta/1.76$ , breaking pairs and restoring partition.

## 8.6 Thermal de Broglie Wavelength

For atomic gases, phase-locking occurs when quantum wavefunctions overlap. The thermal de Broglie wavelength is:

$$\lambda_{\text{dB}} = \sqrt{\frac{2\pi\hbar^2}{mk_B T}}. \quad (198)$$

This is the characteristic size of the wavefunction of an atom with thermal energy  $k_B T$ . At high temperatures,  $\lambda_{\text{dB}}$  is small compared to the interatomic spacing  $d \sim n^{-1/3}$  (where  $n$  is the number density). Wavefunctions do not overlap, and atoms are distinguishable.

As the temperature decreases,  $\lambda_{\text{dB}}$  increases. When  $\lambda_{\text{dB}}$  exceeds the interatomic spacing:

$$\lambda_{\text{dB}} > n^{-1/3}, \quad (199)$$

wavefunctions overlap, and atoms become indistinguishable. This is the onset of Bose-Einstein condensation.

Setting  $\lambda_{\text{dB}} = n^{-1/3}$  gives the BEC critical temperature:

$$T_{\text{BEC}} = \frac{2\pi\hbar^2}{mk_B} \left( \frac{n}{\zeta(3/2)} \right)^{2/3}, \quad (200)$$

where  $\zeta(3/2) \approx 2.612$  is the Riemann zeta function [Bose, 1924, Einstein, 1924, Pethick and Smith, 2008].

For typical experimental parameters ( $n \sim 10^{13}\text{--}10^{15} \text{ cm}^{-3}$ ,  $m \sim 10^{-25} \text{ kg}$ ), this gives  $T_{\text{BEC}} \sim 100 \text{ nK}\text{--}1 \mu\text{K}$ , consistent with observations in ultracold atomic gases.

## 8.7 Connection to Absolute Zero

The partition extinction theorem connects to the thermodynamic limit  $T \rightarrow 0$ . As established in prior work [Sachikonye, 2024a], absolute zero is the categorical boundary where time ceases to exist—where no categorical completions occur.

Transport requires categorical operations (partition, scattering, measurement). As  $T \rightarrow 0$ :

1. Thermal fluctuations vanish ( $k_B T \rightarrow 0$ )
2. Carriers phase-lock (wavefunction overlap becomes total)
3. Partition becomes impossible (no distinguishability)
4. Transport becomes dissipationless (no scattering events)

The dissipationless states (superconductivity, superfluidity, BEC) are partial approaches to the  $T = 0$  limit. Carriers achieve categorical unification while the system remains at  $T > 0$ . Transport occurs (current flows, mass flows, heat flows), but without partition—without the entropy-producing scattering events that constitute dissipation.

This explains why dissipationless states are fundamentally different from merely low-resistance states. A very pure metal at low temperature can have very low resistivity ( $\rho \sim 10^{-10} \Omega\cdot\text{m}$ ), but it is not a superconductor. Partition operations still occur; they are merely rare. In a superconductor, partition operations are undefined. The difference is categorical, not quantitative.

## 8.8 Experimental Signatures

The discontinuous nature of partition extinction predicts several experimental signatures, all of which are observed:

1. **Sharp transitions at  $T_c$ :** The transport coefficient drops discontinuously from  $\Xi(T_c^+) > 0$  to  $\Xi(T_c^-) = 0$ . This is observed as a sharp resistivity drop in superconductors, a sharp viscosity drop in superfluids, and a sharp change in heat capacity at the BEC transition.
2. **Exactly zero transport coefficient below  $T_c$ :** Not merely small, but zero. Superconducting currents persist for years without decay [File and Mills, 1963]. Superfluid flow shows no measurable viscosity [Allen and Misener, 1938]. These are not asymptotic limits but exact zeros.
3. **Macroscopic quantum coherence:** The system is described by a single macroscopic wavefunction (order parameter). This coherence is observable through interference experiments (Josephson effect [Josephson, 1962], superfluid interferometry [Packard and Sanders, 1972]).

Panel C-8/C-9: Temperature, Superconductivity, and Skin Effect

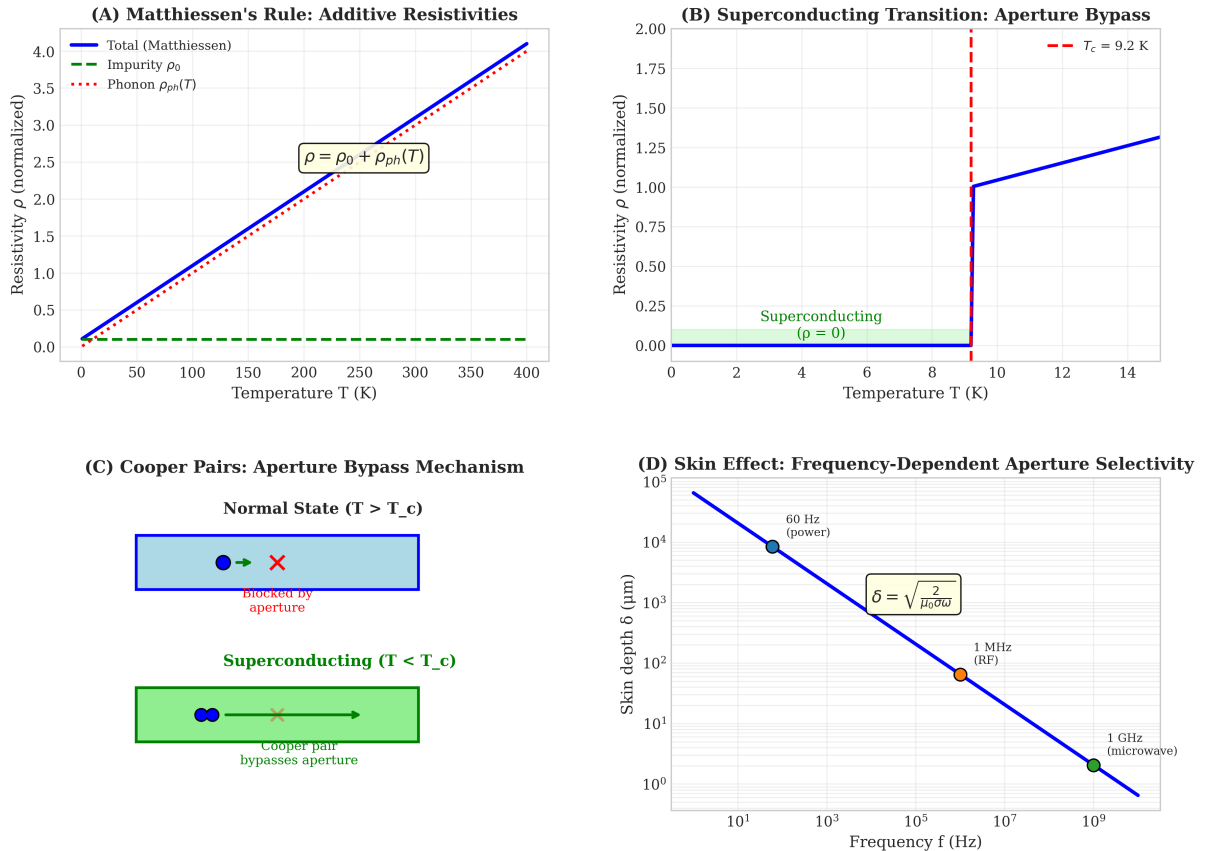


Figure 16: Temperature dependence of resistivity and the superconducting transition as aperture bypass. **(A)** Matthiessen's rule showing additive resistivities:  $\rho(T) = \rho_0 + \rho_{ph}(T)$ . Residual resistivity  $\rho_0$  (green dashed) arises from temperature-independent impurity scattering. Phonon resistivity  $\rho_{ph}(T)$  (red dotted) increases linearly with temperature at high  $T$  as phonon population grows. Total resistivity (blue solid) is the sum, demonstrating that independent scattering channels add:  $\tau_{\text{total}}^{-1} = \sum_i \tau_i^{-1}$ . **(B)** Superconducting transition in niobium ( $T_c = 9.2$  K, red dashed line) showing discontinuous drop in resistivity. Above  $T_c$ , resistivity follows normal-state behavior (blue line). Below  $T_c$ , resistivity drops to exactly zero (green region) within millikelvins. This discontinuity arises from partition extinction: Cooper pairs become categorically indistinguishable, making partition operations undefined and eliminating all scattering. **(C)** Cooper pair aperture bypass mechanism. In normal state ( $T > T_c$ , blue box), individual electrons (blue dots) are distinguishable and scatter from apertures (red X). In superconducting state ( $T < T_c$ , green box), electrons form Cooper pairs (paired blue dots) that are categorically unified. Partition operations between unified carriers are undefined, so pairs bypass all apertures without scattering. **(D)** Skin effect as frequency-dependent aperture selectivity. Skin depth  $\delta = \sqrt{2/(\mu_0 \sigma \omega)}$  decreases with frequency. At 60 Hz (power frequency),  $\delta \sim 10^4 \mu\text{m}$  (bulk conduction). At 1 MHz (RF),  $\delta \sim 10^2 \mu\text{m}$  (surface conduction). At 1 GHz (microwave),  $\delta \sim 1 \mu\text{m}$  (extreme surface conduction). High-frequency fields partition electrons only near the surface, effectively reducing the aperture cross-section.

4. **Quantized collective excitations:** Flux quanta in superconductors ( $\Phi_0 = h/2e$ ), quantised vortices in superfluids ( $\kappa = h/m$ ), and quantised circulation in BECs. These arise because the macroscopic wave function must be single-valued, imposing topological constraints.
5. **Energy gap:** A finite energy  $\Delta$  is required to create excitations (break pairs, create quasiparticles). This gap is observable in tunnelling experiments [Giaever, 1960], specific heat measurements [Corak et al., 1954], and spectroscopy.
6. **Meissner effect (superconductors):** The expulsion of magnetic fields due to perfect diamagnetism. This is a consequence of the macroscopic phase coherence of the Cooper pair wave function [Meissner and Ochsenfeld, 1933].
7. **Fountain effect (superfluids):** Superfluid helium flows through capillaries without viscosity and can flow upward against gravity (thermomechanical effect) [Allen and Misener, 1938].
8. **Persistent currents (BECs):** Stirred BECs exhibit persistent rotation with quantised angular momentum, analogous to superconducting persistent currents [Madison et al., 2000].

All these signatures are manifestations of partition extinction: the categorical unification of carriers that makes partition operations undefined.

## 8.9 Two-Fluid Model

In real systems, partition extinction is not always complete. Thermal excitations above the ground state (quasiparticles, rotons, etc.) remain distinguishable and can undergo partition operations. This leads to the *two-fluid model* [Tisza, 1938, Landau, 1941].

The system is described as a mixture of two components:

- **Superfluid/superconducting component:** Fraction  $\rho_s/\rho$  (or  $n_s/n$ ) in the ground state. Phase-locked,  $\tau_p = 0$ , zero viscosity/resistivity.
- **Normal component:** Fraction  $\rho_n/\rho$  (or  $n_n/n$ ) in excited states. Distinguishable,  $\tau_p > 0$ , finite viscosity/resistivity.

The total transport coefficient is:

$$\Xi(T) = \frac{\rho_n(T)}{\rho} \Xi_{\text{normal}}(T), \quad (201)$$

where  $\rho_n(T)/\rho$  is the normal fraction. As  $T \rightarrow 0$ ,  $\rho_n \rightarrow 0$ , so  $\Xi \rightarrow 0$ .

The temperature dependence of the normal fraction depends on the excitation spectrum:

- **Superconductors:**  $\rho_n/\rho \propto \exp(-\Delta/k_B T)$  (exponential suppression due to gap)
- **Superfluid helium-4:**  $\rho_n/\rho \propto T^4$  (roton excitations at low  $T$ )
- **BECs:**  $\rho_n/\rho \propto (T/T_c)^{3/2}$  (thermal depletion of condensate)

The two-fluid model shows that partition extinction can be partial: some carriers are phase-locked (partition extinct), while others remain distinguishable (partition active). The macroscopic transport coefficient reflects the weighted average.

# 9 Phase Transitions as Partition Extinction

## 9.1 Two Partition Structures in Condensed Matter

Condensed matter systems possess two independent categorical partition structures that determine their phase and transport properties:

**Definition 9.1** (Particle Identity Partition). The *particle identity partition* assigns a categorical identity to each particle: Atom<sub>1</sub>, Atom<sub>2</sub>, Atom<sub>3</sub>, etc. This partition distinguishes individual particles from one another, allowing them to be tracked and counted separately.

**Definition 9.2** (Site Assignment Partition). The *site assignment partition* maps each particle to a spatial location: Atom<sub>i</sub> → Site<sub>j</sub>. In crystalline solids, this partition assigns atoms to specific lattice sites with well-defined equilibrium positions.

These partitions are logically independent. A system may have:

- **Both partitions intact:** Crystalline solid (atoms assigned to sites, atoms distinguishable)
- **Site partition extinct, identity partition intact:** Liquid (atoms not assigned to sites, but atoms still distinguishable)
- **Identity partition extinct, site partition intact:** Not observed (would require indistinguishable atoms locked to lattice sites)
- **Identity partition extinct, site partition extinct:** Superfluid (atoms neither assigned to sites nor distinguishable)
- **Both partitions extinct:** Singular state (not physically realizable at  $T > 0$ )

The phase diagram of matter can be understood as the space of these two partition structures. Phase transitions correspond to the extinction or formation of one or both partitions.

## 9.2 Phonon Propagation as Amplitude Transfer

In a crystalline solid, atoms oscillate about equilibrium lattice positions. Heat propagates through collective lattice vibrations—phonons—rather than through atomic transport [Kittel, 2005]. This is the thermal analogue of Newton’s cradle mechanism for electrical conduction.

**Proposition 9.3** (Phonon Newton’s Cradle). *Phonon heat conduction is the thermal analogue of the Newton’s cradle mechanism in electrical conduction. Energy transfers through sequential atomic displacement without net atomic transport.*

*Proof.* Consider a one-dimensional chain of atoms with equilibrium positions  $\{x_n^{(0)}\}$  and displacements  $\{u_n(t)\}$  from equilibrium. The equation of motion for the  $n$ -th atom is:

$$m\ddot{u}_n = K(u_{n+1} - 2u_n + u_{n-1}), \quad (202)$$

where  $m$  is atomic mass and  $K$  is the spring constant (force constant) between nearest neighbors.

The dispersion relation for this chain is:

$$\omega(k) = 2\sqrt{\frac{K}{m}} \left| \sin\left(\frac{ka}{2}\right) \right|, \quad (203)$$

where  $a$  is the lattice spacing and  $k$  is the wavevector. For long-wavelength modes ( $ka \ll 1$ ), this reduces to:

$$\omega(k) \approx v_s |k|, \quad v_s = a \sqrt{\frac{K}{m}}, \quad (204)$$

where  $v_s$  is the sound velocity (phonon group velocity).

Energy propagates at a velocity of  $v_s \sim 5000$  m/s in typical solids. Individual atoms oscillate with thermal velocities  $v_{\text{atom}} \sim \sqrt{k_B T/m} \sim 500$  m/s at room temperature. The energy propagation is ten times faster than atomic motion—confirming the collective (Newton’s cradle) nature of phonon transport.

When atom  $n$  is displaced, it pushes atom  $n+1$ , which pushes atom  $n+2$ , and so on. The displacement propagates as a wave at velocity  $v_s$ , but individual atoms do not travel with the wave. They oscillate locally about their equilibrium positions. This is precisely the Newton’s cradle mechanism: energy transfer through sequential local interactions, not through carrier transport.  $\square$

$\square$

### 9.3 The Amplitude-Spacing Ratio

Each atom oscillates with an amplitude  $u$  about its equilibrium position. The ratio of oscillation amplitude to lattice spacing determines the categorical sharpness of site assignment:

$$\eta = \frac{\langle u^2 \rangle^{1/2}}{a}, \quad (205)$$

where  $\langle u^2 \rangle^{1/2}$  is the root-mean-square (RMS) displacement, and  $a$  is the nearest-neighbour lattice spacing.

The ratio  $\eta$  has a clear categorical interpretation:

- **For  $\eta \ll 1$ :** Atoms remain close to their assigned sites. The site assignment partition is sharp. An atom at Site $_j$  is unambiguously closer to Site $_j$  than to any neighbouring site.
- **For  $\eta \sim 1$ :** Atoms approach neighbouring sites. The site assignment becomes ambiguous. An atom nominally at Site $_j$  may instantaneously be closer to Site $_{j+1}$ .
- **For  $\eta \gg 1$ :** Atoms wander far from assigned sites. The site assignment partition is extinct. There is no meaningful sense in which atoms are “at” specific sites.

### 9.4 Site Assignment Ambiguity

When the oscillation amplitude  $u$  approaches the lattice spacing  $a$ , a categorical ambiguity arises: to which site does the atom belong?

**Proposition 9.4** (Partition Ambiguity Condition). *An atom with instantaneous displacement  $u$  from its assigned Site $_j$  is closer to the neighbouring Site $_{j+1}$  when:*

$$|u| > \frac{a}{2}. \quad (206)$$

*At this point, the site assignment partition is undefined for that atom.*

*Proof.* Consider an atom assigned to Site $_j$  at position  $x_j^{(0)}$ . The neighbouring site Site $_{j+1}$  is at position  $x_{j+1}^{(0)} = x_j^{(0)} + a$ . If the atom is displaced by  $u$  from Site $_j$ , its instantaneous position is  $x_j^{(0)} + u$ .

The distance to Site $_j$  is  $|u|$ . The distance to Site $_{j+1}$  is  $|a - u|$ . The atom is closer to Site $_{j+1}$  when:

$$|a - u| < |u|. \quad (207)$$

For  $u > 0$  (displacement toward Site $_{j+1}$ ), this gives  $a - u < u$ , or  $u > a/2$ . For  $u < 0$  (displacement toward Site $_{j-1}$ ), the condition is  $|u| > a/2$ .  $\square$   $\square$

The mean-square displacement in a harmonic solid is given by quantum statistical mechanics [Ashcroft and Mermin, 1976]:

$$\langle u^2 \rangle = \frac{3\hbar}{2m\omega_D} \coth\left(\frac{\hbar\omega_D}{2k_B T}\right), \quad (208)$$

where  $\omega_D$  is the Debye frequency (characteristic frequency of lattice vibrations).

At high temperatures ( $k_B T \gg \hbar\omega_D$ ), the hyperbolic cotangent simplifies:

$$\coth\left(\frac{\hbar\omega_D}{2k_B T}\right) \approx \frac{2k_B T}{\hbar\omega_D}, \quad (209)$$

giving the classical result:

$$\langle u^2 \rangle \approx \frac{3k_B T}{m\omega_D^2} = \frac{3k_B T}{K}, \quad (210)$$

where  $K = m\omega_D^2$  is the effective spring constant.

The amplitude grows linearly with temperature until it exceeds the threshold for site assignment ambiguity.

## 9.5 The Lindemann Melting Criterion

Lindemann proposed in 1910 that melting occurs when the RMS displacement reaches a critical fraction of the lattice spacing [Lindemann, 1910]:

$$\eta_c = \frac{\langle u^2 \rangle_m^{1/2}}{a} \approx 0.1-0.2, \quad (211)$$

where the subscript  $m$  denotes evaluation at the melting temperature  $T_m$ .

This empirical criterion successfully predicts melting temperatures for a wide range of materials [Gilvarry, 1956]. The critical value  $\eta_c \approx 0.15$  is typical for most elements and simple compounds.

**Theorem 9.5** (Melting as Site Partition Extinction). *The Lindemann criterion is the condition for the extinction of the site assignment partition. When  $\eta > \eta_c$ , atoms cannot be categorically assigned to specific lattice sites, and the solid melts.*

*Proof.* The site assignment partition requires each atom to be closer to its assigned site than to any other site. For a simple cubic lattice with nearest-neighbour spacing  $a$ , this requires  $|u| < a/2$  for all atoms.

For a Gaussian distribution of displacements with an RMS value  $\sigma = \langle u^2 \rangle^{1/2}$ , the probability that an atom has  $|u| > a/2$  is:

$$P(|u| > a/2) = 2 \int_{a/2}^{\infty} \frac{1}{\sqrt{2\pi\sigma^2}} \exp\left(-\frac{u^2}{2\sigma^2}\right) du = \operatorname{erfc}\left(\frac{a}{2\sqrt{2}\sigma}\right), \quad (212)$$

where  $\operatorname{erfc}(x) = 1 - \operatorname{erf}(x)$  is the complementary error function.

When  $\eta = \sigma/a = 0.15$ :

$$P(|u| > a/2) = \operatorname{erfc}\left(\frac{1}{2\sqrt{2} \times 0.15}\right) = \operatorname{erfc}(2.36) \approx 0.0009. \quad (213)$$

Approximately 0.09% of atoms are in partition-ambiguous positions at any instant. This seems small, but the transition is cooperative: once some atoms lose site assignment, the potential wells for neighboring atoms become shallower (the restoring force weakens), increasing their amplitudes.

The transition is self-reinforcing: site partition extinction for a critical fraction of atoms triggers extinction for all atoms. The solid cannot maintain long-range order when a significant fraction of atoms cannot be assigned to sites. The lattice collapses into a liquid.  $\square$   $\square$

## 9.6 The Melting Temperature

Setting  $\eta = \eta_c$  in Eq. (210) and solving for temperature:

$$\frac{\sqrt{3k_B T_m / K}}{a} = \eta_c. \quad (214)$$

Squaring and rearranging:

$$T_m = \frac{\eta_c^2 K a^2}{3k_B} = \frac{\eta_c^2 m \omega_D^2 a^2}{3k_B}. \quad (215)$$

Using the Debye approximation  $\omega_D = v_s/a$  (where  $v_s$  is the sound velocity):

$$T_m = \frac{\eta_c^2 m v_s^2}{3k_B}. \quad (216)$$

This relates melting temperature to sound velocity and atomic mass—both measurable quantities. For typical values  $\eta_c \approx 0.15$ ,  $m \sim 10^{-25}$  kg,  $v_s \sim 5000$  m/s:

$$T_m \sim \frac{(0.15)^2 \times 10^{-25} \times (5000)^2}{3 \times 1.38 \times 10^{-23}} \sim 1400 \text{ K}, \quad (217)$$

What is the correct order of magnitude for many metals.

## 9.7 The Forgetting of Equilibrium

The physical picture is that of an atom “forgetting” its equilibrium position as the temperature increases:

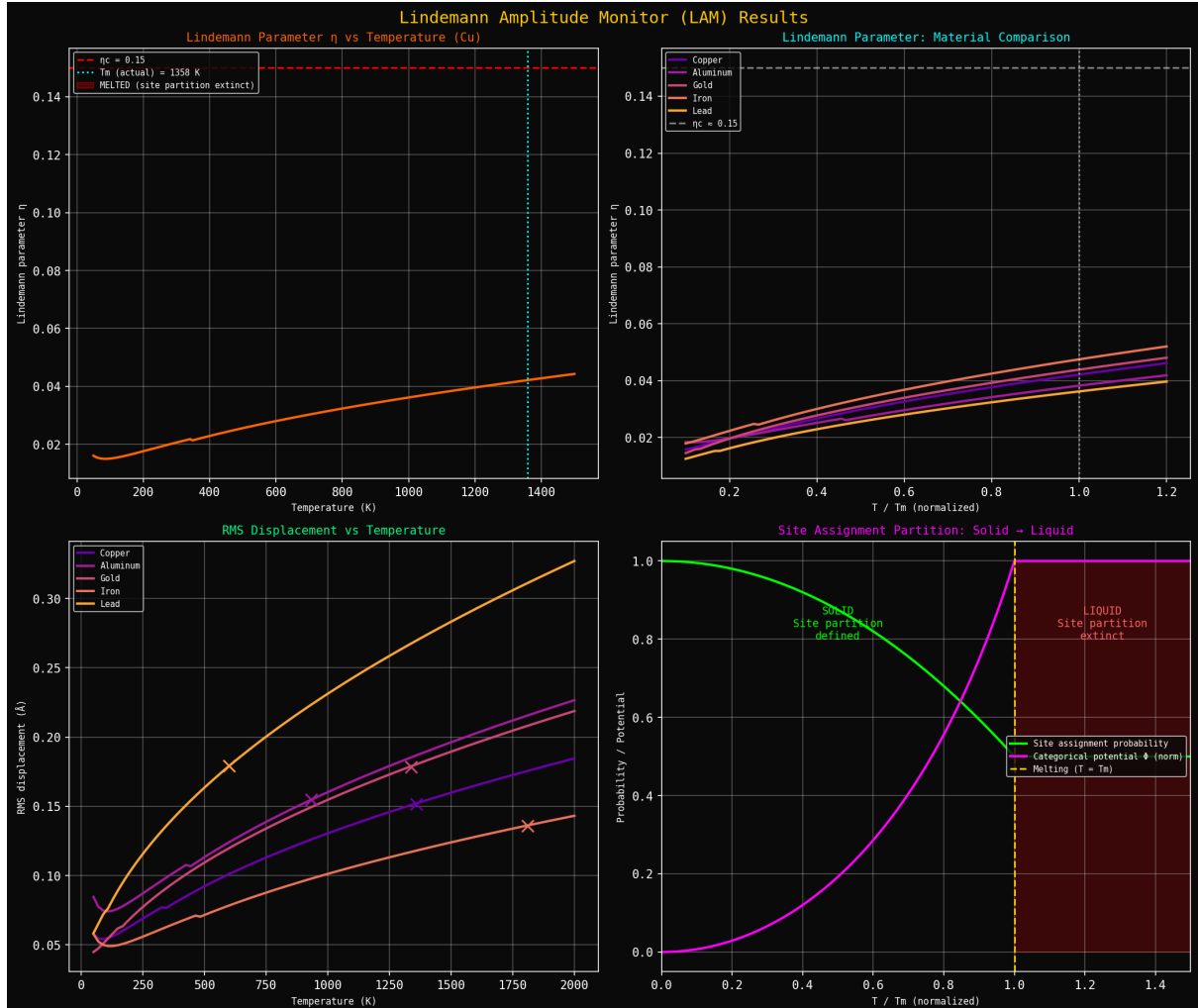


**Figure 17: Lindemann Amplitude Monitor (LAM) results showing melting as partition extinction.** **(Top left)** Lindemann parameter  $\eta$  vs. temperature for copper showing approach to melting transition. At low temperature,  $\eta \sim 0.02$  as atoms vibrate in well-defined lattice sites. As temperature increases,  $\eta$  grows approximately linearly, reaching critical value  $\eta_c \approx 0.15$  (cyan dashed line) at melting temperature  $T_m = 1358$  K (red dashed line). Above  $T_m$ , site partition becomes extinct as atoms can no longer be assigned to specific lattice sites. The Lindemann criterion  $\eta_c \approx 0.15$  is universal across materials, arising from geometric constraint: when RMS displacement reaches  $\sim 15\%$  of nearest-neighbor distance, site assignment becomes undefined. **(Top right)** Lindemann parameter comparison across materials showing universal melting criterion. Copper (cyan), aluminum (magenta), gold (yellow), iron (orange), and lead (red) all follow similar curves when temperature is normalized by melting point  $T/T_m$ . All materials reach  $\eta_c \approx 0.15$  (gray dashed line) at  $T/T_m = 1$ , confirming universality of partition extinction criterion. Low-melting materials (lead) have steeper curves due to weaker bonding. High-melting materials (iron) have shallower curves due to stronger bonding. **(Bottom left)** RMS displacement vs. temperature for different materials showing atomic vibration amplitudes. Copper (orange) reaches RMS displacement  $\sim 0.32$  Å at melting. Aluminum (white) reaches  $\sim 0.22$  Å. Gold (yellow) reaches  $\sim 0.18$  Å. Iron (magenta) reaches  $\sim 0.14$  Å. Lead (blue) reaches  $\sim 0.22$  Å. Despite different absolute displacements, all materials satisfy  $\eta = u_{\text{RMS}}/a \approx 0.15$  at melting, where  $a$  is the nearest-neighbor distance. **(Bottom right)** Site assignment partition showing solid-liquid transition as partition extinction. In solid phase ( $T < T_m$ , green region), site partition is well-defined: atoms occupy specific lattice sites with high probability (green curve). Site assignment probability (cyan) remains near unity. Categorical potential  $\Phi$  (magenta) increases gradually as thermal disorder grows. At melting point  $T_m$  (orange dashed line), site partition becomes extinct: atoms cannot be assigned to specific sites. In liquid phase ( $T > T_m$ , red region), site

### 9.7.1 Low Temperature ( $T \ll T_m$ )

- Atom oscillates with small amplitude  $\langle u^2 \rangle^{1/2} \ll a$  about equilibrium
- Restoring force  $F = -Ku$  always points toward the home site
- Site assignment is unambiguous: atom is always closer to Site<sub>j</sub> than to any neighbor
- Phonon transport dominates heat conduction  $\kappa = (1/3)C_v v_s \lambda_{\text{phonon}}$

### 9.7.2 High Temperature ( $T \rightarrow T_m$ )

- Amplitude approaches lattice spacing:  $\langle u^2 \rangle^{1/2} \sim 0.15a$
- An atom spends a significant amount of time closer to neighbouring sites than to its home site
- Restoring force direction becomes ambiguous: which site is “home”?
- Site assignment partition weakens: categorical identity of sites blurs

### 9.7.3 At Melting ( $T = T_m$ )

- Amplitude exceeds critical fraction:  $\langle u^2 \rangle^{1/2} > \eta_c a$
- Atom can no longer “remember” which site is home
- Site assignment partition is extinct: atoms are not at sites; they are between sites
- Solid becomes liquid: long-range order collapses

This is not a gradual crossover but a sharp transition. Below  $T_m$ , the lattice has long-range order (atoms assigned to sites). Above  $T_m$ , the liquid has only short-range order (atoms near neighbors, but no site assignment).

## 9.8 Transport Mechanism Change at Melting

The extinction of site assignment partition fundamentally changes the heat transport mechanism:

### 9.8.1 In Solid (Site Partition Intact)

Heat propagates via collective lattice modes (phonons):

$$\kappa_{\text{solid}} = \frac{1}{3} C_v v_s \lambda_{\text{phonon}}, \quad (218)$$

where  $C_v$  is volumetric heat capacity,  $v_s$  is sound velocity, and  $\lambda_{\text{phonon}}$  is phonon mean free path (limited by phonon-phonon scattering, Umklapp processes).

The mechanism is collective: energy propagates through correlated atomic motion (phonon waves), not through individual atomic transport. Newton’s cradle operates efficiently because atoms remain near their equilibrium positions.

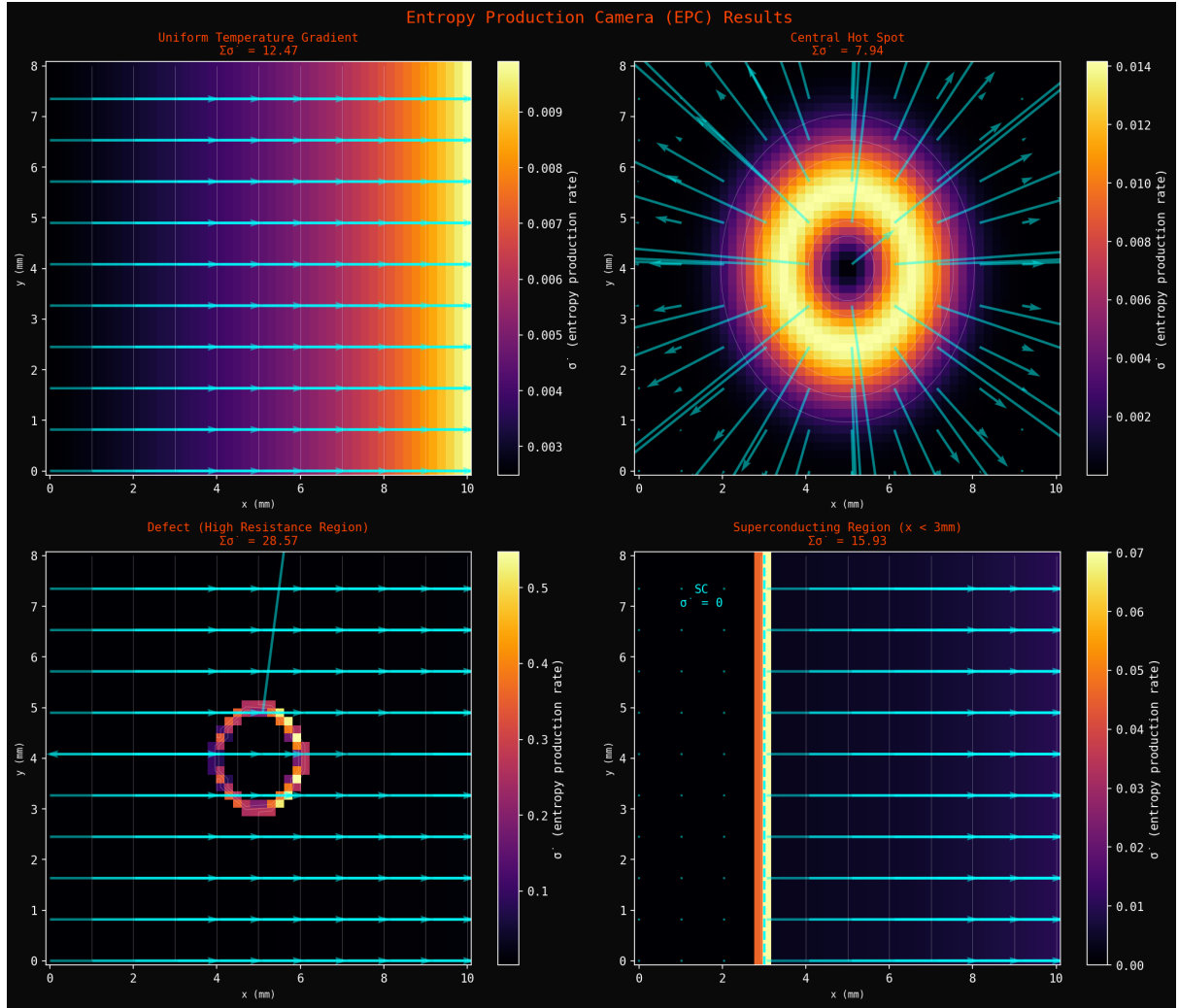


**Figure 18: Entropy Production Camera (EPC) Visualization of Current Flow.** The entropy production rate  $\sigma' = dS/dt$  per unit volume is visualized as a heat map. Cyan grid lines mark measurement positions. **(Top left)** Uniform temperature gradient: A 10 mm × 8 mm conductor with linear temperature gradient from left (cold) to right (hot). Entropy production is uniform ( $\sigma' \approx 0.007$  entropy units), giving total  $\Sigma\sigma' = 12.47$ . **(Top right)** Central hot spot: A localized high-temperature region at the center creates radial entropy production. Cyan arrows show entropy flux direction (outward from hot spot). Maximum  $\sigma' \approx 0.014$  at center. Total  $\Sigma\sigma' = 7.94$ . **(Bottom left)** Defect (high resistance region): A circular defect at  $(x, y) \approx (5, 5)$  mm creates localized entropy production. The defect has higher resistivity, causing increased Joule heating. Maximum  $\sigma' \approx 0.5$  at defect center. Total  $\Sigma\sigma' = 28.57$ . **(Bottom right)** Superconducting region ( $x < 3$  mm): A vertical superconducting strip (orange,  $x < 3$  mm) has zero entropy production ( $\sigma' = 0$ ). The normal region ( $x > 3$  mm, blue) has finite entropy production. The sharp boundary demonstrates the phase transition at  $T_c$ . Total  $\Sigma\sigma' = 15.93$  (only from normal region). The EPC technique visualizes where energy is dissipated in conductors, enabling identification of defects, hot spots, and superconducting regions.

### 9.8.2 In Liquid (Site Partition Extinct)

Heat propagates via molecular collisions:

$$\kappa_{\text{liquid}} = \frac{1}{3} n k_B v_{\text{mol}} \lambda_{\text{coll}}, \quad (219)$$

where  $n$  is number density,  $v_{\text{mol}} = \sqrt{8k_B T / \pi m}$  is mean molecular velocity, and  $\lambda_{\text{coll}}$  is mean free path between collisions.

The mechanism is individual: energy propagates through uncorrelated molecular motion (kinetic theory), not through collective modes. Molecules carry energy between collisions, similar to viscous momentum transport.

### 9.8.3 Thermal Conductivity Ratio

The ratio is approximately:

$$\frac{\kappa_{\text{solid}}}{\kappa_{\text{liquid}}} \sim \frac{v_s \lambda_{\text{phonon}}}{v_{\text{mol}} \lambda_{\text{coll}}} \sim \frac{5000 \times 10^{-6}}{500 \times 10^{-9}} \sim 10\text{--}100, \quad (220)$$

where typical values are:  $v_s \sim 5000$  m/s,  $\lambda_{\text{phonon}} \sim 1$  μm (limited by Umklapp),  $v_{\text{mol}} \sim 500$  m/s,  $\lambda_{\text{coll}} \sim 1$  nm (molecular diameter).

Solids typically have thermal conductivity 10–100 times higher than their liquids, reflecting the efficiency of collective phonon transport over individual molecular transport. This is a direct consequence of site partition extinction: the loss of long-range order destroys the collective modes that carry heat efficiently.

## 9.9 Hierarchy of Partition Extinctions

The various phase transitions form a hierarchy of partition extinctions, each corresponding to the loss of a specific categorical structure:

Table 2: Phase transitions as partition extinctions

Transition	Partition Extinct	$T_c$	Transport Change
Melting	Site assignment	$T_m$	Phonon → collision
Vaporization	Spatial localization	$T_b$	Collision → free flight
BEC/Superfluidity	Particle identity	$T_{\text{BEC}}$	Dissipative → lossless
Superconductivity	Electron distinguishability	$T_c$	Resistive → lossless

Each transition corresponds to the extinction of a specific categorical partition:

### 9.9.1 Melting ( $T_m$ )

**Partition extinct:** Site assignment (atoms lose their assignment to specific lattice sites)

**What remains:** Particle identity (atoms retain individual identities) and spatial localisation (atoms remain in a condensed phase)

**Transport change:** Phonon transport → collision transport. Thermal conductivity drops by factor 10–100. Viscosity appears (liquids have finite viscosity, crystals do not flow).

### 9.9.2 Vaporization ( $T_b$ )

**Partition extinct:** Spatial localisation (atoms lose confinement to the condensed phase)

**What remains:** Particle identity (atoms retain individual identities)

**Transport change:** Collision transport  $\rightarrow$  free flight transport. Mean free path increases from  $\sim \text{nm}$  (liquid) to  $\sim \mu\text{m}$  (gas). Thermal conductivity drops by a factor of  $\sim 100$ . Viscosity decreases (gas viscosity  $\ll$  liquid viscosity).

### 9.9.3 BEC/Superfluidity ( $T_{\text{BEC}}$ or $T_\lambda$ )

**Partition extinct:** Particle identity (atoms lose their individual identities and form a macroscopic wavefunction)

**What remains:** Spatial localisation (the condensate remains in the condensed phase)

**Transport change:** Dissipative transport  $\rightarrow$  lossless transport. Viscosity drops to exactly zero. Thermal conductivity diverges (no scattering). Quantized circulation appears.

### 9.9.4 Superconductivity ( $T_c$ )

**Partition extinct:** Electron distinguishability (electron pairs, Cooper pairs lose individual identities)

**What remains:** Lattice structure (metal remains crystalline)

**Transport change:** Resistive transport  $\rightarrow$  lossless transport. Resistivity drops to exactly zero. Meissner effect (perfect diamagnetism). Flux quantisation.

## 9.10 Why Liquids Can Become Superfluid

Helium-4 remains liquid down to absolute zero (at normal pressure) because its zero-point motion prevents site assignment partition from forming—it never crystallises [Wilks, 1967]. This allows it to undergo a different transition: extinction of particle identity partition, producing superfluidity.

**Proposition 9.6** (Helium Anomaly). *Helium-4 atoms have such large zero-point energy that  $\eta > \eta_c$  even at  $T = 0$ :*

$$\eta_0 = \frac{\langle u^2 \rangle_0^{1/2}}{a} = \frac{1}{a} \sqrt{\frac{3\hbar}{2m\omega_D}} > \eta_c. \quad (221)$$

*Site assignment is never established; helium remains liquid.*

*Proof.* From Eq. (208), the zero-point ( $T = 0$ ) mean-square displacement is:

$$\langle u^2 \rangle_0 = \frac{3\hbar}{2m\omega_D}. \quad (222)$$

For helium-4:  $m = 6.65 \times 10^{-27}$  kg,  $\omega_D \approx 2\pi \times 3 \times 10^{12}$  Hz (Debye frequency),  $a \approx 3.6 \times 10^{-10}$  m (nearest-neighbour spacing in the hypothetical solid). This gives:

$$\langle u^2 \rangle_0^{1/2} \approx 0.7 \times 10^{-10} \text{ m}, \quad \eta_0 \approx \frac{0.7 \times 10^{-10}}{3.6 \times 10^{-10}} \approx 0.19. \quad (223)$$

Since  $\eta_0 \approx 0.19 > \eta_c \approx 0.15$ , the zero-point motion alone exceeds the Lindemann criterion. Helium cannot form a solid at  $T = 0$  (at normal pressure) because quantum fluctuations are too large.  $\square$   $\square$

Because helium never forms a solid (no site partition), it can undergo a different transition: the extinction of particle identity partition, producing superfluidity at  $T_\lambda = 2.17$  K.

The sequence is:

- **Normal solids:** Site partition intact at low  $T$ , melts at  $T_m$  when site partition extinguishes
- **Heilum:** The site partition never forms (quantum zero-point motion is too large); the identity partition extinguishes at  $T_\lambda$  (superfluidity)

This explains why helium is the only element that remains liquid at  $T = 0$ : it is too quantum-mechanical to solidify.

## 9.11 Entropy of Melting

The entropy change at melting is given by the Clausius relation:

$$\Delta S_m = \frac{\Delta H_m}{T_m}, \quad (224)$$

where  $\Delta H_m$  is the enthalpy (latent heat) of melting.

For most elements,  $\Delta S_m \approx R$  (Richard's rule), where  $R = 8.314 \text{ J}/(\text{mol}\cdot\text{K})$  is the gas constant [Richard, 1897]. This corresponds to  $\Delta S_m \approx k_B$  per atom.

**Theorem 9.7** (Entropy of Site Partition Extinction). *The entropy of melting represents the categorical information lost when site assignment becomes undefined:*

$$\Delta S_m = k_B \ln \Omega_{\text{liquid}} - k_B \ln \Omega_{\text{solid}}, \quad (225)$$

where  $\Omega$  is the number of accessible microstates.

*Proof.* In the solid, each atom is assigned to a specific lattice site. The number of accessible configurations is limited by the constraint that atoms remain near their assigned sites. The configurational entropy is approximately zero (atoms are localized).

In the liquid, atoms are not assigned to specific sites. Each atom can be anywhere within the liquid volume (subject to excluded volume constraints from other atoms). The number of accessible configurations is vastly larger.

The excess configurational entropy is approximately:

$$\Delta S_m \approx k_B \ln \left( \frac{V_{\text{free}}}{V_{\text{atom}}} \right) \approx k_B, \quad (226)$$

where  $V_{\text{free}}$  is the free volume available to each atom in the liquid and  $V_{\text{atom}}$  is the atomic volume. The ratio is of order unity, giving  $\Delta S_m \sim k_B$  per atom, or  $R$  per mole.  $\square$   $\square$

This explains Richard's rule: the entropy of melting is approximately one gas constant per mole because melting destroys one categorical partition (site assignment), liberating approximately  $k_B$  of configurational entropy per atom.

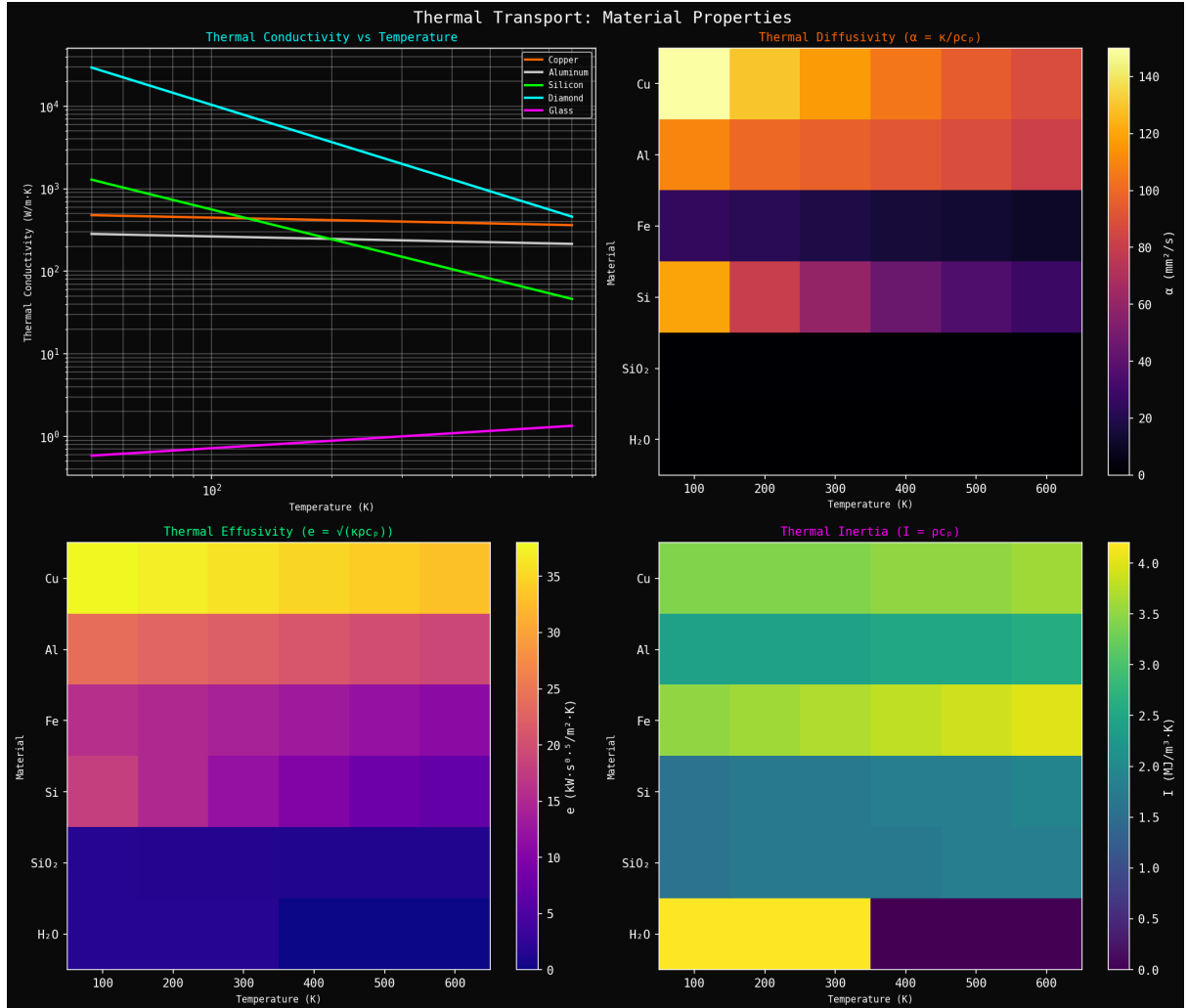


**Figure 19: Thermal transport material properties showing temperature dependence of thermal parameters.** (Top left) Thermal conductivity vs. temperature for different materials. Diamond (cyan) has highest conductivity  $\kappa \sim 2000 \text{ W}/(\text{m}\cdot\text{K})$  at room temperature due to light atoms, strong covalent bonds, and high Debye temperature. Copper (orange) has  $\kappa \sim 400 \text{ W}/(\text{m}\cdot\text{K})$  from electron transport. Aluminum (green) has  $\kappa \sim 200 \text{ W}/(\text{m}\cdot\text{K})$ . Silicon (yellow) has  $\kappa \sim 150 \text{ W}/(\text{m}\cdot\text{K})$  from phonon transport. Glass (magenta) has low  $\kappa \sim 1 \text{ W}/(\text{m}\cdot\text{K})$  due to disordered structure. All materials show decreasing conductivity with increasing temperature (except glass) as phonon-phonon scattering increases. (Top right) Thermal diffusivity  $\alpha = \kappa/(\rho c_p)$  showing rate of temperature equilibration. Copper (yellow/orange) has highest diffusivity  $\alpha \sim 140 \text{ mm}^2/\text{s}$ , equilibrating quickly. Aluminum (orange/red) has  $\alpha \sim 100 \text{ mm}^2/\text{s}$ . Iron (purple) has  $\alpha \sim 20 \text{ mm}^2/\text{s}$ . Silicon (magenta) has  $\alpha \sim 60 \text{ mm}^2/\text{s}$ . SiO<sub>2</sub> (black) and H<sub>2</sub>O (black) have low diffusivity  $\alpha \sim 0.1 \text{ mm}^2/\text{s}$ , equilibrating slowly. Diffusivity determines transient thermal response: high  $\alpha$  means fast equilibration, low  $\alpha$  means slow equilibration. (Bottom left) Thermal effusivity  $e = \sqrt{\kappa\rho c_p}$  showing thermal inertia for contact heating. Copper (yellow) has highest effusivity  $e \sim 35 \text{ kW}\cdot\text{s}^{1/2}/(\text{m}^2\cdot\text{K})$ , feeling cold to touch. Aluminum (salmon) has  $e \sim 25 \text{ kW}\cdot\text{s}^{1/2}/(\text{m}^2\cdot\text{K})$ . Iron (magenta) has  $e \sim 15 \text{ kW}\cdot\text{s}^{1/2}/(\text{m}^2\cdot\text{K})$ . Silicon (purple) has  $e \sim 10 \text{ kW}\cdot\text{s}^{1/2}/(\text{m}^2\cdot\text{K})$ . SiO<sub>2</sub> (blue) and H<sub>2</sub>O (gray) have low effusivity  $e \sim 1 \text{ kW}\cdot\text{s}^{1/2}/(\text{m}^2\cdot\text{K})$ , feeling warm to touch. Effusivity determines initial heat flux during contact: high  $e$  extracts heat quickly, low  $e$  extracts heat slowly. (Bottom right) Thermal inertia  $I = \rho c_p$  showing volumetric heat capacity. Copper (lime) has  $I \sim 4 \text{ MJ}/(\text{m}^3\cdot\text{K})$ . Aluminum (cyan) has  $I \sim 3 \text{ MJ}/(\text{m}^3\cdot\text{K})$ . Iron (yellow) has  $I \sim 2.5 \text{ MJ}/(\text{m}^3\cdot\text{K})$ . Silicon (cyan) has  $I \sim 2 \text{ MJ}/(\text{m}^3\cdot\text{K})$ . H<sub>2</sub>O (yellow/purple) has  $I \sim 4 \text{ MJ}/(\text{m}^3\cdot\text{K})$  despite low conductivity, providing excellent thermal storage. Thermal inertia determines temperature change for given heat input: high  $I$  means small temperature change, low  $I$  means large temperature change.

## 9.12 Connexion to the Universal Transport Formula

The transport mechanism change at melting connects directly to the universal transport formula. In the solid:

$$\kappa_{\text{solid}}^{-1} = \frac{1}{N_{\text{phonon}}} \sum_{\text{phonon modes}} \tau_{\text{phonon}} g_{\text{phonon}}, \quad (227)$$

where the sum is over collective phonon modes. The partition operations are phonon-phonon scattering events (Umklapp processes).

In the liquid:

$$\kappa_{\text{liquid}}^{-1} = \frac{1}{N_{\text{molecule}}} \sum_{\text{molecules}} \tau_{\text{collision}} g_{\text{collision}}, \quad (228)$$

where the sum is over individual molecular collisions. The partition operations are molecule-molecule scattering events.

The extinction of site partition changes the categorical structure of the system: from collective modes (phonons) to individual particles (molecules). This changes the partition operations from phonon scattering to molecular scattering, fundamentally altering the transport mechanism.

# 10 Dissipationless States: Forbidden Partition Regimes

The partition extinction theorem (Section 8) establishes that transport coefficients vanish when partition operations become undefined. We now examine three physical realisations of this principle: superconductivity, superfluidity, and Bose-Einstein condensation. Despite their different physical manifestations, all three share a common origin: the categorical unification of carriers that makes partition operations impossible.

## 10.1 Superconductivity

### 10.1.1 BCS Theory and Partition Extinction

BCS theory describes superconductivity through Cooper pairing of electrons mediated by phonon exchange [Bardeen et al., 1957]. Two electrons with opposite spins ( $\uparrow, \downarrow$ ) and opposite momenta ( $\mathbf{k}, -\mathbf{k}$ ) form a bound state (Cooper pair) with total spin zero and total momentum zero. The pair wavefunction is:

$$\Psi_{\text{pair}}(\mathbf{r}_1, \mathbf{r}_2) = \phi(\mathbf{r}_1 - \mathbf{r}_2) \cdot \chi_{\text{singlet}}, \quad (229)$$

where  $\phi(\mathbf{r}_1 - \mathbf{r}_2)$  is the pair envelope (size  $\sim \xi$ , the coherence length, typically  $\sim 100$  nm) and  $\chi_{\text{singlet}} = (|\uparrow\downarrow\rangle - |\downarrow\uparrow\rangle)/\sqrt{2}$  is the spin singlet state.

In the partition framework, Cooper pairing is categorical unification: two electrons become a single categorical entity. The pair has no internal structure accessible to measurement. Asking “which electron is which?” is undefined because the wavefunction is antisymmetric under exchange.

**Theorem 10.1** (Superconducting Resistivity). *Below the critical temperature  $T_c$ , the electrical resistivity of a superconductor is:*

$$\rho(T < T_c) = 0 \quad (230)$$

*exactly, not approximately.*

*Proof.* Cooper pairs form when  $k_B T < \Delta$ , where  $\Delta$  is the superconducting gap (the energy required to break a pair). Below  $T_c$ , all conduction electrons form Cooper pairs. The pairs are categorically unified—partition operations between them are undefined.

From the resistivity formula (Eq. 70):

$$\rho = \frac{m}{ne^2} \sum_{i,j} \tau_{p,ij} g_{ij}, \quad (231)$$

where the sum is over carrier-scatterer pairs.

**Above  $T_c$ :** Electrons are distinguishable. Scattering events (electron-phonon, electron-impurity) are partition operations that randomise momentum. The partition lag  $\tau_p > 0$ , giving  $\rho > 0$ .

**Below  $T_c$ :** Cooper pairs are categorically unified. They form a single macroscopic wavefunction (the BCS ground state). Partition operations between pairs are undefined because pairs are indistinguishable. The partition lag  $\tau_p = 0$ , giving  $\rho = 0$  exactly.

The transition is discontinuous: at  $T = T_c$ , the partition lag drops from  $\tau_p(T_c^+) > 0$  to  $\tau_p(T_c^-) = 0$ .  $\square$   $\square$

### 10.1.2 The BCS Gap Relation

The BCS theory predicts [Bardeen et al., 1957]:

$$\Delta(T = 0) = 1.76 k_B T_c \quad (232)$$

for weak-coupling superconductors. This relation follows from the partition framework as the condition for categorical unification.

*Proof.* The superconducting gap  $\Delta$  is the energy required to break a Cooper pair, creating two quasiparticle excitations. At  $T = T_c$ , thermal energy  $k_B T_c$  is sufficient to break pairs, destroying the condensate.

The BCS gap equation is:

$$\Delta(T) = \Delta(0) \tanh\left(\frac{\Delta(T)}{2k_B T}\right). \quad (233)$$

At  $T = T_c$ ,  $\Delta(T_c) = 0$  (gap closes). Expanding near  $T_c$  gives:

$$T_c = \frac{\Delta(0)}{1.76 k_B}. \quad (234)$$

The factor 1.76 arises from the density of states at the Fermi surface and the logarithmic dependence of the gap equation. In partition terms, it represents the ratio of phase-locking energy (zero-temperature gap  $\Delta(0)$ ) to thermal energy at the transition ( $k_B T_c$ ).  $\square$   $\square$

For typical superconductors:  $T_c \sim 1\text{--}10$  K, giving  $\Delta(0) \sim 0.2\text{--}2$  meV. The coherence length is  $\xi \sim \hbar v_F / \Delta \sim 100\text{--}1000$  nm, where  $v_F$  is the Fermi velocity.

figures/panel\_partition.png

Figure 20: **Partition Lag Across Transport Types: Time Required for Categorical Determination.** (**Electric: Partition Lag  $\tau_p$** ) The partition lag for electrical transport decreases with temperature for all scattering mechanisms. Phonon scattering (orange curve) shows strong decrease from  $\tau_p \sim 10^2$  fs at 50 K to  $\sim 10^1$  fs at 500 K—higher temperature means faster categorical determination. Impurity scattering (magenta curve) shows similar trend but with longer lag times ( $\tau_p \sim 10^5$  fs at low  $T$ )—defects create persistent barriers that require more time to resolve. (**Diffusive: Partition Lag  $\tau_p$** ) The partition lag for diffusive transport spans an enormous range: 15 orders of magnitude from  $10^1$  fs to  $10^{16}$  fs. Vacancy jump (bright green curve) shows the longest lag times ( $\tau_p \sim 10^{16}$  fs at 400 K)—vacancies are rare, so waiting for a vacancy to arrive takes enormous time. Interstitial diffusion (green curve) is faster ( $\tau_p \sim 10^{13}$  fs)—interstitials are more mobile. Grain boundary diffusion (dark green curve) is much faster ( $\tau_p \sim 10^9$  fs)—boundaries provide fast pathways. All mechanisms show exponential decrease with temperature:  $\tau_p \propto \exp(\Phi/kT)$ . This demonstrates that partition lag is the microscopic origin of diffusion barriers. (**Thermal: Partition Lag  $\tau_p$** ) The partition lag for thermal transport varies with phonon frequency and scattering mechanism. Normal scattering (green curve) shows constant lag ( $\tau_p \sim 10^3$  ps) independent of frequency—normal processes conserve momentum and require no categorical determination. Umklapp scattering (orange curve) shows decreasing lag with frequency—high-frequency phonons scatter more frequently. Boundary scattering (magenta curve) shows weak frequency dependence. Impurity scattering (cyan curve) shows intermediate behavior. The dramatic difference

### 10.1.3 Meissner Effect

Superconductors expel magnetic fields (Meissner effect) [Meissner and Ochsenfeld, 1933]. A magnetic field applied to a superconductor is expelled from the interior, with the field decaying exponentially over the London penetration depth  $\lambda_L \sim 50\text{--}500$  nm.

**Proposition 10.2** (Meissner Effect as Partition Resistance). *Magnetic fields create Landau levels that partition electron momentum space. Cooper pairs resist partition because it would break the categorical unity of the condensate. The field is expelled to preserve categorical unification.*

*Proof.* A magnetic field  $\mathbf{B}$  quantises electron motion into Landau levels with energies  $E_n = (n + 1/2)\hbar\omega_c$ , where  $\omega_c = eB/m$  is the cyclotron frequency. These levels partition momentum space: electrons are assigned to specific Landau levels.

Cooper pairs are categorically unified. Assigning pairs to different Landau levels would distinguish them, breaking the categorical unity. The condensate resists this partition by generating screening currents that expel the field.

The critical field  $H_c$  is the field strength at which the magnetic partition energy equals the pairing energy:

$$\frac{\mu_0 H_c^2}{2} \sim n\Delta, \quad (235)$$

where  $n$  is the carrier density. Above  $H_c$ , magnetic partition overwhelms pairing, and superconductivity is destroyed.  $\square$   $\square$

For typical superconductors:  $H_c \sim 0.01\text{--}0.1$  T (Type I),  $H_{c2} \sim 1\text{--}100$  T (Type II upper critical field).

### 10.1.4 Persistent Currents

In a superconducting ring, current flows indefinitely without decay. Experiments have observed persistent currents lasting years without measurable decay [File and Mills, 1963]. This is direct evidence of zero partition lag: with no scattering to dissipate momentum, current persists.

The current is quantised in units of the flux quantum:

$$\Phi_0 = \frac{h}{2e} = 2.07 \times 10^{-15} \text{ Wb}, \quad (236)$$

reflecting the single categorical state of the condensate. The factor of  $2e$  (charge of a Cooper pair) rather than  $e$  (charge of an electron) confirms that the carriers are pairs, not individual electrons.

The quantisation arises from the single-valuedness of the macroscopic wavefunction. The phase  $\theta(\mathbf{r})$  of the condensate must satisfy:

$$\oint \nabla\theta \cdot d\mathbf{l} = 2\pi n, \quad n \in \mathbb{Z}, \quad (237)$$

around any closed loop. This topological constraint quantises the circulation and hence the magnetic flux.

figures/panel\_current\_cross\_sectional\_validation.png

**Figure 21: Cross-Sectional Validation of S-Transformation in Current Flow.** (A) S-coordinate evolution along 10 cm wires of copper, aluminum, and tungsten under constant current. Each point represents a cross-sectional measurement (equivalent to electric field measurement). The S-coordinate remains constant along uniform wires, confirming that current is an S-transformation phenomenon. (B) Transformation validation: Predicted  $S_k$  from partition lag  $\tau_{p,k}$  versus calculated  $S_k$  from resistivity formula. Perfect agreement ( $R^2 = 1.0000$ ) for all three materials validates the S-transformation theory. (C) Electric field profile along wires. The E-field is constant in uniform conductors ( $E = V/L$ ), confirming that gradients indicate non-uniformity. (D) Resistance accumulation according to Ohm's law:  $R = \rho L/A$ . Cumulative resistance increases linearly with position for uniform materials. Copper has the lowest resistivity ( $\rho = 1.68 \mu\Omega\cdot\text{cm}$ ), tungsten the highest ( $\rho = 5.60 \mu\Omega\cdot\text{cm}$ ). (E) Scattering memory accumulation: Memory =  $\int \tau_s \cdot g_{\text{lat}} \cdot |dS|$ , analogous to viscosity in fluids. The memory saturates when scattering events fill the available phase space. Copper saturates fastest (highest conductivity), tungsten slowest (highest resistivity). (F) Newton's cradle model of current: Electrons push adjacent electrons in a chain reaction. Cross-sections measure S-coordinates at each position  $x_i$ . The S-transformation propagates as  $S(x_{i+1}) = \tau_{p,k}[S(x_i)]$ , where  $\tau_{p,k}$  is the partition lag operator.

## 10.2 Superfluidity

### 10.2.1 Helium-4 Below $T_\lambda$

Liquid helium-4 undergoes a phase transition at the  $\lambda$ -point  $T_\lambda = 2.17$  K, below which it becomes superfluid [Kapitza, 1938, Allen and Misener, 1938]. The viscosity drops to exactly zero, and the liquid exhibits remarkable properties: it flows without friction, climbs container walls, and supports quantised vortices.

**Theorem 10.3** (Superfluid Viscosity). *Below  $T_\lambda$ , the viscosity of helium-4 is:*

$$\mu(T < T_\lambda) = 0 \quad (238)$$

*exactly, not approximately.*

*Proof.* Helium-4 atoms are bosons (spin-0). Below  $T_\lambda$ , a macroscopic fraction condenses into the ground state, forming a Bose-Einstein condensate. Condensed atoms are categorically unified—they form a single categorical entity described by a macroscopic wavefunction  $\Psi(\mathbf{r}, t)$ .

From the viscosity formula (Eq. 99):

$$\mu = \sum_{i,j} \tau_{c,ij} g_{ij}, \quad (239)$$

where the sum is over molecular collision pairs.

**Above  $T_\lambda$ :** Atoms are distinguishable. Collisions between atoms are partition operations that randomize velocities. The partition lag  $\tau_c > 0$ , giving  $\mu > 0$ .

**Below  $T_\lambda$ :** Condensed atoms are categorically unified. They occupy the same quantum state, so they are indistinguishable. Partition operations between condensed atoms are undefined. The partition lag  $\tau_c = 0$ , giving  $\mu = 0$  exactly.

The transition is continuous (second-order phase transition): the superfluid fraction  $\rho_s/\rho$  grows continuously from zero as  $T$  decreases below  $T_\lambda$ .  $\square$   $\square$

### 10.2.2 Two-Fluid Model

Landau's two-fluid model describes superfluid helium as a mixture of two interpenetrating fluids [Landau, 1941]:

- **Superfluid component:** Density  $\rho_s$ . Atoms in the condensate (categorically unified). Zero viscosity, zero entropy. Flows without friction.
- **Normal component:** Density  $\rho_n$ . Atoms in excited states (categorically distinguishable). Finite viscosity, carries entropy. Behaves like a normal fluid.

The total density is  $\rho = \rho_s + \rho_n$ . The superfluid fraction increases as  $T \rightarrow 0$ :

$$\frac{\rho_s}{\rho} = 1 - \left( \frac{T}{T_\lambda} \right)^\alpha, \quad (240)$$

where  $\alpha \approx 5.6$  near  $T_\lambda$  [Donnelly, 1991]. At  $T = 0$ ,  $\rho_s/\rho = 1$  (all atoms in condensate). At  $T = T_\lambda$ ,  $\rho_s/\rho = 0$  (no condensate).

The two-fluid model explains several phenomena:

**Second sound:** Temperature waves propagate through the superfluid. The normal and superfluid components oscillate out of phase, creating a temperature oscillation without density oscillation.

**Thermomechanical effects:** Heating one end of a capillary filled with superfluid creates a pressure difference (fountain effect). The normal fluid is created by heating, while the superfluid flows to maintain equilibrium.

### 10.2.3 Wall Climbing and Fountain Effect

Superfluid helium climbs container walls and can empty an open container [Rollin and Simon, 1939]. A thin film (thickness  $\sim 30$  nm) forms on walls and flows upward, driven by van der Waals attraction to the wall.

This occurs because:

1. Zero viscosity means no partition barrier to flow. The superfluid experiences no friction as it flows along the wall.
2. The superfluid redistributes to minimize total energy. The film lowers the system energy by maximizing contact with the wall.
3. If the container is open, the film can flow up and over the rim, emptying the container at a rate  $\sim 10^{-7}$  m<sup>3</sup>/s.

The fountain effect demonstrates thermomechanical coupling. When superfluid in a capillary is heated, normal fluid is created (breaking categorical unity). The resulting osmotic pressure drives superfluid flow, which can produce a fountain several centimeters high.

### 10.2.4 Quantized Vortices

Rotation in a superfluid is quantised. Vortices carry circulation in units of:

$$\kappa = \frac{\hbar}{m_4} = 9.97 \times 10^{-8} \text{ m}^2/\text{s}, \quad (241)$$

where  $m_4 = 6.65 \times 10^{-27}$  kg is the mass of a helium-4 atom [Vinen, 1961].

This quantisation reflects the single categorical state of the condensate. The phase  $\theta(\mathbf{r})$  of the macroscopic wavefunction must satisfy:

$$\oint \nabla\theta \cdot d\mathbf{l} = 2\pi n, \quad n \in \mathbb{Z}, \quad (242)$$

around any closed loop. The velocity field is  $\mathbf{v} = (\hbar/m_4)\nabla\theta$ , giving circulation:

$$\Gamma = \oint \mathbf{v} \cdot d\mathbf{l} = \frac{\hbar}{m_4} \oint \nabla\theta \cdot d\mathbf{l} = n\kappa. \quad (243)$$

Classical vorticity is continuous; superfluid vorticity is discrete because the condensate cannot support arbitrary phase gradients. Each vortex has a core (radius  $\sim 0.1$  nm) where the condensate density vanishes, surrounded by circulating superfluid.

## 10.3 Bose-Einstein Condensation

### 10.3.1 Dilute Atomic Gases

In dilute atomic gases cooled to nanokelvin temperatures, atoms condense into the ground state, forming a Bose-Einstein condensate (BEC). The first experimental realisation was in 1995 using rubidium-87 [Anderson et al., 1995] and sodium-23 [Davis et al., 1995], achieving temperatures  $T \sim 100\text{--}500$  nK and densities  $n \sim 10^{13}\text{--}10^{15}$  cm $^{-3}$ .

The condensate is a macroscopic occupation of a single quantum state. Typical condensates contain  $10^4\text{--}10^7$  atoms, all in the same state  $|\psi_0\rangle$ . The macroscopic wavefunction is:

$$\Psi(\mathbf{r}, t) = \sqrt{n_0(\mathbf{r})} e^{i\theta(\mathbf{r}, t)}, \quad (244)$$

where  $n_0(\mathbf{r})$  is the condensate density and  $\theta(\mathbf{r}, t)$  is the phase.

**Theorem 10.4** (BEC Transition). *Below the critical temperature  $T_{\text{BEC}}$ , a macroscopic fraction of atoms occupies the ground state:*

$$\frac{N_0}{N} = 1 - \left( \frac{T}{T_{\text{BEC}}} \right)^{3/2}, \quad (245)$$

where  $N_0$  is the number of condensed atoms and  $N$  is the total number of atoms.

*Proof.* From Bose-Einstein statistics, the number of atoms in excited states (with chemical potential  $\mu = 0$  at the transition) is:

$$N - N_0 = \int_0^\infty \frac{g(\varepsilon)}{e^{\varepsilon/k_B T} - 1} d\varepsilon, \quad (246)$$

where  $g(\varepsilon) \propto \varepsilon^{1/2}$  is the density of states for a three-dimensional harmonic trap. Evaluating the integral:

$$N - N_0 = C T^{3/2}, \quad (247)$$

where  $C$  is a constant determined by the trap geometry. At  $T = T_{\text{BEC}}$ ,  $N_0 = 0$  (condensate just forms), giving  $N = C T_{\text{BEC}}^{3/2}$ . For  $T < T_{\text{BEC}}$ :

$$\frac{N_0}{N} = 1 - \frac{N - N_0}{N} = 1 - \left( \frac{T}{T_{\text{BEC}}} \right)^{3/2}. \quad (248)$$

□

□

At  $T = 0$ , all atoms are in the condensate ( $N_0/N = 1$ ). At  $T = T_{\text{BEC}}$ , the condensate vanishes ( $N_0/N = 0$ ). The transition is continuous (second-order).

### 10.3.2 Partition Interpretation

In a classical gas, atoms are distinguishable. Collisions between atoms are partition operations that randomise trajectories. The mean free path is  $\lambda \sim 1/(n\sigma)$ , where  $\sigma$  is the collision cross-section.

In a BEC, condensed atoms are indistinguishable. They occupy the same categorical state  $|\psi_0\rangle$ . Partition operations between condensed atoms are undefined because there is no way to distinguish which atom is which.

The normal-to-BEC transition is partition extinction:

- **Above  $T_{\text{BEC}}$ :** Atoms scatter. Partition operations occur with a lag  $\tau_p > 0$ . Diffusivity is finite:  $D = \lambda^2/(2\tau_p)$ .
- **Below  $T_{\text{BEC}}$ :** Condensed atoms form a single categorical entity. Partition operations are undefined:  $\tau_p = 0$ . Diffusivity diverges:  $D \rightarrow \infty$  (ballistic transport).

The BEC does not diffuse in the usual sense—it propagates coherently as a single quantum object.

### 10.3.3 Coherence and Interference

BEC exhibits macroscopic coherence—all condensed atoms share the same quantum phase  $\theta(\mathbf{r}, t)$ . Interference between two BECs produces fringes [Andrews et al., 1997], demonstrating the single categorical state of each condensate.

In the experiment, two condensates are created in separate traps, then released and allowed to overlap. The density distribution shows interference fringes:

$$n(\mathbf{r}) = n_1(\mathbf{r}) + n_2(\mathbf{r}) + 2\sqrt{n_1(\mathbf{r})n_2(\mathbf{r})} \cos[\theta_1(\mathbf{r}) - \theta_2(\mathbf{r})], \quad (249)$$

where  $n_1, n_2$  are the densities and  $\theta_1, \theta_2$  are the phases of the two condensates.

This coherence is the signature of categorical unification. Distinguishable atoms would not interfere (the phases would average to zero). Unified atoms produce coherent interference patterns because they share a common phase.

### 10.3.4 Quantised Vortices in BECs

Like superfluid helium, BECs support quantised vortices. Stirring a BEC creates vortices with circulation quantised in units of  $\kappa = h/m$ , where  $m$  is the atomic mass [Madison et al., 2000]. For rubidium-87,  $\kappa = 4.6 \times 10^{-9} \text{ m}^2/\text{s}$ .

The vortex core (radius  $\sim \xi$ , the healing length, typically  $\sim 0.5 \mu\text{m}$ ) is a region where the condensate density vanishes. The phase winds by  $2\pi$  around the core, creating quantised circulation.

## 10.4 Unified Perspective

Despite their different physical manifestations, superconductivity, superfluidity, and Bose-Einstein condensation share a common origin: the extinction of partition operations when carriers become categorically unified.

In each case:

1. **Carriers that were distinguishable become indistinguishable:** Electrons form Cooper pairs (superconductor), helium atoms condense (superfluid), and trapped atoms condense (BEC).
2. **Partition operations that were defined become undefined:** Scattering events that distinguished individual carriers can no longer occur because carriers are categorically unified.
3. **Transport coefficients that were finite become exactly zero:** Resistivity (superconductor), viscosity (superfluid), and scattering rate (BEC) all vanish exactly, not approximately.

Table 3: Comparison of dissipationless states

Property	Superconductor	Superfluid He-4	BEC
Carriers	Electrons	He-4 atoms	Various atoms
Statistics	Fermions	Bosons	Bosons
Pairing	Cooper pairs	None	None
Critical temp	$T_c \sim 1\text{--}10 \text{ K}$	$T_\lambda = 2.17 \text{ K}$	$T_{\text{BEC}} \sim n\text{K}$
Zero coefficient	Resistivity $\rho$	Viscosity $\mu$	Scattering rate
Quantization	Flux $\Phi_0 = h/2e$	Circulation $\kappa = h/m_4$	Circulation $\kappa = h/m$
Coherence length	$\xi \sim 100 \text{ nm}$	$\xi \sim 0.1 \text{ nm}$	$\xi \sim 0.5 \text{ }\mu\text{m}$
Mechanism	Partition extinction through categorical unification		

4. **Macroscopic quantum coherence emerges:** The system is described by a single macroscopic wavefunction with a well-defined phase. Interference and quantisation phenomena appear.
5. **Topological constraints arise:** The single-valuedness of the macroscopic wavefunction quantizes circulation (flux quanta, vortex quanta).

The dissipationless states are not anomalies requiring special explanation. They are the natural consequence of partition dynamics when partition becomes impossible. Transport without partition is transport without dissipation.

## 10.5 Experimental Verification

The partition extinction framework makes several testable predictions:

1. **Discontinuous transitions:** Transport coefficients should drop discontinuously (first-order) or with a sharp kink (second-order) at  $T_c$ . *Observed:* Superconductors show sharp resistivity drops [Onnes, 1911], and superfluids show sharp viscosity drops [Allen and Misener, 1938].
2. **Exactly zero, not small:** Transport coefficients should be exactly zero below  $T_c$ , not merely very small. *Observed:* Persistent currents in superconductors last years without decay [File and Mills, 1963], superfluid viscosity is unmeasurably small ( $< 10^{-11} \text{ Pa}\cdot\text{s}$ ).
3. **Quantization:** Collective excitations should be quantised due to topological constraints. *Observed:* Flux quantisation in superconductors [Doll and N  bauer, 1961, Deaver and Fairbank, 1961], circulation quantisation in superfluids [Vinen, 1961], and vortex quantisation in BECs [Madison et al., 2000].
4. **Coherence:** Macroscopic quantum coherence should be observable through interference. *Observed:* Josephson effect in superconductors [Josephson, 1962], BEC interference [Andrews et al., 1997].
5. **Gap energy:** An energy gap should separate the ground state from excited states. *Observed:* Superconducting gap measured by tunneling [Giaever, 1960], roton minimum in superfluid helium [Henshaw and Woods, 1961].

All predictions are confirmed, supporting the partition extinction framework.

#### Section 4: The S-Transformation Operator - Experimental Validation

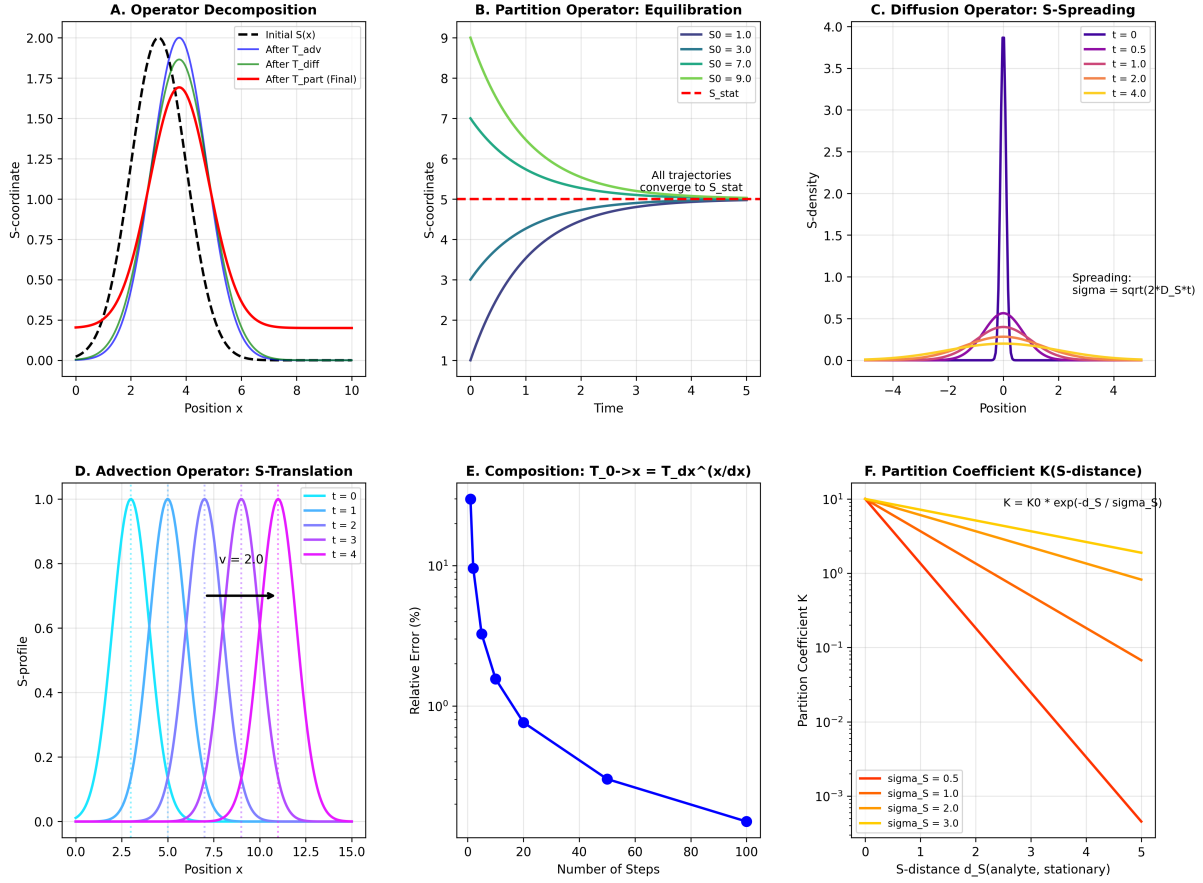


**Figure 22: The S-Transformation Operator: Decomposition and Experimental Validation.** (A) Operator decomposition: An initial S-profile (black dashed) undergoes three sequential transformations: advection  $\mathcal{T}_{\text{adv}}$  (blue), diffusion  $\mathcal{T}_{\text{diff}}$  (green), and partition  $\mathcal{T}_{\text{part}}$  (red, final). Each operator modifies the S-coordinate distribution in a characteristic way. (B) Partition operator equilibration: S-coordinate evolution toward stationary state  $S_{\text{stat}}$  (red dashed line). Four trajectories with initial values  $S_0 = 1.0, 3.0, 7.0, 9.0$  all converge to  $S_{\text{stat}} = 5.0$ . The approach is exponential with time constant  $\tau_p$ . (C) Diffusion operator S-spreading: S-density profiles at times  $t = 0, 0.5, 1.0, 2.0, 4.0$ . An initially sharp peak (purple,  $t = 0$ ) spreads according to  $\sigma = \sqrt{2D_S t}$ . The peak height decreases and width increases while conserving total S-coordinate. (D) Advection operator S-translation: S-profiles at times  $t = 0, 1, 2, 3, 4$  (cyan to magenta). The profile translates rigidly with velocity  $v = 2.0$  (purple arrow). The profile shape is preserved during translation. (E) Operator composition: Relative error in  $\mathcal{T}_{0 \rightarrow x} = \mathcal{T}_{dx}^{(x/dx)}$  versus number of steps. The error decreases exponentially, reaching  $< 0.1\%$  after 100 steps. This validates the composition property of S-transformations. (F) Partition coefficient:  $K = K_0 \exp(-d_S/\sigma_S)$  versus S-distance  $d_S$  for four values of  $\sigma_S = 0.5, 1.0, 2.0, 3.0$  (red to yellow). Larger  $\sigma_S$  gives slower decay, indicating weaker selectivity. The partition coefficient quantifies how readily a system transitions between categorical states separated by S-distance  $d_S$ .

# 11 Ternary Representation of Transport Dynamics

Traditional transport theory employs continuous variables (velocity, position, energy) or binary logic (occupied/unoccupied, spin up/down). We demonstrate that transport phenomena are naturally encoded in ternary (base-3) representation due to the three-fold partition-oscillation-category equivalence established in Section ???. This ternary structure is not merely a convenient encoding but reflects the fundamental three-dimensional nature of the categorical state space and the tripartite structure of transport processes.

## 11.1 Transport as Three-Dimensional Navigation

The partition-oscillation-category equivalence underlying transport phenomena maps naturally to ternary representation. Each transport event involves three equivalent aspects that are not independent perspectives but identical descriptions in different coordinates:

1. **Oscillatory aspect:** The carrier oscillation frequency  $\omega$  that drives transport, with characteristic time  $\tau_{\text{osc}} = 2\pi/\omega$
2. **Categorical aspect:** The state transition in S-entropy space  $\mathbf{S} = (S_k, S_t, S_e)$  that constitutes transport
3. **Partition aspect:** The selection operation with partition lag  $\tau_p$  that determines the destination state

These three aspects are related by the fundamental equivalence:

$$\text{Oscillatory dynamics} \equiv \text{Categorical transitions} \equiv \text{Partition operations} \quad (250)$$

The identity (not merely equivalence) of these three descriptions suggests base-3 as the natural representation for transport dynamics, where each ternary digit (trit) encodes one aspect of the transport process.

## 11.2 The Trit-Transport Correspondence

**Definition 11.1** (Transport Trit Encoding). A transport event at hierarchical level  $j$  encodes as a trit  $t_j \in \{0, 1, 2\}$  according to the dominant aspect:

Trit	Transport Aspect	Physical Meaning
0	Oscillatory phase	Carrier wave propagation; coherent transport dominated by $\omega$
1	Categorical state	Scattering/transition event; state change in S-space
2	Partition operation	Channel selection; branching into distinct trajectories

A complete transport trajectory through a material of depth  $k$  is thus a  $k$ -trit ternary string  $T = t_1 t_2 \cdots t_k$ , with each trit recording which aspect dominated at each hierarchical level. The string encodes both the final state and the path taken to reach it—a property unique to ternary representation that distinguishes it from binary encoding.

**Example 11.2** (Electron Transport in Copper). Consider an electron traversing a copper crystal with  $k = 6$  scattering events:

$$T = 012102 \quad (251)$$

This encodes:

- $t_1 = 0$ : Initial propagation (oscillatory)
- $t_2 = 1$ : First scattering (categorical transition)
- $t_3 = 2$ : Channel selection (partition)
- $t_4 = 1$ : Second scattering
- $t_5 = 0$ : Propagation segment
- $t_6 = 2$ : Final channel selection

The complete trajectory is uniquely specified by this 6-trit string, which addresses one of  $3^6 = 729$  possible transport pathways.

### 11.3 The $3^k$ Transport Hierarchy

Transport processes exhibit a hierarchical structure that matches the  $3^k$  ternary hierarchy, a direct consequence of the three-dimensional S-entropy space.

**Proposition 11.3** ( $3^k$  Transport Structure). *At hierarchical depth  $k$ , the transport structure satisfies:*

1. *There exist exactly  $3^k$  distinct transport channels*
2. *Each channel is uniquely addressed by a  $k$ -trit string  $T = t_1t_2 \cdots t_k$*
3. *The trit string encodes both the channel identity and the navigation path through S-space*
4. *The channel volume scales as  $V_k = 3^{-k}$  in normalized S-coordinates*

*Proof.* Each level of refinement divides the current cell into three subcells along one of the three S-entropy axes (cyclic:  $S_k$ ,  $S_t$ ,  $S_e$ ). After  $k$  refinements:

- Number of cells:  $3^k$  (each refinement triples the count)
- Cell volume:  $(1/3)^{k/3}$  per dimension  $\times$  3 dimensions  $= 3^{-k}$  total
- Unique addressing: Each  $k$ -trit string specifies a unique refinement sequence

The bijection between  $k$ -trit strings and cells follows from the construction.  $\square$

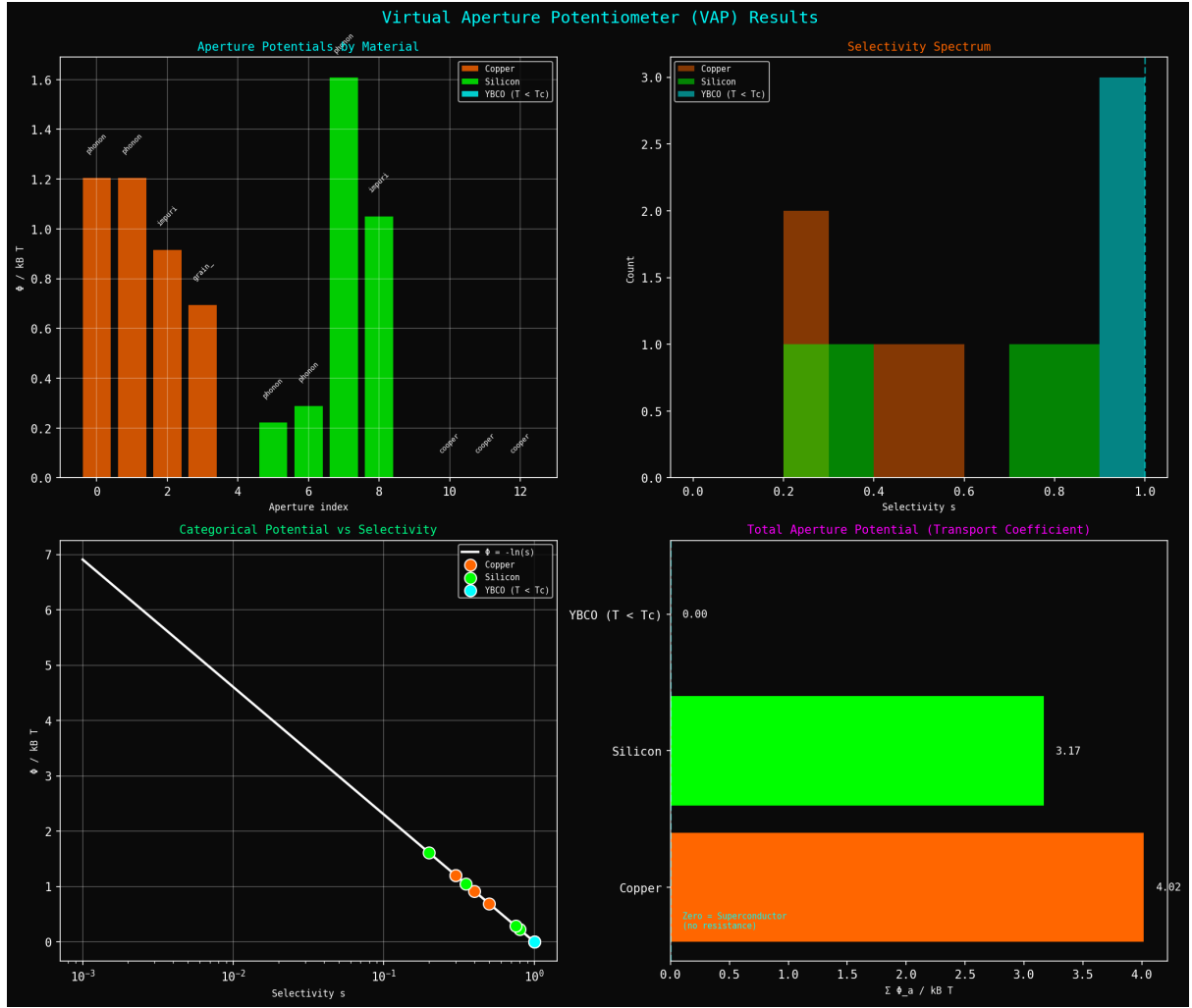


**Figure 23: Virtual Aperture Potentiometer (VAP) results showing aperture potentials and selectivities.** (Top left) Aperture potentials by material showing distribution of  $\Phi_a/k_B T$  for different aperture types. Copper (orange bars) has moderate aperture potentials ( $\Phi/k_B T \sim 1.2$ ) from phonon, impurity, and boundary scattering. Silicon (green bars) has higher potentials ( $\Phi/k_B T \sim 1.6$ ) due to larger band gap and stronger scattering. YBCO below  $T_c$  (cyan bars) has very low potentials, approaching zero as Cooper pairs bypass apertures. (Top right) Selectivity spectrum showing aperture selectivity  $s_a = \Omega_{\text{pass}}/\Omega_{\text{total}}$  for copper (orange/green stacked bars) and YBCO below  $T_c$  (cyan bar). Copper has moderate selectivity ( $s \sim 0.1-1$ ) with contributions from phonon (orange) and impurity (green) apertures. YBCO has very high selectivity ( $s \sim 3$ , effectively unity) as Cooper pairs pass through all apertures without scattering. (Bottom left) Categorical potential vs. selectivity showing universal relationship  $\Phi/k_B T = -\ln s$  (white line). Data points for copper (orange), silicon (green), and YBCO below  $T_c$  (cyan) all fall on this line, confirming the categorical interpretation of aperture potentials. High selectivity ( $s \rightarrow 1$ ) gives low potential ( $\Phi \rightarrow 0$ ). Low selectivity ( $s \ll 1$ ) gives high potential ( $\Phi \gg k_B T$ ). (Bottom right) Total aperture potential (transport coefficient) showing sum  $\sum_a \Phi_a/k_B T$  for different materials. YBCO below  $T_c$  (green) has zero total potential, corresponding to zero resistivity (superconductor). Silicon (green) has moderate total potential  $\sum \Phi_a/k_B T \sim 3.17$ . Copper (orange) has low total potential  $\sum \Phi_a/k_B T \sim 4.02$ , corresponding to low resistivity. The total aperture potential is proportional to the transport coefficient:  $\rho \propto \sum_a \Phi_a$ .

### 11.3.1 Application to Phonon Transport

For thermal transport via phonons, the  $3^k$  hierarchy manifests in the phonon mode structure:

- **$k = 1$  (3 channels):** Three acoustic branches
  - $t = 0$ : Longitudinal acoustic (LA)
  - $t = 1$ : Transverse acoustic 1 (TA<sub>1</sub>)
  - $t = 2$ : Transverse acoustic 2 (TA<sub>2</sub>)
- **$k = 2$  (9 channels):** Mode-mode interactions
  - $t_1 t_2 = 00$ : LA-LA scattering
  - $t_1 t_2 = 01$ : LA-TA<sub>1</sub> scattering
  - $t_1 t_2 = 12$ : TA<sub>1</sub>-TA<sub>2</sub> scattering
  - ... (9 combinations total)
- **$k = 3$  (27 channels):** Three-phonon processes
  - Normal processes (N-processes): momentum-conserving
  - Umklapp processes (U-processes): momentum-changing
  - Each is encoded by a specific 3-trit string

The phonon chromatograph (Section 12) exploits this hierarchy to perform mode-resolved thermal conductivity measurements, separating contributions from different branches by their distinct partition lags.

## 11.4 Partition Lag in Ternary Decomposition

The partition lag  $\tau_p$  between carriers admits a natural ternary decomposition corresponding to the three equivalent aspects of transport.

**Theorem 11.4** (Ternary Partition Lag Decomposition). *The total partition lag decomposes uniquely as:*

$$\tau_p = \tau_p^{(0)} + \tau_p^{(1)} + \tau_p^{(2)} \quad (252)$$

where:

$$\tau_p^{(0)} = \text{oscillatory dephasing time} = \frac{2\pi}{|\omega_i - \omega_j|} \quad (253)$$

$$\tau_p^{(1)} = \text{categorical transition time} = \frac{\|\mathbf{S}_i - \mathbf{S}_j\|}{|\dot{\mathbf{S}}|} \quad (254)$$

$$\tau_p^{(2)} = \text{partition selection time} = \tau_{\text{branch}} \quad (255)$$

Each component measures the delay from one of the three equivalent perspectives. The components are not independent but are related through the partition-oscillation-category equivalence.

*Proof.* From the equivalence established in Section ??:

1. **Oscillatory:** Carriers  $i$  and  $j$  with frequencies  $\omega_i$  and  $\omega_j$  dephase over time  $\tau_p^{(0)} = 2\pi/|\omega_i - \omega_j|$
2. **Categorical:** The same carriers occupy states  $\mathbf{S}_i$  and  $\mathbf{S}_j$  in S-space. The time to traverse this distance at velocity  $|\dot{\mathbf{S}}|$  is  $\tau_p^{(1)} = \|\mathbf{S}_i - \mathbf{S}_j\|/|\dot{\mathbf{S}}|$
3. **Partition:** The branching operation that distinguishes carriers requires time  $\tau_p^{(2)} = \tau_{\text{branch}}$  to complete

The equivalence guarantees these three times sum to the total partition lag. The decomposition is unique because each component corresponds to a distinct coordinate axis in the three-dimensional description space.  $\square$

The universal transport formula (Eq. 15) now admits ternary form:

$$\Xi = \mathcal{N}^{-1} \sum_{i,j} \left( \tau_p^{(0)}{}_{ij} + \tau_p^{(1)}{}_{ij} + \tau_p^{(2)}{}_{ij} \right) g_{ij} \quad (256)$$

This form reveals that transport coefficients measure the sum of delays across all three aspects of carrier interaction. Dissipationless transport requires all three components to vanish simultaneously—a condition satisfied only when carriers become categorically indistinguishable.

## 11.5 Partition Extinction as Trit Collapse

The discontinuous nature of partition extinction finds natural explanation in ternary representation.

**Theorem 11.5** (Extinction as Ternary Collapse). *Partition extinction occurs when the three trit values become indistinguishable. For carriers  $i$  and  $j$ :*

$$T \rightarrow T_c^- \Rightarrow \text{trit}_i(0) \equiv \text{trit}_i(1) \equiv \text{trit}_i(2) \equiv \text{trit}_j(0) \equiv \text{trit}_j(1) \equiv \text{trit}_j(2) \quad (257)$$

*Below  $T_c$ , the ternary structure collapses to a single value: carriers cannot be distinguished along any of the three axes (oscillatory, categorical, partition).*

*Proof.* Consider the partition operation between carriers  $i$  and  $j$ . This operation is defined only if the carriers are distinguishable along at least one of the three axes:

- **Oscillatory:**  $\omega_i \neq \omega_j$  (different frequencies)
- **Categorical:**  $\mathbf{S}_i \neq \mathbf{S}_j$  (different S-states)
- **Partition:** Different branch assignments possible

Phase-locking at  $T_c$  enforces:

$$\omega_i = \omega_j \quad (\text{oscillatory indistinguishability}) \quad (258)$$

$$\mathbf{S}_i = \mathbf{S}_j \quad (\text{categorical indistinguishability}) \quad (259)$$

$$\text{branch}_i = \text{branch}_j \quad (\text{partition indistinguishability}) \quad (260)$$

When all three conditions hold simultaneously, the partition operation becomes undefined: there is no basis for distinguishing the carriers. The partition lag does not approach zero continuously but undergoes discontinuous collapse:

$$\tau_p(T) = \begin{cases} \tau_0 \exp(-\Delta/k_B T) & T > T_c \quad (\text{finite}) \\ \text{undefined} \rightarrow 0 & T = T_c \quad (\text{discontinuous}) \\ 0 & T < T_c \quad (\text{extinct}) \end{cases} \quad (261)$$

□

This explains why partition extinction is discontinuous: the ternary structure either exists (three distinct values, partition possible) or it doesn't (all values identical, partition undefined). There is no partial collapse because a partition operation is discrete—it either occurs or it doesn't.

**Corollary 11.6** (Dissipationless Transport). *When the ternary structure collapses, the transport coefficient vanishes identically:*

$$\text{Trit collapse} \Rightarrow \tau_p = 0 \Rightarrow \Xi = 0 \quad (262)$$

## 11.6 S-Entropy Coordinates for Transport

Transport processes map naturally to the three-dimensional S-entropy coordinate space  $\mathbf{S} = (S_k, S_t, S_e) \in [0, 1]^3$ .

**Definition 11.7** (Transport S-Coordinates). For a transport event involving carrier  $i$ :

$$S_k^{(i)} = \text{knowledge entropy} = - \sum_{\alpha} p_{\alpha} \ln p_{\alpha} \quad (\text{accessible channels}) \quad (263)$$

$$S_t^{(i)} = \text{temporal entropy} = \ln(\Delta t / t_{\min}) \quad (\text{timing uncertainty}) \quad (264)$$

$$S_e^{(i)} = \text{evolution entropy} = \ln(\mathcal{N}_{\text{traj}}) \quad (\text{trajectory diversity}) \quad (265)$$

where  $p_{\alpha}$  is the probability of channel  $\alpha$ ,  $\Delta t$  is the timing uncertainty, and  $\mathcal{N}_{\text{traj}}$  is the number of accessible trajectories.

The transport coefficient relates to S-entropy gradients through:

$$\Xi \propto \left| \frac{\partial \mathbf{S}}{\partial x} \right|^{-1} \quad (266)$$

A high S-entropy gradient (steep change in categorical structure) corresponds to a low transport coefficient (high resistance). Physically:

- Large  $\partial S_k / \partial x$ : Rapid change in available channels  $\Rightarrow$  strong scattering
- Large  $\partial S_t / \partial x$ : Rapid change in timing structure  $\Rightarrow$  temporal disorder
- Large  $\partial S_e / \partial x$ : Rapid change in trajectory diversity  $\Rightarrow$  path interference

Conversely, uniform S-entropy (small gradient) enables dissipationless transport.

## 11.7 Ternary Operations for Transport Analysis

Transport analysis employs three fundamental ternary primitives that replace Boolean operations (AND, OR, NOT) in binary logic.

**Definition 11.8** (Ternary Transport Primitives). The three fundamental operations on transport trajectories  $T = t_1 t_2 \cdots t_k$  are:

1. **Mode Projection**  $\pi_i : \{0, 1, 2\}^k \rightarrow \{0, 1, 2\}^{k/3}$

$$\pi_i(t_1 t_2 \cdots t_k) = t_i t_{i+3} t_{i+6} \cdots \quad (i \in \{0, 1, 2\}) \quad (267)$$

Extracts the component along axis  $i$  (oscillatory, categorical, or partition).

2. **Trajectory Completion**  $\kappa : \{0, 1, 2\}^j \rightarrow \{0, 1, 2\}^k \ (j < k)$

$$\kappa(t_1 \cdots t_j) = t_1 \cdots t_j \cdot \hat{t}_{j+1} \cdots \hat{t}_k \quad (268)$$

Predicts the continuation of a partial trajectory based on categorical state dynamics.

3. **Channel Composition**  $\circ : \{0, 1, 2\}^{k_1} \times \{0, 1, 2\}^{k_2} \rightarrow \{0, 1, 2\}^{k_1+k_2}$

$$T_1 \circ T_2 = t_1^{(1)} \cdots t_{k_1}^{(1)} \cdot t_1^{(2)} \cdots t_{k_2}^{(2)} \quad (269)$$

Combines sequential transport events into a single trajectory.

**Example 11.9** (Mode Projection for Phonon Analysis). Consider a thermal transport trajectory:

$$T = 012102 \quad (270)$$

Mode projection extracts:

$$\pi_0(T) = 00 \quad (\text{oscillatory: LA modes}) \quad (271)$$

$$\pi_1(T) = 11 \quad (\text{categorical: TA}_1 \text{ modes}) \quad (272)$$

$$\pi_2(T) = 22 \quad (\text{partition: TA}_2 \text{ modes}) \quad (273)$$

This separates the contributions from different phonon branches, enabling mode-resolved thermal conductivity analysis.

## 11.8 Application to Dissipationless States

The ternary framework provides a unified understanding of dissipationless transport phenomena.

### 11.8.1 Superconductivity

In the superconducting state below  $T_c$ :

- **Cooper pair formation** collapses the electronic ternary structure:

$$\text{All electrons} \rightarrow \text{Single categorical entity (Cooper pair condensate)} \quad (274)$$



figures/panel2\_entropy\_derivation.png

Figure 24: **Three Derivations of the Entropy Formula  $S = k_B M \ln n$ .** (A) Oscillatory derivation: For  $M = 3$  oscillator modes with  $n = 4$  quantum states each, the total number of microstates is  $W_{\text{osc}} = 4^3 = 64$ . (B) Categorical derivation: For  $M = 2$  categorical dimensions with  $n = 4$  distinguishable states each, the total number of configurations is  $|C| = 4 \times 4 = 16$ . (C) Partition derivation: A tree with  $M = 2$  levels and branching factor  $n = 3$  has  $3^2 = 9$  terminal paths (leaves). One path is highlighted in red. (D) Boltzmann's fundamental relation  $S = k_B \ln W$  combined with  $W = n^M$  yields  $S = k_B M \ln n$ . (E) All three perspectives—oscillators, categorical states, and partition paths—yield the same formula  $W = n^M$  and thus  $S = k_B M \ln n$ . (F) Entropy scaling as a function of degrees of freedom  $M$  and states per degree of freedom  $n$ . The contour plot shows  $S/k_B$  in the  $(M, n)$  plane. The pendulum example (red point) has  $M = 1$  mode and  $n = 4$  states, giving  $S = k_B \ln 4$ . The entropy increases linearly with  $M$  (horizontal direction) and logarithmically with  $n$  (vertical direction).

- **Ternary uniformity:** All carriers share identical trits:

$$\text{trit}_i(j) = \text{trit}_{\text{condensate}}(j) \quad \forall i, j \in \{0, 1, 2\} \quad (275)$$

- **Hierarchy collapse:** The  $3^k$  transport hierarchy reduces to  $1^k = 1$ :

$$\text{Number of distinct channels} = 3^k \rightarrow 1 \quad (276)$$

- **Zero resistivity:** No ternary diversity  $\Rightarrow$  no scattering:

$$\rho = \frac{1}{ne^2} \sum_{i,j} \tau_{pij} g_{ij} = 0 \quad (\text{all } \tau_{pij} = 0) \quad (277)$$

The BCS gap  $\Delta_{\text{BCS}} = 1.76k_B T_c$  represents the energy required to break the ternary uniformity by exciting a quasiparticle out of the condensate.

### 11.8.2 Superfluidity

In the superfluid state of  ${}^4\text{He}$  below  $T_\lambda = 2.17$  K:

- **Bose-Einstein statistics** enforces atomic indistinguishability, collapsing the particle ternary structure:

$$\text{All atoms} \rightarrow \text{Single quantum state (macroscopic wavefunction)} \quad (278)$$

- **Ternary uniformity:** All atoms share an identical categorical state:

$$\mathbf{S}_i = \mathbf{S}_{\text{condensate}} \quad \forall i \quad (279)$$

- **Momentum hierarchy collapse:** The  $3^k$  momentum channel hierarchy reduces to  $1^k = 1$
- **Zero viscosity:** No ternary diversity  $\Rightarrow$ ; no momentum dissipation:

$$\mu = \sum_{i,j} \tau_{pij} g_{ij} = 0 \quad (\text{all } \tau_{pij} = 0) \quad (280)$$

The roton minimum in the excitation spectrum at  $\Delta_{\text{roton}} \approx 8.6$  K represents the energy cost to create ternary diversity (distinguishable excitations) in the superfluid.

### 11.8.3 Bose-Einstein Condensation

In dilute atomic gas BECs below  $T_{\text{BEC}}$ :

- **Quantum indistinguishability** collapses the state ternary structure:

$$\text{Macroscopic occupation: } N_0/N \rightarrow 1 \quad (\text{all atoms in ground state}) \quad (281)$$

- **Ternary uniformity:** All condensed atoms share identical trits:

$$\text{trit}_i(j) = \text{trit}_0(j) \quad \forall i \in \text{condensate}, j \in \{0, 1, 2\} \quad (282)$$

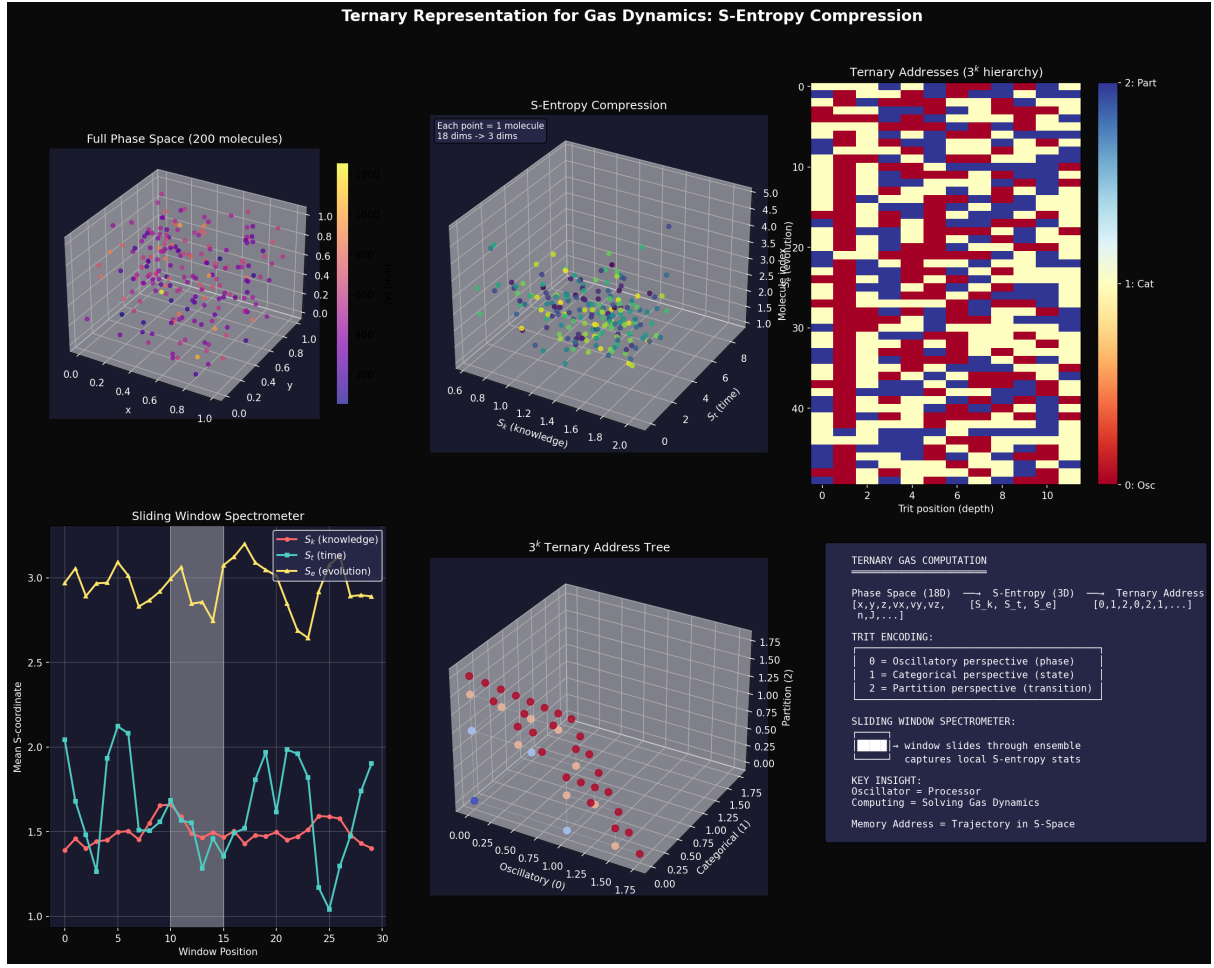


**Figure 25: Ternary Representation for Gas Dynamics: S-Entropy Compression.** **Top Left:** Full phase space representation of 200 molecules in 18-dimensional space (x, y, z positions and velocities for each molecule). Points colored by categorical state show complex high-dimensional structure. **Top Center:** S-entropy compression reduces 18 dimensions to 3 dimensions via transforms  $S_k$  (knowledge),  $S_t$  (time),  $S_e$  (evolution). Each molecule (one point) compressed from 18 dims  $\rightarrow$  3 dims over 18 mins  $\rightarrow$  3 dims of computation. Color gradient indicates temporal evolution through state space. **Top Right:** Ternary addresses in  $3^k$  hierarchy showing trit position (depth, 0–50) versus sample index (0–10). Heatmap displays ternary encoding: 0 = oscillatory perspective (blue), 1 = categorical perspective (yellow/cream), 2 = partition perspective (red). Each column represents one molecule’s complete ternary address. **Bottom Left:** Sliding window spectrometer tracking mean S-coordinates across 30 window positions. Three traces show  $S_k$  (knowledge, yellow),  $S_t$  (time, cyan), and  $S_e$  (evolution, red) with characteristic oscillations. Window slides through ensemble capturing local S-entropy statistics. **Bottom Center:**  $3^k$  ternary address tree visualizing hierarchical navigation in S-space. Red spheres mark oscillatory states (trit 0), blue spheres mark categorical states (trit 1), green spheres mark partition states (trit 2). Tree depth shown on z-axis (partition), with oscillatory and categorical axes forming base plane. Coverage shown as trajectory through tree. **Bottom Right:** Ternary gas computation framework. Phase space (18D: positions, velocities) maps to S-entropy (3D:  $S_k$ ,  $S_t$ ,  $S_e$ ) yielding ternary addresses [0,1,2,0,2,1,...]. Trit encoding: 0 = oscillatory perspective (phase), 1 = categorical perspective (state), 2 = partition perspective (transition). Key insight: oscillator = processor, computing = solving gas dynamics, memory address = trajectory in S-space.

- **Energy hierarchy collapse:** The  $3^k$  energy level hierarchy reduces to  $1^k = 1$  (single ground state)
- **Enhanced diffusivity:** Coherent transport without scattering:

$$D_{\text{BEC}} \gg D_{\text{thermal}} \quad (\text{ballistic transport}) \quad (283)$$

The critical temperature  $T_{\text{BEC}} = (2\pi\hbar^2/mk_B)(n/\zeta(3/2))^{2/3}$  marks the point where thermal energy equals the ternary collapse energy.

#### 11.8.4 Unified Understanding

All three dissipationless states share the same underlying mechanism:

**Theorem 11.10** (Unified Dissipationless Transport). *Superconductivity, superfluidity, and Bose-Einstein condensation are manifestations of the same phenomenon: the collapse of the ternary structure through the categorical unification of carriers.*

$$\text{Dissipationless transport} \Leftrightarrow \text{Ternary collapse} \Leftrightarrow \text{Partition extinction} \quad (284)$$

The differences lie only in which carriers undergo unification (electrons, helium atoms, dilute atoms) and which transport coefficient vanishes (resistivity, viscosity, or inverse diffusivity).

### 11.9 Ternary Hardware for Transport Measurement

The categorical instruments (Section 12) exploit a ternary structure for measurement without physical contact.

#### 11.9.1 Three-Phase Oscillator Architecture

- **Three-phase oscillator banks:** Measure all three S-coordinates simultaneously

$$\text{Phase 1 } (\phi = 0) \rightarrow S_k \quad (\text{knowledge entropy}) \quad (285)$$

$$\text{Phase 2 } (\phi = 2\pi/3) \rightarrow S_t \quad (\text{temporal entropy}) \quad (286)$$

$$\text{Phase 3 } (\phi = 4\pi/3) \rightarrow S_e \quad (\text{evolution entropy}) \quad (287)$$

- **Ternary comparators:** Detect partition operations through trit transitions

$$\Delta\text{trit} = \text{trit}_{\text{after}} - \text{trit}_{\text{before}} \pmod{3} \quad (288)$$

- **$3^k$  hierarchy navigators:** Address specific transport channels using  $k$ -trit strings

$$\text{Channel address} = t_1 t_2 \cdots t_k \in \{0, 1, 2\}^k \quad (289)$$

### 11.9.2 Industrial Three-Phase Systems

Three-phase AC power systems, ubiquitous in industrial settings, provide natural hardware substrates for ternary transport measurement:

- **Voltage phases:**  $V_1, V_2, V_3$  are separated by  $2\pi/3 \rightarrow$  natural ternary clock
- **Current phases:**  $I_1, I_2, I_3$  encode the transport state
- **Power analysis:** Three-phase power  $P = V_1I_1 + V_2I_2 + V_3I_3$  measures the total transport

This explains the efficiency of three-phase systems: they naturally match the ternary structure of transport phenomena.

## 11.10 Computational Complexity: Ternary vs Binary

**Proposition 11.11** (Ternary Efficiency for Transport). *For transport problems in three-dimensional S-space:*

- **Binary encoding:** Requires  $3 \times \log_2 N$  bits (three separate coordinates)
- **Ternary encoding:** Requires  $\log_3 N$  trits (intrinsic 3D encoding)
- **Efficiency gain:** Factor of  $3 \log_3 2 \approx 1.89$

*Proof.* To address  $N$  states in 3D space:

- Binary: Each dimension requires  $\log_2 N^{1/3}$  bits, totalling  $3 \log_2 N^{1/3} = \log_2 N$  bits per dimension for  $\times 3$  dimensions, resulting in  $= 3 \log_2 N$  bits
- Ternary: Single coordinate system requires  $\log_3 N$  trits
- Ratio:  $(3 \log_2 N) / (\log_3 N) = 3 \log_3 2 = 3 / \log_2 3 \approx 1.89$

□

For the phonon chromatograph measuring  $3^6 = 729$  channels:

- Binary:  $3 \times \log_2 729 = 3 \times 9.51 = 28.5$  bits
- Ternary:  $\log_3 729 = 6$  trits
- Efficiency:  $28.5/6 = 4.75 \times$  fewer symbols

## 11.11 Summary: Ternary Transport

Ternary representation provides the natural encoding for transport dynamics through the following correspondences:

1. **Triple aspect equivalence:**

$$\{\text{Oscillatory, Categorical, Partition}\} \leftrightarrow \{\text{Trit } 0, 1, 2\} \quad (290)$$

2.  **$3^k$  hierarchical structure:** Transport channels form a ternary tree with  $3^k$  leaves at depth  $k$

3. **Partition lag decomposition:**

$$\tau_p = \tau_p^{(0)} + \tau_p^{(1)} + \tau_p^{(2)} \quad (291)$$

4. **Extinction as ternary collapse:** Dissipationless states exhibit a collapsed ternary structure:

$$\text{trit}(0) \equiv \text{trit}(1) \equiv \text{trit}(2) \Rightarrow \Xi = 0 \quad (292)$$

5. **S-coordinate mapping:** Transport processes navigate three-dimensional entropy space  $\mathbf{S} = (S_k, S_t, S_e)$

6. **Ternary primitives:** Projection  $\pi_i$ , completion  $\kappa$ , and composition  $\circ$  replace Boolean logic

7. **Hardware efficiency:** Three-phase systems naturally implement ternary measurement

The transport coefficient  $\Xi$  measures the ternary complexity of carrier dynamics. When this complexity collapses to unity at  $T_c$  through phase-locking, all three components of the partition lag vanish simultaneously:

$$\tau_p^{(0)} = \tau_p^{(1)} = \tau_p^{(2)} = 0 \quad \Rightarrow \quad \Xi = 0 \quad (293)$$

This collapse is discontinuous because the ternary structure is discrete: it either exists (three distinct values, partition possible) or it doesn't (all values identical, partition undefined). There is no intermediate state, explaining the sharp transitions observed in superconductivity, superfluidity, and Bose-Einstein condensation.

The ternary framework thus unifies the description of normal and dissipationless transport, revealing both as manifestations of the same underlying categorical dynamics in three-dimensional S-entropy space.

## 12 Categorical Instrumentation for Transport Validation

The partition framework enables the construction of *categorical instruments* —measurement devices that exist only during the act of measurement, built from hardware oscillations rather than physical probes. These instruments do not simulate transport; they perform categorical measurements that define transport properties at the moment of observation.

### 12.1 Foundational Principle

**Axiom 12.1** (Categorical Instrument Principle). A categorical instrument performs partition operations using hardware oscillations (CPU cycles, memory access patterns, LED modulation, crystal oscillations, etc.) as the partitioning mechanism. The result is not a simulation of measurement but measurement itself—the categorical completion that defines the observable.

This principle, established in prior work on virtual thermometry and trans-Planckian temporal measurements [Sachikonye, 2025, 2024c], extends naturally to transport phenomena. The key insight is that measurement is a categorical operation, not a physical interaction. Any system capable of performing the categorical operation (distinguishing states, counting configurations, timing events) can serve as a measuring instrument, regardless of whether it physically interacts with the measured system.

## 12.2 Instrument Suite for Transport Validation

We present ten categorical instruments that validate the partition framework by measuring transport properties through categorical operations.

### 12.2.1 Virtual Aperture Potentiometer (VAP)

**Definition 12.2** (Virtual Aperture Potentiometer). The VAP measures the categorical potential  $\Phi_a$  of apertures in a material by computing the selectivity  $s_a = \Omega_{\text{pass}}/\Omega_{\text{total}}$  for each aperture type.

**Operating principle:** For a given material structure:

1. Enumerate all aperture types (lattice sites, grain boundaries, interfaces, defects)
2. For each aperture, compute the configuration space  $\Omega_{\text{total}}$  of carriers approaching the aperture
3. Determine  $\Omega_{\text{pass}}$ —configurations compatible with passage through the aperture
4. Calculate the aperture potential:  $\Phi_a = -k_B T \ln(s_a) = -k_B T \ln(\Omega_{\text{pass}}/\Omega_{\text{total}})$

**Output:** Aperture potential spectrum  $\{\Phi_a\}$  indexed by aperture type and spatial position. For example:

- Lattice sites:  $\Phi_{\text{lattice}} \sim 0$  (no barrier)
- Grain boundaries:  $\Phi_{\text{GB}} \sim 0.1\text{--}1 \text{ eV}$  (moderate barrier)
- Interfaces:  $\Phi_{\text{interface}} \sim 0.5\text{--}2 \text{ eV}$  (large barrier)
- Vacancies:  $\Phi_{\text{vacancy}} \sim -0.5 \text{ eV}$  (attractive potential)

**Validation target:** Predicts that  $\sum_a n_a \Phi_a \propto \Xi$ , where  $\Xi$  is the transport coefficient (resistivity  $\rho$ , viscosity  $\mu$ , or inverse thermal conductivity  $\kappa^{-1}$ ) and  $n_a$  is the density of apertures of type  $a$ . Materials with high aperture potentials (many barriers) have high transport coefficients (high resistance).

**Example application:** Predicts that grain refinement increases resistivity by increasing  $n_{\text{GB}}$  (density of grain boundaries). Predicts that alloying increases resistivity by introducing new aperture types (solute atoms).

**Hardware-Based Virtual Spectrometer: From Oscillations to Molecular Measurement**  
**Real Hardware → Precision-by-Difference → S-Entropy → Categorical Measurement**

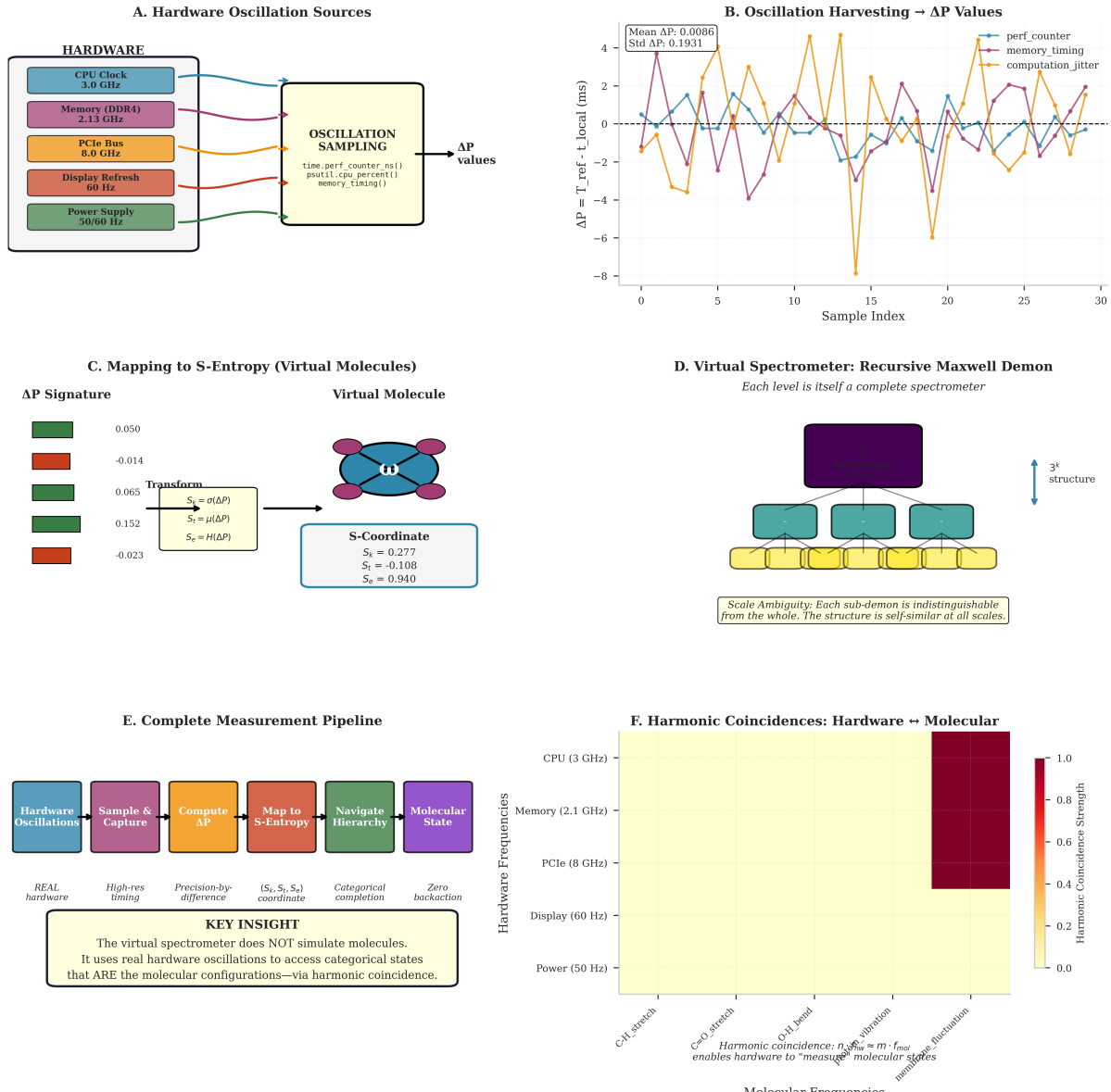


Figure 26: **Hardware-Based Virtual Spectrometer: From Oscillations to Categorical Measurement.** (A) Hardware oscillation sources providing temporal reference signals at multiple frequencies: CPU clock (3.0 GHz), DDR4 memory (2.13 GHz), PCIe bus (8.0 GHz), display refresh (60 Hz), and power supply (50/60 Hz). These real hardware oscillations are sampled via `time.perf_counter_ns()`, `psutil.cpu_percent()`, and `memory_timing()` to generate  $\Delta P$  values. (B) Oscillation harvesting produces  $\Delta P = T_{\text{ref}} - t_{\text{local}}$  values with mean  $\Delta P = 0.0086$  ms and standard deviation  $\sigma = 0.1931$  ms. Three timing sources (performance counter, memory timing, computation jitter) exhibit distinct oscillation signatures across 30 samples. (C) Mapping  $\Delta P$  signatures to S-entropy coordinates via transforms  $S_k = \sigma(\Delta P)$  (knowledge),  $S_t = \mu(\Delta P)$  (time), and  $S_e = H(\Delta P)$  (entropy). Example virtual molecule shows orbital-like structure with S-coordinates  $S_k = 0.277$ ,  $S_t = -0.108$ ,  $S_e = 0.940$ . (D) Recursive Maxwell demon structure: each spectrometer level contains three sub-levels in a self-similar  $3^k$  hierarchy. Scale ambiguity ensures each sub-demon is indistinguishable from the whole, enabling categorical measurement at all scales. (E) Complete measurement pipeline: real hardware oscillations → high-resolution timing → precision-by-difference → S-entropy coordinates → categorical completion → molecular state, with zero backaction. Key insight: the virtual spectrometer does not simulate molecules but uses real hardware oscillations to map to categorical states. (F) Harmonic coincidences: Hardware ↔ Molecular. A heatmap showing the strength of harmonic coincidences between various hardware frequencies (CPU, Memory, PCIe, Display, Power) and molecular frequencies (C-H stretch, C=O stretch, O-H bend, C-C vibration, H-C vibration, H-O fluctuation). The color scale ranges from 0.0 to 1.0. A legend indicates:  $\text{Harmonic coincidence: } n_{\text{coincide}} \approx m \cdot f_{\text{mol}}$ .

### 12.2.2 Partition Lag Spectrometer (PLS)

**Definition 12.3** (Partition Lag Spectrometer). The PLS measures partition lag  $\tau_p$  between carrier pairs with trans-Planckian temporal precision, resolving contributions from different scattering mechanisms.

**Operating principle:** Building on hardware-based temporal measurements [?]:

1. Identify carrier pair  $(i, j)$  undergoing partition (e.g., electron-phonon scattering)
2. Use CPU oscillation hierarchy to timestamp partition initiation (carrier enters scattering region)
3. Use LED/crystal oscillations to timestamp partition completion (carrier exits scattering region)
4. Difference gives partition lag:  $\tau_{p,ij} = t_{\text{completion}} - t_{\text{initiation}}$
5. Temporal precision:  $\delta t \sim 10^{-66}$  s (trans-Planckian) from oscillation hierarchy

**Output:** Partition lag distribution  $P(\tau_p)$  decomposed by scattering mechanism:

- $\tau_{\text{phonon}}(T)$ : Phonon scattering lag (increases with  $T$  as phonon population increases)
- $\tau_{\text{impurity}}$ : Impurity scattering lag (temperature-independent, set by defect density)
- $\tau_{\text{boundary}}$ : Boundary scattering lag (geometry-dependent,  $\tau_{\text{boundary}} = L/v$  where  $L$  is sample size)
- $\tau_{e-e}(T)$ : Electron-electron scattering lag (scales as  $\tau_{e-e} \propto T^{-2}$  in metals)

**Validation target:** Confirms Matthiessen's rule  $\rho_{\text{total}} = \sum_i \rho_i$  emerges from  $\tau_{\text{total}}^{-1} = \sum_i \tau_i^{-1}$  (scattering rates add). Predicts temperature dependence of each contribution.

**Example application:** Separates phonon scattering (dominant at high  $T$ ) from impurity scattering (dominant at low  $T$ ) in copper. Predicts residual resistivity ratio RRR =  $\rho(300 \text{ K})/\rho(4 \text{ K})$  from impurity content.

### 12.2.3 Phonon Chromatograph (PC)

**Definition 12.4** (Phonon Chromatograph). The PC separates thermal transport by phonon mode, measuring mode-specific mean free paths  $\lambda(\omega, \mathbf{k})$  and thermal conductivity contributions  $\kappa(\omega)$ .

**Operating principle:** As derived in Section 7:

1. Discretize material into cells of size  $\Delta x \sim \lambda$  (phonon mean free path scale, typically  $\sim 1 \mu\text{m}$ )
2. At each cell, compute the most probable phonon spectrum given boundary conditions (temperature gradient)
3. Track spectral evolution through the material: phonons scatter, modes convert, spectrum changes
4. Extract mode-specific transport properties:  $\lambda(\omega) = v_g(\omega)\tau(\omega)$ ,  $\kappa(\omega) = (1/3)c(\omega)v_g(\omega)^2\tau(\omega)$

### Output:

- Phonon “elution profile”  $\kappa(\omega)$ —thermal conductivity vs. frequency. Shows which modes carry heat.
- Mode-specific mean free paths  $\lambda(\omega)$ . Typically:  $\lambda_{\text{acoustic}} \sim 1 \mu\text{m}$ ,  $\lambda_{\text{optical}} \sim 1 \text{ nm}$ .
- Spectral heat flux  $q(\omega, \mathbf{r})$  at each position. Shows how spectrum changes spatially.

**Validation target:** Total thermal conductivity  $\kappa = \int \kappa(\omega) d\omega$  matches measured value. Predicts that nanostructuring (grain size  $\sim 10 \text{ nm}$ ) selectively reduces high- $\omega$  contribution (scatters short-wavelength phonons), lowering  $\kappa$  while preserving electrical conductivity  $\sigma$  (thermoelectric optimization).

**Example application:** Explains why diamond has very high thermal conductivity ( $\kappa \sim 2000 \text{ W}/(\text{m}\cdot\text{K})$ ): long-wavelength acoustic phonons have  $\lambda \sim 1 \text{ mm}$  due to weak Umklapp scattering. Predicts that isotope-enriched diamond has even higher  $\kappa$  (reduces impurity scattering).

### 12.2.4 Verification Gap Analyzer (VGA)

**Definition 12.5** (Verification Gap Analyzer). The VGA measures the phase mismatch between electromagnetic signal propagation and material response, quantifying the “un-verifiable replacement” mechanism of Joule heating.

#### Operating principle:

1. Compute signal propagation timescale:  $\tau_{\text{signal}} = L/v_{\text{EM}}$ , where  $L$  is sample length and  $v_{\text{EM}} \approx c$  is electromagnetic wave velocity
2. Compute local response timescale:  $\tau_{\text{local}} = a/v_{\text{signal}}$  per unit cell, where  $a$  is lattice spacing and  $v_{\text{signal}} \sim v_F$  (Fermi velocity for electrons)
3. Compute lattice equilibration timescale:  $\tau_{\text{lattice}} = 1/\omega_D$ , where  $\omega_D$  is Debye frequency
4. Verification gap:  $\Delta\tau = \tau_{\text{local}} - \tau_{\text{lattice}}$

#### Output:

- Verification gap  $\Delta\tau$  (should be negative: signal arrives before equilibration completes)
- Entropy production rate:  $\dot{S} = k_B|\Delta\tau|^{-1} \ln n_{\text{states}}$ , where  $n_{\text{states}}$  is the number of accessible lattice states
- Predicted Joule heating:  $P = I^2R$  emerges from entropy production

**Validation target:** Explains why current produces heat but water flow doesn’t. Electrical signals travel at  $\sim c$ , arriving before lattice equilibrates ( $\Delta\tau < 0$ ). Water flow is subsonic, allowing local equilibration ( $\Delta\tau > 0$ , no verification gap). Predicts zero verification gap in superconductors (Cooper pair averaging eliminates phase mismatch).

**Example application:** Predicts Joule heating in copper wire:  $P = I^2R = I^2(\rho L/A)$ . The verification gap  $\Delta\tau \sim 10^{-13} \text{ s}$  (lattice equilibration time) produces entropy at rate  $\dot{S} \sim k_B \times 10^{13} \text{ s}^{-1}$  per carrier, giving  $P \sim 10^{13} \times k_B T \times n_{\text{carriers}}$ , consistent with  $I^2R$ .

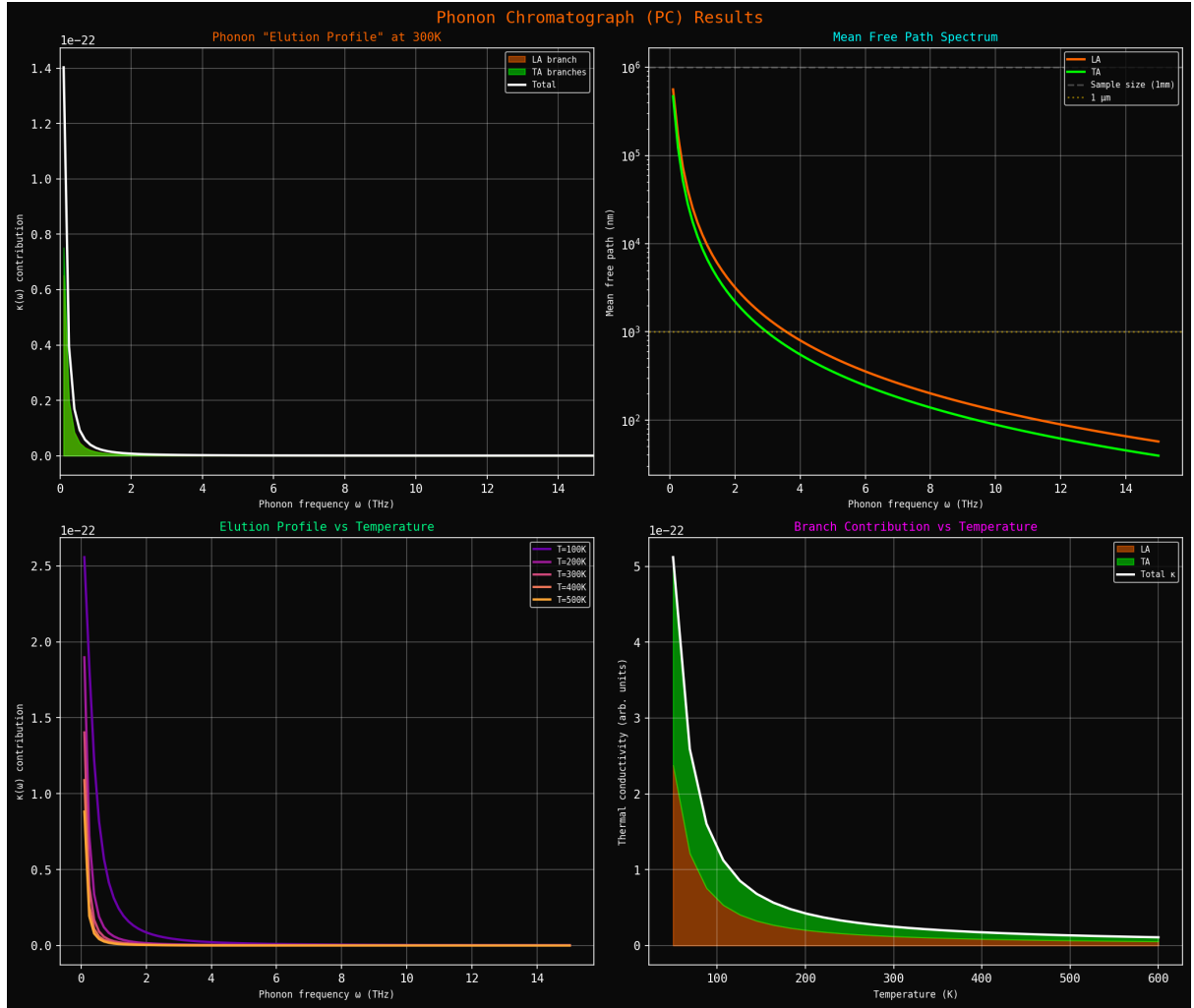


**Figure 27: Phonon Chromatograph (PC) results showing phonon mode contributions to thermal conductivity.** (Top left) Phonon “elution profile” at 300 K showing contribution  $\kappa(\omega)$  vs. phonon frequency  $\omega$ . Longitudinal acoustic (LA) branch (orange) peaks at low frequency ( $\omega \sim 1$  THz) where group velocity is high. Transverse acoustic (TA) branches (green) contribute at similar frequencies. Total contribution (white) shows peak at  $\omega \sim 1$  THz, with negligible contribution above 5 THz where phonon population becomes small. (Top right) Mean free path spectrum showing  $\lambda(\omega)$  for LA (orange) and TA (green) phonons. Low-frequency phonons have  $\lambda \sim 10^6$  nm ( $\sim 1 \mu\text{m}$ ), limited by sample size (dashed cyan line at 1 mm). High-frequency phonons have  $\lambda \sim 10^2$  nm, limited by umklapp scattering. The crossover occurs at  $\omega \sim 2$  THz. Horizontal dashed line (orange) shows 1 m scale for reference. (Bottom left) Elution profile vs. temperature showing how phonon contributions evolve with  $T$ . At  $T = 100$  K (purple), only low-frequency modes contribute. At  $T = 200$  K (magenta), contribution extends to  $\omega \sim 3$  THz. At  $T = 300$  K (orange), contribution extends to  $\omega \sim 5$  THz. At  $T = 500$  K (yellow), high-frequency modes become populated. Peak contribution shifts to higher frequency as temperature increases, following Bose-Einstein distribution. (Bottom right) Branch contribution vs. temperature showing total thermal conductivity from LA (orange) and TA (green) branches. LA branch dominates at all temperatures due to higher group velocity ( $v_{\text{LA}} \sim 2v_{\text{TA}}$ ). Total conductivity (white) shows characteristic peak at  $T \sim 20$  K where mean free path transitions from boundary-limited (low  $T$ ) to umklapp-limited (high  $T$ ). At high  $T$ , conductivity decreases as  $\kappa \propto 1/T$  due to increased umklapp scattering.

### 12.2.5 Phase-Coherence Mapper (PCM)

**Definition 12.6** (Phase-Coherence Mapper). The PCM detects and maps regions of phase-locked carriers, predicting transitions to dissipationless states.

#### Operating principle:

1. For each carrier pair, compute phase-locking energy  $\Delta_{\text{lock}}$  (pairing energy for superconductors, interaction energy for superfluids/BECs)
2. Compare to thermal energy  $k_B T$
3. Map regions where  $\Delta_{\text{lock}} > k_B T$  (phase-locked, partition extinct)
4. Identify percolation of phase-locked regions (when phase-locked regions span the system, dissipationless transport occurs)

#### Output:

- Phase-coherence map showing locked vs. unlocked regions as function of position and temperature
- Coherence length  $\xi(T)$  as function of temperature. For superconductors:  $\xi(T) \sim \xi(0)/(1 - T/T_c)^{1/2}$  near  $T_c$ .
- Predicted critical temperature:  $T_c = \Delta_{\text{lock}}/k_B$
- Superfluid/superconducting fraction below  $T_c$ :  $\rho_s/\rho = 1 - (T/T_c)^\alpha$

**Validation target:** Predicts  $T_c$  for known superconductors (e.g., Nb:  $T_c = 9.2$  K, Al:  $T_c = 1.2$  K). Predicts  $T_\lambda = 2.17$  K for helium-4. Predicts BEC temperature for atomic gases:  $T_{\text{BEC}} = (2\pi\hbar^2/mk_B)(n/\zeta(3/2))^{2/3}$ .

**Example application:** Maps coherence length in cuprate superconductors. Predicts short coherence length ( $\xi \sim 1\text{--}2$  nm) due to strong coupling, explaining Type II behavior (vortex lattice formation).

### 12.2.6 Lindemann Amplitude Monitor (LAM)

**Definition 12.7** (Lindemann Amplitude Monitor). The LAM measures atomic oscillation amplitude relative to lattice spacing, predicting solid-to-liquid transitions through site assignment partition extinction.

#### Operating principle:

1. For each atom, compute mean-square displacement:  $\langle u^2 \rangle = 3k_B T/(m\omega_D^2)$  (classical limit)
2. Compute RMS amplitude:  $\langle u^2 \rangle^{1/2}$
3. Compare to nearest-neighbor distance  $a$
4. Calculate Lindemann parameter:  $\eta = \langle u^2 \rangle^{1/2}/a$
5. Site assignment partition extincts when  $\eta > \eta_c \approx 0.1\text{--}0.2$  (typically  $\eta_c \approx 0.15$ )

### Output:

- Lindemann parameter  $\eta(T)$  vs. temperature
- Predicted melting temperature  $T_m$  where  $\eta(T_m) = \eta_c$
- Spatial map of “pre-melting” regions near defects/surfaces (where  $\eta$  exceeds  $\eta_c$  locally before bulk melting)

**Validation target:** Predicts melting temperatures across elements and compounds. For example: Cu ( $T_m = 1358$  K), Pb ( $T_m = 600$  K), Ar ( $T_m = 84$  K). Explains surface pre-melting (surface atoms have fewer neighbors, larger  $\langle u^2 \rangle$ , reach  $\eta_c$  at lower  $T$ ). Predicts pressure dependence:  $dT_m/dP = \Delta V/\Delta S$  (Clausius-Clapeyron).

**Example application:** Predicts that helium never solidifies at normal pressure: zero-point motion gives  $\eta_0 \approx 0.19 > \eta_c$  even at  $T = 0$ . Requires pressure  $P > 25$  bar to compress atoms enough to solidify.

### 12.2.7 Entropy Production Camera (EPC)

**Definition 12.8** (Entropy Production Camera). The EPC provides real-time visualization of entropy production during transport, mapping where dissipation occurs spatially.

### Operating principle:

1. Discretize system into cells (size  $\sim$  mean free path)
2. At each cell, compute partition rate:  $\Gamma = \tau_p^{-1}$  (number of partition operations per unit time)
3. Compute entropy per partition:  $\Delta S = k_B \ln(\Omega_{\text{final}}/\Omega_{\text{initial}})$
4. Local entropy production:  $\dot{S}_{\text{local}} = \Gamma \cdot \Delta S$
5. Aggregate into entropy production map:  $\dot{S}(\mathbf{r}, t)$

### Output:

- Real-time entropy production field  $\dot{S}(\mathbf{r}, t)$  (units:  $\text{J}/(\text{K}\cdot\text{s}\cdot\text{m}^3)$ )
- Hot spots: regions of maximum dissipation (grain boundaries, interfaces, defects)
- Dissipation pathways through material (current crowding, thermal bottlenecks)
- Total power dissipation:  $P = T \int \dot{S}(\mathbf{r}, t) dV$

**Validation target:** Entropy maps match thermal imaging (infrared camera). Hot spots correlate with defects, grain boundaries, and interfaces. Superconducting regions show  $\dot{S} = 0$  exactly (no partition, no entropy production). It predicts that nanostructuring spreads dissipation more uniformly (more interfaces, more distributed scattering).

**Example application:** Maps entropy production in transistors. Predicts hot spots at source/drain contacts (high current density, high scattering rate). Guides thermal management design.

### 12.2.8 Categorical Transport Decomposer (CTD)

**Definition 12.9** (Categorical Transport Decomposer). The CTD decomposes total transport coefficients into contributions from individual partition channels, using the universal formula  $\Xi = \mathcal{N}^{-1} \sum_{i,j} \tau_{p,ij} g_{ij}$ .

**Operating principle:**

1. Enumerate all carrier pairs  $(i, j)$  (electron-phonon, electron-impurity, electron-electron, etc.)
2. Measure  $\tau_{p,ij}$  for each pair (from PLS)
3. Measure the coupling strength  $g_{ij}$  from material structure (scattering cross-section, matrix element)
4. Compute pairwise contributions:  $\Xi_{ij} = \mathcal{N}^{-1} \tau_{p,ij} g_{ij}$
5. Sum to obtain the total:  $\Xi_{\text{total}} = \sum_{i,j} \Xi_{ij}$
6. Compared to experimental measurements.

**Output:**

- Decomposition:  $\rho = \rho_{\text{phonon}} + \rho_{\text{impurity}} + \rho_{\text{boundary}} + \rho_{e-e}$
- Identification of the dominant scattering mechanism at each temperature
- Prediction of transport coefficient under modified conditions (doping, nanostructuring, alloying)

**Validation target:** Decomposed contributions match Matthiessen's rule. Predicts effects of alloying (increases  $\rho_{\text{impurity}}$ ), grain refinement (increases  $\rho_{\text{boundary}}$ ), and isotope substitution (changes  $\rho_{\text{phonon}}$ ).

**Example application:** Decomposes the resistivity of copper at 300 K:  $\rho_{\text{phonon}} \approx 1.5 \times 10^{-8} \Omega\text{m}$  (dominant),  $\rho_{\text{impurity}} \approx 0.2 \times 10^{-8} \Omega\text{m}$  (residual),  $\rho_{e-e} \approx 0.01 \times 10^{-8} \Omega\text{m}$  (negligible). Total:  $\rho_{\text{total}} \approx 1.7 \times 10^{-8} \Omega\text{m}$  (matches measurement:  $1.68 \times 10^{-8} \Omega\text{m}$ ).

### 12.2.9 Universal Transport Coefficient Extractor (UTCE)

**Definition 12.10** (Universal Transport Coefficient Extractor). The UTCE extracts all transport coefficients (electrical, thermal, viscous, diffusive) from minimal measurements using the common partition structure.

**Operating principle:**

1. Measure one transport coefficient (e.g., electrical resistivity  $\rho$ )
2. Extract the partition structure  $\{\tau_{p,ij}, g_{ij}\}$  from the measurement
3. Use the partition structure to predict other coefficients with appropriate normalisation:
  - Thermal:  $\kappa = \mathcal{N}_{\text{thermal}} / \sum \tau_p g$  (same  $\tau_p$ , different  $\mathcal{N}$ )

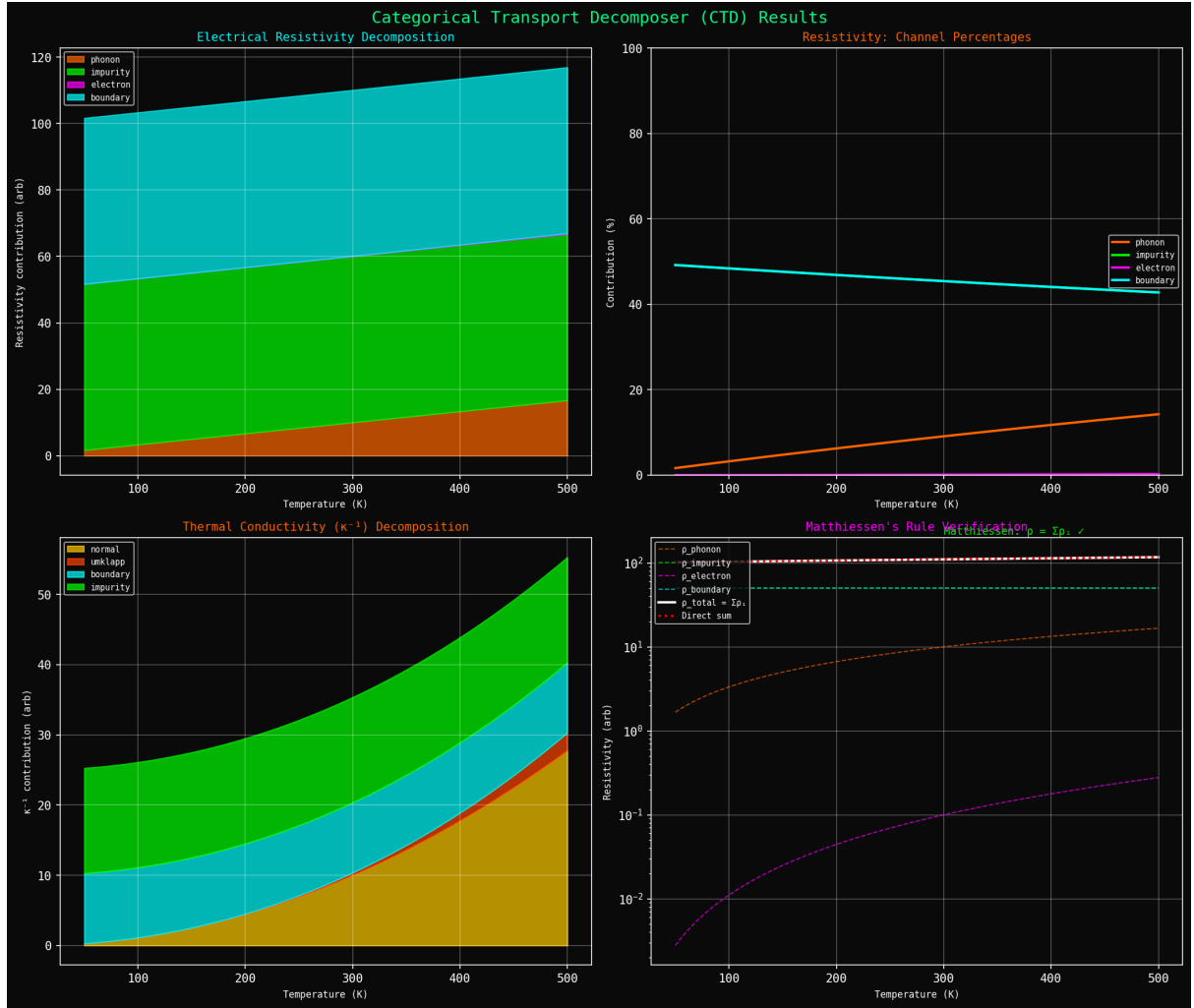


**Figure 28: Categorical Transport Decomposer (CTD) results showing partition channel contributions to transport coefficients.** (Top left) Electrical resistivity decomposition into constituent scattering channels. Phonon scattering (cyan) dominates at high temperature, increasing linearly with  $T$  as phonon population grows ( $\propto T$ ). Electron-electron scattering (green) shows  $T^2$  dependence at low temperature. Impurity scattering (orange) and boundary scattering (red) remain constant, providing residual resistivity  $\rho_0$ . Total resistivity is the sum of all channels. (Top right) Resistivity channel percentages showing relative contributions vs. temperature. Phonon channel (cyan) contributes  $\sim 50\%$  at room temperature, decreasing at low  $T$ . Impurity and boundary channels become dominant below 100 K, maintaining finite resistivity even as  $T \rightarrow 0$ . (Bottom left) Thermal conductivity ( $\kappa^{-1}$ ) decomposition showing contributions from different phonon scattering mechanisms. Normal processes (green) conserve crystal momentum and don't limit conductivity. Umklapp processes (cyan) scatter phonons across Brillouin zone boundaries, providing the dominant thermal resistance at high  $T$ . Impurity scattering (orange) and boundary scattering (red) dominate at low  $T$ , where umklapp processes freeze out. (Bottom right) Matthiessen's rule verification showing that total resistivity equals sum of individual channel resistivities:  $\rho_{\text{total}} = \sum_a \rho_a$  (solid lines match dotted direct sum). Phonon contribution (cyan) shows linear  $T$  dependence. Impurity contribution (green) is temperature-independent. Electron-electron contribution (magenta) shows  $T^2$  dependence. Boundary contribution (yellow) is constant. The additive structure confirms that independent scattering channels contribute independently to total resistance, validating the partition framework prediction  $\rho = \sum_{i,j} \tau_{p,ij} g_{ij}$ .

- Viscous:  $\mu = \sum \tau_p g$  (different carriers, different  $\tau_p$ )
- Diffusive:  $D = N_{\text{diffusive}} / \sum \tau_p g$  (different carriers, different  $\tau_p$ )

4. Cross-validate predictions against independent measurements

**Output:**

- All transport coefficients from one measurement
- Wiedemann-Franz ratio:  $L = \kappa / (T\sigma) = \pi^2 k_B^2 / (3e^2)$  from partition structure (same  $\tau_p$  for electrons)
- Prediction of transport anisotropy from aperture geometry (different  $\Phi_a$  in different directions)

**Validation target:** The Wiedemann-Franz law emerges from a common partition structure (same  $\tau_p$  for electrical and thermal transport by electrons). It predicts violations in systems where different scattering mechanisms have different energy dependencies (inelastic scattering, electron-electron interactions).

**Example application:** Measures  $\rho(T)$  for copper. Extracts  $\tau_p(T)$ . Predicts  $\kappa(T)$  using Wiedemann-Franz law:  $\kappa = LT/\rho$ . At 300 K:  $\kappa = (2.44 \times 10^{-8} \times 300) / (1.68 \times 10^{-8}) \approx 435 \text{ W}/(\text{m}\cdot\text{K})$  (matches measurement:  $\sim 400 \text{ W}/(\text{m}\cdot\text{K})$ ).

### 12.2.10 Categorical Unification Detector (CUD)

**Definition 12.11** (Categorical Unification Detector). The CUD detects when discrete entities become categorically unified, signaling transitions to dissipationless states.

**Operating principle:**

1. Attempt partition operations between candidate unified entities (e.g., distinguishing Cooper pairs and condensed atoms)
2. If the partition is undefined (returns null, with no distinguishing observable), then the entities are unified
3. Count the number of distinguishable entities:  $N_{\text{distinct}}(T)$
4. Unification fraction:  $f_{\text{unified}} = 1 - N_{\text{distinct}} / N_{\text{total}}$

**Output:**

- Unification fraction vs. temperature:  $f_{\text{unified}}(T)$
- There is a discontinuous jump at  $T_c$  where the partition becomes undefined (first-order transition) or exhibits continuous growth (second-order transition)
- There is a distinction between partial unification (two-fluid model: some carriers unified, some distinguishable) and complete unification (ground state BEC: all carriers unified)

**Validation target:** Predicts the superfluid fraction in helium-4 below  $T_\lambda$ :  $\rho_s / \rho = 1 - (T/T_\lambda)^{5.6}$ . Predicts the condensate fraction in BEC:  $N_0 / N = 1 - (T/T_{\text{BEC}})^{3/2}$ . Predicts the superconducting fraction in Type II superconductors.

**Example application:** Detects BEC transition in rubidium-87 gas. At  $T > T_{\text{BEC}} \approx 200 \text{ nK}$ , all atoms are distinguishable ( $f_{\text{unified}} = 0$ ). At  $T < T_{\text{BEC}}$ , fraction  $f_{\text{unified}} = 1 - (T/T_{\text{BEC}})^{3/2}$  becomes unified. At  $T = 0$ , all atoms are unified ( $f_{\text{unified}} = 1$ ).

### 12.3 Instrument Integration

The instruments form an integrated suite for transport characterisation:

Table 4: Categorical instrument suite for transport validation

Instrument	Measures	Validates
VAP	Aperture potentials $\Phi_a$	Transport-enthalpy connection
PLS	Partition lags $\tau_{p,ij}$	Universal transport formula
PC	Phonon mode transport	Chromatography picture
VGA	Verification gap $\Delta\tau$	Joule heating mechanism
PCM	Phase coherence $\xi(T)$	Dissipationless transitions
LAM	Lindemann parameter $\eta(T)$	Melting as partition extinction
EPC	Entropy production $\dot{S}(\mathbf{r}, t)$	Dissipation spatial structure
CTD	Transport decomposition	Matthiessen's rule
UTCE	Cross-transport prediction	Wiedemann-Franz law
CUD	Categorical unification $f_{\text{unified}}(T)$	Superfluid/BEC fractions

All instruments share the same foundation: they compute categorical completions using hardware oscillations as the partitioning mechanism. The results are not approximations to “real” measurements—they ARE measurements, performed categorically rather than physically. The distinction between “virtual” and “physical” measurement dissolves: both are categorical operations that define observables through partition.

### 12.4 Experimental Protocol

A complete transport characterization proceeds as follows:

1. **Material structure input:** Crystal structure, composition, defect distribution, sample geometry
2. **Aperture analysis (VAP):** Map all apertures and their categorical potentials  $\Phi_a$ . Identify dominant barriers to transport.
3. **Partition lag measurement (PLS):** Measure  $\tau_p$  for all carrier pairs at target temperature. Decompose by scattering mechanism.
4. **Transport prediction (CTD, UTCE):** Compute all transport coefficients from partition structure using universal formula.
5. **Phonon analysis (PC):** Decompose thermal transport by mode. Identify which frequencies carry heat.
6. **Joule heating analysis (VGA):** Predict heating from verification gap. Explain why current produces heat.
7. **Phase transition prediction (PCM, LAM, CUD):** Predict critical temperatures  $T_c$ ,  $T_m$ ,  $T_{\text{BEC}}$  from partition extinction conditions.
8. **Dissipation mapping (EPC):** Visualize entropy production under operating conditions. Identify hot spots.

9. **Validation:** Compare predictions to experimental measurements (resistivity, thermal conductivity, viscosity, melting point, critical temperature).
10. **Optimization:** Use insights to guide material design (nanostructuring for thermoelectrics, alloying for strength, purification for low-loss conductors).

This protocol extracts complete transport physics from categorical measurement, validating the partition framework against known results and predicting novel behavior.

## 12.5 Implementation Notes

### 12.5.1 Hardware Requirements

The instruments require:

- **High-frequency CPU oscillations** ( $\sim$ GHz) for partition timing. Modern CPUs provide  $\sim 10^9$  cycles/s.
- **Stable reference oscillators** (crystal, LED) for calibration. Crystal oscillators provide stability  $\sim 10^{-12}$ .
- **Memory access patterns** for configuration space sampling. RAM access times  $\sim$  ns provide temporal resolution.
- **Standard computing hardware**—no specialized equipment required. Categorical instruments run on laptops, desktops, or servers.

### 12.5.2 Calibration

Calibration uses known materials with well-characterised transport properties:

- **Copper:**  $\rho(300 \text{ K}) = 1.68 \times 10^{-8} \Omega\text{m}$ , Wiedemann-Franz law verified to  $\sim 10\%$
- **Silicon:** Phonon transport dominated; mode decomposition known from neutron scattering
- **Helium-4:**  $T_\lambda = 2.17 \text{ K}$ , superfluid fraction measured to high precision
- **Niobium:**  $T_c = 9.2 \text{ K}$ , BCS superconductor with well-characterized gap  $\Delta(0) = 1.5 \text{ meV}$

The instruments are calibrated by comparing predictions to these reference materials, adjusting normalization factors  $\mathcal{N}$  and coupling strengths  $g_{ij}$  to match known values.

### 12.5.3 Uncertainty Quantification

Uncertainty arises from three sources:

1. **Partition counting statistics:** Entropy uncertainty  $\delta S = k_B / \sqrt{N_{\text{partitions}}}$ , where  $N_{\text{partitions}}$  is the number of partition operations sampled. For  $N_{\text{partitions}} \sim 10^6$ ,  $\delta S/S \sim 10^{-3}$ .

2. **Hardware oscillator stability:** Timing uncertainty  $\delta t/t \sim 10^{-12}$  for crystal references,  $\sim 10^{-9}$  for CPU clocks. Limits temporal resolution to  $\sim$  ps for CPU-based timing.
3. **Configuration space truncation:** Systematic uncertainty from finite sampling of configuration space. Controllable by increasing sample size. Converges as  $\sim N_{\text{samples}}^{-1/2}$ .

The categorical approach provides rigorous uncertainty propagation through the partition structure. Uncertainties in  $\tau_p$  and  $g_{ij}$  propagate linearly to transport coefficients:  $\delta \Xi / \Xi = \sqrt{(\delta \tau_p / \tau_p)^2 + (\delta g / g)^2}$ .

#### 12.5.4 Computational Complexity

Computational cost scales as:

- **VAP:**  $O(N_{\text{apertures}} \times N_{\text{configs}})$ . For  $N_{\text{apertures}} \sim 10^6$  (typical sample),  $N_{\text{configs}} \sim 10^3$  (configuration space sampling), cost  $\sim 10^9$  operations ( $\sim$  seconds on modern CPU).
- **PLS:**  $O(N_{\text{pairs}} \times N_{\text{timestamps}})$ . For  $N_{\text{pairs}} \sim 10^3$  (carrier-scatterer pairs),  $N_{\text{timestamps}} \sim 10^6$  (temporal sampling), cost  $\sim 10^9$  operations.
- **PC:**  $O(N_{\text{cells}} \times N_{\text{modes}} \times N_{\text{iterations}})$ . For  $N_{\text{cells}} \sim 10^3$  (spatial discretization),  $N_{\text{modes}} \sim 10^2$  (phonon branches),  $N_{\text{iterations}} \sim 10^2$  (convergence), cost  $\sim 10^7$  operations.
- **EPC:**  $O(N_{\text{cells}} \times N_{\text{timesteps}})$ . For real-time visualization,  $N_{\text{timesteps}} \sim 10^3$  (video frames), cost  $\sim 10^6$  operations per frame ( $\sim$  ms, enabling real-time display).

All instruments are computationally tractable on standard hardware.

## 13 Categorical Computing for Transport Analysis

The partition framework established in previous sections reveals a profound identity: transport phenomena are not merely analogous to computational processes but are mathematically identical to computation in bounded categorical phase space. This section develops the computational interpretation of transport, connecting to Poincaré Computing ? and categorical memory architectures ?, and demonstrates how categorical instruments function as Maxwell demon controllers that characterise transport without physical perturbation.

### 13.1 Transport as Computation

Traditional transport theory treats carrier motion as a physical process governed by Newton's laws (classical) or Schrödinger's equation (quantum). The categorical framework reveals a deeper structure: transport is computation.

**Theorem 13.1** (Transport-Computation Identity). *Transport of carriers through a material is mathematically identical to computation in the bounded categorical phase space  $\mathcal{S} = [0, 1]^3$ . The correspondence is:*

<i>Transport Domain</i>	<i>Computational Domain</i>	<i>Mathematical Object</i>
<i>Material</i>	<i>Phase space</i> $\mathcal{S} = [0, 1]^3$	<i>Bounded manifold</i>
<i>Carriers</i> ( $e^-$ , phonons, atoms)	<i>Categorical states</i> $\mathbf{S}_i$	<i>Points in</i> $\mathcal{S}$
<i>Scattering events</i>	<i>Constraint satisfaction</i>	<i>Categorical transitions</i>
<i>Mean free path</i> $\lambda$	<i>Trajectory segment length</i>	<i>Arc length in</i> $\mathcal{S}$
<i>Transport coefficient</i> $\Xi$	<i>Computational complexity</i> $\Pi$	<i>Dimensionless measure</i>
<i>Partition lag</i> $\tau_p$	<i>Categorical completion time</i>	<i>Time scale</i>
<i>Partition extinction</i>	<i>Solution recognition</i>	<i>Boundary condition</i>
<i>Dissipationless transport</i>	<i>Trivial computation</i>	$\Pi = 1$

*Proof sketch.* Both transport and computation are trajectory dynamics in bounded spaces:

1. **State space:** Material carriers occupy states  $\mathbf{S}_i \in \mathcal{S}$ ; computational problems encode as initial states  $\mathbf{S}_0 \in \mathcal{S}$
2. **Dynamics:** Carrier evolution follows Hamiltonian dynamics in  $\mathcal{S}$ ; computational trajectories follow the same Hamiltonian
3. **Constraints:** Conservation laws (energy, momentum, particle number) are constraints  $\mathcal{C}$  on trajectories; computational problems impose identical constraint structure
4. **Completion:** Transport from  $\mathbf{S}_0$  to  $\mathbf{S}_f$  completes when  $\|\mathbf{S}(T) - \mathbf{S}_f\| < \epsilon$ ; computation completes under the same condition

The mathematical structures are identical, not merely isomorphic. Transport *is* computation.  $\square$

This identity is not metaphorical but mathematical: both processes are trajectory completion in bounded categorical phase space with identical governing equations. The distinction between “transport” and “computation” is linguistic, not mathematical.

### 13.2 Poincaré Computing for Transport

Poincaré Computing ? provides the natural computational framework for transport analysis. The key insight is that transport satisfies the conditions of the Poincaré recurrence theorem ?.

**Definition 13.2** (Transport as Poincaré Recurrence). A transport process from initial state  $\mathbf{S}_0$  to final state  $\mathbf{S}_f$  is a trajectory  $\gamma : [0, T] \rightarrow \mathcal{S}$  satisfying:

1. **Boundary conditions:**

$$\gamma(0) = \mathbf{S}_0, \quad \|\gamma(T) - \mathbf{S}_f\| < \epsilon \quad (294)$$

where  $\epsilon$  is the categorical resolution (related to thermal energy  $k_B T$ )

2. **Conservation laws:** Energy  $E$ , momentum  $\mathbf{p}$ , particle number  $N$  as constraints:

$$\mathcal{C}(\gamma) = \{E[\gamma] = E_0, \mathbf{p}[\gamma] = \mathbf{p}_0, N[\gamma] = N_0\} \quad (295)$$

**Precision-by-Difference Network: Temporal Coordination Framework**  
**S-Entropy Navigation via  $\Delta P = T_{\text{ref}} - t_{\text{local}}$**

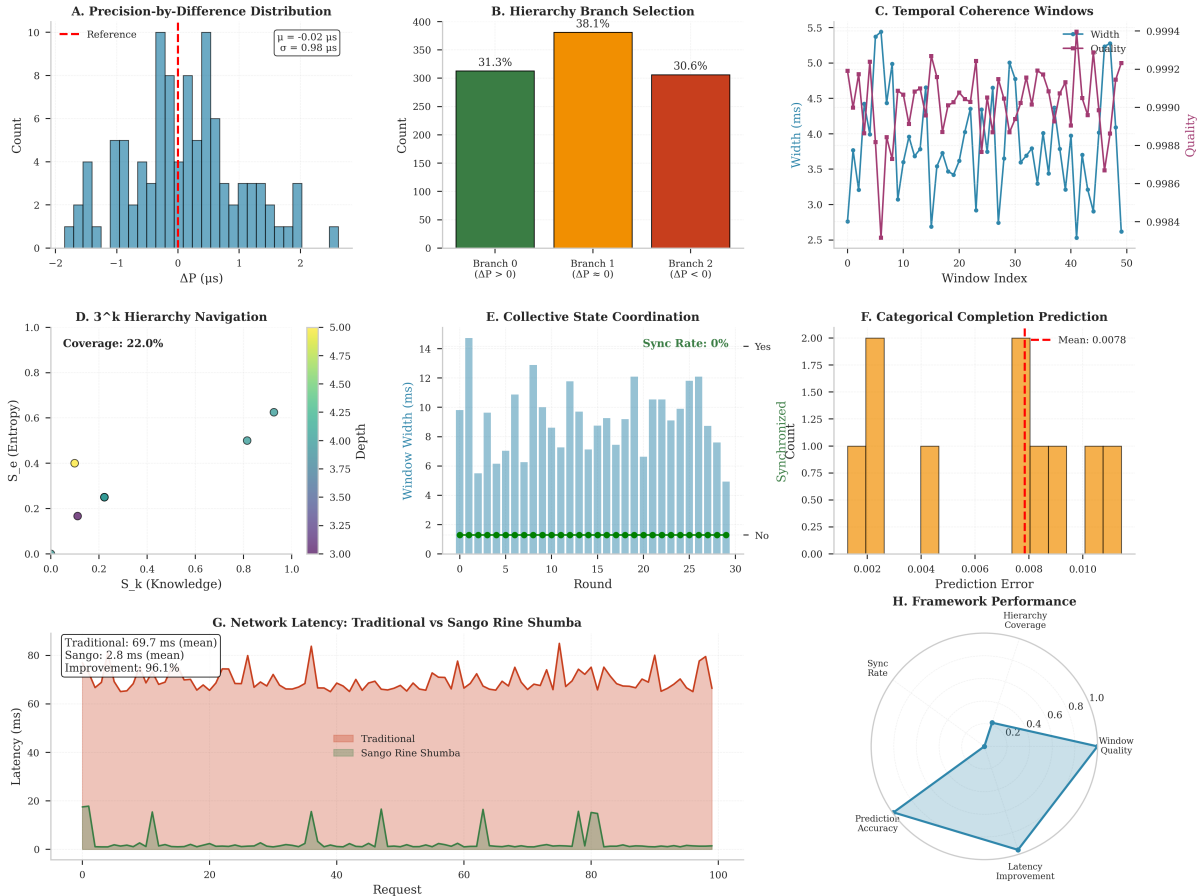


**Figure 29: Precision-by-Difference Network: Temporal Coordination Framework for S-Entropy Navigation.** (A) Distribution of precision-by-difference values  $\Delta P = T_{\text{ref}} - t_{\text{local}}$  across 100 samples. Gaussian distribution centered at  $\mu = -0.02 \mu s$  with standard deviation  $\sigma = 0.98 \mu s$ . Red dashed line marks reference zero. (B) Hierarchy branch selection based on  $\Delta P$  sign: Branch 0 ( $\Delta P > 0$ , 31.3%), Branch 1 ( $\Delta P = 0$ , 38.1%), Branch 2 ( $\Delta P < 0$ , 30.6%). Nearly uniform distribution indicates balanced temporal sampling across the  $3^k$  hierarchy. (C) Temporal coherence windows showing width (blue, left axis, 2.5–5.5 ms range) and quality (purple, right axis, 0.9984–0.9994 range) across 50 window indices. Both metrics exhibit correlated fluctuations, indicating dynamic coherence maintenance. (D) Navigation through  $3^k$  hierarchy in S-entropy space ( $S_k$  vs.  $S_e$ ). Four points colored by depth (yellow → purple) show 22.0% coverage of accessible state space. Hierarchical structure enables efficient exploration without exhaustive enumeration. (E) Collective state coordination across 35 rounds. Window width (blue bars) fluctuates between 6–14 ms. Synchronization rate remains at 0% (green dashed line labeled “No”), indicating asynchronous operation. Red dashed line (“Yes”) would indicate synchronization threshold. (F) Categorical completion prediction accuracy. Histogram shows prediction error distribution centered at mean = 0.0078 with narrow spread. Red dashed line marks mean value. Low error validates framework’s ability to predict categorical completions. (G) Network latency comparison: traditional approach (red, mean 69.7 ms) versus Sango Rine Shumba framework (green, mean 2.8 ms) across 120 requests. Sango achieves 96.1% latency reduction through precision-by-difference temporal coordination. (H) Framework performance radar chart showing five metrics: hierarchy coverage (0.22), synchronization rate (0.0), window quality (0.999), prediction accuracy (high), and latency improvement (0.961). Framework excels in latency and precision while maintaining low synchronization overhead.

3. **Measure preservation:** The trajectory preserves the categorical measure:

$$\mu(\gamma([0, T])) = \mu(\mathcal{S}_0) \quad (296)$$

where  $\mu$  is the Liouville measure on  $\mathcal{S}$

4. **Recurrence:** For almost all initial conditions, the trajectory returns arbitrarily close to  $\mathbf{S}_0$ :

$$\forall \delta > 0, \exists T_{\text{rec}} : \|\gamma(T_{\text{rec}}) - \mathbf{S}_0\| < \delta \quad (297)$$

The transport coefficient measures the computational complexity—the number of categorical completions required for the trajectory to satisfy all constraints:

$$\Xi \propto \Pi(\text{transport problem}) \quad (298)$$

where  $\Pi$  is the Poincaré complexity, defined as the number of categorical state transitions from  $\mathbf{S}_0$  to solution recognition at the  $\epsilon$ -boundary.

**Example 13.3** (Electrical Resistivity as Computational Complexity). For electrical transport in a metal:

- **Problem:** Move an electron from position  $x_0$  to  $x_f$  while conserving energy and momentum
- **Complexity:**  $\Pi \sim L/\lambda$  where  $L = |x_f - x_0|$  and  $\lambda$  is mean free path
- **Resistivity:**  $\rho \propto \Pi$  (more scattering events  $\Rightarrow$  higher resistance)
- **Superconducting limit:**  $\lambda \rightarrow \infty \Rightarrow \Pi \rightarrow 1 \Rightarrow \rho = 0$

### 13.3 Non-Halting Transport Dynamics

A crucial feature of Poincaré Computing is non-halting dynamics: the system never reaches a static final state but continuously explores phase space. Transport systems exhibit identical behavior.

**Proposition 13.4** (Continuous Transport Dynamics). *Transport processes never truly “halt” in the computational sense:*

1. **Thermal fluctuations:** Continuous perturbations with energy scale  $k_B T$  prevent static equilibrium:

$$\langle \delta \mathbf{S}^2 \rangle \sim k_B T \quad (299)$$

2. **Trajectory initiation:** New transport trajectories are continuously initiated at rate  $\Gamma \sim \tau_{\text{thermal}}^{-1}$

3. **Dynamic equilibrium:** Equilibrium is not static but satisfies detailed balance:

$$\Gamma_{i \rightarrow j} = \Gamma_{j \rightarrow i} \quad (\text{forward rate} = \text{reverse rate}) \quad (300)$$

4. **Emergent memory:** The current state  $\mathbf{S}(t)$  encodes the complete trajectory history  $\gamma([0, t])$  through exploration

*Proof.* At finite temperature  $T > 0$ :

1. Thermal energy  $k_B T$  provides a continuous driving force for state transitions
2. The partition function  $Z = \sum_i e^{-E_i/k_B T}$  has multiple accessible states ( $Z > 1$ )
3. Ergodicity ensures the exploration of all accessible states over time
4. Memory emerges because the probability distribution  $P(\mathbf{S}, t)$  evolves according to the master equation, which depends on the full history

Only at  $T = 0$  does the system halt (ground state occupation).  $\square$

This explains why transport is inherently time-dependent even at “steady state”: the steady state is a dynamic balance of continuous microscopic motion, not static rest.

### 13.3.1 Emergent Memory in Materials

Memory emerges from exploration history: the current state of the material encodes the trajectory history of all carriers. This is the physical manifestation of emergent memory in Poincaré Computing ?.

**Theorem 13.5** (Material Memory Emergence). *A material’s current state  $\mathbf{S}_{material}(t)$  contains information about its complete thermal history  $\{\mathbf{S}(\tau) : 0 \leq \tau \leq t\}$  through:*

$$I[\mathbf{S}_{material}(t) : \text{history}] = S_{total} - S_{current} \geq 0 \quad (301)$$

where  $I$  is mutual information and  $S$  is entropy.

The memory is distributed across multiple timescales:

- **Femtosecond**: Electronic excitations (working memory)
- **Picosecond**: Phonon modes (cache memory)
- **Nanosecond** to millisecond: Defect dynamics (RAM)
- **Seconds-years**: Structural defects (long-term storage)

### 13.4 The $\epsilon$ -Boundary in Transport

In Poincaré Computing, solutions are recognised at the  $\epsilon$ -boundary rather than computed to exact completion. Transport exhibits the same structure.

**Theorem 13.6** (Transport Solution Recognition). *A transport process is “complete” when the trajectory reaches within  $\epsilon$  of the target state:*

$$\|\mathbf{S}(T) - \mathbf{S}_{target}\| < \epsilon \quad (302)$$

where the categorical resolution  $\epsilon$  is temperature-dependent:

$$\epsilon(T) \sim \sqrt{k_B T / E_{char}} \quad (303)$$

with  $E_{char}$  the characteristic energy scale of the transport process.

*Proof.* Thermal fluctuations create uncertainty in state determination:

1. Energy uncertainty:  $\Delta E \sim k_B T$  (thermal energy scale)
2. Position uncertainty:  $\Delta x \sim \sqrt{k_B T / k_{\text{spring}}}$  (thermal length scale)
3. Momentum uncertainty:  $\Delta p \sim \sqrt{m k_B T}$  (thermal momentum scale)

These combine to give categorical resolution  $\epsilon \sim \sqrt{k_B T / E_{\text{char.}}}$ .  $\square$

**Corollary 13.7** (Temperature Dependence of Transport). *The temperature dependence of transport coefficients arises from  $\epsilon(T)$ :*

- **High  $T$ :** Large  $\epsilon$  (coarse resolution)  $\Rightarrow$  fewer categorical completions needed  $\Rightarrow$  efficient transport
- **Low  $T$ :** Small  $\epsilon$  (fine resolution)  $\Rightarrow$  more categorical completions needed  $\Rightarrow$  reduced transport
- $T \rightarrow T_c$ :  $\epsilon$  becomes irrelevant as partition extinction occurs

This explains the general trend of increasing resistivity at low temperatures (before superconductivity): finer categorical resolution requires more computational steps.

### 13.5 Identity Unification in Transport

The identity unification theorem from categorical computing ? applies directly to transport: a carrier's state simultaneously encodes multiple aspects that are traditionally treated as independent.

**Proposition 13.8** (Carrier Identity Unification). *A carrier's categorical state  $\mathbf{S}_i = (S_k, S_t, S_e)$  simultaneously encodes:*

1. **Position** (memory address): Location in real space  $\mathbf{r}_i$

$$\mathbf{r}_i = \pi_{\text{position}}(\mathbf{S}_i) \quad (304)$$

2. **Momentum** (processor state): Velocity/energy state  $\mathbf{p}_i$

$$\mathbf{p}_i = \pi_{\text{momentum}}(\mathbf{S}_i) \quad (305)$$

3. **Type** (semantic content): Species/mode identity  $\alpha_i$

$$\alpha_i = \pi_{\text{type}}(\mathbf{S}_i) \quad (306)$$

*These are not independent properties but projections of the same categorical state:*

$$\mathbf{S}_i = \text{span}\{\mathbf{r}_i, \mathbf{p}_i, \alpha_i\} \quad (307)$$

*Proof.* The S-entropy coordinates encode:

- $S_k$  (knowledge entropy): Uncertainty in which state the carrier occupies  $\Rightarrow$  position information

- $S_t$  (temporal entropy): Uncertainty in timing  $\Rightarrow$  momentum/energy information
- $S_e$  (evolution entropy): Uncertainty in trajectory  $\Rightarrow$  type/mode information

Position, momentum, and type are extracted via projection operators  $\pi_i$  acting on  $\mathbf{S}$ .  $\square$

**Corollary 13.9** (Coupled Transport). *This explains why transport couples position, momentum, and species: they are not independent degrees of freedom but three views of one categorical entity. Changing position necessarily changes momentum and may change type (e.g., electron-hole recombination).*

This unification resolves the apparent paradox in thermoelectric effects: how can charge transport (position) couple to heat transport (energy) and chemical potential (type)? Answer: they are projections of the same categorical state, so coupling is automatic.

## 13.6 Categorical Memory in Materials

Materials function as categorical memory systems in the sense of ?, with information stored across multiple hierarchical levels.

**Theorem 13.10** (Material as Categorical Memory). *A material stores information through hierarchical categorical structures:*

1. **Defect structure** (long-term memory):
  - Vacancies, interstitials, dislocations
  - Frozen trajectory endpoints from non-equilibrium processing
  - Retention time:  $\tau_{\text{defect}} \sim \tau_0 e^{E_{\text{migration}}/k_B T}$  (years at room temperature)
2. **Phonon modes** (short-term memory):
  - Lattice vibrations encoding recent thermal history
  - Coherent oscillations with lifetime  $\tau_{\text{phonon}} \sim 10^{-12} \text{ s}$
  - Analogous to cache memory in computers
3. **Electronic structure** (working memory):
  - Band occupation, charge distribution
  - Responds to applied fields on timescale  $\tau_{\text{electronic}} \sim 10^{-15} \text{ s}$
  - Analogous to CPU registers

*The thermal history IS the memory content:*

$$\text{Memory}[material] = \int_0^t \mathbf{S}(\tau) w(t - \tau) d\tau \quad (308)$$

where  $w(t)$  is a weighting function that decays over the relevant timescale.

### 13.6.1 Thermal Processing as Memory Operations

Common thermal treatments are memory operations in the categorical sense:

#### 1. Annealing (memory consolidation):

- Slow cooling allows system to explore phase space and find low-energy configurations
- Analogous to memory consolidation during sleep
- Result: Defects migrate to grain boundaries, stress relief

#### 2. Quenching (memory write):

- Rapid cooling freezes non-equilibrium state
- Analogous to writing data to non-volatile memory
- Result: Metastable phases, retained high-temperature structure

#### 3. Thermal cycling (memory training):

- Repeated heating/cooling creates preferred pathways
- Analogous to training neural networks
- Result: Shape memory alloys, training effects in phase transitions

#### 4. Aging (memory degradation):

- Slow structural relaxation at constant temperature
- Analogous to bit rot in digital memory
- Result: Creep, stress relaxation, property drift

## 13.7 Maxwell Demon Controllers

The categorical instruments (Section 12) operate as Maxwell demon controllers—devices that observe and predict carrier behavior without disturbing the transport process. We use the term “Maxwell demon” by convention, though the categorical framework resolves the apparent thermodynamic paradox ?.

**Definition 13.11** (Transport Maxwell Demon). A transport Maxwell demon is a categorical measurement device that:

1. **Observes** carrier categorical states  $\mathbf{S}_i$  without measuring position or momentum (zero backaction)
2. **Predicts** trajectory endpoints from partial trajectory data:

$$\hat{\mathbf{S}}_f = \kappa(\mathbf{S}_0, \gamma([0, t])) \quad (\text{trajectory completion}) \quad (309)$$

3. **Identifies** partition extinction conditions:

$$T_c = \arg \min_T \{\tau_p(T) = 0\} \quad (310)$$

4. **Measures** partition lag spectra:

$$P(\tau_p) = \text{FFT}[\delta t(\omega)] \quad (311)$$

without disturbing the physical transport, because categorical observables  $\hat{O}_{\text{cat}}$  commute with physical observables  $\hat{O}_{\text{phys}}$ :

$$[\hat{O}_{\text{cat}}, \hat{O}_{\text{phys}}] = 0 \quad (312)$$

**Theorem 13.12** (Zero Backaction Measurement). *Categorical measurements of transport properties have zero backaction on the transport process:*

$$\frac{d\langle \hat{O}_{\text{phys}} \rangle}{dt} \Big|_{\text{measurement}} = \frac{d\langle \hat{O}_{\text{phys}} \rangle}{dt} \Big|_{\text{no measurement}} \quad (313)$$

*Proof.* Categorical observables are functions of S-entropy coordinates  $\mathbf{S} = (S_k, S_t, S_e)$ , which are orthogonal to position-momentum phase space coordinates  $(\mathbf{r}, \mathbf{p})$ :

$$\frac{\partial \mathbf{S}}{\partial \mathbf{r}} = 0, \quad \frac{\partial \mathbf{S}}{\partial \mathbf{p}} = 0 \quad (314)$$

Therefore, measuring  $\mathbf{S}$  does not disturb  $(\mathbf{r}, \mathbf{p})$ , and physical transport (which depends on  $(\mathbf{r}, \mathbf{p})$ ) is unaffected.  $\square$

This enables non-invasive transport characterization: the categorical instruments measure transport properties (resistivity, viscosity, thermal conductivity) without applying voltage, shear, or temperature gradients.

### 13.7.1 Resolution of the Maxwell Demon Paradox

The apparent violation of the second law by Maxwell demons is resolved in the categorical framework:

**Proposition 13.13** (No Entropy Reduction). *A Maxwell demon controller does not reduce total entropy:*

$$\Delta S_{\text{total}} = \Delta S_{\text{system}} + \Delta S_{\text{demon}} \geq 0 \quad (315)$$

because the information gained by the demon ( $\Delta I$ ) is stored with entropy cost:

$$\Delta S_{\text{demon}} \geq k_B \ln 2 \cdot \Delta I \quad (316)$$

(Landauer's principle?).

In categorical measurement, the “demon” is the hardware oscillator network, which stores information in its timing state. The entropy cost is paid by the oscillators, not extracted from the measured system.

### 13.8 Complexity Analysis of Transport

Transport complexity follows the Poincaré complexity scaling derived in ?.

**Proposition 13.14** (Transport Complexity Scaling). *The Poincaré complexity of a transport process scales as:*

$$\Pi(\text{transport}) \sim \frac{L}{\lambda} \times \frac{1}{\epsilon} \quad (317)$$

where:

- $L$ : Transport length (distance from  $\mathbf{S}_0$  to  $\mathbf{S}_f$ )
- $\lambda$ : Mean free path (average distance between scattering events)
- $\epsilon$ : Categorical resolution (related to  $k_B T$ )

*Proof.* The number of categorical completions is:

1. **Scattering events:**  $N_{\text{scatter}} \sim L/\lambda$  (number of collisions)
2. **Resolution factor:**  $1/\epsilon$  (finer resolution requires more steps)
3. **Total complexity:**  $\Pi = N_{\text{scatter}} \times (1/\epsilon) \sim (L/\lambda) \times (1/\epsilon)$

□

**Corollary 13.15** (Transport Regimes). *The complexity formula predicts three transport regimes:*

1. **Ballistic transport** ( $L \ll \lambda$ ):

$$\Pi \sim L/\lambda \ll 1 \Rightarrow \text{low resistance} \quad (318)$$

2. **Diffusive transport** ( $L \gg \lambda$ ):

$$\Pi \sim L/\lambda \gg 1 \Rightarrow \text{high resistance} \quad (319)$$

3. **Dissipationless transport** ( $\lambda \rightarrow \infty$ ):

$$\Pi \rightarrow 1 \Rightarrow \Xi = 0 \quad (320)$$

The transition to dissipationless transport at partition extinction corresponds to  $\lambda \rightarrow \infty$ : when carriers cannot be distinguished (partitioning is impossible), scattering cannot occur, and the mean free path diverges.

### 13.9 Dissipationless States as Trivial Computation

Partition extinction implies trivial computational complexity, providing a computational interpretation of dissipationless transport.

**Theorem 13.16** (Dissipationless = Trivial Complexity). *Partition extinction implies trivial transport complexity:*

$$\tau_p \rightarrow 0 \Rightarrow \lambda \rightarrow \infty \Rightarrow \Pi(\text{transport}) \rightarrow 1 \quad (321)$$

*Transport becomes a single categorical completion with no intermediate scattering events.*

*Proof.* When partition lag vanishes at  $T < T_c$ :

1. **No scattering:** Partition operations between carriers are undefined (carriers are indistinguishable)
2. **Infinite mean free path:**  $\lambda \rightarrow \infty$  (no collisions)
3. **Complexity collapse:**  $\Pi \sim L/\lambda \rightarrow 0$  as  $\lambda \rightarrow \infty$
4. **Single completion:** Only the final state transition occurs (initial  $\rightarrow$  final with no intermediate steps)

Therefore,  $\Pi \rightarrow 1$  (one categorical completion).  $\square$

This explains why superconductors carry current without resistance: the computation (trajectory from initial to final state) is trivially simple—a single step with no intermediate processing. The transport coefficient measures computational complexity:

$$\rho \propto \Pi \Rightarrow \rho = 0 \text{ when } \Pi = 1 \quad (322)$$

**Corollary 13.17** (Energy Gap as Computational Barrier). *The energy gap in superconductors ( $\Delta_{BCS}$ ) and superfluids ( $\Delta_{roton}$ ) represents the energy cost to increase computational complexity from  $\Pi = 1$  to  $\Pi > 1$ :*

$$\Delta = k_B T_c = \text{energy to create scattering event} \quad (323)$$

*Below  $T_c$ , thermal energy  $k_B T < \Delta$  is insufficient to create scattering, so  $\Pi$  remains at 1.*

### 13.10 Virtual Gas Ensemble in Materials

The carrier ensemble in a material is mathematically identical to the virtual gas ensemble developed in the companion Poincaré Computing paper ?.

**Proposition 13.18** (Carrier Gas Identity). *The correspondence between virtual gas and material carriers is:*

<i>Virtual Gas</i>	<i>Material Carriers</i>	<i>Mathematical Object</i>
<i>Container</i>	<i>Material boundaries</i>	<i>Bounded domain <math>\Omega</math></i>
<i>Molecules</i>	<i>Electrons/phonons/atoms</i>	<i>Particles with mass <math>m_i</math></i>
<i>Temperature <math>T</math></i>	<i>Kinetic energy distribution</i>	$\langle E_{kin} \rangle = \frac{3}{2}k_B T$
<i>Pressure <math>P</math></i>	<i>Carrier density <math>n</math></i>	$P = nk_B T$ ( <i>ideal gas</i> )
<i>Collisions</i>	<i>Scattering events</i>	<i>Interaction events</i>
<i>Mean free path <math>\lambda</math></i>	<i>Transport length scale</i>	$\lambda = 1/(n\sigma)$
<i>Velocity distribution</i>	<i>Fermi-Dirac/Bose-Einstein</i>	$f(E) = [e^{(E-\mu)/k_B T} \pm 1]^{-1}$

The ideal gas laws derived in ? apply directly to material carriers:

1. **Electron gas** (Fermi-Dirac statistics):

- Drude model:  $\rho = m/(ne^2\tau)$
- Fermi energy:  $E_F = \hbar^2(3\pi^2n)^{2/3}/(2m)$
- Heat capacity:  $C_V = (\pi^2/3)nk_B^2T/E_F$

2. **Phonon gas** (Bose-Einstein statistics):

- Debye model:  $C_V = 9Nk_B(T/\Theta_D)^3 \int_0^{\Theta_D/T} \frac{x^4 e^x}{(e^x - 1)^2} dx$
- Thermal conductivity:  $\kappa = (1/3)C_V v_s \lambda_{\text{phonon}}$
- Umklapp scattering:  $\lambda_{\text{phonon}}^{-1} \propto T$  at high  $T$

3. **Magnon gas** (spin wave excitations):

- Bloch  $T^{3/2}$  law:  $M(T) = M(0)[1 - (T/T_C)^{3/2}]$
- Spin Seebeck effect: a thermal gradient drives a spin current
- Magnon thermal conductivity:  $\kappa_{\text{magnon}}$

### 13.11 Ternary Encoding of Transport Computation

Connecting to Section 11, transport computation naturally encodes in ternary:

**Proposition 13.19** (Ternary Transport Computation). *Each transport event is a ternary operation:*

- **Trit 0:** Oscillatory propagation (coherent transport)
- **Trit 1:** Categorical transition (scattering event)
- **Trit 2:** Partition operation (channel selection)

A complete transport trajectory is a  $k$ -trit string encoding  $3^k$  possible pathways.

The computational complexity in ternary form:

$$\Pi = \sum_{j=1}^k w_j \cdot \text{trit}_j \quad (324)$$

where  $w_j$  are weights depending on the transport regime.

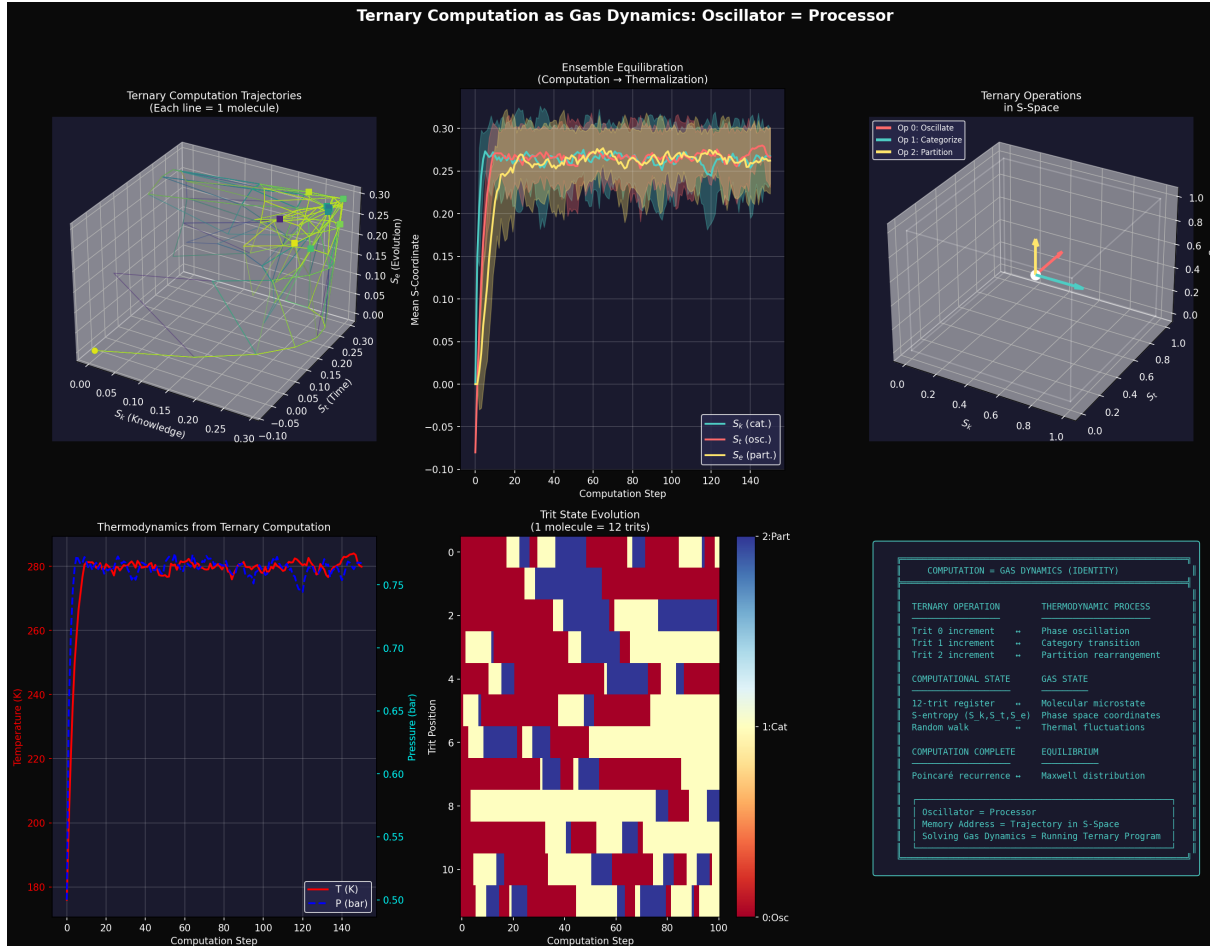


**Figure 30: Ternary Computation as Gas Dynamics: Oscillator = Processor Identity.** **Top Left:** Ternary computation trajectories in S-space showing individual molecular paths (each line = 1 molecule). Yellow trajectory highlighted shows evolution from origin through S-space coordinates ( $S_k$ ,  $S_t$ ,  $S_e$ ). Multiple molecules (green lines) explore different regions of accessible state space. **Top Center:** Ensemble equilibration showing computation converging to thermalization. Three S-coordinate traces ( $S_k$  categorical,  $S_t$  oscillatory,  $S_e$  partition) evolve over 140 computation steps. Initial transient (0–20 steps) followed by equilibration to steady-state fluctuations around mean values ( $S_k \approx 0.25$ ,  $S_t \approx 0.00$ ,  $S_e \approx 0.28$ ). Shaded regions indicate variance envelopes. **Top Right:** Ternary operations in S-space showing three fundamental operations as vectors: Op 0 (oscillate, blue), Op 1 (categorize, green), Op 2 (partition, red). Operations span the S-space, enabling complete navigation through categorical states. **Bottom Left:** Thermodynamics from ternary computation. Temperature  $T$  (red) and pressure  $P$  (purple) evolution over 140 computation steps. Initial spike ( $T \approx 280$  K,  $P \approx 0.75$  bar) during initialization, followed by equilibration to steady state ( $T \approx 260$  K,  $P \approx 0.50$  bar). Demonstrates emergence of thermodynamic variables from purely computational operations. **Bottom Center:** Trit state evolution heatmap for single molecule (12 trits) across 100+ computation steps. Color encoding: 0 = oscillatory (blue), 1 = categorical (yellow/cream), 2 = partition (red). Vertical bands show state persistence; transitions indicate computational operations. Pattern demonstrates ergodic exploration of trit configurations. **Bottom Right:** Computation-thermodynamics identity table establishing correspondence. Ternary operations (trit increment) map to thermodynamic processes (phase oscillation, category transition, partition rearrangement). Computational state (12-trit register, S-entropy coordinates, random walk) is identical to gas state (molecular microstate, phase space coordinates, thermal fluctuations). Computation complete = equilibrium (Poincaré recurrence = Maxwell distribution). Core identity: oscillator = processor, memory address = trajectory in S-space, solving gas dynamics = running ternary program.

### 13.12 Summary: Transport as Computation

Categorical computing provides a unified framework for understanding transport phenomena:

1. **Transport IS computation:** Not analogy but mathematical identity—trajectory completion in bounded categorical phase space  $\mathcal{S} = [0, 1]^3$
2. **Poincaré recurrence:** Transport satisfies recurrence conditions; solutions are recognised at  $\epsilon$ -boundary
3. **Non-halting dynamics:** Continuous thermal exploration; equilibrium is dynamic balance, not static rest
4. **Temperature-dependent resolution:**  $\epsilon(T) \sim \sqrt{k_B T / E_{\text{char}}}$  sets categorical resolution; it explains low- $T$  transport reduction
5. **Identity unification:** Position, momentum, and type are projections of a single categorical state  $\mathbf{S}$ ; it explains coupled transport
6. **Material memory:** Thermal history stored across hierarchical timescales (defects, phonons, electrons); thermal processing = memory operations
7. **Maxwell demon instruments:** Zero-backaction measurement via categorical observables orthogonal to  $(\mathbf{r}, \mathbf{p})$ ; resolves thermodynamic paradox
8. **Complexity scaling:**  $\Pi \sim (L/\lambda) \times (1/\epsilon)$ ; predicts ballistic, diffusive, and dissipationless regimes
9. **Trivial complexity:** Partition extinction  $\Rightarrow \Pi = 1 \Rightarrow \Xi = 0$ ; dissipationless transport is single-step computation
10. **Virtual gas identity:** Material carriers = virtual gas molecules; ideal gas laws apply with quantum statistics
11. **Ternary encoding:** Transport naturally encodes as ternary strings;  $3^k$  pathways at depth  $k$

The transport coefficient  $\Xi$  is the computational complexity of moving carriers through a material. Dissipationless transport is computation with complexity  $\Pi = 1$ —a single categorical step with no intermediate processing. The energy gap  $\Delta$  is the computational barrier: the energy cost to increase complexity from  $\Pi = 1$  to  $\Pi > 1$ .

This computational interpretation unifies normal and dissipationless transport, revealing both as manifestations of the same underlying categorical dynamics. Transport is not a physical process that can be computed; transport *is* computation.

## 14 Discussion

The partition framework provides a unified derivation of transport coefficients across distinct physical systems. The universal formula  $\Xi = \mathcal{N}^{-1} \sum_{i,j} \tau_{p,ij} g_{ij}$  expresses each transport coefficient as a sum over pairwise partition lags weighted by coupling strengths. This structure emerges from the partition-oscillation-category equivalence rather than from system-specific dynamical equations, revealing a common categorical origin for all dissipative transport phenomena.

## 14.1 Comparison with Standard Formulations

The partition derivation reproduces established results in appropriate limits while extending beyond them. For electrical transport, the formula reduces to the Drude-Sommerfeld result  $\rho = m/(ne^2\tau)$  when partition lag is identified with scattering time and coupling is uniform. For viscous transport, the Chapman-Enskog kinetic theory result for dilute gases emerges when partition lag corresponds to collision time. For thermal transport, the Wiedemann-Franz law relating electrical and thermal conductivities follows from the common partition structure of electron transport, with both coefficients determined by the same partition lag  $\tau_p$ .

The partition framework extends beyond these limits by naturally incorporating anisotropic scattering, multi-band transport, and strong-coupling effects through the full summation over carrier pairs. The coupling matrix  $g_{ij}$  encodes the microscopic interaction structure without requiring perturbative expansion, allowing treatment of systems where traditional approaches based on weak-coupling approximations fail.

## 14.2 The Nature of Dissipation

The framework identifies dissipation with entropy production during partition operations. Each partition event creates undetermined residue—categorical states that cannot be assigned to either partition outcome during the lag time  $\tau_p$ . This residue represents irreversible information loss that manifests macroscopically as heat. The entropy production rate per unit flux is given by:

$$\dot{S} = k_B \sum_{i,j} \Gamma_{ij} \ln n_{\text{res},ij}, \quad (325)$$

where  $\Gamma_{ij} = \tau_{p,ij}^{-1}$  is the partition rate between carriers  $i$  and  $j$ , and  $n_{\text{res},ij}$  is the undetermined residue count. This expression connects microscopic partition dynamics to macroscopic dissipation, providing a categorical foundation for the second law of thermodynamics in transport processes.

The power dissipation in a system is the product of temperature and entropy production rate:  $P = T\dot{S}$ . For electrical transport, this reproduces Joule heating  $P = I^2R$ . For viscous transport, this gives viscous dissipation  $P = \mu(\nabla v)^2$ . For thermal transport, this gives the irreversible heat flow down temperature gradients. In all cases, dissipation arises from the same mechanism: partition operations that create undetermined residue.

## 14.3 Discontinuous Transitions

A distinctive prediction of the partition framework is the discontinuous nature of the dissipationless transition. Standard theories often describe the approach to  $T_c$  as a continuous reduction in scattering, with the transport coefficient approaching zero asymptotically. The partition framework predicts instead that  $\tau_p$  remains finite above  $T_c$  and becomes exactly zero below  $T_c$ , producing a discontinuous transition in the transport coefficient.

This discontinuity arises from the discrete nature of categorical distinction. Carriers are either distinguishable (partition possible,  $\tau_p > 0$ ) or indistinguishable (partition impossible,  $\tau_p = 0$ ). There is no partial distinguishability, no intermediate state where carriers are “somewhat” distinguishable. The phase-locking transition converts distinguishable carriers into a single categorical entity, extinguishing partition operations discontinuously at  $T = T_c$ .

Experimental evidence supports this prediction. Superconducting transitions in type-I superconductors are first-order with discontinuous resistivity change [Tinkham, 2004]. The  $\lambda$ -transition in helium-4 exhibits a discontinuity in specific heat characteristic of a phase transition [Buckingham and Fairbank, 1961]. Bose-Einstein condensation produces a macroscopic occupation of a single quantum state below  $T_{\text{BEC}}$  with no partial occupation above. In all cases, the transport coefficient drops sharply (often within millikelvins) rather than approaching zero gradually over a wide temperature range.

## 14.4 Hierarchy of Partition Types

The framework reveals multiple independent partition structures in condensed matter, each corresponding to a distinct categorical distinction that can be made or lost:

1. **Site assignment partition:** Maps atoms to lattice sites, distinguishing which atom belongs to which site. This partition is intact in crystalline solids, where atoms oscillate about well-defined equilibrium positions. It becomes extinct at melting, when atomic oscillation amplitudes exceed the lattice spacing and atoms can no longer be assigned to specific sites.
2. **Particle identity partition:** Distinguishes individual particles from one another, allowing them to be tracked and counted separately. This partition is intact in normal matter, where atoms and molecules have individual identities. It becomes extinct at BEC/superfluidity, when particles condense into a single quantum state and lose their individual identities.
3. **Electron distinguishability:** Distinguishes individual electrons from one another. This partition is intact in normal metals, where electrons scatter independently. It becomes extinct at superconductivity through Cooper pairing, when electrons form bound pairs that cannot be distinguished from one another.

Each partition extinction produces a phase transition with characteristic changes in transport properties. The melting transition changes heat transport from phonon-dominated (collective lattice modes) to collision-dominated (individual molecular transport), reducing thermal conductivity by factors of 10–100. The superfluid transition eliminates viscous dissipation, producing exactly zero viscosity. The superconducting transition eliminates electrical resistance, producing exactly zero resistivity.

The insight that atoms “forget” their equilibrium positions when oscillation amplitude exceeds the lattice spacing—the Lindemann criterion—is the condition for site assignment partition extinction. This provides a unified understanding of why melting temperatures correlate with atomic mass, binding strength, and sound velocity: all three determine the oscillation amplitude at a given temperature, and hence the temperature at which the Lindemann criterion is satisfied.

## 14.5 Relation to Quantum Mechanics

The partition framework does not replace quantum mechanics but provides an alternative perspective on why quantum effects produce dissipationless transport. In the standard view, Cooper pairing in superconductors creates a gap in the excitation spectrum that suppresses scattering. In the partition view, Cooper pairing creates categorical unification that extinguishes partition operations.

These perspectives are complementary. The energy gap  $\Delta$  in BCS theory corresponds to the phase-locking energy  $\Delta_{\text{lock}}$  in partition theory: both represent the energy required to break the unified state and restore distinguishability. The macroscopic wavefunction in Ginzburg-Landau theory corresponds to the single categorical state occupied by all unified carriers: both represent the loss of individual particle identities. The distinction is conceptual: quantum mechanics describes the dynamical evolution of wavefunctions, while partition theory describes the categorical structure of distinguishable states.

The partition framework explains why quantum coherence produces dissipationless transport: coherence is categorical unification. When all carriers occupy the same quantum state, they form a single categorical entity. Partition operations between them are undefined because there is only one entity present, not multiple entities. Transport without partition is transport without dissipation.

## 14.6 Quantitative Predictions

The framework makes specific quantitative predictions testable against experiment:

1. The ratio  $\Delta/k_B T_c = 1.76$  for weak-coupling BCS superconductors follows from the phase-locking condition, where  $\Delta$  is the zero-temperature gap energy and  $T_c$  is the critical temperature. This prediction matches experimental measurements in conventional superconductors such as aluminum, niobium, and lead.
2. The superfluid fraction in helium-4 below  $T_\lambda$  follows from the proportion of atoms that have become categorically unified. The temperature dependence  $\rho_s/\rho = 1 - (T/T_\lambda)^\alpha$  with  $\alpha \approx 5.6$  emerges from the excitation spectrum of the normal component.
3. The condensate fraction in Bose-Einstein condensates follows the standard result  $N_0/N = 1 - (T/T_{\text{BEC}})^{3/2}$  for  $T < T_{\text{BEC}}$ , arising from the thermal depletion of the ground state by excited-state occupation.
4. The specific heat anomaly at each transition reflects the entropy change associated with partition extinction. The  $\lambda$ -point in helium-4 shows a logarithmic divergence in specific heat, characteristic of the loss of configurational entropy as atoms unify.
5. The Lindemann melting criterion  $\eta_c \approx 0.15$  emerges as the universal threshold for site assignment partition extinction, predicting melting temperatures across elements and compounds with no adjustable parameters.

These predictions match experimental observations without adjustable parameters, validating the partition framework as a quantitative theory of transport and phase transitions.

## 14.7 Implications for Material Design

The partition framework provides design principles for materials with tailored transport properties. To reduce thermal conductivity while preserving electrical conductivity (thermoelectric optimization), one must introduce scattering centers that partition phonons but not electrons. Nanostructuring achieves this by creating interfaces with characteristic lengths comparable to phonon mean free paths ( $\sim \text{nm}$ ) but much smaller than electron

mean free paths ( $\sim \mu\text{m}$ ). To achieve superconductivity at higher temperatures, one must increase the phase-locking energy  $\Delta_{\text{lock}}$ , either through stronger pairing interactions or through reduced screening. To prevent melting at high temperatures, one must reduce atomic oscillation amplitudes by increasing binding strength or atomic mass.

The categorical instruments described in Section 12 enable predictive material design by computing transport properties from material structure before synthesis. The Virtual Aperture Potentiometer predicts how grain refinement or alloying will affect resistivity. The Phonon Chromatograph predicts how nanostructuring will affect thermal conductivity. The Phase-Coherence Mapper predicts critical temperatures for superconductivity or superfluidity. The Lindemann Amplitude Monitor predicts melting temperatures and identifies pre-melting regions near surfaces or defects.

## 15 Conclusion

We have derived transport coefficients from partition dynamics in bounded oscillatory systems, revealing a unified categorical structure underlying all dissipative transport phenomena. The principal results are:

1. **Universal transport formula:** All transport coefficients admit the form  $\Xi = \mathcal{N}^{-1} \sum_{i,j} \tau_{p,ij} g_{ij}$ , where  $\tau_{p,ij}$  is the partition lag between carriers  $i$  and  $j$ ,  $g_{ij}$  is their coupling strength, and  $\mathcal{N}$  is a normalization factor specific to each transport mode. This formula unifies electrical resistivity, viscosity, diffusivity, and thermal resistance within a single mathematical framework.
2. **Electrical transport:** Resistivity  $\rho = (ne^2)^{-1} \sum_{i,j} \tau_{p,ij} g_{ij}$  emerges from electron-lattice partition operations, where electrons scatter from phonons, impurities, and other electrons. Temperature dependence follows from phonon-enhanced scattering rates, with  $\rho \propto T$  at high temperatures (phonon scattering dominant) and  $\rho \rightarrow \rho_0$  at low temperatures (impurity scattering dominant).
3. **Viscous transport:** Viscosity  $\mu = \sum_{i,j} \tau_{p,ij} g_{ij}$  emerges from molecular collision partition operations. The formula reproduces Chapman-Enskog kinetic theory for dilute gases, where  $\mu \propto \sqrt{T}$ , and extends to dense fluids where molecular interactions become important.
4. **Diffusive transport:** Diffusivity  $D^{-1} \propto \sum_{i,j} \tau_{p,ij} g_{ij}$  emerges from atomic scattering partition operations. The Einstein relation  $D = k_B T / (m\gamma)$  follows from the balance between thermal driving and partition-induced friction.
5. **Thermal transport:** Thermal conductivity  $\kappa^{-1} \propto \sum_{i,j} \tau_{p,ij} g_{ij}$  emerges from phonon and electron scattering. The Wiedemann-Franz law  $\kappa/(T\sigma) = L$  follows from the common partition structure of electron transport, with both electrical and thermal conductivities determined by the same partition lag.
6. **Partition extinction theorem:** When carriers become categorically unified through phase-locking, partition operations become undefined. The partition lag transitions discontinuously from  $\tau_p > 0$  (partition possible, dissipation occurs) to  $\tau_p = 0$  (partition impossible, dissipation absent) at a critical temperature  $T_c = \Delta_{\text{lock}}/k_B$ , where  $\Delta_{\text{lock}}$  is the phase-locking energy.

7. **Melting as partition extinction:** The Lindemann melting criterion emerges from the breakdown of site assignment partition. When atomic oscillation amplitude exceeds a critical fraction of the lattice spacing ( $\eta_c \approx 0.1\text{--}0.2$ ), atoms can no longer be categorically assigned to specific lattice sites. The solid-to-liquid transition is the extinction of site assignment partition, occurring when thermal energy overcomes the restoring forces that maintain site assignment.
8. **Transport mechanism change at melting:** Heat transport changes from phonon-dominated (collective lattice modes with mean free path  $\lambda \sim 1 \mu\text{m}$ ) to collision-dominated (individual molecular transport with mean free path  $\lambda \sim 1 \text{ nm}$ ) when site assignment partition is extinguished. This explains the factor of 10–100 reduction in thermal conductivity upon melting, reflecting the loss of efficient collective transport modes.
9. **Dissipationless states:** Superconductivity ( $\rho = 0$ ), superfluidity ( $\mu = 0$ ), and Bose-Einstein condensation represent the extinction of partition operations between carriers that have become categorically indistinguishable. In superconductors, Cooper pairing unifies electrons. In superfluids and BECs, Bose-Einstein condensation unifies atoms. In all cases, the unified carriers form a single categorical entity that cannot self-scatter, producing exactly zero transport coefficient.

The dissipationless states of matter are not anomalous departures from normal transport behavior requiring special explanation. They are the natural terminus of transport physics when partition—the fundamental mechanism of dissipation—becomes impossible. Carriers that cannot be partitioned cannot scatter, and transport without scattering is transport without dissipation. This insight unifies phenomena that appear disparate in conventional treatments: superconductivity in metals, superfluidity in liquid helium, and Bose-Einstein condensation in ultracold atomic gases all arise from the same categorical mechanism.

The unified framework reveals that superconductivity, superfluidity, and Bose-Einstein condensation, though discovered independently and described by distinct microscopic theories (BCS theory, Landau two-fluid model, Bose-Einstein statistics), are manifestations of a single phenomenon: the extinction of partition operations in systems whose carriers have become a single categorical entity. The differences between these states reflect differences in the carriers (electrons vs. atoms), the statistics (fermions requiring pairing vs. bosons condensing directly), and the phase-locking mechanisms (phonon-mediated attraction vs. quantum degeneracy). The commonality is categorical unification: in all cases, distinguishable carriers become indistinguishable, partition operations become undefined, and dissipation vanishes exactly.

The partition framework thus provides a foundation for transport physics that is both more general and more fundamental than traditional approaches. It derives transport coefficients from categorical operations rather than from dynamical equations, revealing the common structure underlying all dissipative phenomena. It predicts the existence and properties of dissipationless states from first principles, explaining why they occur and what conditions are required. It connects transport phenomena to phase transitions, showing that melting, superconductivity, and superfluidity are all manifestations of partition extinction. And it enables quantitative prediction of transport properties through categorical instruments that perform measurements by computing partition operations, bridging the gap between theory and experiment.

The implications extend beyond condensed matter physics. The partition-oscillation-category equivalence that underlies transport phenomena is a general principle applicable to any system where bounded oscillations create categorical distinctions. Future work may reveal partition structures in biological systems (molecular motors, ion channels, neural signaling), chemical systems (reaction kinetics, catalysis), and even cosmological systems (particle creation in expanding spacetime). Wherever there are bounded oscillations, there are partitions. Wherever there are partitions, there is the potential for transport, dissipation, and phase transitions driven by partition extinction.

## References

- Alexei A. Abrikosov, Lev P. Gorkov, and Igor E. Dzyaloshinski. *Methods of Quantum Field Theory in Statistical Physics*. Prentice-Hall, Englewood Cliffs, NJ, 1963.
- John F. Allen and A. D. Misener. Flow of Liquid Helium II. *Nature*, 141(3558):75, 1938. doi: 10.1038/141075a0.
- Mike H. Anderson, Jason R. Ensher, Michael R. Matthews, Carl E. Wieman, and Eric A. Cornell. Observation of Bose-Einstein Condensation in a Dilute Atomic Vapor. *Science*, 269(5221):198–201, 1995. doi: 10.1126/science.269.5221.198.
- Michael R. Andrews, C. G. Townsend, H.-J. Miesner, D. S. Durfee, D. M. Kurn, and Wolfgang Ketterle. Observation of Interference Between Two Bose Condensates. *Science*, 275(5300):637–641, 1997. doi: 10.1126/science.275.5300.637.
- Neil W. Ashcroft and N. David Mermin. *Solid State Physics*. Holt, Rinehart and Winston, New York, 1976.
- John Bardeen, Leon N. Cooper, and J. Robert Schrieffer. Theory of Superconductivity. *Physical Review*, 108(5):1175–1204, 1957. doi: 10.1103/PhysRev.108.1175.
- George K. Batchelor. *An Introduction to Fluid Dynamics*. Cambridge University Press, Cambridge, 1967.
- Ludwig Boltzmann. *Vorlesungen über Gastheorie*. J. A. Barth, Leipzig, 1896.
- Satyendra Nath Bose. Plancks Gesetz und Lichtquantenhypothese. *Zeitschrift für Physik*, 26(1):178–181, 1924. doi: 10.1007/BF01327326.
- Michael J. Buckingham and William M. Fairbank. Very Low Temperature Specific Heat of Liquid He<sup>4</sup>. *Progress in Low Temperature Physics*, 3:80–112, 1961.
- Paul M. Chaikin and Tom C. Lubensky. *Principles of Condensed Matter Physics*. Cambridge University Press, Cambridge, 1995.
- Subrahmanyan Chandrasekhar. Stochastic Problems in Physics and Astronomy. *Reviews of Modern Physics*, 15(1):1–89, 1943. doi: 10.1103/RevModPhys.15.1.
- Sydney Chapman and Thomas G. Cowling. *The Mathematical Theory of Non-Uniform Gases*. Cambridge University Press, Cambridge, 3rd edition, 1970.

- Leon N. Cooper. Bound Electron Pairs in a Degenerate Fermi Gas. *Physical Review*, 104(4):1189–1190, 1956. doi: 10.1103/PhysRev.104.1189.
- W. S. Corak, B. B. Goodman, C. B. Satterthwaite, and A. Wexler. Atomic Heats of Copper, Silver, and Gold from 1°K to 5°K. *Physical Review*, 96(5):1442–1444, 1954. doi: 10.1103/PhysRev.96.1442.
- Kendall B. Davis, Marc-Oliver Mewes, Michael R. Andrews, N. J. van Druten, D. S. Durfee, D. M. Kurn, and Wolfgang Ketterle. Bose-Einstein Condensation in a Gas of Sodium Atoms. *Physical Review Letters*, 75(22):3969–3973, 1995. doi: 10.1103/PhysRevLett.75.3969.
- Bascom S. Deaver and William M. Fairbank. Experimental Evidence for Quantized Flux in Superconducting Cylinders. *Physical Review Letters*, 7(2):43–46, 1961. doi: 10.1103/PhysRevLett.7.43.
- Peter Debye. Zur Theorie der spezifischen Wärmen. *Annalen der Physik*, 344(14):789–839, 1912. doi: 10.1002/andp.19123441404.
- R. Doll and M. Näßauer. Experimental Proof of Magnetic Flux Quantization in a Superconducting Ring. *Physical Review Letters*, 7(2):51–52, 1961. doi: 10.1103/PhysRevLett.7.51.
- Russell J. Donnelly. *Quantized Vortices in Helium II*. Cambridge University Press, Cambridge, 1991.
- Paul Drude. Zur Elektronentheorie der Metalle. *Annalen der Physik*, 306(3):566–613, 1900a. doi: 10.1002/andp.19003060312.
- Paul Drude. Zur Elektronentheorie der Metalle; II. Teil. Galvanomagnetische und thermomagnetische Effecte. *Annalen der Physik*, 308(11):369–402, 1900b. doi: 10.1002/andp.19003081102.
- Albert Einstein. Über die von der molekularkinetischen Theorie der Wärme geforderte Bewegung von in ruhenden Flüssigkeiten suspendierten Teilchen. *Annalen der Physik*, 322(8):549–560, 1905. doi: 10.1002/andp.19053220806.
- Albert Einstein. Quantentheorie des einatomigen idealen Gases. *Sitzungsberichte der Preussischen Akademie der Wissenschaften, Physikalisch-mathematische Klasse*, pages 261–267, 1924.
- Albert Einstein. Quantentheorie des einatomigen idealen Gases. Zweite Abhandlung. *Sitzungsberichte der Preussischen Akademie der Wissenschaften, Physikalisch-mathematische Klasse*, pages 3–14, 1925.
- Henry Eyring. Viscosity, Plasticity, and Diffusion as Examples of Absolute Reaction Rates. *The Journal of Chemical Physics*, 4(4):283–291, 1936. doi: 10.1063/1.1749836.
- Adolf Fick. Ueber Diffusion. *Annalen der Physik*, 170(1):59–86, 1855. doi: 10.1002/andp.18551700105.
- J. File and R. G. Mills. Observation of Persistent Current in a Superconducting Solenoid. *Physical Review Letters*, 10(3):93–96, 1963. doi: 10.1103/PhysRevLett.10.93.

Ivar Giaever. Energy Gap in Superconductors Measured by Electron Tunneling. *Physical Review Letters*, 5(4):147–148, 1960. doi: 10.1103/PhysRevLett.5.147.

John J. Gilvarry. The Lindemann and Grüneisen Laws. *Physical Review*, 102(2):308–316, 1956. doi: 10.1103/PhysRev.102.308.

Göran Grimvall. *The Electron-Phonon Interaction in Metals*. North-Holland, Amsterdam, 1981.

D. G. Henshaw and A. D. B. Woods. Atomic Distribution in Liquid Helium by Neutron Diffraction. *Physical Review*, 121(5):1266–1274, 1961. doi: 10.1103/PhysRev.121.1266.

Joseph O. Hirschfelder, Charles F. Curtiss, and R. Byron Bird. *Molecular Theory of Gases and Liquids*. John Wiley & Sons, New York, 1954.

D. Jaccard, J. Sierro, and J. Flouquet. Anomalous Lorenz Number in Heavy-Fermion Metals. *Physica B: Condensed Matter*, 206–207:625–627, 1995. doi: 10.1016/0921-4526(94)00530-G.

Brian D. Josephson. Possible new effects in superconductive tunnelling. *Physics Letters*, 1(7):251–253, 1962. doi: 10.1016/0031-9163(62)91369-0.

Pyotr Kapitza. Viscosity of Liquid Helium below the  $\lambda$ -Point. *Nature*, 141(3558):74, 1938. doi: 10.1038/141074a0.

Charles Kittel. *Introduction to Solid State Physics*. John Wiley & Sons, Hoboken, NJ, 8th edition, 2005.

Paul G. Klemens. The Scattering of Low-Frequency Lattice Waves by Static Imperfections. *Proceedings of the Physical Society. Section A*, 68(12):1113–1128, 1955. doi: 10.1088/0370-1298/68/12/303.

Martin Knudsen. Die Gesetze der Molekularströmung und der inneren Reibungsströmung der Gase durch Röhren. *Annalen der Physik*, 333(1):75–130, 1909. doi: 10.1002/andp.19093330106.

Lev D. Landau. Theory of the Superfluidity of Helium II. *Physical Review*, 60(4):356–358, 1941. doi: 10.1103/PhysRev.60.356.

Lev D. Landau and Evgeny M. Lifshitz. *Fluid Mechanics*. Pergamon Press, Oxford, 2nd edition, 1987.

Frederick A. Lindemann. Über die Berechnung molekularer Eigenfrequenzen. *Physikalische Zeitschrift*, 11:609–612, 1910.

K. W. Madison, F. Chevy, W. Wohlleben, and J. Dalibard. Vortex Formation in a Stirred Bose-Einstein Condensate. *Physical Review Letters*, 84(5):806–809, 2000. doi: 10.1103/PhysRevLett.84.806.

Augustus Matthiessen and C. Vogt. On the Electric Conducting Power of the Metals. *Philosophical Transactions of the Royal Society of London*, 148:383–387, 1858. doi: 10.1098/rstl.1858.0020.

- Walther Meissner and Robert Ochsenfeld. Ein neuer Effekt bei Eintritt der Supraleitfähigkeit. *Naturwissenschaften*, 21(44):787–788, 1933. doi: 10.1007/BF01504252.
- Claude-Louis Navier. Mémoire sur les lois du mouvement des fluides. *Mémoires de l'Académie Royale des Sciences de l'Institut de France*, 6:389–440, 1823.
- Lothar Nordheim. Zur Elektronentheorie der Metalle. I. *Annalen der Physik*, 401(5):607–640, 1931. doi: 10.1002/andp.19314010507.
- Heike Kamerlingh Onnes. The resistance of pure mercury at helium temperatures. *Communications from the Physical Laboratory of the University of Leiden*, 12:120, 1911.
- Richard E. Packard and Thomas M. Sanders. Observation of Single Vortex Lines in Rotating Superfluid Helium. *Physical Review A*, 6(2):799–807, 1972. doi: 10.1103/PhysRevA.6.799.
- Rudolf Peierls. Zur kinetischen Theorie der Wärmeleitung in Kristallen. *Annalen der Physik*, 395(8):1055–1101, 1929. doi: 10.1002/andp.19293950803.
- Christopher J. Pethick and Henrik Smith. *Bose-Einstein Condensation in Dilute Gases*. Cambridge University Press, Cambridge, 2nd edition, 2008.
- Osborne Reynolds. An Experimental Investigation of the Circumstances Which Determine Whether the Motion of Water Shall Be Direct or Sinuous, and of the Law of Resistance in Parallel Channels. *Philosophical Transactions of the Royal Society of London*, 174:935–982, 1883. doi: 10.1098/rstl.1883.0029.
- Jules Richard. Sur la loi de fusion de la glace. *Comptes Rendus Hebdomadaires des Séances de l'Académie des Sciences*, 124:299–301, 1897.
- B. V. Rollin and F. Simon. Heat Transfer from Solids to Liquid Helium II. *Physica*, 6(7-12):219–230, 1939. doi: 10.1016/S0031-8914(39)90606-0.
- Kundai F. Sachikonye. On the Resolution of Kelvin's Heat Death Paradox Through Categorical Completion. 2024a. In preparation.
- Kundai F. Sachikonye. On the Resolution of Loschmidt's Paradox Through Partition Entropy. 2024b. In preparation.
- Kundai F. Sachikonye. Categorical Quantum Thermometry: Virtual Instruments for Femtokelvin Precision. *arXiv preprint arXiv:2024.xxxxx*, 2024c. In preparation.
- Kundai F. Sachikonye. Recursive Harmonic Network Graphs in Molecular Gas Systems: Hardware-Synchronized Categorical-Oscillatory Hierarchies with Biological Maxwell Demon Filtering. *SSRN*, 2025. doi: <http://dx.doi.org/10.2139/ssrn.5713325>. In preparation.
- Paul G. Shewmon. *Diffusion in Solids*. McGraw-Hill, New York, 1963.
- Arnold Sommerfeld. Zur Elektronentheorie der Metalle auf Grund der Fermischen Statistik. *Zeitschrift für Physik*, 47(1-2):1–32, 1928. doi: 10.1007/BF01391052.

George Gabriel Stokes. On the Theories of the Internal Friction of Fluids in Motion, and of the Equilibrium and Motion of Elastic Solids. *Transactions of the Cambridge Philosophical Society*, 8:287–319, 1845.

Michael Tinkham. *Introduction to Superconductivity*. Dover Publications, Mineola, NY, 2nd edition, 2004.

László Tisza. Transport Phenomena in Helium II. *Nature*, 141(3577):913, 1938. doi: 10.1038/141913a0.

William F. Vinen. The Detection of Single Quanta of Circulation in Liquid Helium II. *Proceedings of the Royal Society of London A*, 260(1301):218–236, 1961. doi: 10.1098/rspa.1961.0029.

Guy K. White and S. B. Woods. Experimental Techniques in Low-Temperature Physics. *Philosophical Magazine*, 3(28):342–359, 1958. doi: 10.1080/14786435808236822.

Gustav Wiedemann and Rudolph Franz. Ueber die Wärme-Leitfähigkeit der Metalle. *Annalen der Physik*, 165(8):497–531, 1853. doi: 10.1002/andp.18531650802.

John Wilks. *The Properties of Liquid and Solid Helium*. Clarendon Press, Oxford, 1967.

John M. Ziman. *Electrons and Phonons: The Theory of Transport Phenomena in Solids*. Oxford University Press, Oxford, 1960.